



**Journal of
Mechanics of
Materials and Structures**

Volume 5, No. 5

May 2010

JOURNAL OF MECHANICS OF MATERIALS AND STRUCTURES

<http://www.jomms.org>

Founded by Charles R. Steele and Marie-Louise Steele

EDITORS

CHARLES R. STEELE Stanford University, U.S.A.
DAVIDE BIGONI University of Trento, Italy
IWONA JASIUK University of Illinois at Urbana-Champaign, U.S.A.
YASUhide SHINDO Tohoku University, Japan

EDITORIAL BOARD

H. D. BUI École Polytechnique, France
J. P. CARTER University of Sydney, Australia
R. M. CHRISTENSEN Stanford University, U.S.A.
G. M. L. GLADWELL University of Waterloo, Canada
D. H. HODGES Georgia Institute of Technology, U.S.A.
J. HUTCHINSON Harvard University, U.S.A.
C. HWU National Cheng Kung University, R.O. China
B. L. KARIHALOO University of Wales, U.K.
Y. Y. KIM Seoul National University, Republic of Korea
Z. MROZ Academy of Science, Poland
D. PAMPLONA Universidade Católica do Rio de Janeiro, Brazil
M. B. RUBIN Technion, Haifa, Israel
A. N. SHUPIKOV Ukrainian Academy of Sciences, Ukraine
T. TARNAI University Budapest, Hungary
F. Y. M. WAN University of California, Irvine, U.S.A.
P. WRIGGERS Universität Hannover, Germany
W. YANG Tsinghua University, P.R. China
F. ZIEGLER Technische Universität Wien, Austria

PRODUCTION

PAULO NEY DE SOUZA Production Manager
SHEILA NEWBERY Senior Production Editor
SILVIO LEVY Scientific Editor

Cover design: Alex Scorpan

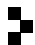
Cover photo: Wikimedia Commons

See inside back cover or <http://www.jomms.org> for submission guidelines.

JoMMS (ISSN 1559-3959) is published in 10 issues a year. The subscription price for 2010 is US \$500/year for the electronic version, and \$660/year (+ \$60 shipping outside the US) for print and electronic. Subscriptions, requests for back issues, and changes of address should be sent to Mathematical Sciences Publishers, Department of Mathematics, University of California, Berkeley, CA 94720-3840.

JoMMS peer-review and production is managed by EditFLOW™ from Mathematical Sciences Publishers.

PUBLISHED BY

 **mathematical sciences publishers**
<http://www.mathscipub.org>

A NON-PROFIT CORPORATION

Typeset in L^AT_EX

©Copyright 2010. Journal of Mechanics of Materials and Structures. All rights reserved.

AXIAL COMPRESSION OF HOLLOW ELASTIC SPHERES

ROBERT SHORTER, JOHN D. SMITH, VINCENT A. COVENEY AND JAMES J. C. BUSFIELD

When thin-walled hollow elastic spheres are compressed between two parallel rigid surfaces, there is an initial flattening of the sphere in the contact regions, followed by a snap-through buckling of the flattened surface. As the compression increases the sphere undergoes further buckling modes as a number of ridges and folds are formed. This elastic buckling deformation is investigated using a finite element analysis (FEA) technique. It is shown that the ratio of displacement at buckling to wall thickness depends weakly not only on Poisson's ratio, ν , but also on the ratio of the geometric wall thickness, h , to sphere radius, R . This approach is validated by comparison with experimental compression results on microspheres of approximately $40\ \mu\text{m}$ in diameter to table tennis balls with a diameter of 40 mm.

The analysis shows that a simple axial compression of a thin-walled hollow sphere can be used to measure both the average wall thickness of the sphere, from the deformation at the buckling snap-through, and the modulus from the force at this point. This provides a good technique to fully characterise the geometry and the elastic behaviour of thin-walled spheres of any size.

Introduction

Hollow thin-walled spheres are used for a variety of applications ranging from the recreational (table tennis balls, tennis balls, footballs), the industrial (lightweight and syntactic foams), through to the medical (the use of ultrasonic contrast agents to enhance ultrasonic imaging). In many of these applications the mechanical properties of the spherical shell play an important role, yet reliable measurements of those properties are often difficult to obtain. For example, with sintered foam structures made from hollow spheres, such as that proposed in [Taguchi and Karushige 2007; Peng et al. 2000], it is important that the mechanical properties of the individual spheres are known. With polymer spheres, even if samples of the polymer constituent are available, the manufacturing method may influence the final mechanical properties. This is often the case for example with polymers made by blow or injection moulding where an in-situ measurement may be desirable.

The situation is even starker for microscopic fillers: for example, with ultrasonic contrast agents where experimental evidence indicates that the elasticity and thickness of the shell are important components to the overall dynamics [Leong-Poi et al. 2002; Ketterling et al. 2007]. Such shells often have a diameter of a few μm and are constructed of proteins and lipids. Another type of hollow sphere, commercially available as Expancel[®] microspheres, are encountered in industrial applications as either a way of reducing weight or to act as a blowing agent. These range in diameter from 20 to $55\ \mu\text{m}$ with shell thicknesses of approximately $0.1\ \mu\text{m}$. In [Trivett et al. 2006], when the behaviour of these microspheres was studied in castor oil, the Young's modulus of the shell was estimated to be $\sim 3\ \text{GPa}$ from the sound speed of the

Keywords: compression, buckling, instability, hollow spheres, finite element analysis,

mixture, but in this case the spheres are formed by a chemical reaction in-situ and it is not possible to obtain a test sample of the shell polymer to confirm this estimate.

The axial compression of either hollow hemispheres and spheres between parallel rigid planes has been studied in [Updike and Kalnins 1970; 1972; Taber 1983; Pauchard and Rica 1998]. In the first of these references an axisymmetric elastic solution was developed and it was shown that during compression the initial response is to form a flat surface followed at larger deformations by a buckled solution. Updike and Kalnins [1972] extended this work to larger displacements and derived a solution that indicates that a nonsymmetric solution exists where contact lobes are formed on the contact ring. Taber [1983] tackled the problem of what happens if the sphere is filled with a pressurised fluid. It was found experimentally in [Pauchard and Rica 1998] that, for low applied forces, the shell flattens against the surfaces as predicted in [Updike and Kalnins 1970]. As the force is increased the shell suddenly buckled when the deformation was close to twice the thickness of the shell. Using the Föppl–von Kármán theory for thick shells [Föppl 1907, § 24, pp. 132–144; Ben and Pomeau 1997; Pomeau 1998], together with the observed configuration of the deformation, Pauchard and Rica deduced the form of the energy of an axially symmetric deformed spherical shell. This expression qualitatively explains the observed features but it contains a set of unknown parameters that, on dimensional grounds, are only expected to depend on the Poisson’s ratio of the shell material. In this paper these various earlier approaches are re-examined using a finite-element analysis (FEA) numerical investigation into the dependence of the buckling transition and associated force-deflection curve on the material and geometric properties. It is shown that the ratio of displacement at buckling to wall thickness depends weakly not only on Poisson’s ratio but also weakly on the geometric wall thickness to sphere radius ratio as well.

The precise form of the force-deflection curve before buckling is also found to be dependent on Poisson’s ratio, the sphere geometry and the modulus. It should therefore be possible to derive master curves of buckling force and displacement at specified Poisson’s ratios which can then be used to determine the Young’s modulus and thickness of a sphere, from a measurement of the force at a specified displacement together with the displacement at the point of the buckling instability. This is clearly a very useful extension of previous work. The theory is tested here using experimental results measured during the axial compression of table tennis balls and Expancel microspheres.

1. Theory

Pauchard and Rica [1998] considered the contact of a spherical shell with a rigid plate. Before buckling, the situation is assumed to conform to Configuration I of Figure 1, in which the top and bottom contact surface of the sphere flatten against the flat rigid plates, the total deflection being $2x$. After buckling it is assumed that the deformed sections of the sphere invert and the situation corresponds to Configuration II in the figure. The theory used to derive our dimensional approach is given in the Appendix. The displacements here are expressed as a dimensionless term given as the ratio of the deflection to the thickness ratio of the shell, $\varepsilon = x/h$.

Equation (A-3) implies that the scaled displacement to buckle the shell, ε_b is expected to depend only on Poisson’s ratio and is independent of the Young’s modulus and the size of the sphere whereas (A-5) states that the reduced force, RF/Eh^3 , is a function only of ε and Poisson’s ratio. It should be noted that, if the functions f , g_I and g_{II} depend only weakly on ν , then ε_b is approximately constant and the

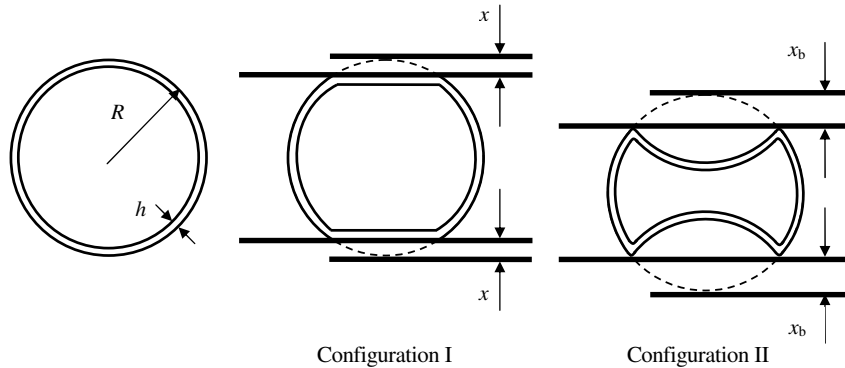


Figure 1. Assumed configurations of sphere and plate before buckling (Configuration I) and after (Configuration II).

reduced force lies on an approximately universal curve which is the same for any sphere, regardless of size or material parameters. The assumed forms of the energy expressions leading to the results (A-5) and (A-6) appear to be based on thin shell theory however the exact nature of some of the approximations is unclear. It is to be expected however that the buckling displacement arises from the root of an equation of the form of (A-3) and the reduced force will have a form similar to (A-5) however the exact functional dependence could be more complicated. This will be explored using the numerical model presented in the following section.

This paper focuses on the initial elastic buckling phenomena observed when a thin-walled shell is compressed between two rigid flat plates. An approach similar to that proposed in [Maalawi 2008] has been used to derive dimensionless functions to make the work applicable to a very wide range of conditions. In this work the measured or predicted force, F , is plotted in a normalised dimensionless form suggested by (A-5) as RF/Eh^3 and the scaled displacement is plotted as ϵ . Initial modelling also confirmed that the force scales directly with the applied modulus. Figure 2 shows a schematic for the full

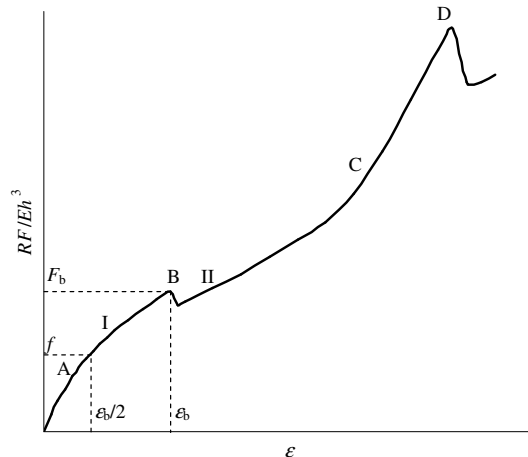


Figure 2. Schematic of the force-deflection curve for the compression of a spherical shell between two rigid plates.

compression of a hollow sphere until it is totally crushed. In the figure we are primarily concerned with the small strain initial elastic buckling behaviour. There is an initial inflexion in the curve at A: this is predicted by the form of $(A-6)_1$ and is associated with the dominance with increasing deformation of the energy associated with the compressed material on the flat portion of Configuration I over the energy in the fold, however it is typically more pronounced in practice. The second kink in the curve, labelled B, is the buckling instability that is the major focus of this paper. Immediately above B the sphere resembles Configuration II in Figure 1. As the displacement increases further (C) the graph stiffens further due to the onset of self contact between the internal top and bottom surfaces meeting inside the sphere. The further peaks in the force behaviour, labelled D, result from detailed buckling and folding as the sphere becomes fully compressed.

2. Numerical methods

The initial compression and buckling instability of the hollow spheres was modelled using ABAQUS finite element software. Previous studies [Kelly and Takhirov 2007] showed that ABAQUS was a suitable software package for modelling simple elastic buckling phenomena. Trials showed that the best way to model the elastic buckling behaviour required the use of the explicit dynamics package, with the time step set to model a pseudostatic analysis. Initially full three-dimensional models using solid continuum three-dimensional reduced integration (C3D8R) elements were used, a typical example of which is shown in Figure 3, left. Mesh sensitivity studies indicated that to replicate the buckling modes correctly, at least four elements had to be used through the thickness. The studies also showed that the most reproducible results were obtained for models based on elements that were approximately cubic. This put a significant demand on the model creation for thin, full three-dimensional models, as when the thinnest models were attempted it was necessary to use over 200,000 elements, which required significant solution time to solve. It was clearly possible to add the additional elements only in the regions of contact and buckling; however at large displacement the contact regions moved substantially, making it easier to use a uniform

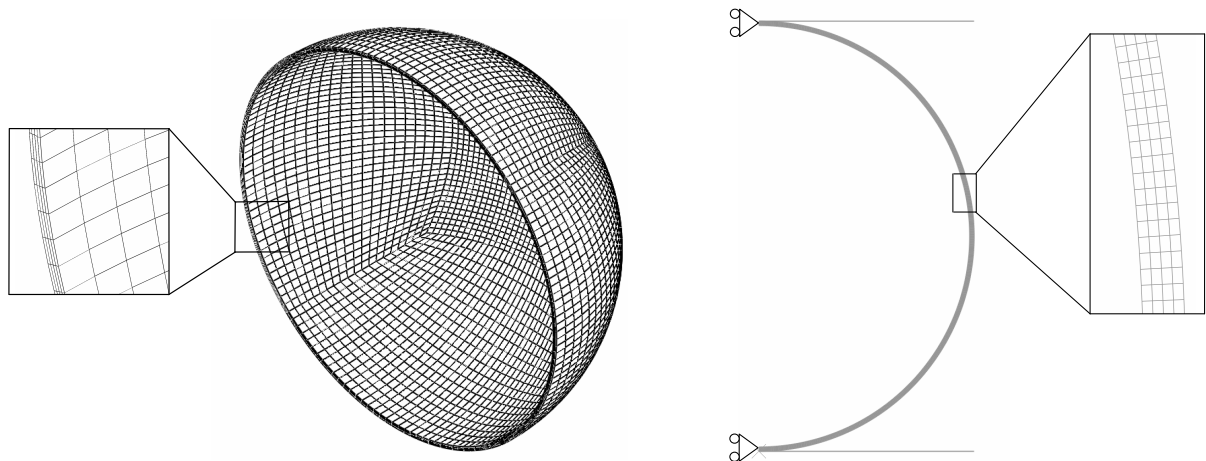


Figure 3. Left: Three-dimensional model showing mesh. Right: Axisymmetric model showing mesh and boundary conditions.

mesh. Next a model that incorporated thin shell finite elements was used. Wong and Pellegrino [2006a; 2006b] have shown that buckling phenomena of thin shell structures can in general be well modelled using this approach. However, in the case presented here this approach had difficulty resolving all the contact constraints. An alternative modelling approach that used a 2D axisymmetric model with continuum axisymmetric four node (CAX4) elements was produced. A typical model adopted is shown in Figure 3, right, with the appropriate symmetry and boundary conditions highlighted. In this case it was not computationally too expensive to use a large number of elements.

The numerical methods introduce an inherent uncertainty in the prediction of the point of instability, ϵ_b . To minimise this, a standard approach was adopted where the separation between the top contacting node in the model and the rigid surface was monitored throughout the analysis. The buckling was taken to be when the rate of change of this separation with time was at a maximum. The error in determining the maximum for a particular model is therefore determined by the discretisation of the time step and has a value of about 3%. The mesh convergence studies suggested that the errors due to meshing were much smaller and hence the overall estimate for the error is thought to be about 3%. This is the source of the error bars shown in some of the figures.

Figure 4 plots normalised buckling instability displacement ϵ_b for a range of different shell thickness to sphere radius ratios (h/R) predicted using both the three-dimensional models and the axisymmetric models for a Poisson’s ratio of 0.3. Clearly there is very little to distinguish between the two sets of results. This confirms, that at least for this initial snap-through elastic buckling, the behaviour is axisymmetric and no out of plane buckling arises that would require the use of a full three-dimensional model. It is also worth noting that the work presented here has a very similar buckling displacement to that seen in [Updike and Kalnins 1970] who reported for similar geometries a scaled buckling displacement, ϵ_b , of between 2.2 and 2.3. To speed up the analysis all the initial elastic buckling work reported in the rest of the paper uses the axisymmetric modelling approach.

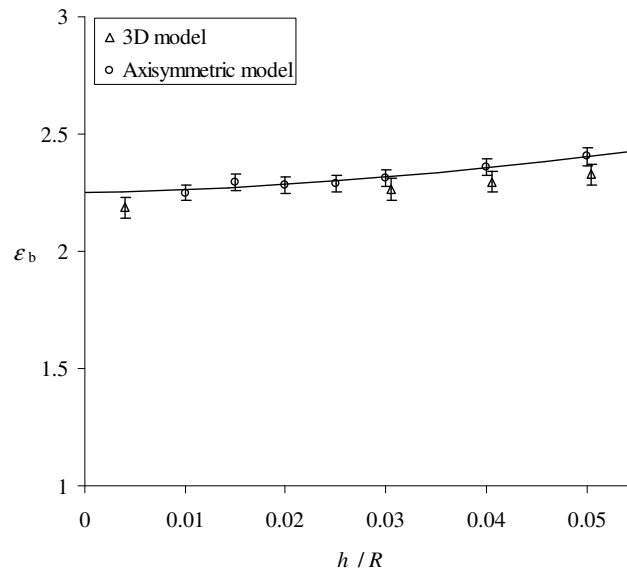


Figure 4. Snap-through deflection as a function of sphere radius when $\nu = 0.3$.

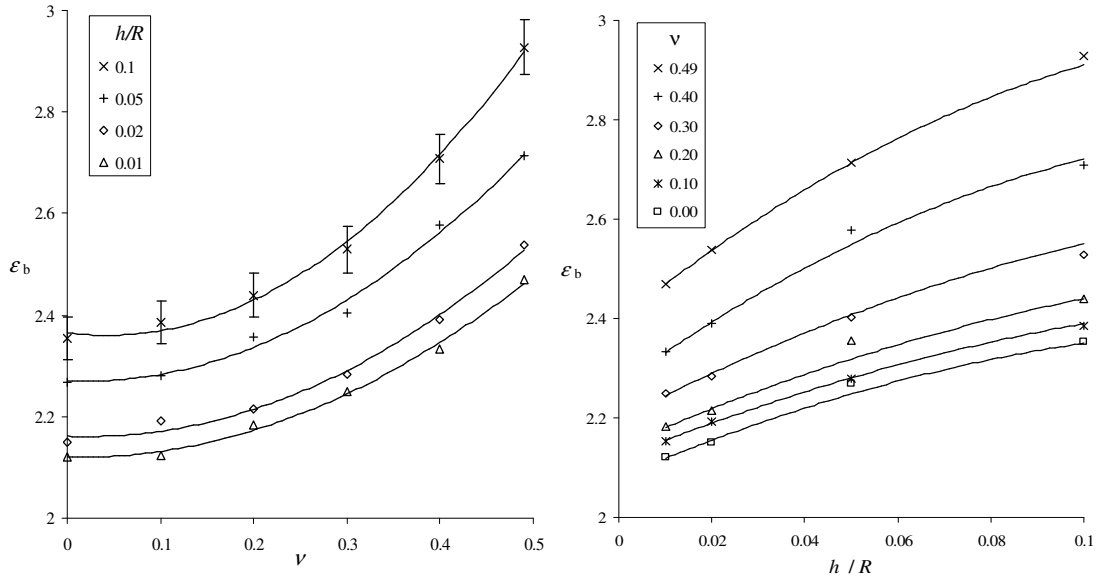


Figure 5. Left: Snap-through buckling point ε_b versus Poisson's ratio ν for a range of thickness-to-radius ratios (h/R) (left), and versus h/R for a range of values of ν (right).

The two parts of Figure 5 plot the dependence of the buckling instability displacement on the Poisson's ratio of the material and also for a wide range of ratios of wall thickness to sphere radius. Pauchard and Rica [1998] approach as given by (A-1) suggests that each of the various different geometries should superimpose to a single master curve when the buckling point is plotted against Poisson's ratio. Clearly this is not the case as there is a small but clear geometric dependence as well. Pauchard and Rica suggested a value of about 2 for ε_b and this is comparable with the values that we have derived for the thinnest spheres. It is not clear from their paper but it appears likely that their approach is only valid for very thin shells. A principal aim of this work is to produce curves to allow the wall thickness to be measured from a simple measure of the buckling displacement provided that the Poisson's ratio for the material is known.

The second aim of this paper is to use the buckling force to deduce the modulus for the sphere. However, there is a problem, as even though the actual buckling displacement was relatively insensitive to mesh shape producing errors of less than 3%, the maximum force, F_b (shown in Figure 2) achieved at this displacement was sensitive to discretisation details and produced much more significant errors of about 15%. An approach was adopted here to reduce this artefact of the modelling; this used the force, f , at the point half way to buckling, $\varepsilon_b/2$. As this point is far from the buckling instability, it is much less sensitive to small changes in the mesh geometry or the precise detail of the discretisation of the time step.

The wide range of geometric variations shown in Figure 5 are again plotted in Figure 6, but this time to show how the normalised force at half of the buckling displacement varies with Poisson's ratio and for different values of normalised wall thickness. Again, there is a clear geometric dependence that is not predicted in [Pauchard and Rica 1998]. Knowledge of this dependence, as shown in the graph,

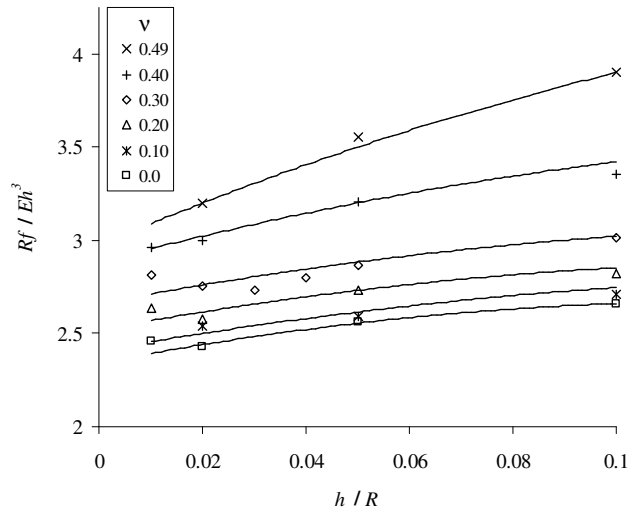


Figure 6. Normalised force versus radius. The value given is for the force at half of the buckling point, f .

allows one to identify the modulus of the sphere from a knowledge of the force at the point half way to buckling, f . Figure 6 also verifies that the data for similar geometries and Poisson’s ratio reduce to the same normalised force when modelled at different moduli.

3. Experimental comparison and discussion

Initially this theory was validated by experiments on table tennis balls, where independent measurements can be made of both the wall thickness and the modulus. Similar validation experiments were attempted on a series of Expancel spheres. It did however prove much harder to measure the modulus and experiments that tried to break open individual spheres to measure their wall thickness resulted in the spheres being damaged too extensively.

The experimental process to test the stiffness of the table tennis balls required for each ball to be placed on a flat rigid steel plate, as shown in Figure 7. Table tennis balls are manufactured in two halves with a welded seam joining the two parts. The balls were placed so that the seam was horizontal. A 1 kN load cell was used to measure the force and the displacement was measured by the movement of the crosshead which moved at a rate of 5 mm/min. The average scaled buckling displacement, ϵ_b , measured over 12 samples was 2.30. Assuming that the Poisson’s ratio was 0.3, taken from [Nakamura et al. 2004] and the measured radius for the table tennis ball of 19.85 mm \pm 0.05 mm, the prediction for the wall thickness deduced from Figure 5 was 0.42 mm. This compares well to the average experimentally measured wall thickness value of 0.40 mm \pm 0.04 mm. Similarly the average experimentally measured force at the half buckling point for the same geometry gives a prediction using Figure 6 for the modulus for the table tennis ball of 2.19 MPa.

An independent measure for the elasticity modulus was made using a dynamic mechanical thermal analyser (DMTA) on samples cut from the shells of the table tennis balls. In this machine a forced oscillation is applied with both the displacement and the force measured during the loading cycle. From this

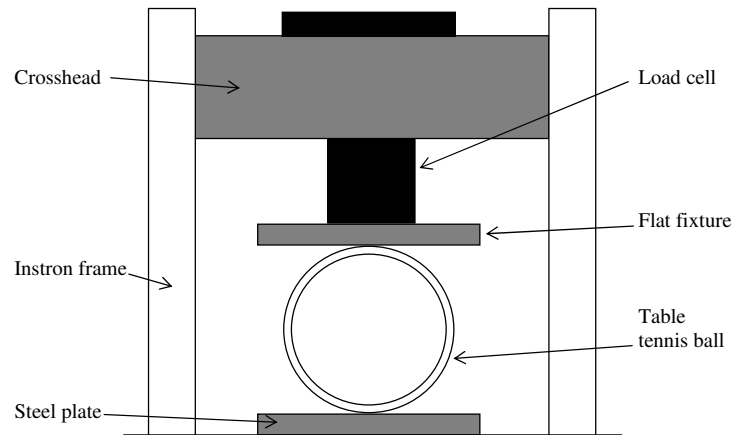


Figure 7. A schematic of the experimental setup used to measure the compression behaviour of the table tennis balls.

is derived the elastic behaviour. These properties were measured both in tension and then in three point bending. Both techniques delivered similar values for the tensile modulus of 2.2 MPa which compares very well with the value deduced from the compression experiment. Stresses taken from the model at buckling show that the maximum stresses were well below the yield stress measured at 60 MPa on a dumbbell shaped tensile test piece also cut from the table tennis ball shell.

Figure 8 plots the force versus displacement (on the appropriate dimensionless axes) from an axisymmetric model of the initial buckling of the table tennis ball with the modulus data in the model being

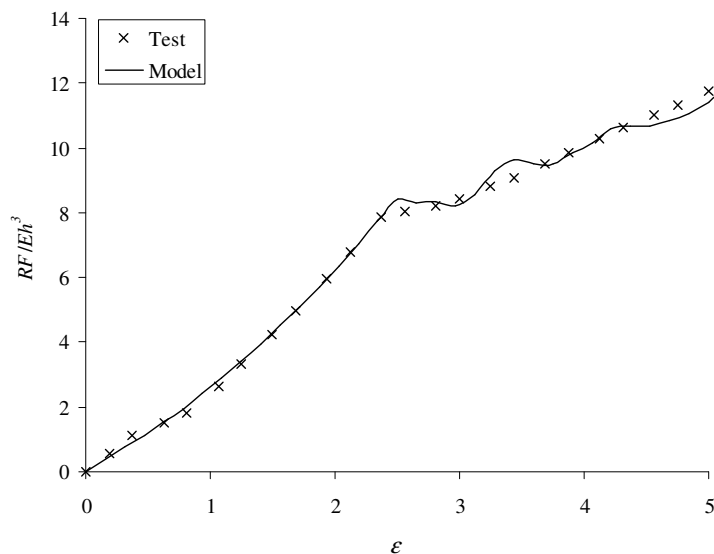


Figure 8. Finite element axisymmetric model compared to experimental compression of a table tennis ball of radius 20 mm and wall thickness 0.4 mm, FEA prediction uses a modulus of 2.2 MPa.

taken from the DMTA tests and the geometry from the measured results. This is compared with an experimentally measured data set for the compression of a table tennis ball. It is clear that the general behaviour is well predicted by the FEA approach, with the initial buckling displacement, ε_b being predicted accurately. The small oscillations observed in the model response are due to small discrete changes in the number of elements that are in contact with the rigid surfaces throughout the model. A separate model, not shown, with a realistic amount of plasticity introduced in the model, had no influence on this initial buckling phenomenon.

Next a series of different Expancel spheres were compressed using a UMIS 2000 nano-indentation machine. The machine was calibrated using the incorporated video microscope display and the X , Y coordinates set at a reference point. A small number of microspheres were placed on a microscope slide and were dispersed using distilled water, which was allowed to evaporate. The microscope slide was placed onto a specimen plinth using dental wax, which was melted at approximately 40°C and allowed to cool and set. The plinth was then placed in the nano-indentation machine and initially single microspheres were located using the video microscope display. Clearly it was important to compress just a single sphere. The indenter tip was 1 mm in diameter and made from a ruby, it was initially placed above the microsphere and allowed to stabilise for thirty minutes.

The indentation was achieved by moving the indenter tip in the $-Z$ direction by approximately 50% of the microsphere diameter. The process was repeated for a number of microspheres of differing measured diameters. Figure 9 shows the typical behaviour of the initial elastic compression of one of the microspheres with a radius of $24\ \mu\text{m}$. Assuming a Poisson's ratio of 0.3 as in [Nakamura et al. 2004], from the buckling point it is possible to identify the wall thickness to be $0.38\ \mu\text{m} \pm 0.02\ \mu\text{m}$ and from the force at the half way to buckling point the modulus was deduced as being 3.4 MPa. This gives a good indication of the values that we can expect for the wall thickness and the modulus. This will be

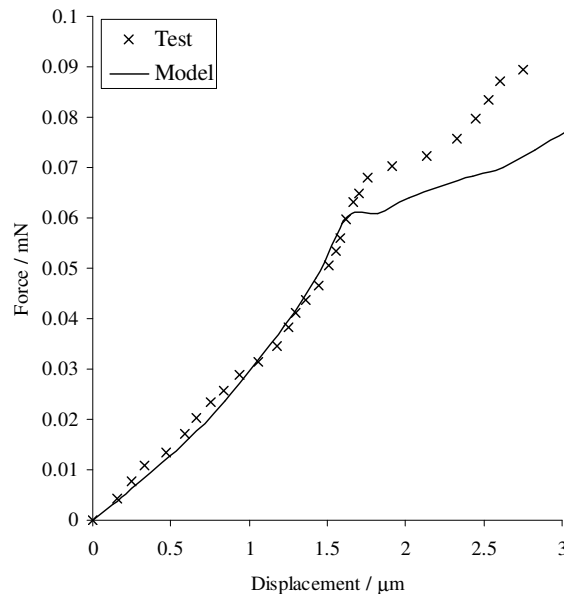


Figure 9. Experimental compression of a single microsphere ($R = 20.24\ \mu\text{m}$). The predicted curve has wall thickness $0.4\ \mu\text{m}$, modulus 3.4 MPa and Poisson's ratio 0.3.

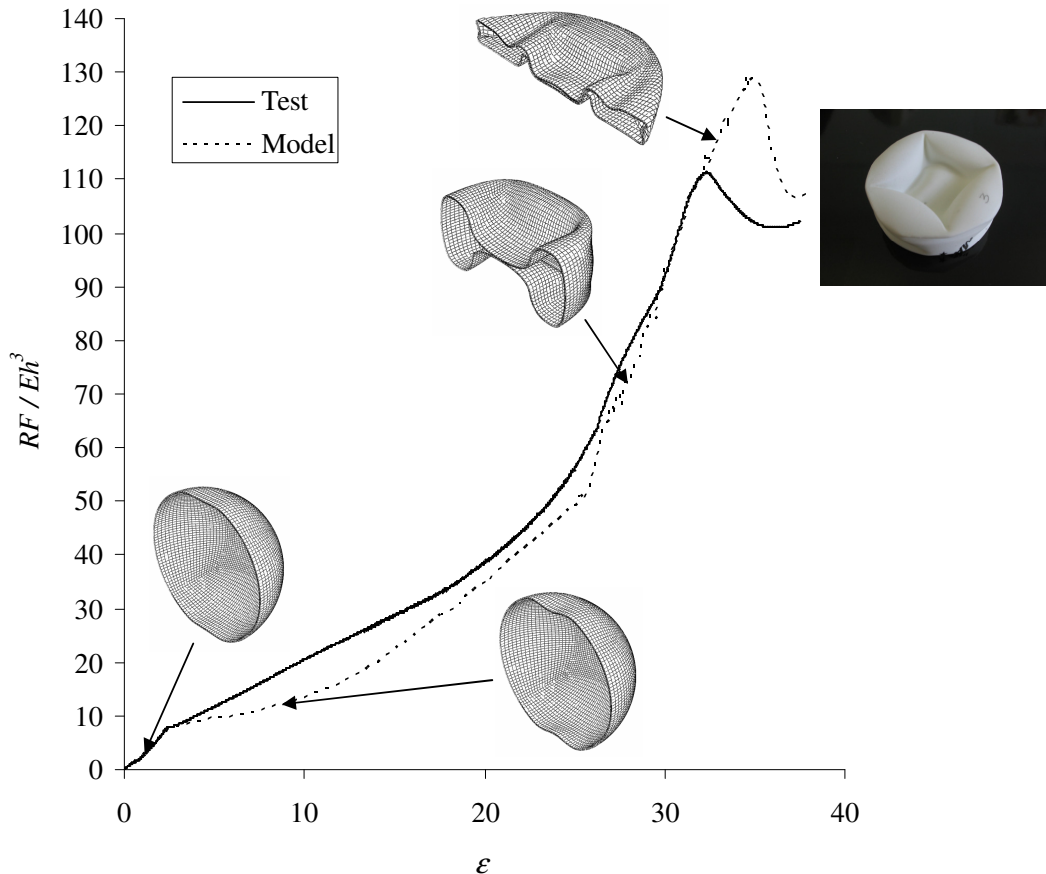


Figure 10. Finite element three-dimensional model compared to experimental compression of a table tennis ball.

particularly important in future work whereby we aim to model the influence of these microspheres on the physical properties when incorporated as a filler into rubber.

Whilst the post-buckling behaviour is beyond the scope of this paper, Figure 10 shows what happens beyond the initial buckling for a table tennis ball. In this test the ball has been compressed to just 6% of the original diameter of 40 mm, between two flat rigid plates using a screw-driven Instron 5584 test machine. This experiment is compared to a full three-dimensional model, as a two-dimensional axisymmetric model gave a much stiffer post-buckling response since it constrained the model to having only symmetric buckling modes. Clearly the elastic limit for the material is exceeded in this experiment and so to get an accurate model it was necessary to model the sphere using elastoplastic behaviour. In this case the properties were derived from a tensile test strip cut from the wall of the sphere. The plastic behaviour used had an initial yield stress of 50 MPa and then the materials became perfectly plastic at a plastic strain of 0.012 and at a stress of 60 MPa. Under these conditions not only is the initial buckling predicted well but also the final folding. A model without plasticity introduced was far too stiff. The FEA model gives too soft a response in the middle range. This is most likely to result from inaccuracies associated by ignoring the weld line in the model.

4. Conclusions

The compression of a thin-walled hollow elastic sphere between two parallel rigid surfaces is predicted well using an explicit dynamics finite element analysis package. The observed initial flattening of the sphere in the contact regions, followed by a snap-through buckling of the flattened surface are all modelled well. The ratio of displacement at buckling at point *B* in Figure 2 to wall thickness was seen to not only depend weakly upon the Poisson's ratio, as predicted in [Pauchard and Rica 1998], but there was also a dependence upon the geometric wall thickness to sphere radius ratio that had not previously been reported. This approach was validated by comparison with experimental compression results on microspheres of approximately 20 μm in radius and table tennis balls with a radius of 20 mm.

The analysis shows that a simple axial compression of a thin-walled hollow sphere can be used to measure both the average wall thickness of the sphere from the deformation at the buckling snap-through and the modulus from the force at the point half way to the point of the snap-through. This provides a good technique to fully characterise the geometry and the elastic behaviour of thin-walled spheres of any size.

Acknowledgements

The authors thank Andy Bushby in the Department of Materials at QMUL, for his support and guidance in using the nano-indentation technique. One of the authors, Robert Shorter, would also like to thank DITC and EPSRC for the funding for his research studentship.

Appendix

Pauchard and Rica [1998] considered the contact of a spherical shell with a rigid plate. In the limit that the wall thickness, h , tends to zero, the situation before buckling is assumed to conform to configuration (I) of Figure 1, in which the top and bottom contact surface of the sphere flatten against the flat rigid plates, the plate having moved through a deflection, $2x$. When the shell has Young's modulus, E , and radius, R , the energy of this configuration has the form

$$U_I = \frac{c_0}{4} \frac{Eh^{5/2}}{R} x^{3/2} + c_1 \frac{Eh}{R} x^3. \quad (\text{A-1})$$

The first term is the energy of the axisymmetric fold and is deduced from the results for flat plates [Pauchard and Rica 1998; Ben and Pomeau 1997; Pomeau 1998]. The second term is the contribution from the compression of a portion of the sphere.

After buckling a section of the sphere inverts and the situation corresponds to Configuration II of Figure 1, which has energy given as

$$U_{II} = c_0 \frac{Eh^{5/2}}{R} x^{3/2} + c_2 \frac{Eh^3}{R} x. \quad (\text{A-2})$$

Here the first term is the contribution from the steeper axisymmetric fold and the second is due to the inversion of the spherical section by the flat surface. When x is small $U_I < U_{II}$ and Configuration I is energetically favourable. As x increases however, U_I increases faster than U_{II} (due to the x^3 dependence) and hence a point will be reached at which Configuration II is energetically more favourable and I is

unstable. This critical deformation corresponds to the energies being equal and thus depends on h and the parameters c_0 , c_1 and c_2 . The force in each of the configurations is given by the first derivatives of Equations (A-1) and (A-2), and is expected to be discontinuous at the transition for an experiment where the displacement increases monotonically. It is worth considering that the changes in the internal pressure as a result of the buckling are very small as a simple calculation of sphere volume shows that buckling introduces modest changes of only about 1% to the volume. The resulting pressure changes would have almost no contribution to the buckling forces.

The arguments leading to Equations (A-1) and (A-2) for the energies in the different configurations are essentially statements on the functional dependence of x from shell theory, hence the parameters c_0 , c_1 and c_2 , although dimensionless, can still be expected to depend on the material properties of the shell through Poisson's ratio, ν . In addition, these expressions strictly hold when the radius of the shell is much larger than the thickness and the deflections are larger than the fold radius of curvature.

Rather than derive the exact form of (A-1) and (A-2), this numerical investigation seeks to adopt the dimensionless approach of [Pauchard and Rica 1998]. Two hypotheses follow from this, which can be expressed in terms of the ratio of the deflection to the thickness ratio of the shell,

$$\varepsilon = x/h.$$

There is a critical value of ε at which buckling occurs, ε_b , which is the solution of a relation of the form

$$f(\varepsilon_b, \nu) = 0, \quad (\text{A-3})$$

where (in terms of the Pauchard parameters)

$$f(\varepsilon, \nu) = c_1(\nu)\varepsilon^3 - \frac{3}{4}c_0(\nu)\varepsilon^{3/2} - c_2(\nu)\varepsilon. \quad (\text{A-4})$$

By differentiating the expressions for the energy in each of the configurations, the functional dependence of the force, F , needed for a particular scaled deflection, ε , on the material and geometric parameters can be determined. In terms of the Young's modulus of the shell, E , its outer radius, R , and the shell thickness, h , this dependence is found to be

$$\frac{R}{Eh^3}F = \begin{cases} g_I(\varepsilon, \nu) & \text{if } \varepsilon < \varepsilon_b, \\ g_{II}(\varepsilon, \nu) & \text{if } \varepsilon > \varepsilon_b, \end{cases} \quad (\text{A-5})$$

and

$$g_I(\varepsilon, \nu) = \frac{3}{8}c_0(\nu)\varepsilon^{1/2} + 3c_1(\nu)\varepsilon^2, \quad g_{II}(\varepsilon, \nu) = \frac{3}{2}c_0(\nu)\varepsilon^{1/2} + c_2(\nu). \quad (\text{A-6})$$

References

- [Ben and Pomeau 1997] A. M. Ben and Y. Pomeau, "Crumpled paper", *Proc. R. Soc. Lond. A* **453**:1959 (1997), 729–755.
- [Föppl 1907] A. Föppl, *Vorlesungen über technische Mechanik, Bd. 5: die wichtigsten Lehren der höheren Elastizitätstheorie*, vol. 5, Teubner, Leipzig, 1907.
- [Kelly and Takhirov 2007] J. M. Kelly and S. M. Takhirov, "Tension buckling in multilayer elastomeric isolation bearings", *J. Mech. Mater. Struct.* **2**:8 (2007), 1591–1605.
- [Ketterling et al. 2007] J. A. Ketterling, J. Mamou, J. S. Allen III, O. Aristizábal, R. G. Williamson, and D. H. Turnbull, "Excitation of polymer-shelled contrast agents with high-frequency ultrasound", *J. Acoust. Soc. Am.* **121**:1 (2007), EL48–EL53.

- [Leong-Poi et al. 2002] H. Leong-Poi, J. Song, S. J. Rim, J. Christiansen, S. Kaul, and J. R. Lindner, "Influence of microbubble shell properties on ultrasound signal: implications for low-power perfusion imaging", *J. Am. Soc. Echocardiogr.* **15**:10 (2002), 1269–1276.
- [Maalawi 2008] K. Y. Maalawi, "Optimal buckling design of anisotropic rings/long cylinders under external pressure", *J. Mech. Mater. Struct.* **3**:4 (2008), 775–793.
- [Nakamura et al. 2004] K. Nakamura, M. Wada, S. Kuga, and T. Okano, "Poisson's ratio of cellulose I β and cellulose II", *J. Polym. Sci. B Polym. Phys.* **42**:7 (2004), 1206–1211.
- [Pauchard and Rica 1998] L. Pauchard and S. Rica, "Contact and compression of elastic spherical shells: the physics of a 'ping-pong' ball", *Philos. Mag. B* **78**:2 (1998), 225–233.
- [Peng et al. 2000] H. X. Peng, Z. Fan, J. R. G. Evans, and J. J. C. Busfield, "Microstructure of ceramic foams", *J. Eur. Ceram. Soc.* **20**:7 (2000), 807–813.
- [Pomeau 1998] Y. Pomeau, "Buckling of thin plates in the weakly and strongly nonlinear regimes", *Philos. Mag. B* **78**:2 (1998), 235–242.
- [Taber 1983] L. A. Taber, "Compression of fluid-filled spherical shells by rigid indenters", *J. Appl. Mech. (ASME)* **50**:4a (1983), 717–722.
- [Taguchi and Karushige 2007] I. Taguchi and M. Karushige, "Macroscopic elastic properties of randomly packed balloons", *J. Mech. Mater. Struct.* **2**:3 (2007), 529–555.
- [Trivett et al. 2006] D. H. Trivett, H. Pincon, and P. H. Rogers, "Investigation of a three-phase medium with a negative parameter of nonlinearity", *J. Acoust. Soc. Am.* **119**:6 (2006), 3610–3617.
- [Updike and Kalnins 1970] D. P. Updike and A. Kalnins, "Axisymmetric behaviour of an elastic spherical shell compressed between rigid plates", *J. Appl. Mech. (ASME)* **37** (1970), 635–640.
- [Updike and Kalnins 1972] D. P. Updike and A. Kalnins, "Axisymmetric postbuckling and nonsymmetric buckling of a spherical shell compressed between rigid plates", *J. Appl. Mech. (ASME)* **39** (1972), 172–178.
- [Wong and Pellegrino 2006a] Y. W. Wong and S. Pellegrino, "Wrinkled membranes, I: experiments", *J. Mech. Mater. Struct.* **1**:1 (2006), 3–25.
- [Wong and Pellegrino 2006b] Y. W. Wong and S. Pellegrino, "Wrinkled membranes, III: numerical simulations", *J. Mech. Mater. Struct.* **1**:1 (2006), 63–95.

Received 17 Oct 2008. Revised 15 Jun 2010. Accepted 8 Jul 2010.

ROBERT SHORTER: r.shorter@qmul.ac.uk

Department of Materials, Queen Mary University of London, Mile End Road, London, E1 4NS, United Kingdom

JOHN D. SMITH: jdsmith@dstl.gov.uk

Defence Science and Technology Laboratory, Porton Down, SP4 0JQ, United Kingdom

VINCENT A. COVENEY: vince.coveney@uwe.ac.uk

Engineering and Medical Technology Research Centre, University of the West of England, Bristol, BS16 1QY, United Kingdom

JAMES J. C. BUSFIELD: j.busfield@qmul.ac.uk

Department of Materials, Queen Mary University of London, Mile End Road, London, E1 4NS, United Kingdom

COUPLING OF PERIDYNAMIC THEORY AND THE FINITE ELEMENT METHOD

BAHATTIN KILIC AND ERDOGAN MADENCI

The finite element method is widely utilized for the numerical solution of structural problems. However, damage prediction using the finite element method can be very cumbersome because the derivatives of displacements are undefined at the discontinuities. In contrast, the peridynamic theory uses displacements rather than displacement derivatives in its formulation. Hence, peridynamic equations are valid everywhere, including discontinuities. Furthermore, the peridynamic theory does not require an external criterion for crack initiation and propagation since material failure is invoked through the material response. However, the finite element method is numerically more efficient than the peridynamic theory. Hence, this study presents a method to couple the peridynamic theory and finite element analysis to take advantage of both methods. The regions where failure is expected are modeled using peridynamics while remaining regions are modeled utilizing the finite element method. Finally, the present approach is demonstrated through a simple problem and predictions of the present approach are compared against both the peridynamic theory and finite element method. The damage simulation results for the present method are demonstrated by considering a plate with a circular cutout.

1. Introduction

Over the past several decades, the finite element method has become the most commonly accepted technique for the numerical solution of the equations of classical continuum mechanics. The success of the finite element method comes from its straightforward formulation, which primarily involves three basic steps. The first step is the approximate representation of the equations by either the variational or weighted residual method. The second step concerns construction of a system of governing algebraic equations by discretizing the region into finite elements. The last step involves the effective solution of the finite element equations. There are many commercial computer programs, such as ANSYS, ABAQUS, etc., and these programs enable the analysis of many engineering problems without much difficulty. However, the use of the finite element method can be quite challenging for damage prediction. This difficulty arises from the presence of spatial derivatives of displacements in the equations of classical continuum mechanics. These derivatives are undefined when the displacements are discontinuous, such as across cracks or interfaces. Hence, failure simulation based on stresses becomes invalid at these discontinuities because stresses asymptotically approach infinity. However, linear elastic fracture mechanics provides external failure criteria based on the stress intensity factor, energy release rate, etc.

Also, these criteria are often limited to the prediction of the smallest load for crack propagation and the direction of initial crack growth. In order to circumvent these shortcomings, the cohesive crack growth is introduced into the finite element method. As explained in [Moës and Belytschko 2002], there are

Keywords: peridynamics, finite element, coupling, damage.

two main procedures for predicting crack growth: discrete interelement cracks and discrete intraelement cracks. In the interelement method, cohesive zone elements, as interelements, are placed in between each pair of neighboring elements in the mesh. However, these elements require a priori knowledge of the crack growth path, which might not be available unless an extremely fine mesh is employed.

The intraelement procedure incorporates a discontinuous mode at the element level and this method is used to model crack and shear band propagation. The use of an embedded discontinuous mode does not require remeshing but stability issues need to be considered in these methods [Moës and Belytschko 2002]. A comparative study of finite element methods with embedded discontinuous modes is given in [Jirásek 2000].

Belytschko and Black [1999] and Moës et al. [1999] introduced the extended finite element method X-FEM, which incorporates discontinuity in the displacement field along the crack path regardless of crack location and exploits the partition of the unity property of finite elements [Melenk and Babuška 1996]. In this method, the solution space is enriched by a priori knowledge about the behavior of the solution near any discontinuity and the additional number of degrees of freedom is minimized since the enrichment only includes the nodes that belong to the elements cut by cracks [Zi et al. 2007]. As explained in this last reference, there is a blending region that includes the neighboring elements of the tip element in which the crack tip is positioned. Partial enrichment exists for the elements in the blending region for which the partition of unity does not hold. Hence, the solution becomes inaccurate in the blending region.

Silling [2000], realizing the limitations, completely reformulated the basic equations of continuum mechanics. The resulting approach is known as the peridynamic theory. The main difference between the peridynamic theory and classical continuum mechanics is that the former utilizes displacement components without their spatial derivatives. This feature allows damage initiation and propagation at multiple sites with arbitrary paths inside the material without resorting to special crack growth criteria. In the peridynamic theory, internal forces are expressed through nonlocal interactions between pairs of material points within a continuous body, and damage is a part of this interaction. Interfaces between dissimilar materials have their own properties, and damage can propagate when and where it is energetically favorable for it to do so.

The peridynamic theory was utilized successfully for damage prediction of many problems. Silling [2003] considered the Kalthoff–Winkler experiment in which a plate having two parallel notches was impacted by a cylindrical impactor, and the peridynamic simulations successfully captured the angle of crack growth observed in the experiments. Impact damage was also predicted using peridynamics by Silling and Askari [2004; 2005]. This last paper considered a plate with a center crack to show the convergence of their numerical method. The peridynamic theory was applied to damage analysis of plain and reinforced concrete structures in [Gerstle and Sau 2004]. A new constitutive model was introduced for tearing and stretching of rubbery materials in [Silling and Askari 2005]. Using this model, they predicted oscillatory crack path when a blunt tool is forced through a membrane. The peridynamic theory was also applied successfully in [Askari et al. 2006] and [Colavito et al. 2007b] to predict damage in laminated composites subjected to low-velocity impact. Colavito et al. [2007a] used the peridynamic theory for damage prediction of woven composites subjected to static indentation. Xu et al. [2007] and Kilic [2008] considered notched laminated composites under biaxial loads.

Although the peridynamic theory provides deformation as well as damage initiation and growth without resorting to an external criterion, it is computationally more demanding than the finite element method

(FEM). Furthermore, the finite element method is very effective for modeling problems without damage. In order to take advantage of the computational robustness of FEM, Macek and Silling [2007] implemented the peridynamic model in a conventional finite element analysis code, ABAQUS by representing the peridynamic interactions with truss elements and using embedded element technique for the overlap region. However, the present study presents a direct approach to couple the peridynamic theory and finite element method to take advantage of their salient features. The regions involving failure are modeled using the peridynamic theory while the finite element method is utilized for the regions without failure. The coupling introduces an overlap region in which both the peridynamic and finite element equations are used simultaneously.

2. Peridynamic theory

The nonlocal peridynamic theory is concerned with the physics of a material body at a material point that interacts with all points within its range, as shown in Figure 1. As in the classical (local) continuum theory, the material points of a body are continuous, as opposed to discrete in the case of molecular dynamics. However, the main difference between the peridynamic and the classical continuum theories is that the former is formulated using integrodifferential equations, as opposed to partial differential equations that include spatial derivatives of the displacement components. Displacement derivatives do not appear in peridynamic equations, which allows the peridynamic formulation to be valid everywhere whether or not displacement discontinuities are present. As described in [Silling 2000], the peridynamic equation of motion at a reference configuration of position \mathbf{x} and time t is given as

$$\rho \frac{\partial^2 \mathbf{u}}{\partial t^2} = \int_{\mathcal{R}} dV_{\mathbf{x}'} \mathbf{f}(\mathbf{u}(\mathbf{x}, t), \mathbf{u}(\mathbf{x}', t), \mathbf{x}', t) + \mathbf{b}(\mathbf{x}, t), \quad (1)$$

in which \mathcal{R} is the domain of integration, \mathbf{u} is the displacement vector field, \mathbf{b} is a prescribed body-force density field, and ρ is mass density. The response function, \mathbf{f} , is defined as the force vector per unit volume squared that the material point at \mathbf{x}' exerts on the material point at \mathbf{x} . The integral equation (1) represents a distinct mathematical system that is not derivable from the classical partial differential equations (PDEs).

2.1. Response function. Within the realm of the peridynamic theory, the material points interact with each other directly through a prescribed response function, which contains all the constitutive information associated with the material. The forces within the material are treated through interactions between pairs of material points in the continuum. The deformed position of a given material point is determined by the summation of forces between itself and all other material points with which it interacts. However, the response functions must obey the linear and angular admissibility conditions, which are examined in detail in [Silling 2000]. Any function satisfying the admissibility conditions is a valid response function. Therefore, the response functions are not restricted to be linear, which makes the peridynamic equation of motion given by (1) valid for both linear and nonlinear analyses. However, the response functions appearing in the literature and in this study assume pairwise interactions, which limits the Poisson's ratio to 0.25. Also, the limiting values of the Poisson's ration under plane stress and plane strain assumptions are explained in [Gerstle et al. 2005]. The response function relates the dependence of the interaction force on reference positions and displacements of any material point pairs. This interaction force can also

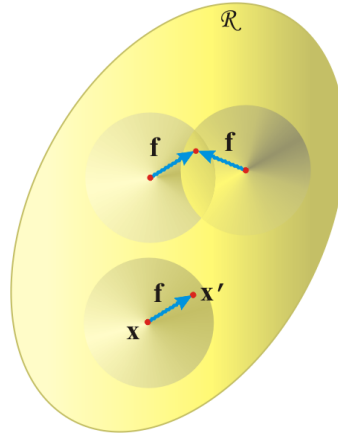


Figure 1. Pairwise interaction of a material point with its neighboring points.

be viewed as a bond force between the material points. The present study utilizes the response function described in [Kilic 2008], which can be written as

$$f(\eta, \xi) = \frac{\xi + \eta}{|\xi + \eta|} \mu(\xi, t) \frac{9k}{\pi l^4} e^{-(|\xi|/l)^2} s, \quad (2)$$

in which k is the bulk modulus and l is the internal length, which is the measure of nonlocal behavior. The locality of interactions depends on the internal length l and interactions become more local with decreasing internal length, as shown in Figure 2. The relative position, ξ , can be expressed as $\xi = x' - x$ in the reference configuration, as illustrated in Figure 3. The relative displacement, η , can be written as

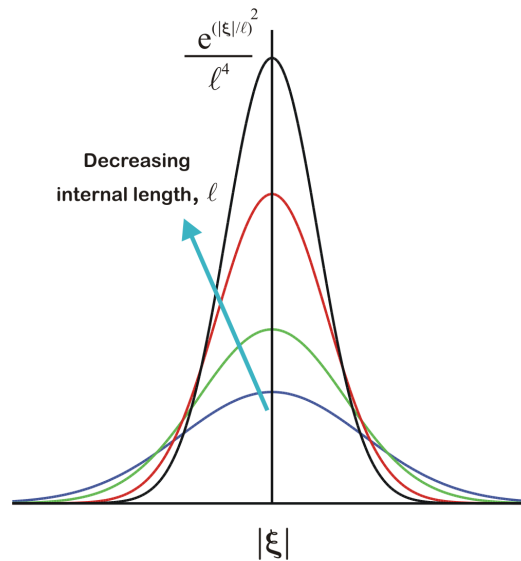


Figure 2. Effect of internal length on the locality of interactions.

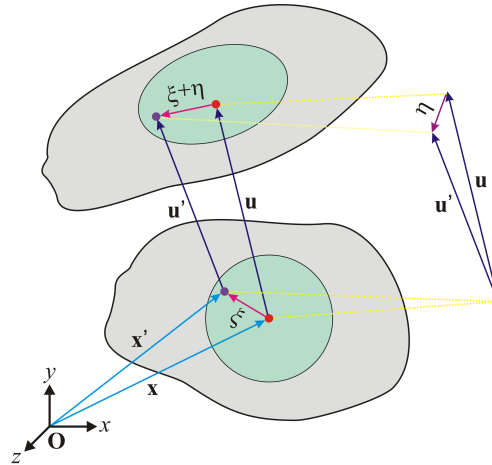


Figure 3. Definition of geometric parameters.

$\eta = u - u'$ between points x' and x , as shown in Figure 3. The stretch, s , is given as

$$s = \frac{|\xi + \eta| - |\xi|}{|\xi|} \tag{3}$$

and it is the ratio of the change in distance to initial distance between points x' and x . Failure is included in the material response through a history-dependent scalar-valued function μ (see [Silling and Bobaru 2005]), defined as

$$\mu(\xi, t) = \begin{cases} 1 & \text{if } s(t', \xi) < s_0 \text{ for all } 0 < t' < t, \\ 0 & \text{otherwise,} \end{cases} \tag{4}$$

in which s_0 is the critical stretch for failure to occur, as shown in Figure 4. In the solution phase, the displacements and stretches between pairs of material points are computed. When the stretch between two points exceeds the critical stretch, s_0 , failure occurs and these two points cease to interact. As derived in [Silling and Askari 2005], the critical stretch value can be related to the well-known fracture parameters such as the energy release rate. Thus, damage in a material is simulated in a much more realistic manner

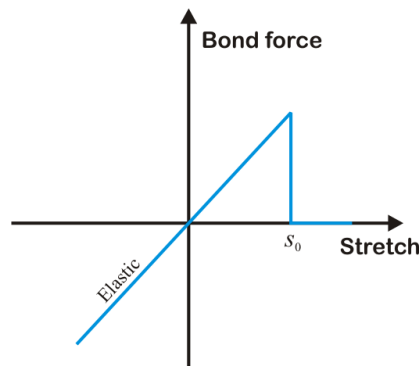


Figure 4. Model for bond failure.

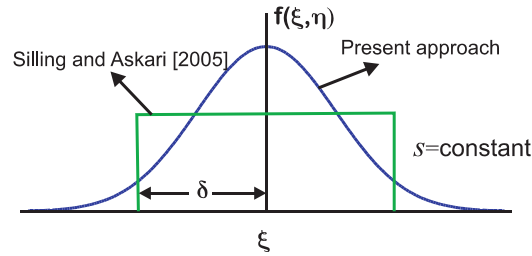


Figure 5. Comparison of response functions under constant stretch.

compared to the classical continuum-based methods. The inexplicit nature of local damage at a point, arising from the introduction of failure in the constitutive model, is removed by defining the local damage as

$$\varphi(x, t) = 1 - \frac{\int_{\mathcal{R}} dV_{x'} \mu(t, \xi) e^{-(|\xi|/l)^2}}{\int_{\mathcal{R}} dV_{x'} e^{-(|\xi|/l)^2}}. \quad (5)$$

Thus, the local damage is the weighted ratio of the amount of the broken interactions to the total amount of interactions.

The present response function is more complicated than that given in [Silling and Askari 2005] due to the exponential term in (2). The behavior of this response function under constant stretch is illustrated in Figure 5. As shown in this figure, Silling and Askari's response function suggests that interaction force remains the same within the horizon regardless of the distance between the interacting points. However, the forces acting among bodies decrease with increasing distances. Hence, present method utilizes the response function in (2) in which interaction force decreases with increasing distance between the two material interaction points.

Because the peridynamic theory is nonlocal, material points interact across the interfaces. Hence, the response function needs to be specified for the interface, in addition to the response functions for individual materials. Therefore, the peridynamic theory is capable of modeling different adhesion strengths of the materials. If the domain consists of two dissimilar materials (Figure 6), three different interactions need to be specified. Two of these interactions occur between material points having the same material, labeled 1 and 2 in the figure, and the material properties used by the response function are trivially chosen to be those of the material point. In the case of interactions across the interface, labeled 3, the numerical experiments revealed that displacement predictions are insensitive to properties of the interface material if the numbers of interactions across the interfaces are much smaller than those for material points having the same material. Also, when the numbers of interactions across the interfaces are comparable to those

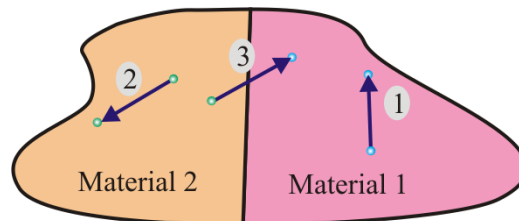


Figure 6. Interactions among material points.

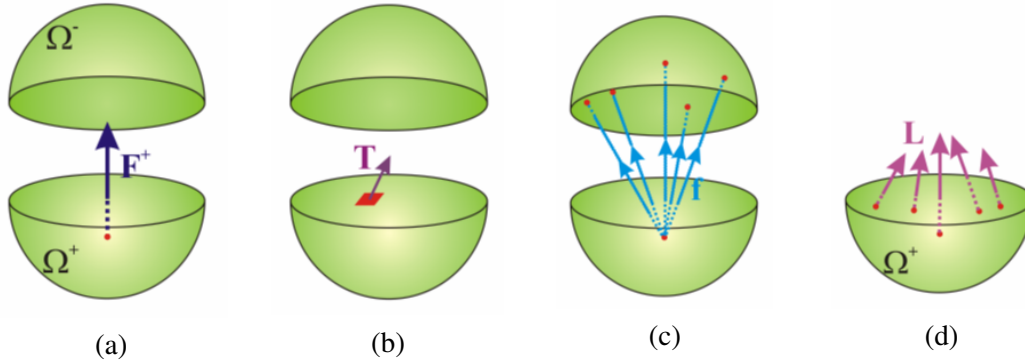


Figure 7. Boundary conditions: (a) domain of interest; (b) tractions in classical continuum mechanics; (c) interaction of a point in the domain Ω^+ with the domain Ω^- ; (d) force densities acting on the domain Ω^+ due to the domain Ω^- .

between the material points having the same material the use of the smaller of the bulk moduli of the two materials gives better results. Hence, the response function for interactions across the interface utilizes the material properties of the region having the smaller bulk modulus.

2.2. Boundary conditions. Since peridynamics is a nonlocal theory and its equations of motion utilize integrodifferential equations as opposed to partial differential equations in the case of the classical continuum theory, the application of boundary conditions is also very different from that of the classical continuum theory. The difference can be illustrated by considering a body that is subjected to mechanical loads. If this body is fictitiously divided into two domains, Ω^- and Ω^+ as shown in Figure 7a, there must be a net force, \mathbf{F}^+ , that is exerted to domain Ω^+ by domain Ω^- so that force equilibrium is satisfied.

According to the classical continuum mechanics, the force \mathbf{F}^+ can be determined by integrating surface tractions over the cross section area, $\partial\Omega$, of the domains Ω^- and Ω^+ :

$$\mathbf{F}^+ = \int_{\partial\Omega} dA \mathbf{T}, \quad (6)$$

in which \mathbf{T} denotes the surface tractions (Figure 7b). In the case of the peridynamic theory, the material points located in Ω^+ interact with the other material points in Ω^- (Figure 7c). Hence, the force densities, \mathbf{L} , acting on points in Ω^+ must be determined by integrating the response function over Ω^- :

$$\mathbf{L}(\mathbf{x}) = \int_{\Omega^-} dV \mathbf{f}(\mathbf{x}, \mathbf{x}'). \quad (7)$$

Finally, the force \mathbf{F}^+ can be computed by volume integration of these force densities (Figure 7d) over Ω^+ :

$$\mathbf{F}^+ = \int_{\Omega^+} dV \mathbf{L}(\mathbf{x}). \quad (8)$$

Hence, the tractions or point forces cannot be applied as boundary conditions since their volume integrations result in a zero value. Therefore, the boundary conditions are applied over the volumes as body forces, displacements, and velocities.

3. Numerical implementation

In order to solve (1), a collocation method is adopted and the numerical treatment involves the discretization of the domain of interest into subdomains (Figure 8). Collocation (integration) points are subsequently placed into subdomains in order to reduce the peridynamic equation of motion into a finite sum as

$$\rho \ddot{\mathbf{u}}(\mathbf{x}_i, t) = \mathbf{b}(\mathbf{x}_i, t) + \sum_{e=1}^N \sum_{j=1}^{N_e} w_j \mathbf{f}(\mathbf{u}(\mathbf{x}_i, t), \mathbf{u}(\mathbf{x}'_k, t), \mathbf{x}_i, \mathbf{x}'_k, t), \quad (9)$$

where \mathbf{x}_i is the position vector located at the i -th collocation point, N is the number of subdomains, and N_e is the number of collocation points in the e -th subdomain. The position vector \mathbf{x}'_k represents the j -th integration point of the e -th subdomain. The parameter w_j is the integration weight of the point \mathbf{x}'_k . Present discretization becomes identical to that given in [Silling and Askari 2005] when the number of collocation points is set to 1.

In this study, volume integration is performed using hexahedron-shaped subdomains utilizing eight integration points. This type of discretization leads to a large number of collocation points in some problems. Therefore, parallel processing using OpenMP is also employed to reduce computation time while utilizing uniform grids as arrays of linked lists as described in [Kilic 2008]. A binary space

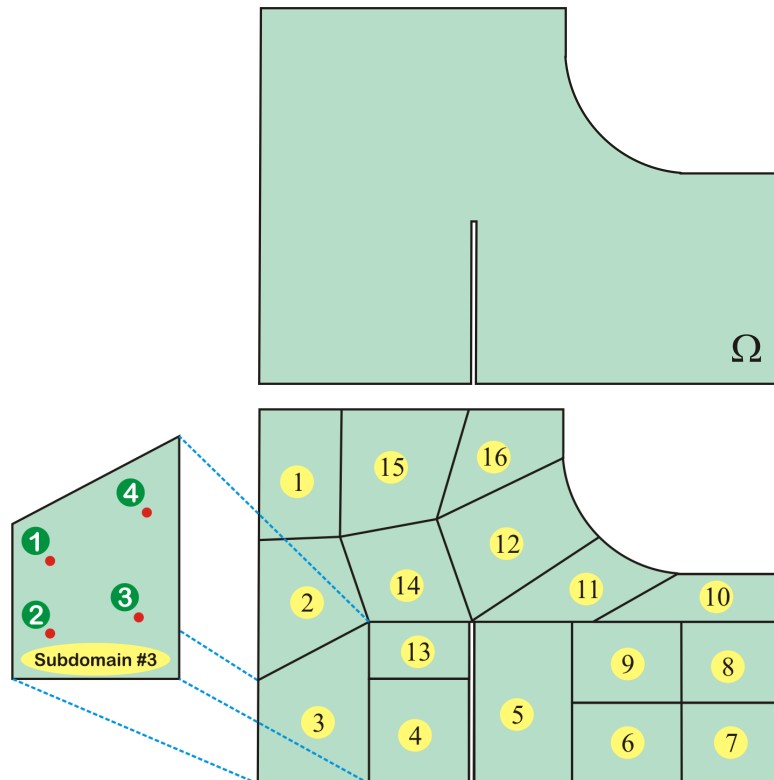


Figure 8. Discretization of the domain of interest.

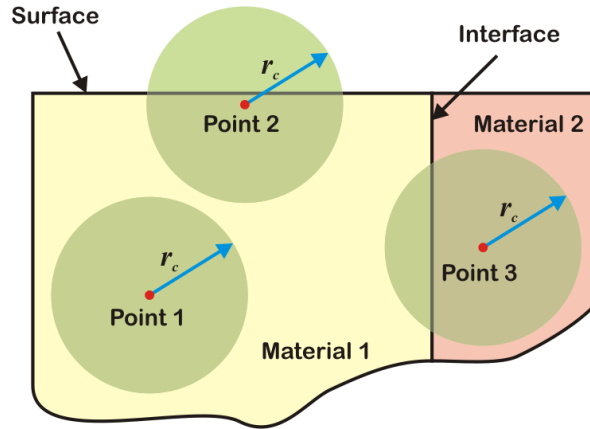


Figure 9. Surface effects in the domain of interest.

decomposition introduced in [Berger and Bokhari 1987; Kilic 2008] is used to obtain good load balancing on each processor. The decomposition involves division of the space into two subunits, with an approximately equal number of collocation points. Each subunit is then continuously divided into two subunits until the number of subunits and processors become equal. Division is performed only on the x -, y -, or z -plane, with the constraint of minimum division surface to reduce the communication cost among the processors.

Also, the response function given by (2) is derived with the assumption that the point located at \mathbf{x} is in an infinite domain consisting of a single material. However, this assumption becomes invalid when the material point is close to free surfaces or material interfaces (Figure 9). Therefore, there is a reduction in material stiffness near the free surfaces. On the other hand, stiffness near the interface can exhibit an increase or reduction, depending upon how dissimilar material regions interact across their interface. Since free surfaces and material interfaces vary from one problem to another, it is impractical to resolve this issue analytically. Therefore, the stiffness reduction or increase due to surfaces is corrected numerically as explained in Appendix A.

The problems considered herein necessitate the determination of steady-state and quasistatic solutions. However, the system of ordinary nonlinear differential equations given in (9) includes dynamic terms that need to be eliminated. Thus, the adaptive dynamic relaxation method given in [Kilic 2008] is utilized to obtain a steady-state solution. The dynamic relaxation method is based on the fact that the static solution is the steady-state part of the transient response of the solution. An artificial damping is introduced to guide the solution into the steady-state regime as fast as possible. Although this method is successfully utilized by Silling and his coworkers in the Emu code, it is not always possible to determine the most effective damping coefficient. Alternate to the numerical (artificial) damping, Underwood [1983] introduced an adaptive dynamic relaxation method in which the damping coefficient is changed adaptively in each time step. This method was recently extended in [Kilic 2008] for the solution of peridynamic equations in the present numerical method in which (9) is modified at time step n as

$$\ddot{\mathbf{U}}^n(\mathbf{X}, t_n) + c\dot{\mathbf{U}}^n(\mathbf{X}, t_n) = \mathbf{\Lambda}^{-1}\mathbf{F}^n(\mathbf{U}^n, \mathbf{U}^n, \mathbf{X}, \mathbf{X}'), \quad (10)$$

in which c is the damping coefficient and $\mathbf{\Lambda}$ is the fictitious diagonal density matrix that is expressed in [Kilic 2008] as

$$\lambda_{ii} \geq \frac{1}{4} \Delta t^2 \max \left(\sum_{e=1}^N \sum_{j=1}^{N_e} \text{abs}(\boldsymbol{\xi}) w_j \frac{18k}{\pi l^4} e^{-(|\boldsymbol{\xi}|/l)^2} \frac{1}{|\boldsymbol{\xi}|^2} \right), \quad (11)$$

where \max is the function that returns the value of the maximum component of the three-dimensional vector in its argument. Hence, the densities associated with a particular material point are the same in every direction of the coordinate frame, making them frame invariant. The function $\text{abs}(\cdot)$ returns a three-dimensional vector whose components are the absolute values of the three components of the vector in its argument. The vectors \mathbf{X} and \mathbf{U} represent positions and displacements at the collocation points, respectively, and they can be expressed as

$$\mathbf{X}^T = \{\mathbf{x}, \mathbf{x}_2, \dots, \mathbf{x}_M\}, \quad (12)$$

$$\mathbf{U}^T = \{\mathbf{u}(\mathbf{x}_1, t), \mathbf{u}(\mathbf{x}_2, t), \dots, \mathbf{u}(\mathbf{x}_M, t)\}, \quad (13)$$

where M is the total number of collocation points. Finally, the vector \mathbf{F} is the summation of internal and external forces, and its i -th component can be written as

$$\mathbf{F}_i = \mathbf{b}(\mathbf{x}_i, t) + \sum_{e=1}^N \sum_{j=1}^{N_e} w_j \mathbf{f}(\mathbf{u}(\mathbf{x}_i, t), \mathbf{u}(\mathbf{x}'_k, t), \mathbf{x}_i, \mathbf{x}'_k, t)). \quad (14)$$

3.1. Finite element equations. The theory for the development of the finite element method is well established [Belytschko 1983; Bathe 1982; Zienkiewicz 1977]; however, this section briefly describes the assembly of finite element equations and the solution of the assembled equations using the adaptive dynamic relaxation technique. The finite element formulation utilized in this study can be found in most finite element textbooks such as [Zienkiewicz 1977]. Hence, details will not be given here but the interested reader can refer to [Kilic 2008]. The present study utilizes direct assembly of finite element equations without constructing the global stiffness matrix. Hence, the element stiffness vector can be expressed as

$$\mathbf{f}^{(e)} = \mathbf{k}^{(e)} \mathbf{u}^{(e)}, \quad (15)$$

in which $\mathbf{k}^{(e)}$ is the element stiffness matrix described in [Zienkiewicz 1977] and $\mathbf{u}^{(e)}$ is the vector representing the nodal displacements of the e -th element. The element stiffness vector, $\mathbf{f}^{(e)}$, includes internal forces resulting from the deformation of the element. They can be assembled into a global array of internal forces by using the convention of [Belytschko 1983] as

$$\mathbf{f}^{\text{int}} = \mathbf{A}_e \mathbf{f}^{(e)}, \quad (16)$$

where \mathbf{A} is the assembly operator. These operations are strictly performed as additions. Finally, the equations of motion for adaptive dynamic relaxation can be written as

$$\ddot{\mathbf{u}}^n + c_n \dot{\mathbf{u}}^n = \mathbf{M}^{-1} \mathbf{F}^n, \quad (17)$$

in which \mathbf{M} is the mass matrix, c is the damping coefficient, and n indicates the n -th time increment. The force vector \mathbf{F} can be expressed as

$$\mathbf{F}^n = \mathbf{f}^{\text{ext}}(t^n) - \mathbf{f}^{\text{int}}(\mathbf{u}^n) \quad (18)$$

where t is time and \mathbf{f}^{ext} is the vector of external forces. As suggested in [Underwood 1983], components of the diagonal mass matrix can be effectively computed using

$$m_{ii} \geq \frac{1}{4} \Delta t^2 \sum_j |K_{ij}|, \quad (19)$$

where K_{ij} is the global stiffness matrix. However, the global stiffness matrix necessitates the use of a large amount of computer memory, which is herein avoided by constructing the mass matrix approximately as

$$\mathbf{M} = \mathbf{I} \tilde{\mathbf{m}}, \quad (20)$$

in which \mathbf{I} is the identity matrix. The mass vector, $\tilde{\mathbf{m}}$, is constructed as

$$\tilde{\mathbf{m}} = \mathbf{A} \hat{\mathbf{m}}^{(e)}, \quad (21)$$

where the components of vector $\hat{\mathbf{m}}^{(e)}$ can be written as

$$\hat{m}_i^{(e)} = \sum_{j=1}^8 |k_{ij}^{(e)}|, \quad (22)$$

in which $k_{ij}^{(e)}$ indicates the components of the element stiffness matrix given in [Zienkiewicz 1977]. This approach for the construction of a mass matrix is not as effective as that given in (19). However, it is not intended in this study to present a numerically efficient adaptive dynamic relaxation method for the finite element method; the choice of this method is solely based on simplicity of the numerical implementation. The components of the mass matrix given in (20) always satisfy the inequality given in (19) because the construction of the global matrix involves addition of positive and negative values and the present approach uses summation of their absolute values.

3.2. Coupling of peridynamic theory and finite element method. In order to take full advantage of the peridynamic theory and finite element method, the domain of interest is partitioned into two regions. These regions are modeled using the finite element method and the peridynamic theory, as shown in Figure 10a. In order to reduce the peridynamic equation of motion to its discrete form, the peridynamic region is discretized into subdomains (Figure 10b), and Gaussian integration points are placed into each subdomain (Figure 10b). As explained in [Kilic 2008], subdomains with different shapes can be utilized during the discretizations. However, this study only considers subdomains with a hexahedral shape and volume integration is performed by employing eight integration points.

According to the response function given in (2), a material point interacts with all other points within the problem domain. However, it is computationally expensive to include the interaction of a large number of collocation points. As shown in Figure 2, the magnitude of the response function fortunately decreases rapidly when the distance between the points increases. Thus, a cutoff radius, r_c , is introduced to reduce the computation time by limiting the interaction range (described in detail in [Kilic 2008]). However, the internal length, l , cannot be chosen arbitrarily small since the accuracy of volume integrals in (1) is dependent on the variation of the response function within the subdomains. Kilic [2008] numerically investigated the effect of the internal length and cutoff radius on the numerical predictions in detail.

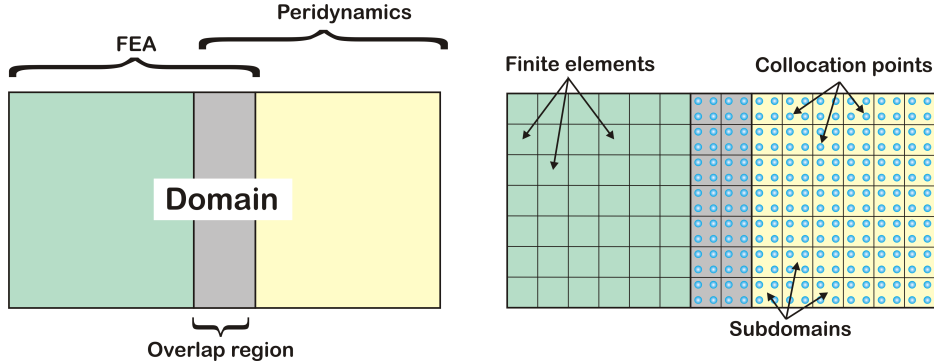


Figure 10. Schematic for coupling of the finite element method and peridynamics. Left: finite element (FEA) and peridynamic regions. Right: discretization.

Based on his findings, the internal length, l , is chosen to be approximately the maximum edge length of the hexahedral subdomains and the cutoff radius, r_c , is then set to 2.5 times the internal length, l .

The finite element region is also discretized to construct (17) by using hexahedral elements (Figure 10, right). In the region of overlap shown in Figure 10, left, both the peridynamic and the finite element equations are utilized. to achieve the appropriate coupling, the discrete peridynamic equation of motion is rewritten as

$$\begin{Bmatrix} \ddot{\underline{\underline{U}}}_p^n \\ \ddot{\underline{\underline{U}}}_p^n \end{Bmatrix} + c_n \begin{Bmatrix} \dot{\underline{\underline{U}}}_p^n \\ \dot{\underline{\underline{U}}}_p^n \end{Bmatrix} = \begin{bmatrix} \underline{\underline{\Lambda}}^{-1} & 0 \\ 0 & \underline{\underline{\Lambda}}^{-1} \end{bmatrix} \begin{Bmatrix} \underline{\underline{F}}_p^n \\ \underline{\underline{F}}_p^n \end{Bmatrix}, \quad (23)$$

where $\underline{\underline{U}}$ is a vector that contains displacements at the collocation points, subscript p denotes the variables associated with the peridynamic region, and single and double underscores denote the variables located outside and inside the overlap region, respectively. The finite element equations are also rewritten as

$$\begin{Bmatrix} \ddot{\underline{\underline{U}}}_f^n \\ \ddot{\underline{\underline{U}}}_f^n \end{Bmatrix} + c_n \begin{Bmatrix} \dot{\underline{\underline{U}}}_f^n \\ \dot{\underline{\underline{U}}}_f^n \end{Bmatrix} = \begin{bmatrix} \underline{\underline{M}}^{-1} & 0 \\ 0 & \underline{\underline{M}}^{-1} \end{bmatrix} \begin{Bmatrix} \underline{\underline{F}}_f^n \\ \underline{\underline{F}}_f^n \end{Bmatrix}, \quad (24)$$

in which subscript f denotes the variables associated with the finite element region. The solution vector $\underline{\underline{U}}_p$, representing displacements at the collocation points, is expressed in terms of the solution vector $\underline{\underline{U}}_f$, denoting nodal displacements of finite element interpolation functions, as

$$\underline{\underline{u}}_p = \sum_{i=1}^8 N_i \underline{\underline{u}}_i^{(e)} \quad (25)$$

where N_i are the shape functions given in [Zienkiewicz 1977]. The vector $\underline{\underline{u}}_i^{(e)}$ is the i -th nodal displacements of the e -th element and it is extracted from the global solution vector, $\underline{\underline{U}}_f$. The vector $\underline{\underline{u}}_p$ represents displacements of a collocation point located inside the e -th element. Since vector $\underline{\underline{U}}_p$ can be computed using (25), the force density vector $\underline{\underline{F}}_p^n$ can then be computed by utilizing (14). Furthermore, the body force densities at the collocation points are lumped into the nodes as

$$\underline{\underline{f}}_I^{(e)} = \int_{V_e} dV_e N_I \rho \underline{\underline{g}} \quad (26)$$

in which ρ is the mass density of the e -th element, \mathbf{g} is the body force density, and I indicates the I -th node of the e -th element. Hence, $f_i^{(e)}$ indicates the external force acting on the I -th node. The body force density is only known at the collocation points. Fortunately, the collocation points are placed by using a Gaussian integration technique. This allows the numerical evaluation of (26) by using collocation points as integration points for the e -th element. Furthermore, $\underline{\underline{\mathbf{F}}}_f^n$ is constructed by assembling the nodal forces given by (26). Finally, the coupled system of equations can be expressed as

$$\ddot{\underline{\mathbf{U}}}^n + c_n \dot{\underline{\mathbf{U}}}^n = \underline{\underline{\mathbf{M}}}^{-1} \underline{\underline{\mathbf{F}}}^n, \quad (27)$$

in which

$$\dot{\underline{\mathbf{U}}} = \{\dot{\underline{\mathbf{U}}}_p^n \quad \dot{\underline{\mathbf{U}}}_f^n \quad \dot{\underline{\underline{\mathbf{U}}}}_f^n\}^T \quad \text{and} \quad \ddot{\underline{\mathbf{U}}} = \{\ddot{\underline{\mathbf{U}}}_p^n \quad \ddot{\underline{\mathbf{U}}}_f^n \quad \ddot{\underline{\underline{\mathbf{U}}}}_f^n\}^T \quad (28)$$

are the first and second time derivatives of the displacements, the matrix $\underline{\underline{\mathbf{M}}}$ is given by

$$\underline{\underline{\mathbf{M}}} = \begin{bmatrix} \underline{\underline{\mathbf{A}}} & 0 & 0 \\ 0 & \underline{\underline{\mathbf{M}}} & 0 \\ 0 & 0 & \underline{\underline{\mathbf{M}}} \end{bmatrix}, \quad (29)$$

and the vector $\underline{\underline{\mathbf{F}}}$ by

$$\underline{\underline{\mathbf{F}}}^n = \{\underline{\mathbf{F}}_p^n \quad \underline{\mathbf{F}}_f^n \quad \underline{\underline{\mathbf{F}}}_f^n\}^T. \quad (30)$$

As suggested in [Underwood 1983], the damping coefficient c_n can be written as

$$c_n = 2\sqrt{((\underline{\underline{\mathbf{U}}}^n)^T \mathbf{K}^n \underline{\underline{\mathbf{U}}}^n) / ((\underline{\underline{\mathbf{U}}}^n)^T \underline{\underline{\mathbf{U}}}^n)} \quad (31)$$

in which \mathbf{K}^n is the diagonal ‘‘local’’ stiffness matrix expressed as

$${}^1K_{ii}^n = -(\underline{\underline{F}}_i^n / \underline{\underline{m}}_{ii} - \underline{\underline{F}}_i^{n-1} / \underline{\underline{m}}_{ii}) / \dot{\underline{\underline{U}}}_i^{n-1/2} \quad (32)$$

(see [Underwood 1983]). The time integration is performed using central-difference explicit integration, with a time step size of unity; explicitly,

$$\dot{\underline{\mathbf{U}}}^{n+1/2} = ((2 - c_n) \dot{\underline{\mathbf{U}}}^{n-1/2} + 2 \underline{\underline{\mathbf{M}}}^{-1} \underline{\underline{\mathbf{F}}}^n) / (2 + c_n), \quad (33)$$

$$\underline{\mathbf{U}}^{n+1} = \underline{\mathbf{U}}^n + \dot{\underline{\mathbf{U}}}^{n+1/2}. \quad (34)$$

However, the integration algorithm given by (33) and (34) cannot be used to start the integration due to an unknown velocity field at $t^{-1/2}$. Integration can be started by assuming that $\underline{\mathbf{U}}^0 \neq 0$ and $\dot{\underline{\mathbf{U}}}^0 = 0$:

$$\dot{\underline{\mathbf{U}}}^{1/2} = \frac{1}{2} \underline{\underline{\mathbf{M}}}^{-1} \underline{\underline{\mathbf{F}}}^{1/2}. \quad (35)$$

4. Numerical results

The present approach is demonstrated by considering a bar subjected to tension and a plate with a circular cutout. The bar under tension is considered to compare the displacements of the present coupled analysis, the peridynamic theory, and finite element methods while not allowing for failure to occur. The damage prediction capability of the coupled analysis is then illustrated by considering a plate with a circular cutout. Although the numerical values of the material properties are representative of engineering materials, they are not specific to a particular material. Also, the effects of the peridynamic parameters

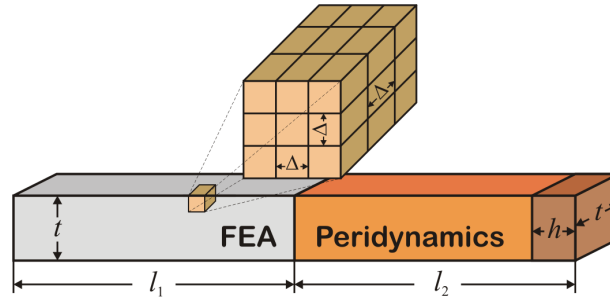


Figure 11. Dimensions and discretization of the bar.

and discretization on the convergence of the results are established by considering a rectangular plate subjected to uniaxial tension. The details of this convergence study are given in Appendix B.

4.1. Bar subjected to tension. Figure 11 describes the geometry of a bar having square cross section. The material is isotropic with Young's modulus and Poisson's ratio of $E = 10^7$ psi and $\nu = 0.25$, respectively. The bar is divided into two regions, which are modeled by using the finite element method and peridynamic theory. Furthermore, the lengths of these regions are specified to be $l_1 = 5$ in and $l_2 = 5$ in for the finite element and peridynamic regions, respectively. The bar has a square cross section with an edge length of $t = 0.4$ in. Moreover, the bar is free of any displacement constraints and subjected to uniaxial tension of 1600 lb. Because of the nonlocal nature of peridynamics, the point and surface loads cannot be applied directly. Hence, the body force density term in (1) is utilized to act as a uniaxial tension. Rectangular volume at the end of the bar is then subjected to the uniform body force density of 2×10^5 lb/in³, and its length is chosen to be $h = 0.05$ in. In the case of a finite element region, the tensile load is applied as uniform point forces on the nodes located at the surface of the bar.

The three-dimensional model is constructed to obtain a steady-state displacement field in the bar under uniform tension. Both finite element and peridynamic regions are discretized using cubic subdomains with edge lengths of $\Delta = 0.05$ in; see Figure 11. In order to obtain the discrete form of the peridynamic equation of motion, eight integration points are then placed into subdomains of the peridynamic region. The parameter defining the internal length, l , and the cutoff radius, r_c , are chosen to be 0.05 in and 0.125 in, respectively.

In order to validate the present results, the bar is also modeled using only the peridynamic theory and the finite element method. In the case of the finite element model, the SOLID45 brick element of ANSYS is utilized, and the uniaxial tension is applied as surface tractions at the end surfaces of the bar. The comparison of the displacements among the present coupled analysis, the peridynamic theory, and the finite element method is shown in Figure 12. There is approximately a 5% difference between the models using only the peridynamic theory and finite element method. Furthermore, the peridynamic theory cannot capture Poisson's ratio exactly as explained in [Kilic 2008]. Hence, a small jump is observed at the intersection of the peridynamic and finite element regions.

4.2. Plate with a circular cutout. Figure 13 describes the geometry of the plate with a circular cutout. The length and width of the plate are specified as $a = 9$ in and $b = 3$ in respectively. The thickness of the plate has a value of $t = 0.2$ in and the circular cutout has a radius of $r = 0.4$ in. The plate is isotropic

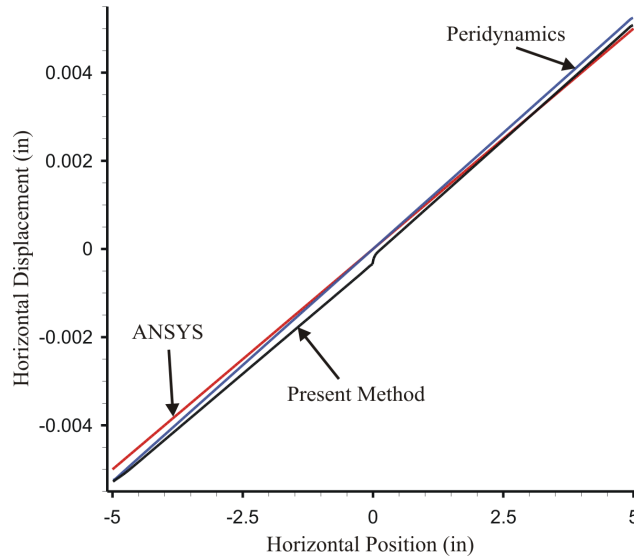


Figure 12. Comparison of horizontal displacements of the bar.

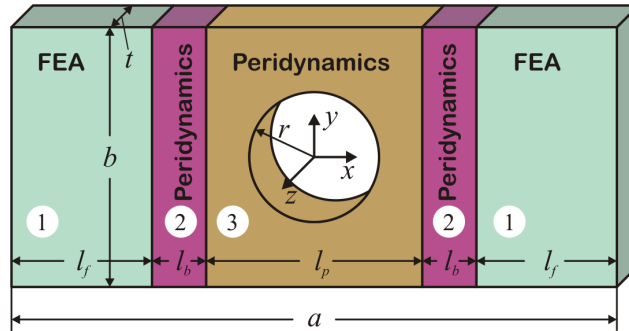


Figure 13. Dimensions of the plate with a circular cutout.

with Young’s modulus and Poisson’s ratio of $E = 10^7$ psi and $\mu = 0.25$, respectively. Furthermore, the critical stretch, s_0 , is assumed to be 0.0025. The plate is partitioned into five regions, as shown in the figure. The finite element method is employed to model the regions, which are labeled 1; the length, l_f , of these regions is specified to be 2.5 in. The regions labeled as 2 and 3 in Figure 10 are modeled by employing the peridynamic theory; the lengths of these regions are chosen to be $l_b = 0.5$ in and $l_p = 3$ in, respectively. Because of the expected errors near the peridynamic and finite element boundaries, damage is not allowed in region 2 in order to avoid premature failures near these boundaries.

The three-dimensional model is constructed by discretizing the domain into subdomains, as shown in Figure 14. Subdomains are hexahedron shaped with edge lengths of approximately 0.05 in. Hence, the internal length, l , and the cutoff radius, r_c , are chosen to be 0.05 in and 0.125 in, respectively. An integration scheme using eight collocation (integration) points is employed for the peridynamic regions.

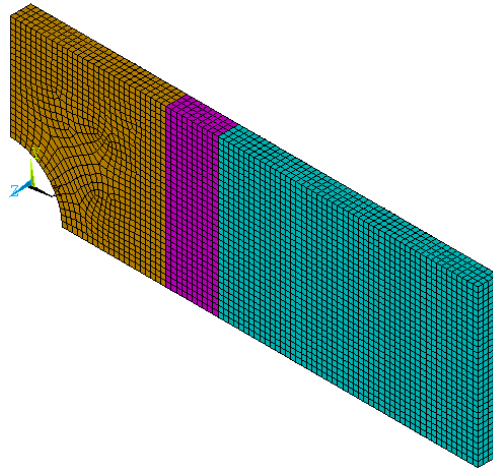


Figure 14. Discretization of the plate with a circular cutout.

The validity of the peridynamic predictions is first established in the absence of failure by comparing the steady-state displacements against the peridynamic theory and the finite element method using ANSYS, a commercially available program. In the case of no failure, the plate is subjected to a uniaxial tension of 6000 lb. Also, the plate is free of any displacement constraints. Both the peridynamic and finite element models are constructed by utilizing the same discretization as that of the peridynamic model shown in Figure 14. In the case of the peridynamic model, the tensile load is applied through a uniform body force over the volumes having the length 0.05 in. Hence, the value of the body force corresponds to 2.0×10^5 lb/in³. In the case of the finite element model, the SOLID45 brick elements of ANSYS are utilized to approximate the displacements. The uniaxial tension is applied through surface tractions of 1.0×10^4 lb/in². In the case of coupled analysis, the tensile load is applied by using uniform point forces at the nodes located at $x = \pm a/2$ and their values are determined by dividing applied tension by the number of nodes located at $x = \pm a/2$.

Figure 15 shows the horizontal and vertical displacements along the bottom line of the plate. The comparison of horizontal displacements indicates a close agreement (Figure 15, left). Although there is also good correlation of the vertical displacements obtained from the coupled analysis, the peridynamic theory, and the finite element method (Figure 15, right), the deviation is more significant for vertical displacements than for horizontal displacements. The vertical displacements from the coupled analysis and peridynamic methods are in agreement near the cutout since both methods use the peridynamic theory in this region. However, the finite element results display a larger deviation because the Poisson's ratio of 0.25 is not exactly satisfied for thin plates, as explained in [Kilic 2008]. For the same reason, a small jump is observed near the boundary between regions 1 and 2.

The plate with a circular cutout is further investigated for failure simulation. Most experiments involving failure are performed under quasistatic conditions. Therefore, it may not be practical to solve quasistatic problems using standard explicit time integrators because explicit time integrations often require very small time steps, limiting the total time of the simulation. Therefore, the adaptive dynamic relaxation is used to simulate failure.

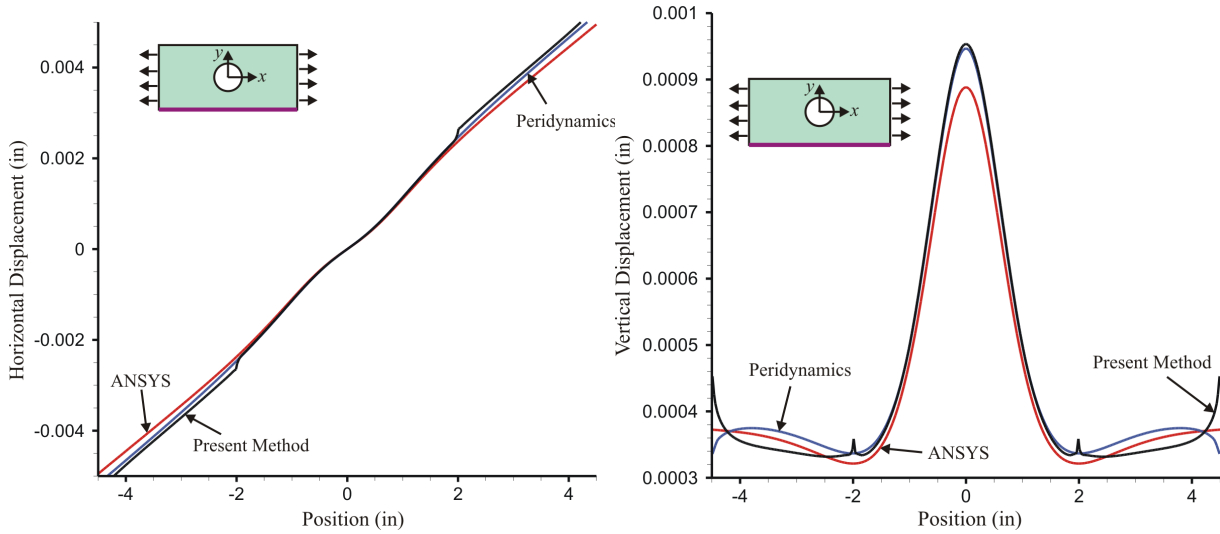


Figure 15. Horizontal (left) and vertical (right) displacements along the bottom line.

As explained in [Kilic 2008], the loading rate might significantly affect the failure patterns since the dynamic problems locally reach higher displacement gradients than under quasistatic conditions because of the traveling elastic waves.

In order to circumvent premature failure due to high local displacement gradients, the tensile load is gradually applied by incrementing the displacement at each iteration of the adaptive dynamic relaxation with a constant value of 3.125×10^{-8} in. This is a small enough value that does not create high local displacement gradients. As evidenced with this type of loading, the plate is subjected to constant displacement, and that they are applied on nodes located at $x = \pm a/2$. Furthermore, the resulting damage pattern in the peridynamic region is illustrated in Figure 16 as a contour plot of local damage given by (5). As expected, the crack initiates at the cutout, near which high displacement gradients exist (Figure 16, top left), and then propagates toward the edges of the plate (top right), until ultimate failure of the plate (bottom). The local damage index in Figure 14 is computed by (5). The local damage being 0.5 is fairly good indicator of material separation. In Figure 16, the local damage value of 0.38 indicates extensive damage not necessarily material separation.

5. Conclusions

Coupling between the peridynamic theory and finite element method was presented in order to take advantage of both methods. Since the finite element is numerically more efficient than the peridynamic theory, the regions without failure were simulated using the finite element method. Furthermore, the peridynamic theory was utilized for the regions where material failure was expected. The coupling was introduced by defining an overlap region. Both the peridynamic and finite element equations were used within this region. Furthermore, the displacement and velocity fields were determined using finite element equations in the overlap region. These fields were then utilized to compute the body force densities using the peridynamic theory. Finally, these body force densities served as external forces for finite elements in the overlap region.

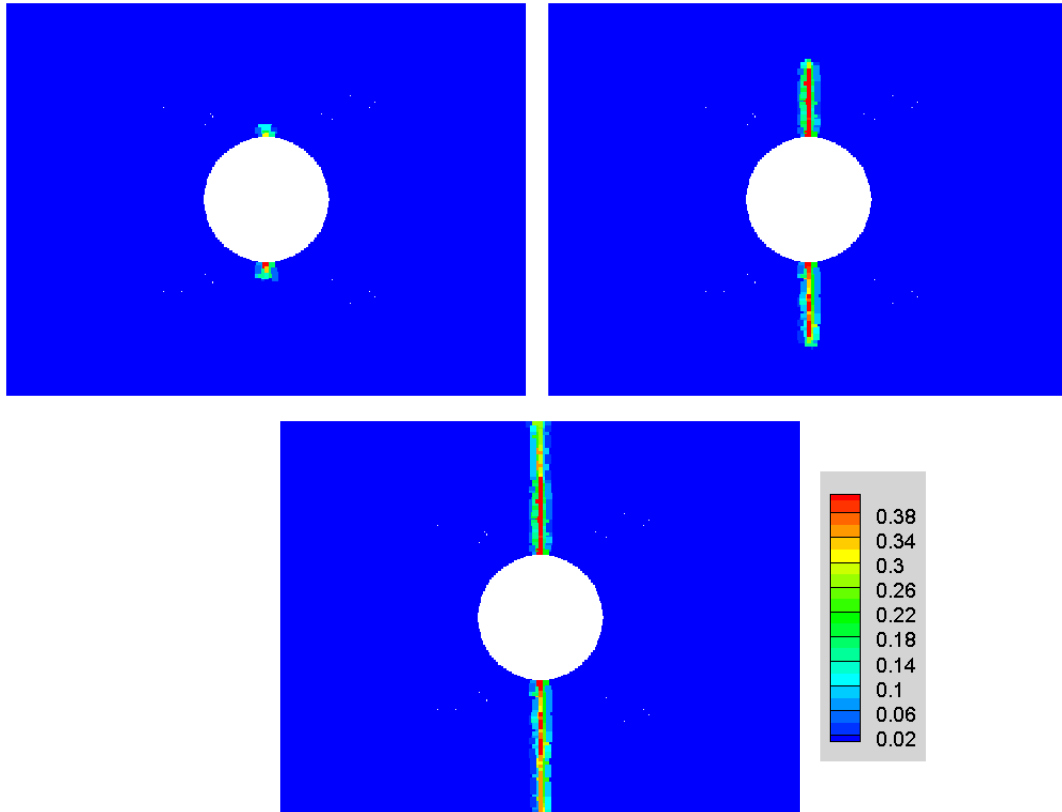


Figure 16. Contour plot of local damage. Clockwise from top left: crack initiation, crack propagation, and ultimate failure. The color scale is the same for each plot.

Material points near free surfaces and interfaces experience increases or decreases in material stiffness since the response function is obtained with the assumption that a point and its surrounding points have the same material properties. Thus, surface corrections are introduced through application of uniform extensions. It is also showed that the Poisson's ratio is not $\frac{1}{4}$ for problems having a thickness less than the cutoff radius. The results showed that the Poisson's ratio is close to $\frac{1}{3}$ for very thin plates and it approaches $\frac{1}{4}$ with increasing plate thickness. However, the surface correction method uses a Poisson's ratio of $\frac{1}{4}$ regardless of the plate thickness, which resulted in a numerical error for thin plates. The effects of internal length and cutoff radius were also investigated. It was found that internal length has a lower bound due to the discretization. Results indicate that the smallest internal length should be in the range of the edge length of the subdomains for integration schemes using eight integration points. The cutoff radius needs to be larger than 2.5 times the internal length for accurate volume integration.

The present approach has been validated by considering a bar with a square cross section and a rectangular plate with a circular cutout, both under tension. In the case of the bar, steady-state displacements were determined for the coupled problem and compared against predictions of the peridynamic theory and finite element method. Comparisons indicate very good agreement but a small displacement jump was observed at the intersection of the peridynamic and finite element regions because the peridynamic

theory does not exactly satisfy its theoretical Poisson’s ratio of 0.25. In the case of the plate with the cutout, the steady-state results show trends similar to the bar problem when compared against predictions of the peridynamics and finite element methods. The failure simulation was also performed for a plate with a cutout. As expected, two cracks initiated at the cutout and they propagated with increasing tensile load until ultimate failure of the plate.

Appendix A

The correction factor is determined based on the application of uniaxial tensile loadings to the actual finite domain of interest and the infinite domain. As illustrated in Figure A1, the correction procedure first involves the application of uniaxial tension in the x -direction, and the resulting displacement field can be expressed at the point \mathbf{x} as

$$\mathbf{u}^T(\mathbf{x}) = \left\{ \frac{\partial u^*}{\partial x}x \quad -\nu \frac{\partial u^*}{\partial x}y \quad -\nu \frac{\partial u^*}{\partial x}z \right\}^T, \tag{A1}$$

in which $\partial u^*/\partial x$ is the applied constant displacement gradient. The Poisson’s ratio $\nu = 0.25$ because the response function given in (2) is restricted to a pairwise interaction.

Based on numerical experimentation with varying values of displacement gradients, there exists no significant effect on the surface corrections. Thus, the displacement gradient, $\partial u^*/\partial x$ is assigned a value of 0.001. The contractions in the y - and z -directions are ν times the applied displacement gradient, $\partial u^*/\partial x$.

The force density in the x -direction, $g_x(\mathbf{x})$, due to the applied displacement gradient given in (A1) is expressed as

$$g_x(\mathbf{x}) = \left(\int_{\Omega^+} dV' f(\mathbf{u}', \mathbf{u}, \mathbf{x}', \mathbf{x}) - \int_{\Omega^-} dV' f(\mathbf{u}', \mathbf{u}, \mathbf{x}', \mathbf{x}) \right)_x, \tag{A2}$$

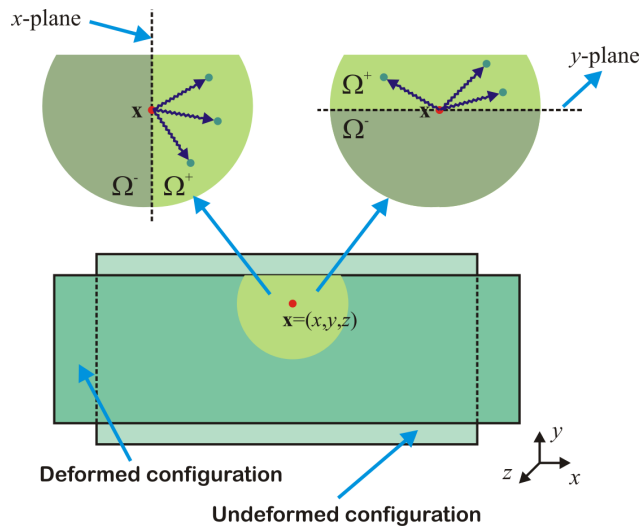


Figure A1. Schematic showing the application of uniaxial tension in the x -direction.

where Ω^+ and Ω^- are the volumes in which integration is performed and are defined to be the right and left sides of the x -plane (Figure A1). The subscript x indicates the x -component of the resulting volume integration. For a point, \mathbf{x} embedded in a single material, the value of $g_x(\mathbf{x})$ will become 2.

Moreover, by applying the displacement gradient in the y -direction, the force density, $g_y(\mathbf{x})$, can be written as

$$g_y(\mathbf{x}) = \left(\int_{\Omega^+} dV' \mathbf{f}(\mathbf{u}', \mathbf{u}, \mathbf{x}', \mathbf{x}) - \int_{\Omega^-} dV' \mathbf{f}(\mathbf{u}', \mathbf{u}, \mathbf{x}', \mathbf{x}) \right)_y, \quad (\text{A3})$$

where Ω^+ and Ω^- are the volumes in which integration is performed; they are defined to be the upper and lower sides of the y -plane (Figure A1). The force densities, $g_x(\mathbf{x})$ and $g_y(\mathbf{x})$, are clearly different due to dissimilar volumes of integrations. Hence, the domain under uniaxial tension exhibits directional dependence. In other words, depending on the direction of uniaxial tension, the points closer to the free surfaces or interfaces experience different force densities, which is not physically acceptable. Therefore, the uniaxial tension is also applied in the y - and z -directions, which leads to three different responses at each integration point and can be expressed in vector form

$$\mathbf{g}^T(\mathbf{x}) = \{g_x \quad g_y \quad g_z\}, \quad (\text{A4})$$

in which x , y , and z represent the directions of applied uniaxial tension.

It is assumed that there is a fictitious domain composed of a single material (Figure A2). The material in this domain is assumed to have the same properties as those given for point \mathbf{x} of the actual domain of interest (Figure A1). As illustrated in Figure A2, the point located at $\mathbf{x}^T = \{0, 0, 0\}$ is surrounded by other points so that there is no surface within the cutoff radius, r_c . Hence, this point does not show any directional dependence, and it is sufficient to apply uniaxial tension only in one direction. In order to compute the force density due to uniaxial tension given in (A1), the fictitious domain is discretized using cubic subdomains (Figure A2). The edge length of the cube, Δ_∞ , is typically chosen to be one fiftieth of the cutoff radius, r_c . Furthermore, the displacement field is assumed to be constant within each

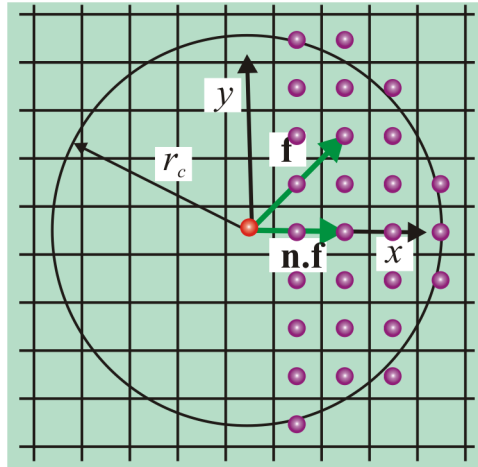


Figure A2. Discretization of infinite domain with cubes.

subdomain. Under these considerations, the force density in this domain can be approximated as,

$$g_\infty = 2 \sum_{i=0}^{\infty} \sum_{j=0}^{\infty} \sum_{k=0}^{\infty} n_x \cdot f(\mathbf{u} = \mathbf{0}, \mathbf{u}', \mathbf{x}', \mathbf{x} = \mathbf{0}, t) \Delta_\infty^3, \tag{A5}$$

in which n_x is the unit vector in the x -direction. The position vector \mathbf{x}' is defined as

$$\mathbf{x}' = \Delta_\infty \left\{ i + \frac{1}{2} \quad j + \frac{1}{2} \quad k + \frac{1}{2} \right\}^T = \{x' \quad y' \quad z'\}^T. \tag{A6}$$

Finally, the displacement vector \mathbf{u}' can be written as

$$\mathbf{u}' = \left\{ \frac{\partial \mathbf{u}^*}{\partial \mathbf{x}} x' \quad -\nu \frac{\partial \mathbf{u}^*}{\partial \mathbf{x}} y' \quad -\nu \frac{\partial \mathbf{u}^*}{\partial \mathbf{x}} z' \right\}^T. \tag{A7}$$

If the material point is surrounded by material points of the same material and there is no interface or free surfaces within the cutoff radius, which is shown as point 1 in Figure 9, each component of the vector given in (A4) should be equal to the response given in (A5). However, this does not occur due to the approximations in the computation of the integral given in (1). Therefore, the present approach also attempts to correct not only the material stiffness variations due to surface effects but also the approximations in the numerical integration. Therefore, the correction is applied to all collocation points regardless of their position.

As illustrated in Figure A3, the scaling constant g_{ij} between the pair of material points located at \mathbf{x}_i and \mathbf{x}_j is calculated by assuming an ellipsoidal variation as

$$g_{ij} = \left((n_x/g_{ijcx})^2 + (n_y/g_{ijcy})^2 + (n_z/g_{ijcz})^2 \right)^{-1/2}, \tag{A8}$$

in which n_x, n_y, n_z are the components of the normal vector, \mathbf{n} in the undeformed configuration between the pair of material point; it is defined as

$$\mathbf{n} = \zeta / |\zeta| = \{n_x, n_y, n_z\}^T. \tag{A9}$$

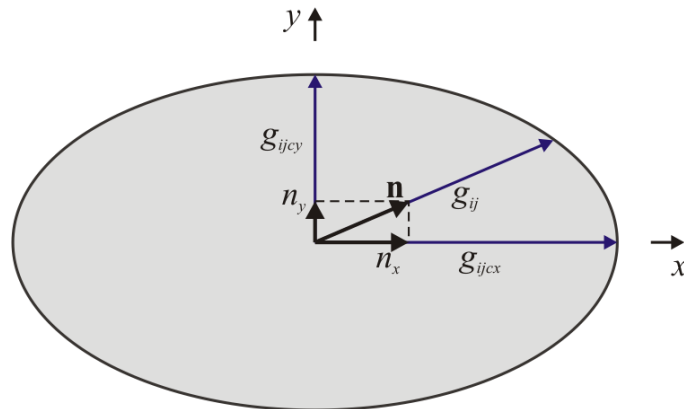


Figure A3. Graphical representation of scaling coefficient.

The average coefficient vector \mathbf{g}_{ijc} can be written as

$$\mathbf{g}_{ijc} = (\mathbf{g}_{ci} + \mathbf{g}_{cj})/2, \quad (\text{A10})$$

in which

$$\mathbf{g}_c^T(\mathbf{x}) = \{g_{xc}, g_{yc}, g_{zc}\} = \{g_\infty/g_{xc}, g_\infty/g_{yc}, g_\infty/g_{zc}\}. \quad (\text{A11})$$

After considering the surface effects, the discrete form of the equations of motion given in (9) is corrected as

$$\rho \ddot{\mathbf{u}}(\mathbf{x}_i, t) = \mathbf{b}(\mathbf{x}_i, t) + \sum_{e=1}^N \sum_{j=1}^{N_e} g_{ij} w_j \mathbf{f}(\mathbf{u}(\mathbf{x}_i, t), \mathbf{u}(\mathbf{x}'_k, t), \mathbf{x}_i, \mathbf{x}'_k, t). \quad (\text{A12})$$

According to (A10), the vector \mathbf{g}_{ijc} is computed by taking the average of the coefficients given in (A11) for two interacting material points. As a result, the surface correction given in (A8) is underestimated for the material point with the larger scaling coefficient and overestimated for the material point with the smaller scaling coefficient. Hence, a single iteration is generally not sufficient to determine the scaling coefficients. Therefore, the scaling coefficients in (A10) are computed iteratively. Each component given in (A10) is set to unity at the beginning of the first iteration step, and then the method outlined above is utilized to determine the coefficients given in (A10). Then, the present method is repeated n times, during which the results of the previous iteration are used as a scaling coefficient. After numerical investigation, it was found that the change in the coefficients in (A10) is insignificant after approximately twenty iterations. Hence, the number of iterations, n , is taken to be twenty in this study. Although this method enables the correction to material behavior due to the surface effects and approximations during the numerical integration, it is still not exact.

Appendix B

The effects of the peridynamic parameters and discretization are established by considering a rectangular plate (Figure B1). The length and width of the plate are specified as $a = 10$ in and $b = 4$ in, respectively. The plate is free of any displacement constraints and is subjected to uniaxial tension in the x -direction.

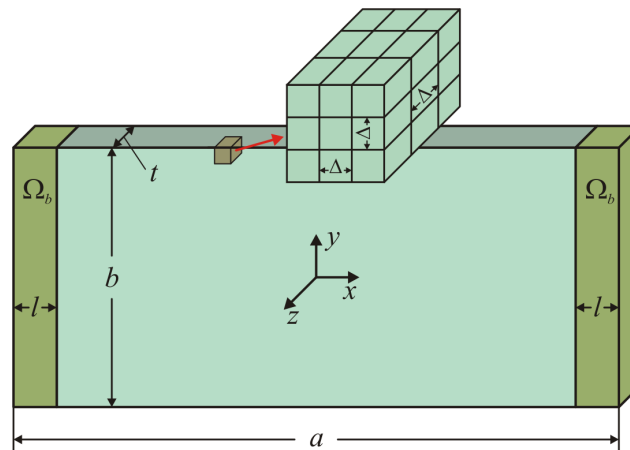


Figure B1. Dimensions and discretization of the plate.

However, point and surface loads cannot be applied directly because the peridynamic equation of motion involves a volume integral that gives rise to zero for point and surface loads. Thus, the uniaxial tension is applied as uniform body forces over the volumes, Ω_b , along the vertical edges having a length, l , of 0.08 in (Figure B1). The longitudinal component of the applied body force is specified as $b_x = 234375.0 \text{ lb/in}^3$. Hence, the applied tension, F , can be computed in terms of the plate dimensions as $F = lbtb_x$.

The material of the plate is isotropic with Young’s modulus and Poisson’s ratio of $E = 10^7 \text{ psi}$ and $\nu = 0.25$, respectively. The three-dimensional peridynamic model is constructed by discretization of the plate using cubic subdomains (Figure B1). In each subdomain, eight integration points are utilized to reduce the peridynamic equation of motion to its discrete form. The steady-state solutions are obtained by using the adaptive dynamic relaxation.

Within the realm of molecular dynamics, it is well known that the Poisson’s ratio is restricted to $\frac{1}{4}$ in three dimensions and $\frac{1}{3}$ in two dimensions if atomic interactions are pairwise and do not exhibit any directional dependence. Gerstle et al. [2005] showed that the same restrictions apply to peridynamics equations under the same conditions. Hence, the thickness of the plate affects the observed Poisson’s ratio. Figure B2 shows the variation of the Poisson’s ratio with increasing plate thickness. The Poisson’s ratio is calculated using steady-state displacements at the point located at \mathbf{x}_0 , which can be expressed as

$$\mathbf{x}_0^T = \{x_0 = 2.5, y_0 = 1.0, z_0 = 0.0\} \tag{B1}$$

and the displacement field at \mathbf{x}_0 can be written as

$$\mathbf{u}_0^T = \{u_{x0}, u_{y0}, u_{z0}\}. \tag{B2}$$

Hence, the Poisson’s ratio is approximated by using initial positions and displacements as

$$\nu = -\frac{u_{y0}/y_0}{u_{x0}/x_0}. \tag{B3}$$

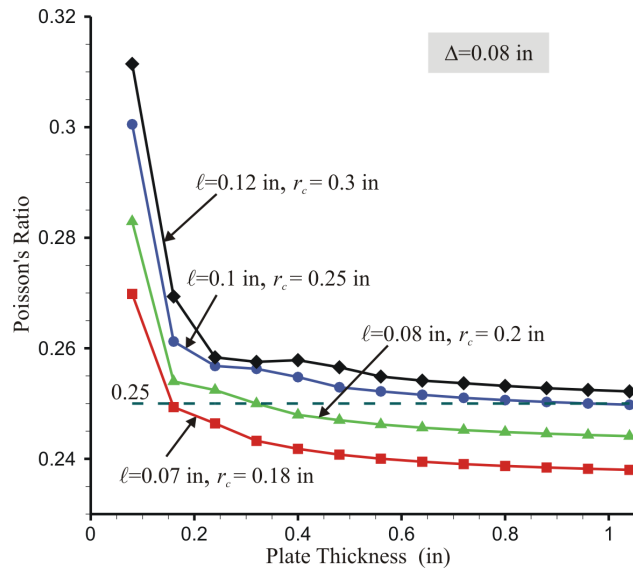


Figure B2. Effect of internal length on Poisson’s ratio with increasing plate thickness.

It is apparent in Figure B2 that the Poisson's ratio approaches its theoretical value of $\frac{1}{4}$ with increasing plate thickness. Conversely, the Poisson's ratio approaches $\frac{1}{3}$ with decreasing plate thickness. The internal length also affects the Poisson's ratio substantially (Figure B2). The number of interactions for points shown in Figure 9 can be determined by finding the volume of points whose distance to point of interest is less than the cutoff radius. Hence, the number of interactions for a point located at \mathbf{x} can be computed as

$$\chi(\mathbf{x}) = \int_{|\mathbf{x}'-\mathbf{x}|<r_c} dV_{\mathbf{x}'}. \quad (\text{B4})$$

According to (B4), a point can have the highest number of interactions if it is completely surrounded by other points within the range of the cutoff radius. Hence, the highest number of interactions is the volume of a sphere, which can be expressed as

$$\chi_{\max} = \frac{4}{3}\pi r_c^3. \quad (\text{B5})$$

For thin structures whose thickness is less than the cutoff radius, χ_{\max} is never reached. Furthermore, the ratio of the number of interactions to χ_{\max} reduces with increasing internal length due to its proportionality with the cutoff radius. Therefore, the plate behaves more like a two-dimensional medium with increasing internal length since most interactions are in the x - y plane. As a result, the Poisson's ratio increases with increasing internal length, especially for thin plates (Figure B2).

It is also expected that the plate thickness affects the displacement fields because the surface correction is based on the assumption that the Poisson's ratio is $\frac{1}{4}$. However, the Poisson's ratio is not necessarily $\frac{1}{4}$ for thin structures (Figure B2). Thus, longitudinal displacements deviate from the results of the finite element analysis with decreasing plate thickness (Figure B3, left). The finite element results are obtained using SOLID45 brick elements of ANSYS. The three-dimensional finite element mesh is constructed

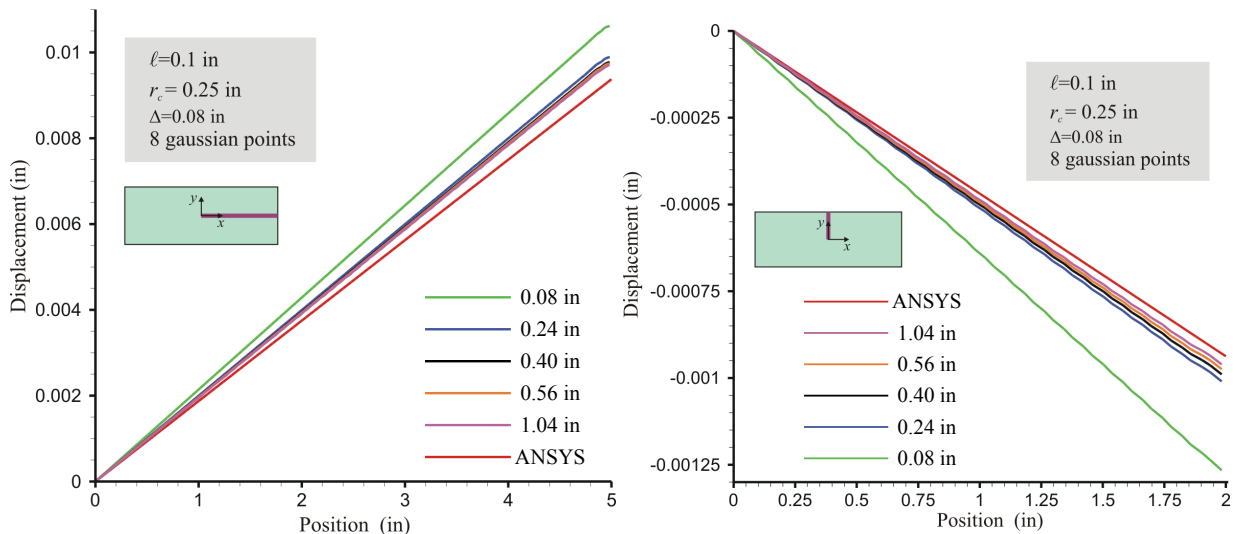


Figure B3. Effect of layer thickness on displacements in the x -direction (left) and the y -direction (right). In each graph, the curves are stacked in the same order as in the legend.

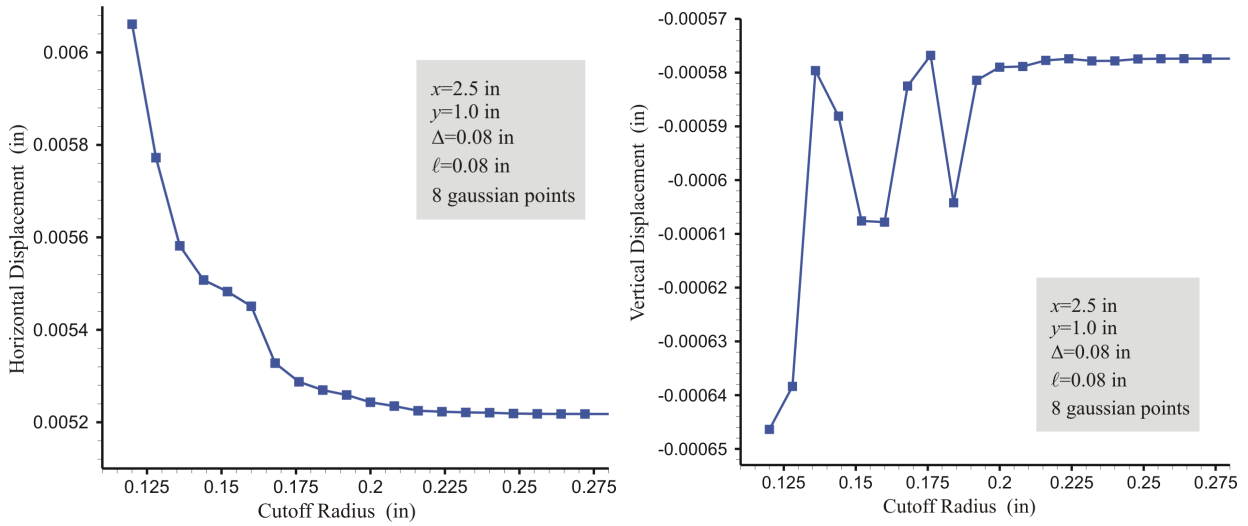


Figure B4. Effect of cutoff radius on displacements in the x -direction (left) and the y -direction (right).

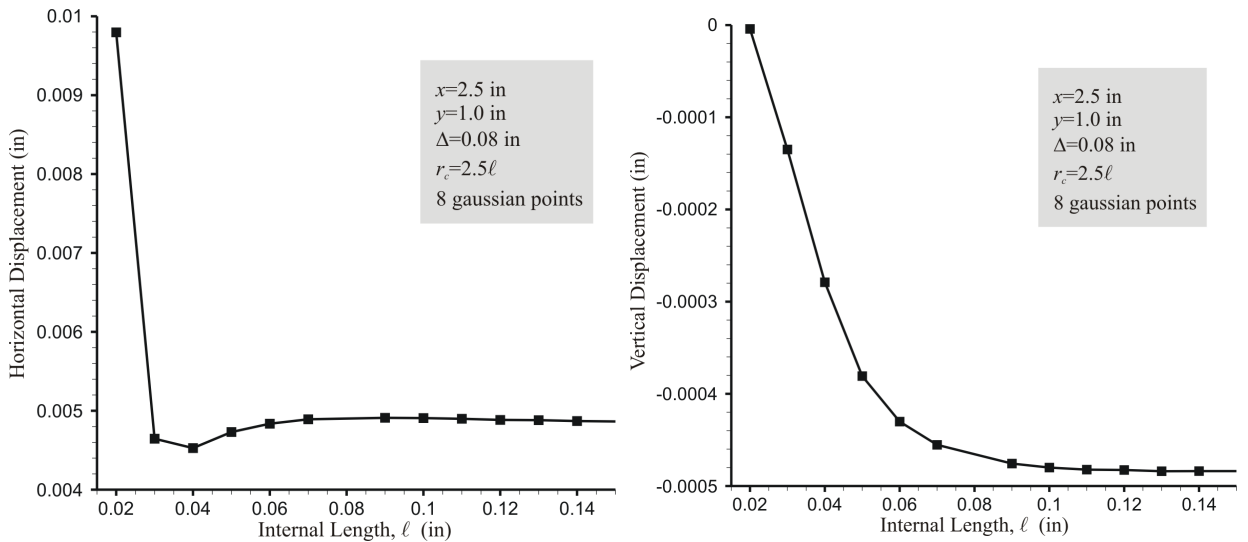


Figure B5. Effect of internal length on displacements in the x -direction (left) and the y -direction (right).

using the discretization shown in Figure B1, and the Poisson’s ratio is specified as $\frac{1}{4}$. The differences in results are more pronounced for displacements in the transverse direction (Figure B3, right) because they are influenced by both the surface correction and the Poisson’s ratio. However, the results converge to that of the finite element method with increasing plate thickness (Figure B3).

Determination of the internal length and cutoff radius for a specific problem is another source of uncertainty or approximation. The computational resources typically limit the number of subdomains.

This limitation might be due to the available computational space and/or memory. However, the primary limitation on the number of subdomains is the total computational time, which depends on the number of time steps. The computational time can be minimized by using the smallest possible cutoff radius for a given discretization. On the contrary, the accuracy of numerical integration provides a lower bound for the cutoff radius. Here, in order to quantify the effect of the cutoff radius on the numerical predictions, the internal length is specified as 0.08 in and the cutoff radius is varied. Figure B4 shows the change in displacements at the point located at $\{2.5 \ 1.0 \ 0.0\}^T$ with an increasing cutoff radius. In this case, the plate thickness is defined as 0.08 in. The volume integral given in (1) is performed over the domain (Figure B1). However, the cutoff radius is introduced to reduce the computational time by taking advantage of the rapidly decaying exponential term in the response function. For a small cutoff radius, the volume integration is not performed accurately because the exponential term is still significant beyond the cutoff radius. Therefore, some of the stiffness of the material is lost, resulting in high longitudinal displacements (Figure B4, left). However, the longitudinal displacement converges with increasing cutoff radius (Figure B4). When the cutoff radius is larger than 0.2 in, no significant difference is observed in the displacement results. The cutoff radius of 0.2 is 2.5 times the internal length. Therefore, the present study utilizes a cutoff radius that is 2.5 times the internal length for the remaining computations.

After determining the cutoff radius in terms of the internal length, the internal length is also varied for a plate with a thickness of 0.8 in. Figure B5 shows the variation of the displacements at the point located at $\{2.5 \ 1.0 \ 0.0\}^T$ with an increasing internal length. As expected, the numerical integration is not accurate for a small internal length because the exponential term decays very fast. A material point is mostly influenced by the nearest points, for which the exponential term is very small. For small internal length, there is also a loss in stiffness of the material since most of the stiffness is localized near the material point that is not captured by the numerical integration correctly. However, the displacements converge with increasing internal length. Results do not significantly change for internal lengths larger than 0.08 in. This specific value is the size of the cubic subdomain in the discretization and the present study utilizes the highest edge length of the subdomains as the internal length.

References

- [Askari et al. 2006] E. Askari, J. Xu, and S. Silling, "Peridynamic analysis of damage and failure in composites", in *44th AIAA Aerospace Sciences Meeting and Exhibit* (Reno, NV, 2006), AIAA, Reston, VA, 2006. Paper #2006-88.
- [Bathe 1982] K. J. Bathe, *Finite element procedures in engineering analysis*, Prentice-Hall, Englewood Cliffs, NJ, 1982. Revised in 1996.
- [Belytschko 1983] T. Belytschko, "An overview of semidiscretization and time integration procedures", pp. 1–65 in *Computational methods for transient analysis*, edited by T. Belytschko and T. J. R. Hughes, North-Holland, Amsterdam, 1983.
- [Belytschko and Black 1999] T. Belytschko and T. Black, "Elastic crack growth in finite elements with minimal remeshing", *Int. J. Numer. Methods Eng.* **45**:5 (1999), 601–620.
- [Berger and Bokhari 1987] M. J. Berger and S. H. Bokhari, "A partitioning strategy for nonuniform problems on multiprocessors", *IEEE Trans. Comput.* **C-36**:5 (1987), 570–580.
- [Colavito et al. 2007a] K. W. Colavito, B. Kilic, E. Celik, E. Madenci, E. Askari, and S. Silling, "Effect of void content on stiffness and strength of composites by a peridynamic analysis and static indentation test", in *48th AIAA/ASME/ASCE/AHS/ASC Structures, Structural Dynamics, and Materials Conference* (Honolulu, HI, 2007), AIAA, Reston, VA, 2007. Paper #2007-2251.

- [Colavito et al. 2007b] K. W. Colavito, B. Kilic, E. Celik, E. Madenci, E. Askari, and S. Silling, “Effects of nanoparticles on stiffness and impact strength of composites”, in *48th AIAA/ASME/ASCE/AHS/ASC Structures, Structural Dynamics, and Materials Conference* (Honolulu, HI, 2007), AIAA, Reston, VA, 2007. Paper #2007-2021.
- [Gerstle and Sau 2004] W. H. Gerstle and N. Sau, “Peridynamic modeling of concrete structures”, pp. 949–956 in *Fracture mechanics of concrete structures: proceedings of the Fifth International Conference on Fracture Mechanics of Concrete and Concrete Structures* (Vail, CO, 2004), vol. 2, edited by V. C. Li et al., Ia-FraMCos, Evanston, IL, 2004.
- [Gerstle et al. 2005] W. Gerstle, N. Sau, and S. Silling, “Peridynamic modeling of plain and reinforced concrete structures”, pp. 54–68 in *Proceedings of the 18th International Conference on Structural Mechanics in Reactor Technology (SMiRT 18)* (Beijing, 2005), edited by Y. Zhou et al., Atomic Energy Press, Beijing, 2005. Paper #SMiRT18-B01-2.
- [Jirásek 2000] M. Jirásek, “Comparative study on finite elements with embedded discontinuities”, *Comput. Methods Appl. Mech. Eng.* **188**:1–3 (2000), 307–330.
- [Kilic 2008] B. Kilic, *Peridynamic theory for progressive failure prediction in composite materials*, Ph.D. thesis, University of Arizona, Tucson, AZ, 2008.
- [Macek and Silling 2007] R. W. Macek and S. A. Silling, “Peridynamics via finite element analysis”, *Finite Elem. Anal. Des.* **43**:15 (2007), 1169–1178.
- [Melenk and Babuška 1996] J. M. Melenk and I. Babuška, “The partition of unity finite element method: basic theory and applications”, *Comput. Methods Appl. Mech. Eng.* **139**:1–4 (1996), 289–314.
- [Moës and Belytschko 2002] N. Moës and T. Belytschko, “Extended finite element method for cohesive crack growth”, *Eng. Fract. Mech.* **69**:7 (2002), 813–833.
- [Moës et al. 1999] N. Moës, J. Dolbow, and T. Belytschko, “A finite element method for crack growth without remeshing”, *Int. J. Numer. Methods Eng.* **46**:1 (1999), 131–150.
- [Silling 2000] S. A. Silling, “Reformulation of elasticity theory for discontinuities and long-range forces”, *J. Mech. Phys. Solids* **48**:1 (2000), 175–209.
- [Silling 2003] S. A. Silling, “Dynamic fracture modeling with a meshfree peridynamic code”, pp. 641–644 in *Second MIT Conference on Computational Fluid and Solid Mechanics* (Cambridge, MA, 2003), edited by K. J. Bathe, Elsevier, Amsterdam, 2003.
- [Silling and Askari 2004] S. A. Silling and E. Askari, “Peridynamic modeling of impact damage”, *ASME Conf. Proc.* **2004** (2004), 197–205. Paper No. PVP2004-3049.
- [Silling and Askari 2005] S. A. Silling and E. Askari, “A meshfree method based on the peridynamic model of solid mechanics”, *Comput. Struct.* **83**:17–18 (2005), 1526–1535.
- [Silling and Bobaru 2005] S. A. Silling and F. Bobaru, “Peridynamic modeling of membranes and fibers”, *Int. J. Non-Linear Mech.* **40**:2–3 (2005), 395–409.
- [Underwood 1983] P. Underwood, “Dynamic relaxation”, pp. 245–265 in *Computational methods for transient analysis*, edited by T. Belytschko and T. J. R. Hughes, North-Holland, Amsterdam, 1983.
- [Xu et al. 2007] J. Xu, A. Askari, O. Weckner, H. Razi, and S. Silling, “Damage and failure analysis of composite laminates under biaxial loads”, in *48th AIAA/ASME/ASCE/AHS/ASC Structures, Structural Dynamics, and Materials Conference* (Honolulu, HI, 2007), AIAA, Reston, VA, 2007. Paper #2007-2315.
- [Zi et al. 2007] G. Zi, T. Rabczuk, and W. Wall, “Extended meshfree methods without branch enrichment for cohesive cracks”, *Comput. Mech.* **40**:2 (2007), 367–382.
- [Zienkiewicz 1977] O. C. Zienkiewicz, *The finite element method*, 3rd ed., McGraw-Hill, London, 1977. 6th ed. published in 2005.

Received 31 Oct 2008. Revised 2 Feb 2010. Accepted 5 Feb 2010.

BAHATTIN KILIC: bkilic@gmail.com

Department of Aerospace and Mechanical Engineering, The University of Arizona, Tucson, AZ 85716, United States

ERDOGAN MADENCI: madenci@email.arizona.edu

Department of Aerospace and Mechanical Engineering, The University of Arizona, Tucson, AZ 85716, United States

<http://www.ame.arizona.edu/faculty/madenci/madenci.php>

GENETIC PROGRAMMING AND ORTHOGONAL LEAST SQUARES: A HYBRID APPROACH TO MODELING THE COMPRESSIVE STRENGTH OF CFRP-CONFINED CONCRETE CYLINDERS

AMIR HOSSEIN GANDOMI, AMIR HOSSEIN ALAVI,
PARVIN ARJMANDI, ALIREZA AGHAEIFAR AND REZA SEYEDNOUR

The main objective of this paper is to apply genetic programming (GP) with an orthogonal least squares (OLS) algorithm to derive a predictive model for the compressive strength of carbon fiber-reinforced plastic (CFRP) confined concrete cylinders. The GP/OLS model was developed based on experimental results obtained from the literature. Traditional GP-based and least squares regression analyses were performed using the same variables and data sets to benchmark the GP/OLS model. A subsequent parametric analysis was carried out and the trends of the results were confirmed via previous laboratory studies. The results indicate that the proposed formula can predict the ultimate compressive strength of concrete cylinders with an acceptable level of accuracy. The GP/OLS results are more accurate than those obtained using GP, regression, or several CFRP confinement models found in the literature. The GP/OLS-based formula is simple and straightforward, and provides a valuable tool for analysis.

1. Introduction

Concrete is a frictional material with considerable sensitivity to hydrostatic pressure. Lateral stress has advantageous effects on concrete strength and deformation. When concrete is uniaxially loaded and cannot dilate laterally, it exhibits increased strength and axial deformation capacity, indicated as confinement. Concrete confinement can generally be provided through transverse reinforcement in the form of spirals, circular hoops, or rectangular ties or by encasing the concrete columns in steel tubes that act as permanent formwork [de Lorenzis 2001]. Fiber-reinforced polymers (FRPs) are also used for the confinement of concrete columns. Compared to steel [Fardis and Khalili 1982], FRPs present several advantages, such as ease and speed of application, continuous confining action to the entire cross-section, lack of change in the shape and size of the strengthened elements, and corrosion resistance [de Lorenzis 2001]. A typical response of FRP-confined concrete is shown in Figure 1, where normalized axial stress is plotted against axial, lateral, and volumetric strains. The stress is normalized with respect to the unconfined strength of the concrete core. The figure shows that both axial and lateral responses are bilinear with a transition zone at or near the peak strength of the unconfined concrete core. The volumetric response shows a similar transition toward volume expansion. However, as soon as the jacket takes over, the volumetric response undergoes another transition which reverses the dilation trend and results in volume compaction. This behavior is shown to be remarkably different from plain concrete and steel-confined concrete [Mirmiran et al. 2000].

Keywords: genetic programming, orthogonal least squares, CFRP confinement, concrete compressive strength, formulation.

Carbon fiber-reinforced plastic (CFRP) is one of the main types of FRP composites. The advantages of CFRP include anticorrosion, easy cutting and construction, as well as high strength-to-weight ratio and high elastic modulus. These features caused widely usage of CFRP in the retrofitting and strengthening of reinforced concrete structures for over 50 years. A typical CFRP-confined concrete cylinder is illustrated in Figure 2.

Several studies have been conducted to analyze the effect of CFRP confinement on the strength and deformation capacity of concrete columns. On the basis of this research, a number of empirical and theoretical models have been developed [de Lorenzis 2001]. In spite of the extensive research in this field, the existing models have significant limitations, such as specific loading systems and conditions,

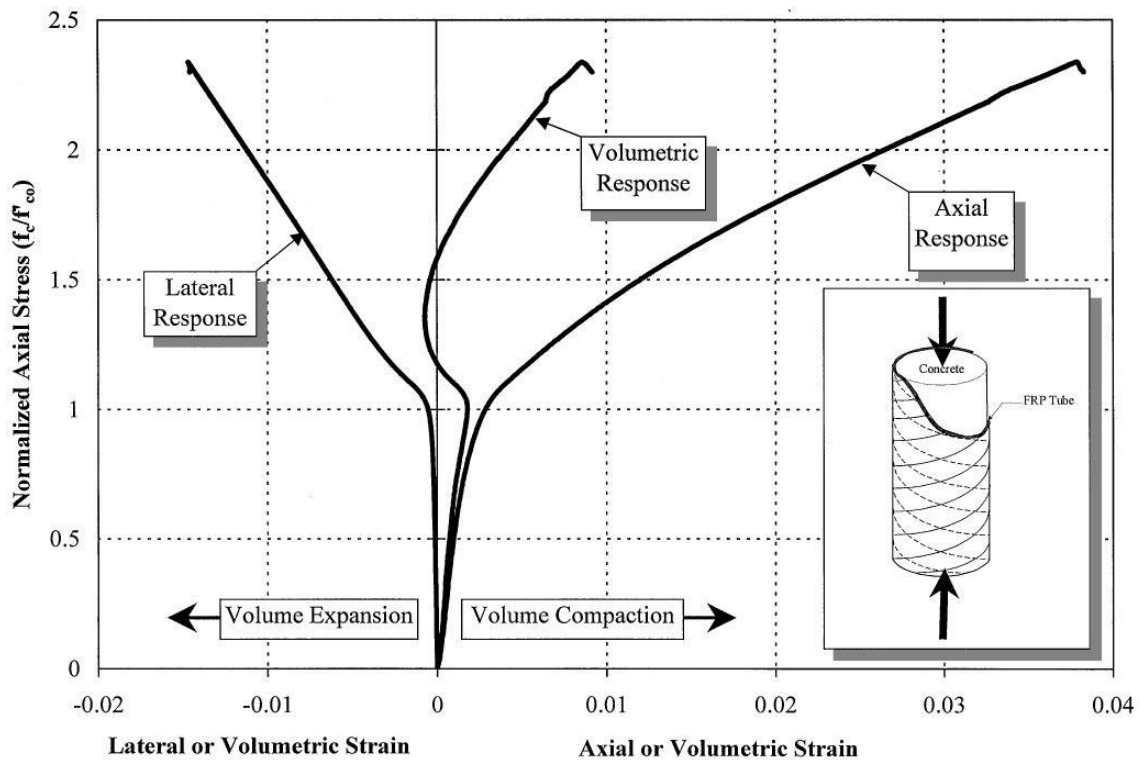


Figure 1. Typical response of FRP-confined concrete [Mirmiran et al. 2000].

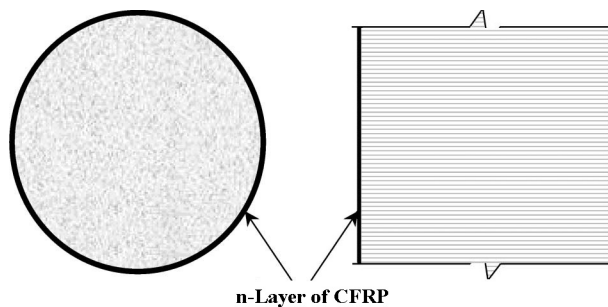


Figure 2. A typical CFRP-confined concrete cylinder.

and the need for calibration of parameters. These limitations suggest the necessity of developing more comprehensive mathematical models for assessing the behavior of CFRP-confined concrete columns.

Genetic programming (GP) [Koza 1992; Banzhaf et al. 1998] is a developing subarea of evolutionary algorithms, where programs are represented as tree structures (see Section 3). GP and its variants have successfully been applied to various kinds of civil engineering problems [Alavi et al. 2010; Gandomi et al. 2009; 2010; Alavi and Gandomi \geq 2010].

The orthogonal least squares (OLS) algorithm [Billings et al. 1988; Chen et al. 1989] is an effective algorithm for determining which terms are significant in a linear-in-parameters model. The OLS algorithm introduces the error reduction ratio, which is a measure of the decrease in the variance of output by a given term. [Madár et al. 2005b; 2005c] combined GP and OLS to make a hybrid algorithm with better efficiency, showing that introducing OLS to the GP process results in more robust and interpretable models. GP/OLS uses the data alone to determine the structure and parameters of the model. This technique has rarely been applied to civil engineering problems [Gandomi and Alavi 2010]. The GP/OLS approach can be substantially useful in deriving empirical models for characterizing the compressive strength behavior of CFRP-confined concrete cylinders by directly extracting the knowledge contained in the experimental data.

The main purpose of this paper is to utilize GP/OLS to generate a linear-in-parameters predictive model of the compressive strength of CFRP concrete cylinders represented by tree structures. The predictor variables included in the analysis were unconfined concrete strength and ultimate confinement pressure. Traditional GP and least squares regression models were developed to benchmark the derived model. A reliable database of previously published test results was utilized to develop the models.

2. Previous research on behavior of CFRP-confined concrete

The characteristic response of confined concrete includes three distinct regions of uncracked elastic deformation, crack formation and propagation, and plastic deformation. It is generally assumed that concrete behaves like an elastic-perfectly plastic material after reaching its maximum strength capacity. The failure surface is considered to be fixed in stress space. Constitutive models for concrete should be concerned with pressure sensitivity, path dependence, stiffness degradation, and cyclic response. Existing plasticity models include nonlinear elasticity, endochronic plasticity, classical plasticity, multilaminate or micro-plane plasticity, and bounding surface plasticity. Many of these models, however, are only suitable in specific applications and loading systems for which they are devised and may give unrealistic results in other cases. Also, some of these models require several parameters to be calibrated based on experimental results [Mirmiran et al. 2000]. Considerable experimental research has been performed on the behavior of CFRP-confined concrete columns [Miyachi et al. 1997; Kono et al. 1998; Matthys et al. 1999; Rochette and Labossière 2000; Shahawy et al. 2000; Micelli et al. 2001; Rousakis 2001]. Numerous studies have concentrated on assessing the strength enhancement of CFRP-wrapped concrete cylinders in the literature. Some of the most important models in this field are shown in Table 1.

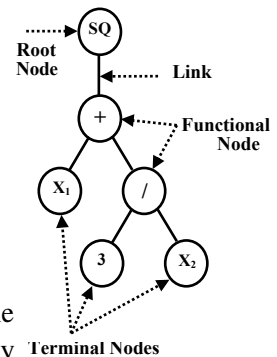
By extending developments in computational software and hardware, several alternative computer-aided data mining approaches have been developed. Thus, Cevik and Guzelbey [2008] presented an application of neural networks (NN) to the modeling of the compressive strength of a CFRP-confined concrete cylinder. They also obtained the explicit formulation of the compressive strength using NN.

ID	Authors	Expression for f'_{cc}/f'_{co}
1	[Fardis and Khalili 1981]	$1 + 3.7(p_u/f'_{co})^{0.85}$
2	[Mander et al. 1988]	$2.254\sqrt{1 + 7.94P_u/f'_{co}} - 2P_u/f'_{co} - 1.254$
3	[Miyachi et al. 1997]	$1 + 3.485(p_u/f'_{co})$
4	[Xiao and Wu 2000]	$1.1 + (4.1 - 0.75f'_{co}{}^2/E_l)p_u/f'_{co}$
5	[Samaan et al. 1998]	$1 + 0.6p_u^{0.7}$
6	[Lam and Teng 2001]	$1 + 2(p_u/f'_{co})$
7	[Toutanji 1999]	$1 + 3.5(p_u/f'_{co})^{0.85}$
8	[Saafi et al. 1999]	$1 + 2.2(p_u/f'_{co})^{0.84}$
9	[Spoelstra and Monti 1999]	$0.2 + 3\sqrt{p_u/f'_{co}}$
10	[Karbhari and Gao 1997]	$1 + 2.1(p_u/f'_{co})^{0.87}$
11	[Richart et al. 1928]	$1 + 4.1(p_u/f'_{co})$
12	[Berthet et al. 2006]	$1 + K_1 \frac{P_u}{f'_{co}}, \quad K_1 = \begin{cases} 3.45 & \text{if } 20 \leq f'_{co}/\text{MPa} \leq 50 \\ 0.95(f'_{co})^{-1/4} & \text{if } 50 \leq f'_{co}/\text{MPa} \leq 200 \end{cases}$
13	[Li et al. 2003] (L-L Model)	$1 + \tan(45^\circ - \frac{1}{2}\phi)(P_u/f'_{co}), \quad \phi = 36^\circ + 1^\circ(f'_{co}/35) \leq 45^\circ$
14	[Vintzileou and Panagiotidou 2008]	$1 + 2.8(P_u/f'_{co})$

Table 1. Different models for the strength enhancement of FRP confined concrete cylinders. f'_{co} is the compressive strength of the unconfined concrete cylinder, f'_{cc} the ultimate compressive strength of the confined concrete cylinder, P_u the ultimate confinement pressure ($P_u = E_l \cdot \varepsilon_f = 2t \cdot f'_{com}/D$), E_l the lateral modulus, ε_f the ultimate tensile strain of the FRP laminate, f'_{com} the ultimate tensile strength of the FRP layer, t the thickness of the FRP layer, and D the diameter of concrete cylinder.

3. Genetic programming

GP is a symbolic optimization technique that creates computer programs to solve problems using the principle of natural selection [Koza 1992]. GP may generally be defined as a supervised machine learning technique that searches a program space instead of a data space [Banzhaf et al. 1998]. The symbolic optimization algorithms present the potential solutions by structural ordering of several symbols. In GP, a random population of individuals (trees) is created to achieve high diversity. A population member in GP is a hierarchically structured tree comprising functions and terminals. The functions and terminals are selected from appropriate sets. For example, the function set F can contain the basic arithmetic operations (+, −, ×, /, et cetera), Boolean logic functions (AND, OR, NOT, et cetera), or any other mathematical functions. The terminal set T contains the arguments for the functions and can consist of numerical constants, logical constants, variables, et cetera. The functions and terminals are chosen at random and combined to form a computer model in a tree-like structure with a root point with branches extending from each function and ending in a terminal. For example, the tree shown on the right represents the GP model $(X_1 + 3/X_2)^2$.



The creation of the initial population is a blind random search for solutions in the large space of possible solutions. Once a population of models has been randomly

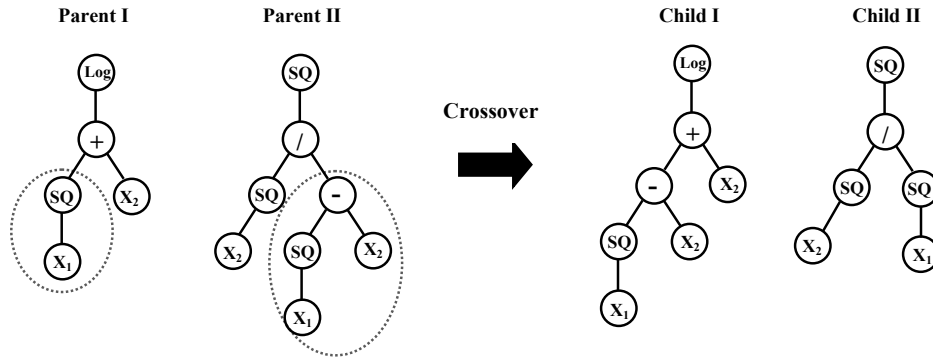


Figure 3. Typical crossover operation in GP.

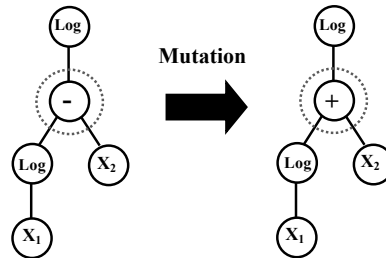


Figure 4. Typical mutation operation in GP.

created, the GP algorithm evaluates the individuals, selects individuals for reproduction, generates new individuals by mutation, crossover, and direct reproduction, and finally creates the new generation in all iterations [Koza 1992].

During the crossover procedure, a point on a branch of each solution (program) is randomly selected and the set of terminals and/or functions from each program is then swapped to create two new programs, as can be seen in Figure 3. The evolutionary process continues by evaluating the fitness of the new population and starting a new round of reproduction and crossover. During this process, the GP algorithm occasionally selects a function or terminal at random from a model and mutates it (see Figure 4).

3.1. GP for linear-in-parameters models. In general, GP creates not only nonlinear models but also linear-in-parameters models. In order to avoid parameter models, the parameters must be removed from the set of terminals. That is, it contains only variables: $T = \{x_0(k), \dots, x_i(k)\}$, where $x_i(k)$ denotes the i -th regressor variable. Hence, a population member represents only F_i nonlinear functions [Pearson 2003]. The parameters are assigned to the model after extracting the F_i function terms from the tree, and determined using a least square (LS) algorithm [Reeves 1997]. A simple technique for the decomposition of the tree into function terms can be used. The subtrees, representing the F_i function terms, are determined by decomposing the tree starting from the root and going as far as nonlinear nodes (nodes distinct from “+” or “-”). As can be seen in Figure 5, the root node is a + operator; therefore, it is possible to decompose the tree into two subtrees A and B . The root node of the A tree is again a linear operator; therefore, it can be decomposed into C and D trees. As the root node of the B tree is a nonlinear node (/), it cannot be decomposed. The root nodes of the C and D trees are

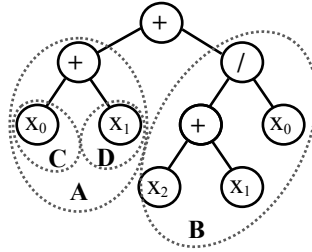


Figure 5. Decomposition of a tree to function terms [Madár et al. 2005a].

also nonlinear. Consequently, the final decomposition procedure results in three subtrees: *B*, *C*, and *D*. According to the results of the decomposition, it is possible to assign parameters to the functional terms represented by the obtained subtrees. The resulting linear-in-parameters model for this example is $y : p_0 + p_1(x_2 + x_1)/x_0 + p_2x_0 + p_3x_1$.

GP can be used for selecting from special model classes, such as polynomial models. To achieve this, the set of operators must be restricted and some simple syntactic rules must be introduced. For instance, if the set of operators is defined as $F = \{\times, +\}$ and there is a syntactic rule that exchanges the internal nodes that are below \times -type internal nodes to \times -type nodes, GP will generate only polynomial models [Koza 1992; Madár et al. 2005a].

3.2. OLS algorithm. The great advantage of using linear-in-parameter models is that the LS method can be used for identifying the model parameters. This is much less computationally demanding than other nonlinear optimization algorithms, because the optimal $p = [p_1, \dots, p_m]^T$ parameter vector can analytically be calculated:

$$p = (U^{-1}U)^T U_y, \quad (1)$$

where $y = (y(1), \dots, y(N))^T$ is the measured output vector and the U regression matrix is

$$U = \begin{pmatrix} U_1(x(1)) & \cdots & U_M(x(1)) \\ \vdots & \ddots & \vdots \\ U_1(x(N)) & \cdots & U_M(x(N)) \end{pmatrix}. \quad (2)$$

The OLS algorithm [Billings et al. 1988; Chen et al. 1989] is an effective algorithm for determining which terms are significant in a linear-in-parameters model. The OLS technique introduces the error reduction ratio (err), which is a measure of the decrease in the variance of the output by a given term. The matrix form corresponding to the linear-in-parameters model is

$$y = U_p + e, \quad (3)$$

where U is the regression matrix, p is the parameter vector, and e is the error vector. The OLS method transforms the columns of the U matrix into a set of orthogonal basis vectors to inspect the individual contributions of each term [Cao et al. 1999]. It is assumed in the OLS algorithm that the regression matrix U can be orthogonally decomposed as $U = WA$, where A is a M by M upper triangular matrix (that is, $A_{ij} = 0$ if $i > j$) and W is a N by M matrix with orthogonal columns in the sense that $WTW = D$ is a diagonal matrix (N is the length of the y vector and M is the number of repressors). After this

decomposition, the OLS auxiliary parameter vector g can be calculated as

$$g = D^{-1}W^T y, \tag{4}$$

where g_i represents the corresponding element of the OLS solution vector. The output variance $(y^T y)/N$ can be described as

$$y^T y = \sum_{i=1}^M g_i^2 w_i^T w_i + e^T e. \tag{5}$$

Therefore, the error reduction ratio $[\text{err}]_i$ of the U_i term can be expressed as

$$[\text{err}]_i = \frac{g_i^2 w_i^T w_i}{y^T y}. \tag{6}$$

This ratio offers a simple mean for order and selects the model terms of a linear-in-parameters model on the basis of their contribution to the performance of the model.

3.3. Hybrid GP/OLS algorithm. Application of OLS to the GP algorithm leads to significant improvements in the performance of GP. The main feature of this hybrid approach is to transform the trees into simpler trees which are more transparent, but with accuracy close to that of the original trees. In this coupled algorithm, GP generates a lot of potential solutions in the form of a tree structure during the GP operation. These trees may have better and worse terms (subtrees) that contribute more or less to the accuracy of the model represented by the tree. OLS is used to estimate the contribution of the branches of the tree to the accuracy of the model; using the OLS, one can select the less significant terms in a linear regression problem. According to this strategy, terms (subtrees) having the smallest error reduction ratio are eliminated from the tree [Pearson 2003]. This “tree pruning” approach is realized in every fitness evaluation before the calculation of the fitness values of the trees. Since GP works with the tree structure, the further goal is to preserve the original structure of the trees as far as possible. The GP/OLS method always guarantees that the elimination of one or more function terms of the model can be done by pruning the corresponding subtrees, so there is no need for structural rearrangement of the tree after this operation. The way the GP/OLS method works on its basis is simply demonstrated in Figure 6. Assume that the function which must be identified is $y(x) = 0.8u(x - 1)^2 + 1.2y(x - 1) - 0.9y(x - 2) - 0.2$. As can be seen in Figure 6, the GP algorithm finds a solution with four terms: $u(x - 1)^2$, $y(x - 1)$, $y(x - 2)$, and $u(x - 1) \times u(x - 2)$. Based on the OLS algorithm, the subtree with the least error reduction ratio ($F_4 = u(x - 1) \times u(x - 2)$) is eliminated from the tree. Subsequently, the error reduction ratios and mean

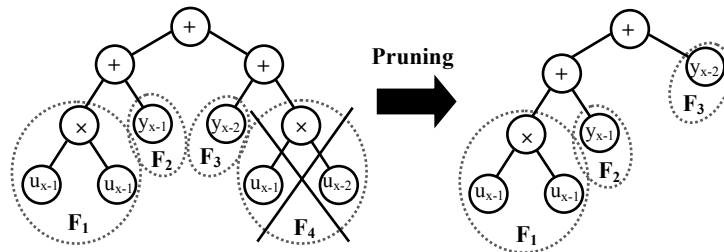


Figure 6. Pruning of a tree with OLS.

square error values (and model parameters) are calculated again. The new model (after pruning) may have a higher mean square error but it obviously has a more adequate structure.

4. Experimental database

A comprehensive experimental database was obtained for the compressive strength of CFRP-wrapped concrete cylinders from the literature [Cevik and Guzelbey 2008]. The database contains 101 samples from seven separate studies. The ranges of different input and output parameters used for the model development are given in Table 2. To visualize the sample distribution, the data are presented in Figure 7.

Parameter	min.	max.	range	SD	skewness	kurtosis	mean
Unconfined ultimate concrete strength	19.40	82.13	62.73	17.35	0.781	-0.175	45.11
Ultimate confinement pressure	3.44	38.38	34.94	8.69	1.483	1.803	13.51
Confined ultimate concrete strength	33.8	137.9	104.1	23.03	0.389	-0.566	78.32

Table 2. Ranges of parameters in database (SD is the standard deviation); values in MPa.

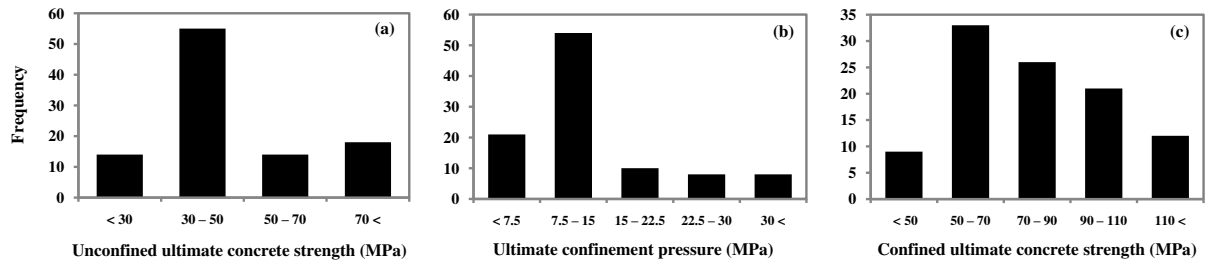


Figure 7. Histograms of the variables used in the model development.

5. Building a GP/OLS predictive model for compressive strength

Thus, the main goal of this study is to derive an explicit formulation for the compressive strength of CFRP-confined concrete cylinders (f'_{cc}) as follows:

$$f'_{cc} = f(f'_{co}, P_u) \quad (7)$$

in which f'_{co} is the unconfined ultimate concrete strength and P_u is the ultimate confinement pressure.

In the FRP confinement models developed by other researchers, f'_{co} and P_u are the most widely used parameters. As indicated in Table 1, P_u is a function of the diameter of the concrete cylinder (D), the thickness of the CFRP layer (t), and the ultimate tensile strength of the CFRP layer (f'_{com}) [Spoelstra and Monti 1999]. Therefore, the effects of D , t , and (f'_{com}) were implicitly incorporated into the model development.

For the analysis, the data sets were randomly divided into training and testing subsets (75 data sets were used as training and the rest as testing). In order to obtain a consistent data division, several combinations of the training and testing sets were considered. The selection was such that the maximum, minimum, mean, and standard deviation of the parameters were consistent in the training and testing data sets. The

GP/OLS approach was implemented using MATLAB. The best GP/OLS model was chosen on the basis of a multiobjective strategy as follows:

- The total number of inputs involved in each model.
- The best model fitness value on the training set of data.

During the evolutionary process, different participating parameters were gradually picked up in order to form the equations representing the input-output relationship. After checking several normalization methods [Swingler 1996; Rafiq et al. 2001], the following method was used for normalizing the data. The inputs and output of the GP/OLS model were normalized between 0 and 0.91 using the rule

$$X_n = \frac{X_i}{1.1 X_{i,\max}}, \quad (8)$$

where $X_{i,\max}$ are the maximum values of X_i and X_n is the normalized value. Various parameters are involved in the GP/OLS algorithm. The parameter selection will affect the generalization capability of GP/OLS. The GP/OLS parameters were selected based on some previously suggested values [Madár et al. 2005c] and after a trial and error approach. The parameter values are shown in Table 3. The correlation coefficient (R), the mean absolute percent error (MAPE), and the root mean squared error (RMSE) were used as the target error parameters to evaluate the performance of the models.

The GP/OLS-based formulation of the compressive strength f'_{cc} in terms of f'_{co} and P_u is

$$f'_{cc} = \left(\frac{P_u}{25} + \frac{2}{3} \right) f'_{co} + 25. \quad (9)$$

Figure 8 shows the expression tree of the best GP model formulation. A comparison of the GP/OLS predicted and experimental compressive strengths of the CFRP-wrapped concrete cylinder is shown in Figure 9.

Parameter	Values
Function set	+, −, ×, /
Population size	1000
Maximum tree depth	3-8
Maximum number of evaluated individuals	2500
Generation	100
Type of selection	roulette-wheel
Type of mutation	point-mutation
Type of crossover	one-point (2 parents)
Type of replacement	elitist
Probability of crossover	0.5
Probability of mutation	0.5
Probability of interchanging terminal and nonterminal nodes during mutation	0.25

Table 3. Parameter values for GP/OLS.

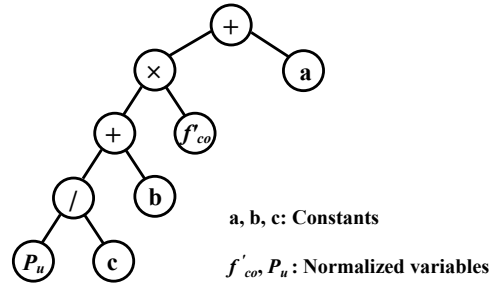


Figure 8. Expression tree of the best GP/OLS model.

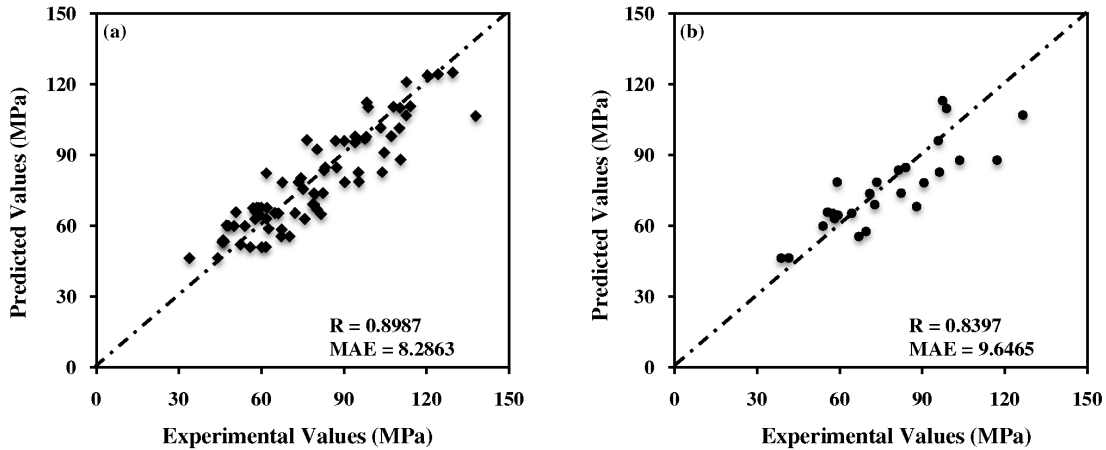


Figure 9. Predicted versus experimental compressive strengths using the GP/OLS model: (a) training data and (b) testing data.

6. Building models for benchmarking the GP/OLS model

6.1. Traditional GP predictive model for compressive strength. A tree-based GP analysis was performed to compare the GP/OLS technique with a traditional GP approach. The general parameter settings for the tree-based GP model are similar to those of GP/OLS. The tree-based GP software GPLAB [Silva 2007] was used, in conjunction with subroutines coded in MATLAB.

Similarly to the use in the GP/OLS model, out of the 101 data sets, 75 were used as the training data and 26 were used for the testing of the GP model. The formulation of f'_{cc} in terms of f'_{co} and P_u , for the best results from the GP, is

$$f'_{cc} = f'_{co} - \frac{P_u((f'_{co} - 8) - (f'_{co} - 5))}{8} + P_u - \left(\frac{f'_{co}}{P_u} - 2\right) + 4 - \left(\frac{P_u}{f'_{co}}\right) + \frac{f'_{co}}{4}. \quad (10)$$

The GP-based equation was obtained by converting the related expression tree into a mathematical form. A comparison of the GP predicted and experimental compressive strengths of the CFRP-wrapped concrete cylinder is shown in Figure 10.

6.2. LSR predictive model for compressive strength. A multivariable LSR analysis was performed to assess the predictive power of the GP/OLS technique, in comparison with a classical statistical approach. The LSR method is extensively used in regression analysis primarily because of its interesting nature. Under certain assumptions, LSR has some attractive statistical properties that have made it one of the most powerful and popular methods of regression analysis. The major task is to determine the multivariable LSR-based equation connecting the input variables to the output variable:

$$f'_{cc} = \alpha_1 f'_{co} + \alpha_2 P_u + \alpha_3, \tag{11}$$

where f'_{cc} is the compressive strength of the CFRP-confined concrete cylinders, f'_{co} is the unconfined ultimate concrete strength, P_u is the ultimate confinement pressure, and α denotes the coefficient vector. The software package EViews [Maravall and Gomez 2004] was used to perform the regression analysis.

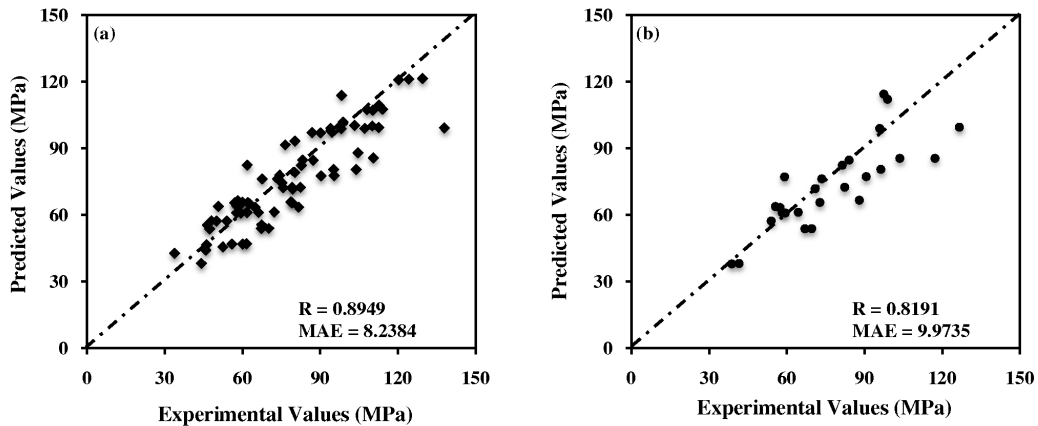


Figure 10. Predicted versus experimental compressive strengths using the GP model: (a) training data and (b) testing data.

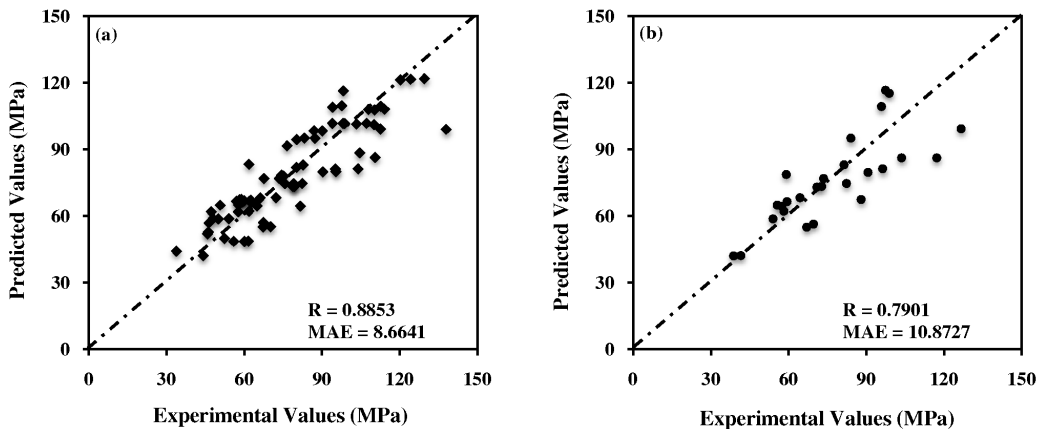


Figure 11. Predicted versus experimental compressive strengths using the LSR model: (a) training data and (b) testing data.

The formulation of f'_{cc} in terms of f'_{co} and P_u , for the best result from the LSR, is

$$f'_{cc} = 1.118f'_{co} + 1.479P_u + 7.903. \quad (12)$$

A comparison of the LSR predicted and experimental compressive strengths of the CFRP-wrapped concrete cylinder is shown in Figure 11. The resulting Fisher value (F) of the performed regression analysis is equal to 130.4.

7. Comparison of the CFRP confinement models

A GP/OLS-based formula was obtained for the compressive strength of CFRP-wrapped concrete cylinders. A comparison of the ratios between the predicted compressive strength values from the GP/OLS, GP, and LSR models, as well as those found in the literature, and the experimental values is shown in Figure 12. Some other models in the literature, such as the second formula of [Karbhari and Gao 1997], require additional details that are not available in the experimental database. Thus, they were not included in the comparative study.

The performance statistics of the formulas obtained by the different methods on the whole of the data are summarized in Table 4. As can be seen in Figures 9–12 and Table 4, the GP/OLS-based formula has provided the best performance on the training, testing, and whole data sets compared with the GP, LSR, and existing FRP confinement models.

Model ID	correlation of exper. and predicted f'_{cc}			exper./predicted f'_{cc}	
	R	MAPE	RMSE	mean	SD
1	0.752	24.04	31.46	1.33	0.28
2	0.871	18.19	22.15	1.08	0.22
3	0.704	16.91	25.56	1.2	0.29
4	0.23	29.43	38.25	1	0.46
5	0.847	10.12	12.46	1.06	0.17
6	0.833	11.09	14.18	0.94	0.16
7	0.769	21.62	8.6	1.29	0.27
8	0.851	10.11	12.45	1.03	0.16
9	0.812	11.81	13.86	1.01	0.19
10	0.702	16.28	24.94	1.19	0.28
11	0.659	23.16	34.2	1.31	0.35
12	0.854	9.8	12.14	1	0.16
13	0.791	26.5	30.02	0.67	0.12
14	0.763	12.86	17.39	1.25	0.2
LSR	0.863	9.23	11.59	1.01	0.15
GP	0.877	9.23	11.59	0.98	0.14
GP/OLS	0.885	8.64	10.69	1.01	0.16

Table 4. Performance statistics of the compressive strength predictive models. For the meaning of the columns, see page 743.

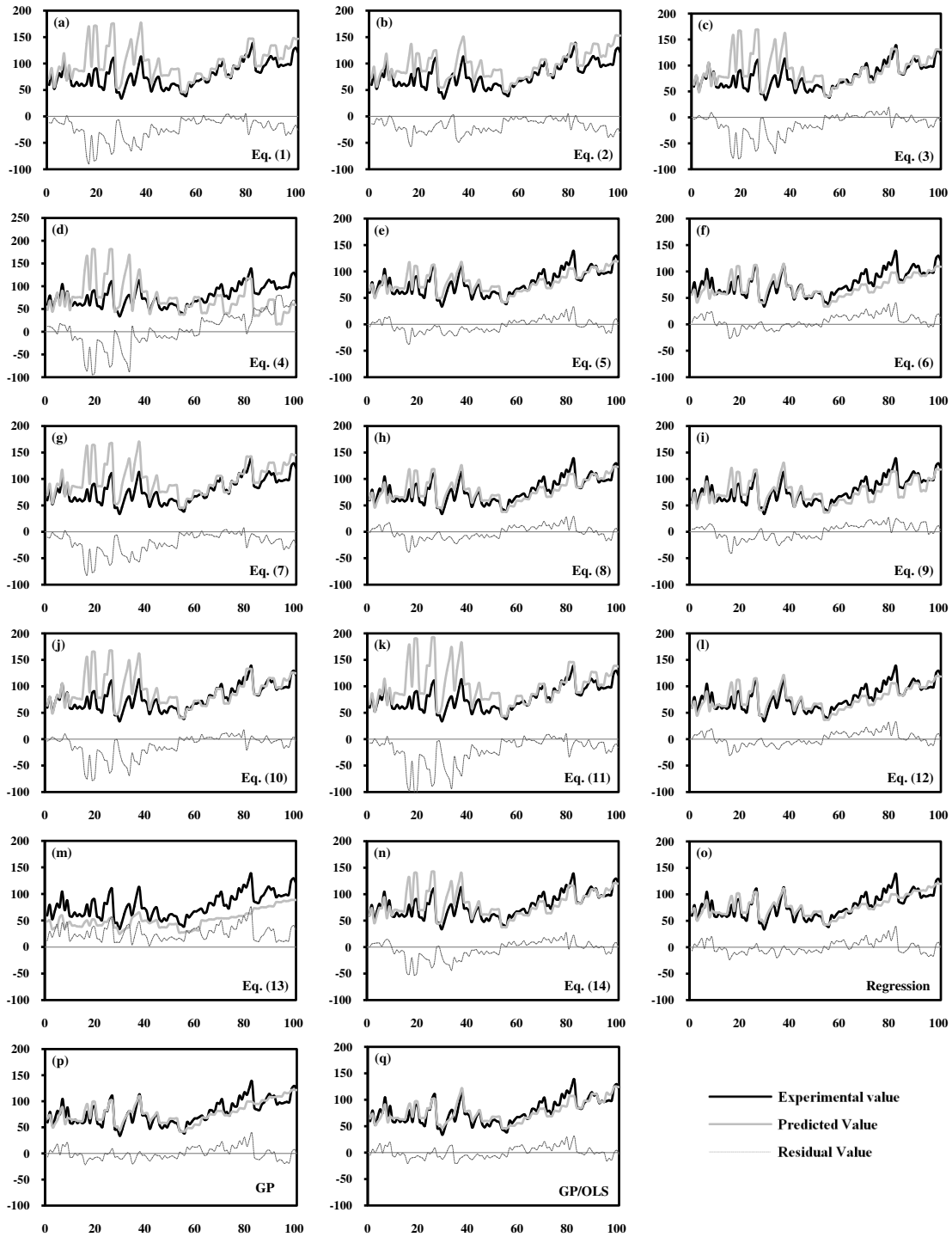


Figure 12. Comparison of the ratios between the predicted f'_{cc} values (in MPa, on the vertical axes) and experimental values (test number, on the horizontal axes) using different methods.

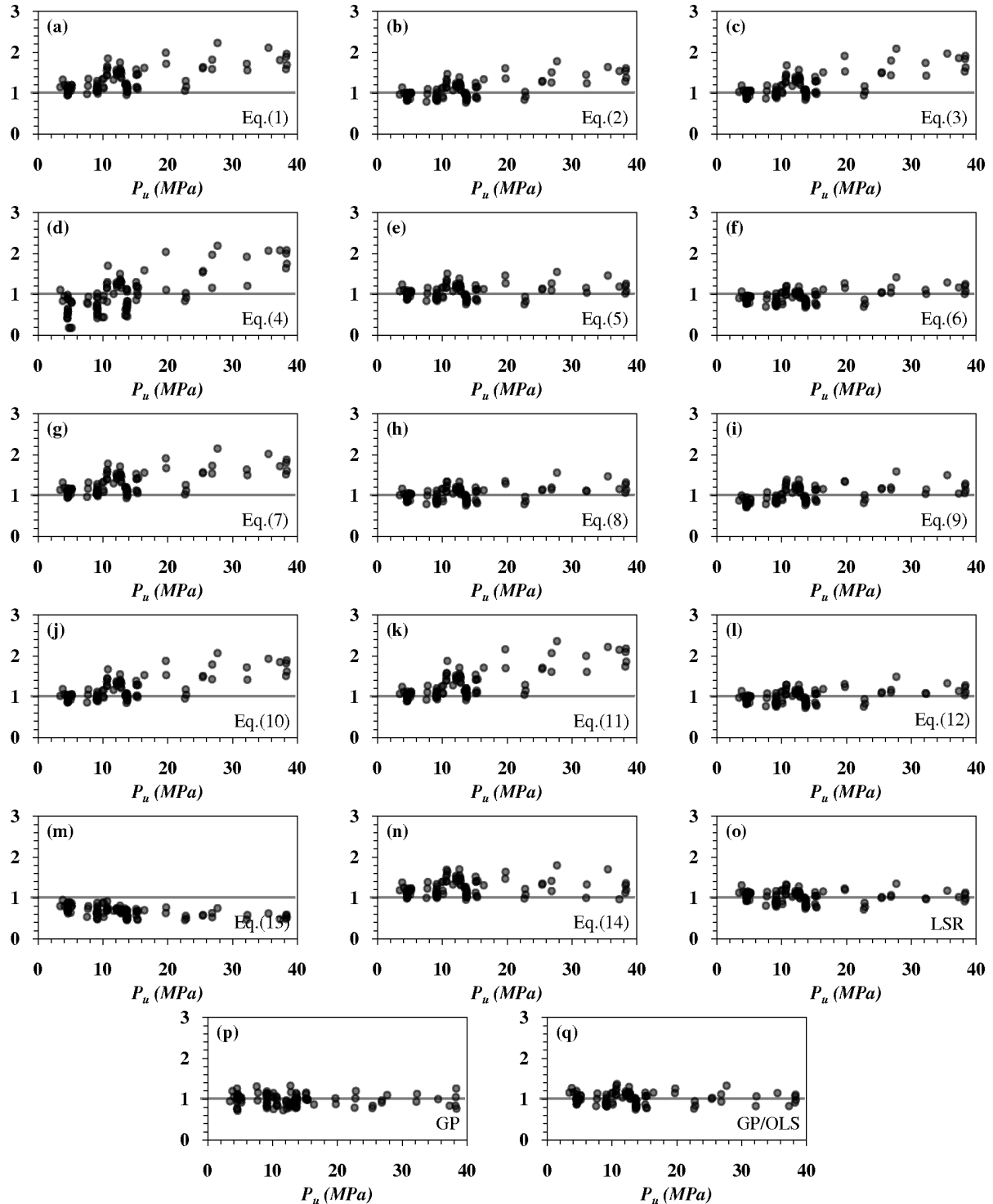


Figure 13. The ratios between the predicted and experimental compressive strength values with respect to P_u . Vertical axes in units of f'_{cc} predicted/ f'_{cc} experimental.

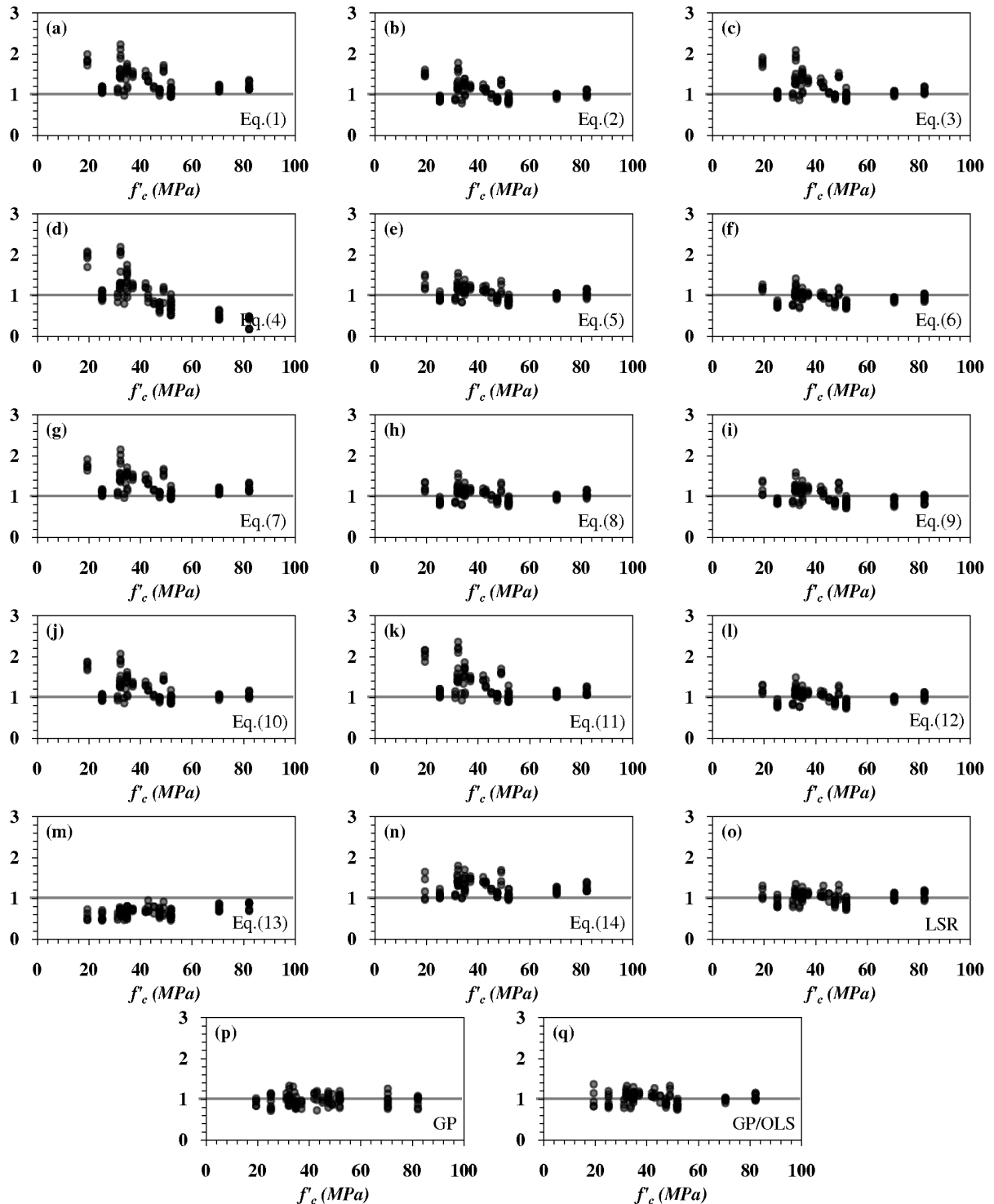


Figure 14. The ratios between the predicted and experimental compressive strength values with respect to f'_{cc} . Vertical axes in units of f'_{cc} predicted/ f'_{cc} experimental.

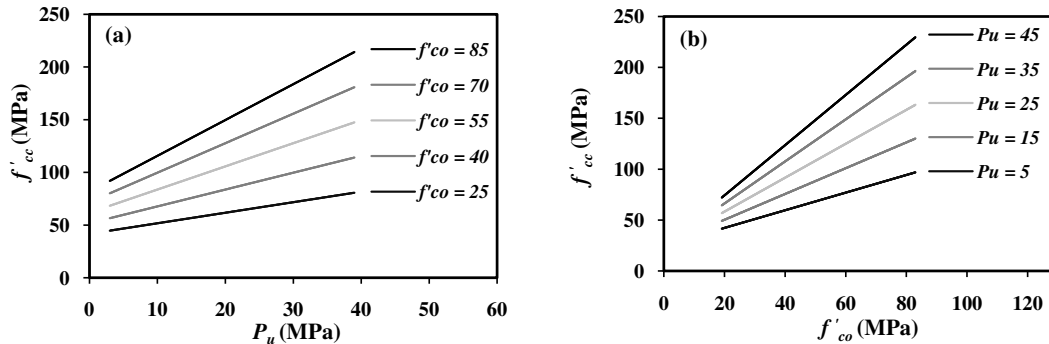


Figure 15. Parametric analysis of f'_{cc} in the GP/OLS model.

Because of the tree pruning process, the GP/OLS-based equation is very short and simple, especially in comparison with the traditional GP model. The GP/OLS predictive equation can reliably be used for routine design practice via hand calculations. However, the proposed GP/OLS-based formula is valid for the ranges of the database used for the training of the model. It can also be seen that the developed GP and LSR models perform better than most of the available FRP confinement models.

Although the proposed regression-based model yields good results for the current database, empirical modeling based on statistical regression techniques has significant limitations. Most commonly used regression analyses can have large uncertainties, which has major drawbacks for the idealization of complex processes, approximation, and averaging widely varying prototype conditions. In regression analyses, modeling of the nature of the corresponding problem is attempted by a predefined linear or nonlinear equation, which is not always true.

Equation (9), obtained by means of GP/OLS, can be expressed similarly to the form of the other formulas presented in Table 1:

$$\frac{f'_{cc}}{f'_{co}} = \frac{P_u}{25} + \frac{25}{f'_{co}} + \frac{2}{3}. \quad (13)$$

Figures 13 and 14 show the ratios of the compressive strength values predicted by different methods to the experimental values, with respect to P_u and f'_{co} . It can be observed from these figures that predictions by the models found in the literature, in most cases, are scattered with respect to both P_u and f'_{co} . The scattering decreases with increasing f'_{co} and increases as P_u increases. Figures 13 and 14 indicate that the predictions obtained by the proposed methods have good accuracy with no significant trends with P_u or f'_{co} . The predictions made by the GP/OLS model, with a mean value of 1.01, are slightly better compared with those obtained by the GP and LSR models.

8. Parametric analysis

For further verification of the GP/OLS model, a parametric analysis was performed. The main goal was to find the effect of each parameter on the values of compressive strength of the CFRP-wrapped concrete cylinders. The methodology was based on the change of only one input variable at a time while other input variables were kept constant at the average values of their entire data sets. Figure 15 presents the predicted strengths of concrete cylinders after CFRP confinement as a function of each parameter. The change in the predictions with variations in P_u and unconfined f'_{co} can be determined from these figures.

The results of the parametric study indicate that f'_{cc} increases continuously with increasing P_u and f'_{co} . The results obtained are in close agreement with those reported in [Karbhari and Gao 1997; Spoelstra and Monti 1999], for example.

9. Conclusions

A combined genetic programming and orthogonal least squares algorithm (GP/OLS) was employed to predict the complex behavior of carbon fiber-reinforced plastic (CFRP)-confined concrete columns. A simplified predictive equation was derived for the compressive strength by means of GP/OLS. A reliable database including previously published test results of the ultimate strength of concrete cylinders after CFRP confinement was used for developing the models. The GP/OLS model was benchmarked against the traditional GP, regression-based, and several CFRP confinement models found in the literature. The major findings obtained are as follows:

- The GP/OLS model is capable of predicting the ultimate strength of concrete cylinders with reasonable accuracy. The formula evolved by GP/OLS outperforms the GP, regression, and other models found in the literature.
- The GP/OLS-based predictive equation is very simple compared with the formula generated via traditional GP. This is mainly because of the important role of the tree pruning process in the GP/OLS algorithm.
- The proposed GP/OLS formula can be used for practical preplanning and design purposes in that it was developed upon on a comprehensive database with a wide range of properties.
- The results of the parametric analysis are in close agreement with the physical behavior of the CFRP-confined concrete cylinders. The results confirm that the proposed design equation is robust and can confidently be used.
- Using the GP/OLS approach, the compressive strength can accurately be estimated without carrying out destructive, sophisticated, and time-consuming laboratory tests.
- A major advantage of GP/OLS for determining the compressive strength lies in its powerful ability to model the mechanical behavior without any prior assumptions or simplifications.
- As more data becomes available, including that for other types of FRP, these models can be improved to make more accurate predictions for a wider range.

References

- [Alavi and Gandomi \geq 2010] A. H. Alavi and A. H. Gandomi, "A robust data mining approach for formulation of geotechnical engineering systems", *Eng. Comput.* In press.
- [Alavi et al. 2010] A. H. Alavi, A. H. Gandomi, M. G. Sahab, and M. Gandomi, "Multi expression programming: a new approach to formulation of soil classification", *Eng. Comput.* **26**:2 (2010), 111–118.
- [Banzhaf et al. 1998] W. Banzhaf, P. Nordin, R. Keller, and F. Francone, *Genetic programming: an introduction on the automatic evolution of computer programs and its application*, dpunkt/Morgan Kaufmann, Heidelberg/San Francisco, 1998.
- [Berthet et al. 2006] J. F. Berthet, E. Ferrier, and P. Hamelin, "Compressive behavior of concrete externally confined by composite jackets, B: Modeling", *Constr. Build. Mater.* **20**:5 (2006), 338–347.
- [Billings et al. 1988] S. A. Billings, M. J. Korenberg, and S. Chen, "Identification of non-linear output-affine systems using an orthogonal least-squares algorithm", *Int. J. Syst. Sci.* **19**:8 (1988), 1559–1568.

- [Cao et al. 1999] H. Cao, J. Yu, L. Kang, Y. Chen, and Y. Chen, "The kinetic evolutionary modeling of complex systems of chemical reactions", *Comput. Chem. Eng.* **23**:2 (1999), 143–152.
- [Cevik and Guzelbey 2008] A. Cevik and I. H. Guzelbey, "Neural network modeling of strength enhancement for CFRP confined concrete cylinders", *Build. Environ.* **43**:5 (2008), 751–763.
- [Chen et al. 1989] S. Chen, S. A. Billings, and W. Luo, "Orthogonal least squares methods and their application to non-linear system identification", *Int. J. Control* **50**:5 (1989), 1873–1896.
- [Fardis and Khalili 1981] M. N. Fardis and H. Khalili, "Concrete encased in fiberglass-reinforced plastic", *ACI J. Proc.* **78**:6 (1981), 440–446.
- [Fardis and Khalili 1982] M. N. Fardis and H. Khalili, "FRP-encased concrete as a structural material", *Mag. Concr. Res.* **34**:121 (1982), 191–202.
- [Gandomi and Alavi 2010] A. H. Gandomi and A. H. Alavi, *Hybridizing genetic programming with orthogonal least squares for modeling of soil liquefaction*, IGI Global Publishing, Hershey, PA, 2010. In press.
- [Gandomi et al. 2009] A. H. Gandomi, A. H. Alavi, S. Kazemi, and M. M. Alinia, "Behavior appraisal of steel semi-rigid joints using linear genetic programming", *J. Constr. Steel Res.* **65**:8–9 (2009), 1738–1750.
- [Gandomi et al. 2010] A. H. Gandomi, A. H. Alavi, and M. G. Sahab, "New formulation for compressive strength of CFRP confined concrete cylinders using linear genetic programming", *Mater. Struct.* **43**:7 (2010), 963–983.
- [Karbhari and Gao 1997] V. M. Karbhari and Y. Q. Gao, "Composite jacketed concrete under uniaxial compression: verification of simple design equations", *J. Mater. Civ. Eng. (ASCE)* **9**:4 (1997), 185–193.
- [Kono et al. 1998] S. Kono, M. Inazumi, and T. Kaku, "Evaluation of confining effects of CFRP sheets on reinforced concrete members", pp. 343–355 in *Proceedings of the 2nd International Conference on Composites in Infrastructure (ICCI'98)* (Tucson, AZ, 1998), edited by H. Saadatmanesh and M. R. Ehsani, University of Arizona, Tucson, AZ, 1998.
- [Koza 1992] J. R. Koza, *Genetic programming: on the programming of computers by means of natural selection*, MIT Press, Cambridge, MA, 1992.
- [Lam and Teng 2001] L. Lam and J. G. Teng, "Strength models for circular concrete columns confined by FRP composites", pp. 835–844 in *FRPRCS-5: Fiber-reinforced Plastics for Reinforced Concrete Structures* (Cambridge, 2001), vol. 2, edited by C. J. Burgoyne, Thomas Telford, London, 2001.
- [Li et al. 2003] Y.-F. Li, C.-T. Lin, and Y.-Y. Sung, "A constitutive model for concrete confined with carbon fiber reinforced plastics", *Mech. Mater.* **35**:3–6 (2003), 603–619.
- [de Lorenzis 2001] L. A. de Lorenzis, *Comparative study of models on confinement of concrete cylinders with FRP composites*, Ph.D. thesis, Chalmers University of Technology, Division for Building Technology, Göteborg, 2001. Published with joint author Ralejs Tefers in *J. Compos. Constr. (ASCE)* **7**:3 (2003), 219–237.
- [Madár et al. 2005a] J. Madár, J. Abonyi, and F. Szeifert, "Genetic programming for system identification", pp. 43–48 in *Proceedings of ISDA 2004: IEEE 4th Conference on Intelligent Systems Design and Applications* (Budapest, 2004), Budapesti Műszaki Főiskola, Budapest, 2005.
- [Madár et al. 2005b] J. Madár, J. Abonyi, and F. Szeifert, "Genetic programming for the identification of nonlinear input-output models", *Ind. Eng. Chem. Res.* **44**:9 (2005), 3178–3186.
- [Madár et al. 2005c] J. Madár, J. Abonyi, and F. Szeifert, "Genetic programming for the identification of nonlinear input-output models", white paper, University of Veszprém, Department of Process Engineering, Veszprém, 2005, available at <http://www.fmt.vein.hu/softcomp/gp/ie049626e.pdf>.
- [Mander et al. 1988] J. B. Mander, M. J. N. Priestley, and R. Park, "Theoretical stress-strain model for confined concrete", *J. Struct. Eng. (ASCE)* **114**:8 (1988), 1804–1826.
- [Maravall and Gomez 2004] A. Maravall and V. Gomez, "EViews Software", 2004, available at <http://www.eviews.com>. Version 5.
- [Matthys et al. 1999] S. Matthys, L. Taerwe, and K. Audenaert, "Tests on axially loaded concrete columns confined by fiber reinforced polymer sheet wrapping", pp. 217–228 in *Proceedings of the 4th International Symposium on Fiber Reinforced Polymer Reinforcement for Reinforced Concrete Structures (FRPRCS-4)* (Baltimore, MD, 1999), edited by C. W. Dolan et al., Special Publication **188**, American Concrete Institute, Farmington Hills, MI, 1999.
- [Micelli et al. 2001] F. Micelli, J. J. Myers, and S. Murthy, "Effect of environmental cycles on concrete cylinders confined with FRP", pp. 317–322 in *Composites in construction: proceedings of the International Conference Composites in Construction—CCC2001* (Porto, 2001), edited by J. A. Figueiras et al., Balkema, Lisse, 2001.

- [Mirmiran et al. 2000] A. Mirmiran, K. Zagers, and W. Yuan, "Nonlinear finite element modeling of concrete confined by fiber composites", *Finite Elem. Anal. Des.* **35**:1 (2000), 79–96.
- [Miyachi et al. 1997] K. Miyachi, S. Nishibayashi, and S. Inoue, "Estimation of strengthening effects with carbon fiber sheet for concrete column", pp. 217–224 in *Non-metallic (FRP) reinforcement for concrete structures: proceedings of the 3rd International Symposium (FRPRCS-3)* (Sapporo, 1997), vol. 1, Japan Concrete Institute, Tokyo, 1997.
- [Pearson 2003] R. K. Pearson, "Selecting nonlinear model structures for computer control", *J. Process Control* **13**:1 (2003), 1–26.
- [Rafiq et al. 2001] M. Y. Rafiq, G. Bugmann, and D. J. Easterbrook, "Neural network design for engineering applications", *Comput. Struct.* **79**:17 (2001), 1541–1552.
- [Reeves 1997] C. R. Reeves, "Genetic algorithms for the operations researcher", *Inf. J. Comput.* **9**:3 (1997), 231–250.
- [Richart et al. 1928] F. E. Richart, A. Brandtzaeg, and R. L. Brown, "A study of the failure of concrete under combined compressive stresses", Bulletin 185, University of Illinois, Engineering Experimental Station, Urbana, IL, 1928.
- [Rochette and Labossière 2000] P. Rochette and P. Labossière, "Axial testing of rectangular column models confined with composites", *J. Compos. Constr. (ASCE)* **4**:3 (2000), 129–136.
- [Rousakis 2001] T. Rousakis, "Experimental investigation of concrete cylinders confined by carbon FRP sheets, under monotonic and cyclic axial compressive load", Research Report, Chalmers University of Technology, Göteborg, 2001.
- [Saafi et al. 1999] M. Saafi, H. A. Toutanji, and Z. Li, "Behavior of concrete columns confined with fiber reinforced polymer tubes", *ACI Mater. J.* **96**:4 (1999), 500–509.
- [Samaan et al. 1998] M. Samaan, A. Mirmiran, and M. Shahawy, "Model of concrete confined by fiber composites", *J. Struct. Eng. (ASCE)* **124**:9 (1998), 1025–1031.
- [Shahawy et al. 2000] M. Shahawy, A. Mirmiran, and T. Beitelmann, "Tests and modeling of carbon-wrapped concrete columns", *Compos. B Eng.* **31**:6–7 (2000), 471–480.
- [Silva 2007] S. Silva, "GPLAB: a genetic programming toolbox for MATLAB", 2007, available at <http://gplab.sourceforge.net>.
- [Spoelstra and Monti 1999] M. R. Spoelstra and G. Monti, "FRP-confined concrete model", *J. Compos. Constr. (ASCE)* **3**:3 (1999), 143–150.
- [Swingler 1996] K. Swingler, *Applying neural networks: a practical guide*, Academic Press, New York, 1996.
- [Toutanji 1999] H. Toutanji, "Stress-strain characteristics of concrete columns externally confined with advanced fiber composite sheets", *ACI Mater. J.* **96**:3 (1999), 397–404.
- [Vintzileou and Panagiotidou 2008] E. Vintzileou and E. Panagiotidou, "An empirical model for predicting the mechanical properties of FRP-confined concrete", *Constr. Build. Mater.* **22**:5 (2008), 841–854.
- [Xiao and Wu 2000] Y. Xiao and H. Wu, "Compressive behavior of concrete confined by carbon fiber composite jackets", *J. Mater. Civ. Eng. (ASCE)* **12**:2 (2000), 139–146.

Received 10 Mar 2009. Revised 17 Nov 2009. Accepted 31 Mar 2010.

AMIR HOSSEIN GANDOMI: a.h.gandomi@gmail.com
College of Civil Engineering, Tafresh University, Tafresh, Iran

AMIR HOSSEIN ALAVI: ah_alavi@hotmail.com
am_alavi@civileng.iust.ac.ir
School of Civil Engineering, Iran University of Science and Technology, Tehran, Iran

PARVIN ARJMANDI: parvin.arjmandi@gmail.com
College of Civil Engineering, Tafresh University, Tafresh, Iran

ALIREZA AGHAEIFAR: ar_aghaie@yahoo.com
Department of Civil Engineering, Islamic Azad University, Kashmar Branch, Kashmar, Iran

REZA SEYEDNOUR: reza.seyednour@gmail.com
Department of Research, University of Social Welfare and Rehabilitation Sciences, Tehran, Iran

APPLICATION OF THE KIRCHHOFF HYPOTHESIS TO BENDING THIN PLATES WITH DIFFERENT MODULI IN TENSION AND COMPRESSION

XIAO-TING HE, QIANG CHEN, JUN-YI SUN, ZHOU-LIAN ZHENG AND SHAN-LIN CHEN

When materials that exhibit different mechanical behaviors in tension and compression must be analyzed, Ambartsumyan's bimodular model for isotropic materials can be adopted. It deals with the principal stress state in a point, which is particularly important in the analysis and design of reinforced concrete structures. However, due to the inherent complexity of the constitutive relation, it is difficult to solve analytically for bending components with bimoduli except in particular simple problems. Here we propose a simplified mechanical model, based on the classical Kirchhoff hypothesis, used for the solution of the bimodular thin plates in bending. We first use the Kirchhoff hypothesis to judge the existence of the elastic neutral layers of bimodular thin plates in small-deflection bending. Based on the existent neutral layers, we extend the solution from the case of pure bending into the case of lateral force bending. We use the displacement variation method to illustrate the application of the proposed model, and compare it with FEM results strictly based on Ambartsumyan's materials model. The comparisons show that the proposed mechanical model is valid and helpful for analyzing bending structures with bimodularity.

1. Introduction

Many studies have indicated that most materials, including concrete, ceramics, graphite, and some composites, exhibit different tensile and compressive strains given the same stress applied in tension and compression. These materials are known as bimodular materials [Jones 1976; 1977]. Overall, there are two basic material models widely used in theoretical analysis within the engineering profession. One of these models is the criterion of positive-negative signs in the longitudinal strain of fibers proposed in [Bert 1977]. This model is mainly applicable to orthotropic materials, and is therefore widely used for research on laminated composites [Bert and Gordaninejad 1983; Reddy and Chao 1983; Srinivasan and Ramachandra 1989; Ganapathi et al. 2004; Patel et al. 2004; 2005a; 2005b; Baykara et al. 2005; Khan et al. 2009; Maceri and Vairo 2009]. Another model is the criterion of positive-negative signs of principal stress proposed by Ambartsumyan [1965; 1969; 1982]. This model is mainly applicable to isotropic materials [Kamiya 1974; 1975a; 1975b; El-Tahan et al. 1989]. In civil engineering, the principal stress state is a key point in the analysis and design of some bending components like beams, columns, plates, and shells. Shear stresses and the resulting diagonal tension must also be carefully considered in the design of reinforced concrete. This paper will focus on discussion of the latter model based on principal direction.

Keywords: bimodulus, tension and compression, Kirchhoff hypothesis, plates, neutral layer.

This work was supported by the Fundamental Research Funds for the Central Universities, P. R. China (No. CDJXS11 20 11 66). The authors thank the reviewers for their valuable comments.

The bimodular materials model proposed by Ambartsumyan asserts that Young's modulus of elasticity depends not only on material properties, but also on the stress state of that point. There are only a few applications of the constitutive equation to stress analyses of components because of the inherent complexity in analysis of bimodular materials, that is, the elastic constants involved in the governing equations, which depend on the stress state of that point, are not correctly indicated beforehand. In other words, except in particularly simple problems it is not easy to estimate a priori the stress state in a point in the deformed body. In some complex problems, it is necessary to resort to FEM based on an iterative strategy [Zhang and Wang 1989; Ye et al. 2004]. Because the stress state of the point in question is unknown in advance, we have to begin with a single modulus problem, thus gaining the initial stress state to form a corresponding elasticity matrix for each element. Generally, direct iterative methods based on an incrementally evolving stiffness have been adopted by many researchers; they include an improved algorithm in which the shear stress and shear strain are set to zero to formulate the elastic matrix [Zhang and Wang 1989; Liu and Zhang 2000; He et al. 2009], an improved algorithm keeping Poisson's ratio constant while modifying the elastic matrix [Ye 1997], the initial stress technique [Yang et al. 1999], and the smoothing function technique [Yang and Zhu 2006; Yang and Wang 2008].

Analytical solutions are available in a few cases, all involving beams and columns. By taking the isolated body and then considering its static equilibrium, Yao and Ye derived the analytical solution of a bending-compression column with different moduli in tension and compression [2004a], and then the analytical solution of the bimodular retaining wall [2004b]. In the context of a bimodular beam in lateral force bending, they proposed the assumption that shear stress makes no contribution to the position of the neutral axis [Yao and Ye 2004c], deriving from it the analytical solution of a lateral force bending beams with different moduli in tension and compression.

In [He et al. 2007a], to simplify the derivation, we proposed that the bimodular beams may be turned into classical beams by the equivalent section method. Under the condition that the stress varies continuously along the direction perpendicular to neutral axis, we obtained the approximate analytical solution of a bimodular deep beam under uniformly-distributed loads [2007b], and the approximate elasticity solution of a bimodular bending-compression column [2008].

All these solutions involve beams and columns; up to now, analytical solutions based on bimodular plates have not been found. The key problem lies in how to construct a simplified mechanical model to solve this problem analytically.

In this paper, we use the Kirchhoff hypothesis to judge the existence of the elastic neutral layers of bimodular thin plates in small-deflection bending. Based on the existent neutral layers, we extend the solution from the case of pure bending, which strictly satisfies the constitutive model proposed by Ambartsumyan, to the case of lateral force bending. We use the displacement variation method to illustrate the application of the proposed model, and compare with FEM results.

2. Mechanical model

2.1. Bimodular material model. Ambartsumyan [1982] linearized the bimodular materials model by two straight lines whose tangents at the origin are discontinuous, as shown in Figure 1. The basic assumptions of this model are as follows:

- The body under study is continuous, homogeneous, and isotropic.

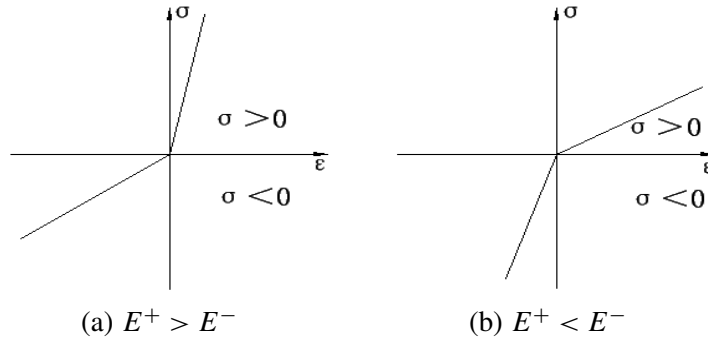


Figure 1. Constitutive model of bimodulus materials proposed by Ambartsumyan.

- Small deformation is assumed.
- The Young’s modulus and Poisson’s ratio of the materials are E^+ and μ^+ when the materials are in tension along a certain direction and E^- and μ^- when they are in compression.
- When the three principal stresses are uniformly positive or uniformly negative, the three basic equations are essentially the same as those of classical theory; when the signs of the three principal stresses are different, the differential equations of equilibrium and the geometrical equations are the same as those of classical materials theory, with the exception of the physical equations.
- $\mu^+/E^+ = \mu^-/E^-$, to ensure that the flexibility matrix is symmetric.

In a spatial problem, let the stress and strain components in the principal coordinates $\alpha, \beta,$ and γ be, respectively, $\{\sigma_I\} = (\sigma_\alpha \ \sigma_\beta \ \sigma_\gamma)^T$ and $\{\varepsilon_I\} = (\varepsilon_\alpha \ \varepsilon_\beta \ \varepsilon_\gamma)^T$. The constitutive model proposed by Ambartsumyan is

$$\begin{Bmatrix} \varepsilon_\alpha \\ \varepsilon_\beta \\ \varepsilon_\gamma \end{Bmatrix} = \begin{bmatrix} a_{11} & a_{12} & a_{13} \\ a_{21} & a_{22} & a_{23} \\ a_{31} & a_{32} & a_{33} \end{bmatrix} \begin{Bmatrix} \sigma_\alpha \\ \sigma_\beta \\ \sigma_\gamma \end{Bmatrix},$$

where a_{ij} ($i, j = 1, 2, 3$) denote the flexibility coefficients determined by the polarity of the signs of the principal stresses. For instance, if $\sigma_\alpha > 0, \sigma_\beta < 0,$ and $\sigma_\gamma > 0$, the flexibility coefficients in the physical relation should be $a_{11} = a_{33} = 1/E^+, a_{22} = 1/E^-, a_{21} = a_{31} = a_{13} = a_{23} = -\mu^+/E^+,$ and $a_{12} = a_{32} = -\mu^-/E^-$. The rest of the physical equations may be deduced analogously.

Because the stress state of the point in question is unknown in advance, we have to begin with a single modulus problem, thus gaining the initial stress state to form a corresponding elasticity matrix for each element. This method is only available for the numerical iterative technology based on FEM. For the analytical solution of such a problem, however, we will find that, since the physical equations originally built on the principal stress direction α, β, γ are rebuilt on general coordinates x, y, z via coordinate conversion, many nonlinear items concerning the principal stress and its direction cosine are generated in the physical equations. Therefore, solving becomes very difficult and it is necessary to simplify the mechanical model to obtain the approximate analytical solution.

2.2. Existence of neutral layers. In the small-deflection bending of thin plates, let the stress components be $\sigma_x, \sigma_y, \sigma_z, \tau_{xy}, \tau_{yz},$ and τ_{zx} and the strain components be $\varepsilon_x, \varepsilon_y, \varepsilon_z, \gamma_{xy}, \gamma_{yz},$ and γ_{zx} . The components

of displacement at a point, in the x and y directions, are denoted by u and v , respectively. Due to lateral loading, deformation takes place; the midsurface at any point has deflection w . From the Kirchhoff hypothesis we deduce that

$$\varepsilon_x = \frac{1}{E}(\sigma_x - \mu\sigma_y), \quad \varepsilon_y = \frac{1}{E}(\sigma_y - \mu\sigma_x), \quad \gamma_{xy} = \frac{2(1+\mu)}{E}\tau_{xy}, \quad (1)$$

$$(u)_{z=0} = 0, \quad (v)_{z=0} = 0, \quad (2)$$

$$(\varepsilon_x)_{z=0} = 0, \quad (\varepsilon_y)_{z=0} = 0, \quad (\gamma_{xy})_{z=0} = 0. \quad (3)$$

The last line says that the midsurface remains unstrained under bending: there is no normal strain in tension and compression and no shear strain. Therefore, we may think of the midsurface as the neutral layer of thin plates in bending. From (1) and (3), we have

$$(\sigma_x)_{z=0} = \mu(\sigma_y)_{z=0}, \quad (\sigma_y)_{z=0} = \mu(\sigma_x)_{z=0}, \quad (\tau_{xy})_{z=0} = 0. \quad (4)$$

Substituting the second expression in (4) into the first one, we have

$$(\sigma_x)_{z=0} = \mu^2(\sigma_x)_{z=0}. \quad (5)$$

Under the condition $(\sigma_x)_{z=0} \neq 0$, $\mu^2 = 1$ may be obtained. However, it is obvious that $\mu^2 = 1$ fails to satisfy the physical meaning which isotropic materials should have. Only under the condition $(\sigma_x)_{z=0} = 0$, (5) holds. Similarly, we also obtain $(\sigma_y)_{z=0} = 0$. Therefore, $(\sigma_x)_{z=0} = 0$ and $(\sigma_y)_{z=0} = 0$ are the conditions which the stress components should satisfy in the neutral layer.

The above conclusion is obtained based on the Kirchhoff hypothesis, that is, it is a classical single modulus problem. But here we consider different moduli in tension and compression of materials. However, from the viewpoint of phenomenalism, a bending thin plate, either with a single modulus or with a bimodulus, will uniformly generate a deflected shape under a lateral force, where the lower layer of the plate is in tension and the upper layer is in compression. Therefore, the neutral layer in tension free and compression does exist, like the case of classical plate, and is determined by the conditions

$$\sigma_x = 0, \quad \sigma_y = 0. \quad (6)$$

For materials without consideration of the bimodulus, the neutral layer is exactly the midsurface of the plate. When considering the bimodularity of materials, however, the neutral layer is no longer located in the midsurface of the plate. It will be located in a certain layer depending on tensile and compressive Young's modulus of elasticity and Poisson's ratio of the materials. Next, we will determine the unknown neutral layer.

3. Bimodular plates in bending

3.1. Pure bending. Having demonstrated that a neutral layer exists when the bimodular plate is in pure bending, we now consider such a plate in which the xy plane parametrizes the unknown neutral layer. Bounded by the unknown neutral layer, the full cross sections in the x and y directions are divided into tensile and compressive sections, as shown in Figure 2, where t is the thickness of the plate, t_1 and t_2 are the thicknesses in tension and compression, respectively, and M_x and M_y are the bending moments in the x and y directions, respectively.

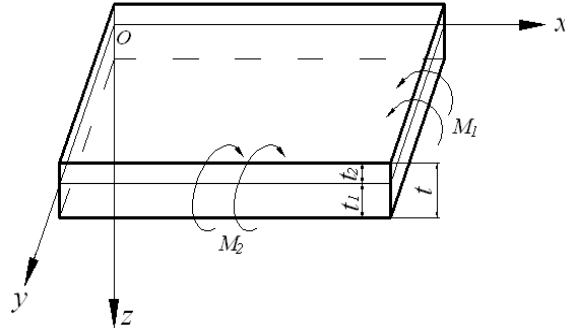


Figure 2. Bimodular thin plate under pure bending.

Because the normal stresses in the x and y directions coincide with the principal stresses in the α and β directions, according to the materials model proposed by Ambartsumyan, the constitutive relations of the plate in tension and compression should be, respectively,

$$\sigma_x^+ = \frac{E^+}{1 - (\mu^+)^2} (\varepsilon_x + \mu^+ \varepsilon_y), \quad \sigma_y^+ = \frac{E^+}{1 - (\mu^+)^2} (\varepsilon_y + \mu^+ \varepsilon_x), \quad (7)$$

and

$$\sigma_x^- = \frac{E^-}{1 - (\mu^-)^2} (\varepsilon_x + \mu^- \varepsilon_y), \quad \sigma_y^- = \frac{E^-}{1 - (\mu^-)^2} (\varepsilon_y + \mu^- \varepsilon_x), \quad (8)$$

where E^\pm and μ^\pm are defined on page 757. Considering the conclusions of Section 2.2, we may express the stress components in terms of deflection w as

$$\sigma_x^+ = -\frac{E^+ z}{1 - (\mu^+)^2} \left(\frac{\partial^2 w}{\partial x^2} + \mu^+ \frac{\partial^2 w}{\partial y^2} \right), \quad \sigma_y^+ = -\frac{E^+ z}{1 - (\mu^+)^2} \left(\frac{\partial^2 w}{\partial y^2} + \mu^+ \frac{\partial^2 w}{\partial x^2} \right), \quad 0 \leq z \leq t_1, \quad (9)$$

and

$$\sigma_x^- = -\frac{E^- z}{1 - (\mu^-)^2} \left(\frac{\partial^2 w}{\partial x^2} + \mu^- \frac{\partial^2 w}{\partial y^2} \right), \quad \sigma_y^- = -\frac{E^- z}{1 - (\mu^-)^2} \left(\frac{\partial^2 w}{\partial y^2} + \mu^- \frac{\partial^2 w}{\partial x^2} \right), \quad -t_2 \leq z \leq 0. \quad (10)$$

Since the stress formulas in the whole thickness of the plate are different, it is necessary to integrate in subsection to obtain the bending moments and normal forces along the x and y directions. Using (9) and (10) we may compute these quantities as follows:

$$N_x = \int_0^{t_1} \sigma_x^+ dz + \int_{-t_2}^0 \sigma_x^- dz = -\frac{E^+ t_1^2}{2[1 - (\mu^+)^2]} \left(\frac{\partial^2 w}{\partial x^2} + \mu^+ \frac{\partial^2 w}{\partial y^2} \right) + \frac{E^- t_2^2}{2[1 - (\mu^-)^2]} \left(\frac{\partial^2 w}{\partial x^2} + \mu^- \frac{\partial^2 w}{\partial y^2} \right) = 0, \quad (11)$$

$$N_y = \int_0^{t_1} \sigma_y^+ dz + \int_{-t_2}^0 \sigma_y^- dz = -\frac{E^+ t_1^2}{2[1 - (\mu^+)^2]} \left(\frac{\partial^2 w}{\partial y^2} + \mu^+ \frac{\partial^2 w}{\partial x^2} \right) + \frac{E^- t_2^2}{2[1 - (\mu^-)^2]} \left(\frac{\partial^2 w}{\partial y^2} + \mu^- \frac{\partial^2 w}{\partial x^2} \right) = 0,$$

$$M_x = \int_0^{t_1} \sigma_x^+ z dz + \int_{-t_2}^0 \sigma_x^- z dz = -\frac{E^+ t_1^3}{3[1 - (\mu^+)^2]} \left(\frac{\partial^2 w}{\partial x^2} + \mu^+ \frac{\partial^2 w}{\partial y^2} \right) - \frac{E^- t_2^3}{3[1 - (\mu^-)^2]} \left(\frac{\partial^2 w}{\partial x^2} + \mu^- \frac{\partial^2 w}{\partial y^2} \right), \quad (12)$$

$$M_y = \int_0^{t_1} \sigma_y^+ z dz + \int_{-t_2}^0 \sigma_y^- z dz = -\frac{E^+ t_1^3}{3[1 - (\mu^+)^2]} \left(\frac{\partial^2 w}{\partial y^2} + \mu^+ \frac{\partial^2 w}{\partial x^2} \right) - \frac{E^- t_2^3}{3[1 - (\mu^-)^2]} \left(\frac{\partial^2 w}{\partial y^2} + \mu^- \frac{\partial^2 w}{\partial x^2} \right).$$

From (11), we obtain

$$\frac{E^+ t_1^2}{1 - \mu^+} = \frac{E^- t_2^2}{1 - \mu^-}. \quad (13)$$

Combining $t_1 + t_2 = t$, we solve for the thicknesses of the plate in tension and compression as follows:

$$t_1 = \frac{\sqrt{E^-(1 - \mu^+)}}{\sqrt{E^+(1 - \mu^-)} + \sqrt{E^-(1 - \mu^+)}} t, \quad t_2 = \frac{\sqrt{E^+(1 - \mu^-)}}{\sqrt{E^+(1 - \mu^-)} + \sqrt{E^-(1 - \mu^+)}} t. \quad (14)$$

Thus, the position of the unknown neutral layer of the plate in pure bending is finally determined analytically.

3.2. Lateral force bending. While the plate is in lateral force bending, for example, under the uniformly distributed loads, q , as shown in Figure 3, not only the torsional stress, τ_{xy} , but also the transverse shear stresses, τ_{zx} and τ_{zy} , as well as the extrusion stress, σ_z , exist in the plate. However, according to the conclusion in Section 2.2, the neutral layer does exist if the thickness of the plate is small compared with the deflection of the plate. Therefore, the torsional stresses in the plate in tension and compression may be expressed in terms of the deflection w as, respectively,

$$\tau_{xy}^+ = -\frac{E^+ z}{1 + \mu^+} \frac{\partial^2 w}{\partial x \partial y}, \quad 0 \leq z \leq t_1, \quad (15a)$$

$$\tau_{xy}^- = -\frac{E^- z}{1 + \mu^-} \frac{\partial^2 w}{\partial x \partial y}, \quad -t_2 \leq z \leq 0. \quad (15b)$$

The twist moment M_{xy} may be computed as

$$M_{xy} = \int_0^{t_1} \tau_{xy}^+ z dz + \int_{-t_2}^0 \tau_{xy}^- z dz = -\frac{1}{3} \left(\frac{E^+ t_1^3}{1 + \mu^+} + \frac{E^- t_2^3}{1 + \mu^-} \right) \frac{\partial^2 w}{\partial x \partial y}. \quad (16)$$

Under uniformly distributed loads, q , the differential equation of equilibrium for bending of thin plates is

$$\frac{\partial^2 M_x}{\partial x^2} + 2 \frac{\partial^2 M_{xy}}{\partial x \partial y} + \frac{\partial^2 M_y}{\partial y^2} + q = 0. \quad (17)$$

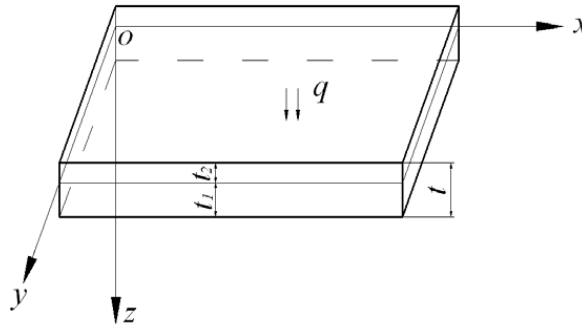


Figure 3. Bimodular thin plate under lateral force bending.

Substituting (12) and (16) into (17), we obtain

$$\left\{ \frac{E^+ t_1^3}{3[1 - (\mu^+)^2]} + \frac{E^- t_2^3}{3[1 - (\mu^-)^2]} \right\} \nabla^4 w = q. \quad (18)$$

Equation (18) is the governing differential equation of the neutral layer. If we let

$$D^* = \frac{E^+ t_1^3}{3[1 - (\mu^+)^2]} + \frac{E^- t_2^3}{3[1 - (\mu^-)^2]}, \quad (19)$$

where D^* is the flexural rigidity of the bimodular plate, (18) may be written in a familiar form:

$$D^* \nabla^4 w = q. \quad (20)$$

Note that the transverse shear stresses τ_{zx} and τ_{zy} and the extrusion stress σ_z acting on the sections in tension and compression have not been determined. Due to the lack of longitudinal loads and the body force being zero, the first two expressions of the differential equations of equilibrium in tension may be written as

$$\frac{\partial \tau_{zx}^+}{\partial z} = -\frac{\partial \sigma_x^+}{\partial x} - \frac{\partial \tau_{yx}^+}{\partial y}, \quad \frac{\partial \tau_{zy}^+}{\partial z} = -\frac{\partial \sigma_y^+}{\partial y} - \frac{\partial \tau_{xy}^+}{\partial x}. \quad (21a)$$

Substituting (9) and (15a) into (21a) and considering $\tau_{yx}^+ = \tau_{xy}^+$ as well as the stress boundary conditions at the bottom of the thin plate,

$$(\tau_{zx}^+)_{z=t_1} = 0, \quad (\tau_{zy}^+)_{z=t_1} = 0, \quad (22a)$$

we obtain

$$\tau_{zx}^+ = \frac{E^+}{2[1 - (\mu^+)^2]} (z^2 - t_1^2) \frac{\partial}{\partial x} \nabla^2 w, \quad \tau_{zy}^+ = \frac{E^+}{2[1 - (\mu^+)^2]} (z^2 - t_1^2) \frac{\partial}{\partial y} \nabla^2 w, \quad 0 \leq z \leq t_1. \quad (23a)$$

The third expression of the differential equations of equilibrium in tension is

$$\frac{\partial \sigma_z^+}{\partial z} = -\frac{\partial \tau_{xz}^+}{\partial x} - \frac{\partial \tau_{yz}^+}{\partial y}. \quad (24a)$$

Substituting (23a) into (24a) and considering $\tau_{xz}^+ = \tau_{zx}^+$ and $\tau_{yz}^+ = \tau_{zy}^+$ as well as the stress boundary conditions at the bottom of the plate,

$$(\sigma_z^+)_{z=t_1} = 0, \quad (25a)$$

we obtain

$$\sigma_z^+ = \frac{E^+}{2[1 - (\mu^+)^2]} \left(t_1^2 z - \frac{z^3}{3} - \frac{2}{3} t_1^3 \right) \nabla^4 w, \quad 0 \leq z \leq t_1. \quad (26a)$$

Similarly, the first two expressions of the differential equations of equilibrium in compression may be written as

$$\frac{\partial \tau_{zx}^-}{\partial z} = -\frac{\partial \sigma_x^-}{\partial x} - \frac{\partial \tau_{yx}^-}{\partial y}, \quad \frac{\partial \tau_{zy}^-}{\partial z} = -\frac{\partial \sigma_y^-}{\partial y} - \frac{\partial \tau_{xy}^-}{\partial x}. \quad (21b)$$

Substituting (10) and (15b) into (21b) and considering $\tau_{yx}^- = \tau_{xy}^-$ as well as the stress boundary conditions at the top of the thin plate,

$$(\tau_{zx}^-)_{z=-t_2} = 0, \quad (\tau_{zy}^-)_{z=-t_2} = 0, \quad (22b)$$

we obtain

$$\tau_{zx}^- = \frac{E^-}{2[1 - (\mu^-)^2]} (z^2 - t_2^2) \frac{\partial}{\partial x} \nabla^2 w, \quad \tau_{zy}^- = \frac{E^-}{2[1 - (\mu^-)^2]} (z^2 - t_2^2) \frac{\partial}{\partial y} \nabla^2 w. \quad -t_2 \leq z \leq 0. \quad (23b)$$

The third expression of the differential equations of equilibrium in compression is

$$\frac{\partial \sigma_z^-}{\partial z} = -\frac{\partial \tau_{xz}^-}{\partial x} - \frac{\partial \tau_{yz}^-}{\partial y}. \quad (24b)$$

Substituting (23b) into (24b) and considering $\tau_{xz}^- = \tau_{zx}^-$ and $\tau_{yz}^- = \tau_{zy}^-$ as well as the stress boundary conditions at the top of the plate,

$$(\sigma_z^-)_{z=-t_2} = -q, \quad (25b)$$

we obtain

$$\sigma_z^- = \frac{E^-}{2[1 - (\mu^-)^2]} \left(t_2^2 z - \frac{z^3}{3} - \frac{2}{3} t_2^3 \right) \nabla^4 w, \quad -t_2 \leq z \leq 0. \quad (26b)$$

Thus, all stress components have been expressed in terms of w , as shown in (9), (10), (15), (23a), (23b), (26a), and (26b).

Using (23a) and (23b), we may compute the transverse shear forces Q_x and Q_y as follows:

$$Q_x = \int_0^{t_1} \tau_{xz}^+ dz + \int_{-t_2}^0 \tau_{xz}^- dz = -D^* \frac{\partial}{\partial x} \nabla^2 w, \quad Q_y = \int_0^{t_1} \tau_{yz}^+ dz + \int_{-t_2}^0 \tau_{yz}^- dz = -D^* \frac{\partial}{\partial y} \nabla^2 w. \quad (27)$$

Thus, the bending moments, the torsional moment and the transverse shear forces have been expressed in terms of w , as shown in (12), (16), and (27).

3.3. Application of the displacement variation method. For a variety of boundary conditions, the displacement of plates along the thickness direction, w , may be taken as different expressions to satisfy the given boundary conditions and then be determined via the differential (20). For example, for a rectangular thin plate with four simply supported sides, the Navier solution may be adopted; for such a plate with two opposite simply supported sides, the Levy solution may be adopted. However, in some cases, it is convenient to use the displacement variation method to solve such a problem. For example, for a rectangular thin plate with four sides fixed, the Galerkin approach may be adopted; for such a plate with two opposite sides fixed, the Ritz approach may be adopted. In this paper, for the purpose of comparison with the existent FEM results [Gao et al. 1998], we take a bimodular rectangular thin plate with two long sides fixed as our object of study, as shown in Figure 4, where $2a$ and $2b$ are the short and long sides, respectively, and the plate is under the action of normal uniformly distributed loads, q . Due to the existence of free sides, we adopt the Ritz approach to solve this problem.

The displacement boundary conditions at the fixed sides is

$$(w)_{x=\pm a} = 0, \quad \left(\frac{\partial w}{\partial x} \right)_{x=\pm a} = 0, \quad (28)$$

and the boundary condition at the free sides should satisfy

$$(w)_{y=\pm b, x \neq \pm a} \neq 0, \quad \left(\frac{\partial w}{\partial y} \right)_{y=\pm b, x \neq \pm a} \neq 0. \quad (29)$$

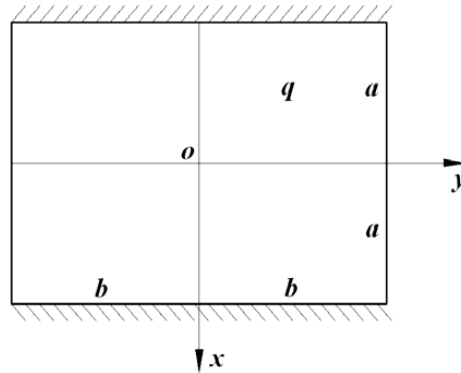


Figure 4. A bimodular plate under normal uniformly distributed loads.

Therefore, after considering the symmetry of this problem, we take the formula of w as

$$w = C_1 w_m = C_1 (x^2 - a^2)^2 \left[\left(\frac{y}{4b} \right)^2 + 1 \right], \tag{30}$$

where C_1 is an undetermined coefficient and it is obvious that the above formula can satisfy boundary conditions (28) and (29). If we let the strain potential energy be U , from the Ritz approach, we have the following formula:

$$\frac{\partial U}{\partial C_1} = \iint q w_m dx dy. \tag{31}$$

Next, we will derive the formula for U in the case of different moduli in tension and compression.

In the small-deflection bending problem of a bimodular thin plate, according to the computational hypotheses, the strain components $\varepsilon_z, \gamma_{yz}, \gamma_{zx}$ may be neglected; therefore, the strain potential energy U may be simplified as

$$U = \frac{1}{2} \int_{-a}^a \int_{-b}^b \int_0^{t_1} (\sigma_x^+ \varepsilon_x + \sigma_y^+ \varepsilon_y + \tau_{xy}^+ \gamma_{xy}) dx dy dz + \frac{1}{2} \int_{-a}^a \int_{-b}^b \int_{-t_2}^0 (\sigma_x^- \varepsilon_x + \sigma_y^- \varepsilon_y + \tau_{xy}^- \gamma_{xy}) dx dy dz, \tag{32}$$

where t_1 and t_2 are the thickness of the plate in tension and compression, respectively, and may be obtained from (14). The strain components $\varepsilon_x, \varepsilon_y, \gamma_{xy}$ are

$$\varepsilon_x = -\frac{\partial^2 w}{\partial x^2} z, \quad \varepsilon_y = -\frac{\partial^2 w}{\partial y^2} z, \quad \gamma_{xy} = -2 \frac{\partial^2 w}{\partial x \partial y} z. \tag{33}$$

Substituting (9), (10), (15), and (33) into (32), after integrating over z , we have

$$U = \frac{E^+ t_1^3}{6[1 - (\mu^+)^2]} \int_{-a}^a \int_{-b}^b \left\{ (\nabla^2 w)^2 - 2(1 - \mu^+) \left[\frac{\partial^2 w}{\partial x^2} \frac{\partial^2 w}{\partial y^2} - \left(\frac{\partial^2 w}{\partial x \partial y} \right)^2 \right] \right\} dx dy + \frac{E^- t_2^3}{6[1 - (\mu^-)^2]} \int_{-a}^a \int_{-b}^b \left\{ (\nabla^2 w)^2 - 2(1 - \mu^-) \left[\frac{\partial^2 w}{\partial x^2} \frac{\partial^2 w}{\partial y^2} - \left(\frac{\partial^2 w}{\partial x \partial y} \right)^2 \right] \right\} dx dy. \tag{34}$$

From (30), we may have

$$\frac{\partial^2 w}{\partial x^2} = 4C_1(3x^2 - a^2) \left[\left(\frac{y}{4b} \right)^2 + 1 \right], \quad \frac{\partial^2 w}{\partial y^2} = \frac{C_1}{8b^2}(x^2 - a^2)^2, \quad \frac{\partial^2 w}{\partial x \partial y} = \frac{C_1}{2b^2}(x^3 - a^2x)y. \quad (35)$$

Substituting (35) into (34), after integrating we obtain

$$U = \left\{ \frac{E^+ t_1^3}{6[1 - (\mu^+)^2]} F^+ + \frac{E^- t_2^3}{6[1 - (\mu^-)^2]} F^- \right\} C_1^2, \quad (36)$$

where

$$F^+ = \frac{8}{315} \frac{a^9}{b^3} + \left(\frac{16}{315} - \mu^+ \frac{136}{105} \right) \frac{a^7}{b} + \frac{4003}{75} a^5 b, \quad F^- = \frac{8}{315} \frac{a^9}{b^3} + \left(\frac{16}{315} - \mu^- \frac{136}{105} \right) \frac{a^7}{b} + \frac{4003}{75} a^5 b. \quad (37)$$

The right end of (31) may be computed as

$$\int_{-a}^a \int_{-b}^b q w_m dx dy = \int_{-a}^a \int_{-b}^b q (x^2 - a^2)^2 \left[\left(\frac{y}{4b} \right)^2 + 1 \right] dx dy = \frac{98}{45} q a^5 b. \quad (38)$$

Substituting (36) and (38) into (31), we may obtain the formula for C_1 . After substituting it into (30), we finally obtain the formula for w :

$$w = \frac{\frac{98}{15} q a^5 b}{\frac{E^+ t_1^3}{1 - (\mu^+)^2} F^+ + \frac{E^- t_2^3}{1 - (\mu^-)^2} F^-} (x^2 - a^2)^2 \left[\left(\frac{y}{4b} \right)^2 + 1 \right], \quad (39)$$

where t_1 and t_2 are known and may be obtained from (14). The maximum deflection takes place at the midpoints of the two free sides, that is, while $x = 0$ and $y = \pm b$, we have

$$w_{\max} = \frac{\frac{833}{120} q a^9 b}{\frac{E^+ t_1^3}{1 - (\mu^+)^2} F^+ + \frac{E^- t_2^3}{1 - (\mu^-)^2} F^-}. \quad (40)$$

4. Comparisons and discussions

4.1. Comparisons with FEM based on Ambartsumyan's model. The bimodular problem attributes non-linearity to materials. Since existent commercial FEM programs do not include the bimodular materials model proposed by Ambartsumyan, it is necessary to work out a numerical program based on an iterative technique. Because the stress state of the point in question is unknown in advance, we have to begin with a single modulus problem, thus gaining the initial stress state to form a corresponding elasticity matrix for each element. Generally, direct iterative methods based on an incrementally evolving stiffness have been adopted by many researchers.

Based on an incrementally evolving stiffness, Gao et al. [1998] analyzed a bimodular thin plate by the direct iterative method. In the FEM analysis, the elements of the plate should be layered along the direction of the plate thickness and each layer may be considered as being in the same stress state.

A rectangular thin plate fixed at its two longer sides is under the action of normal uniformly-distributed loads, as shown in Figure 5. For convenience, all the quantities are taken as dimensionless, specifically, the plate thickness is 0.24, the length and width of the plate are 8 and 6, respectively, and the intensity of

	$E^+/E^-:$	1.4	1.25	1.0	0.85	0.75	0.5
Node 2	(a)	0.0330	0.0553	0.0628	0.0681	0.0738	0.0839
	(b)	0.0450	0.0574	0.0646	0.0706	0.0757	0.0957
Node 4	(a)	0.1731	0.1863	0.2107	0.2281	0.2440	0.2856
	(b)	0.1749	0.1858	0.2095	0.2288	0.2453	0.3001
Node 18	(a)	0.1665	0.1786	0.2034	0.2222	0.2431	0.2763
	(b)	0.1672	0.1776	0.2002	0.2188	0.2345	0.2964
Node 32	(a)	0.1601	0.1778	0.2028	0.2205	0.2387	0.2737
	(b)	0.1646	0.1749	0.1971	0.2154	0.2309	0.2918

Table 1. The deflection results of FEM and analytical formulas ($\times 10^{-2}$). Results from (a) [Gao et al. 1998] and (b) this paper.

the uniformly distributed loads is 1. Considering the values of different moduli in tension and compression, we fix the values $E^- = 1.4 \times 10^6$ and $\mu^- = 0.2$, and set the values of E^+ and μ^+ only by changing their ratio $E^+/E^- = \mu^+/\mu^-$. We plot the maximum deflections of the plate, which is obtained by FEM and the analytical method presented in this paper, as shown in Figure 6. We also list some numerical results based on analytical formulas (39) derived in this paper, as shown in Table 1. It is easily seen that, if $E^+/E^- > 0.6$, the analytical solutions obtained in this paper agree well with the FEM results strictly based on Ambartsumyan's model.

In order to demonstrate the validity of the simplified model, we also list some results in the cases of different layer numbers while $E^+/E^- = 0.85$, as shown in Table 2. From the table, we see that when the whole plate is divided into two layers along the thickness direction, the numerical results are relatively accurate compared with the other cases in which the plate is divided into a greater number of layers. For the iterative results of the deflection, we see that more layering does little to improve the computational accuracy. The simplified model proposed in this paper is founded just on the fact that the whole plate is divided into two layers along the direction of plate thickness, one in tension and the other in compression.

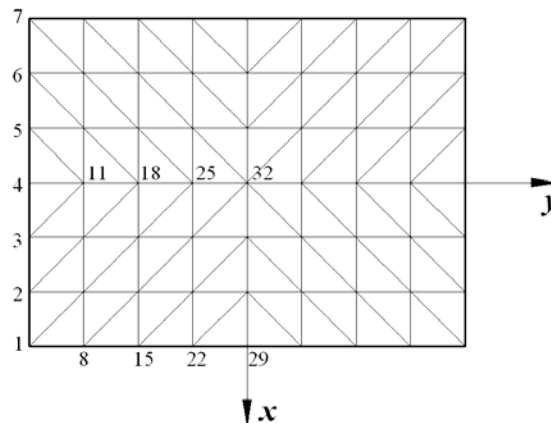


Figure 5. An FEM computation of a bimodular thin plate [Gao et al. 1998].

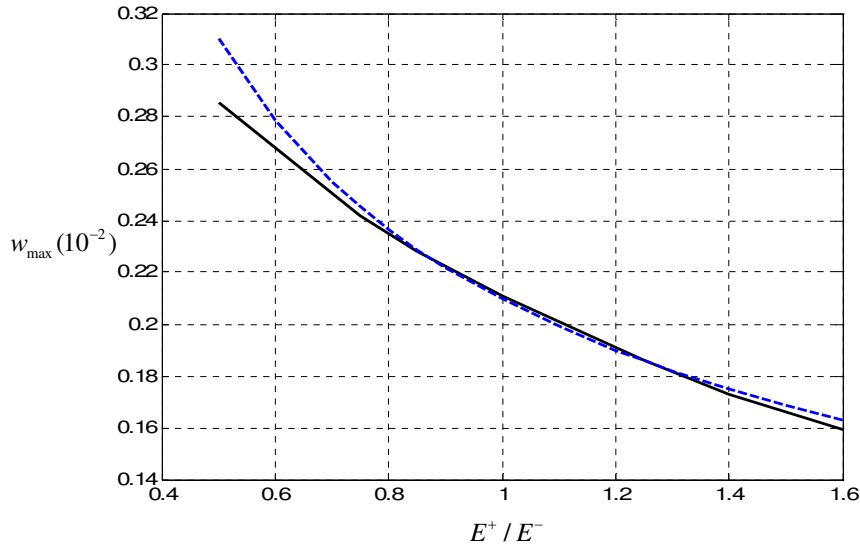


Figure 6. The relation between the maximum deflections (node 4) and E^+/E^- . (The solid line shows results for FEM, the dashed line for analytical solutions.)

From the analyses above, it may be seen that our simplified model may be valid for a bimodular thin plate in bending.

4.2. Discussions.

Regression and advantage of the analytical solutions. We observe that in (14), (19), and (20), while $E^+ = E^-$ and $\mu^+ = \mu^-$, we have $t_1 = t_2 = t/2$, $D = Et^3/(12(1 - \mu^2))$, and $D\nabla^4 w = q$. Moreover, the strain potential energy (34) derived in this paper can also be reduced to the classical formula. In fact, all the analytical formulas for bimodular plates in bending may be reduced to the classical problem of plates. These regressions show that the derivation process in this paper is reasonable.

In this paper, we introduce a new quantity, the flexural stiffnesses of bimodular thin plates, D^* . The flexural stiffness we introduce plays an important role in solving for bimodular plates. The study above indicates that the bimodularity of materials has great influence on the structural rigidity. In most cases, the influence of the bimodularity of materials may be integrated into the flexural stiffness. By simple

Number of layers	$-w_4 (\times 10^{-2})$	$-w_{32} (\times 10^{-2})$	Number of iterations
2	0.2283	0.2203	3
4	0.2280	0.2206	4
6	0.2281	0.2205	4
8	0.2281	0.2205	5
10	0.2281	0.2205	6

Table 2. The results in cases of different number of layers when $E^+/E^- = 0.85$ [Gao et al. 1998].

substitution of the flexural stiffness, we can readily obtain the solutions for bimodular thin plates directly from the classical solutions of plates for a variety of boundary conditions. Since solutions of the Kirchhoff plate theories for a variety of boundary conditions are easily determined or are available in most textbooks on mechanics of materials, the simplified model presented herein makes it easier to analyze bimodular thin plates analytically.

Essence and limitations of the simplified model. In civil engineering, the principal stress state is a key point in the analysis and design of bending components like beams, columns, plates, and shells. Shear stresses and the resulting diagonal tensions must also be carefully considered in the design of reinforced concrete. In this paper, the application of the Kirchhoff hypothesis tests the existence of the neutral layer and realizes the subarea in tension and compression. The simplified mechanical model proposed in this paper essentially regards the whole bending plate as a laminated structure consisting of only two layers, one in tension and another in compression.

The results obtained in this paper are founded on the Kirchhoff hypothesis, which are for relatively thin plates, and thus the results are not applicable to the analysis of bimodular thick plates. In thick plates, the shearing stresses are important. Such bimodular thick plates should be treated by means of a more general theory owing to the fact that some assumptions of the Kirchhoff hypotheses are no longer appropriate.

5. Concluding remarks

Based on the classical Kirchhoff hypothesis, we propose a simplified mechanical model used in solving bimodular thin plates in small-deflection bending. The following main conclusions can be drawn.

- The application of the Kirchhoff hypothesis tests the existence of the elastic neutral layers of bimodular thin plates in small-deflection bending, and opens up possibilities for subareas in tension and compression.
- The application of the Kirchhoff hypothesis may extend the solution from the case of pure bending, which strictly follows the bimodular materials model proposed by Ambartsumyan, into the case of lateral force bending.
- The flexural stiffnesses derived in this paper enables us to obtain easily the analytical solutions of bimodular thin plates via the classical problems for a variety of boundary conditions.

This work will be helpful for predicting the mechanical behaviors of bimodular materials. In particular, these results may be useful in analyzing concrete-like materials and fiber-reinforced composite materials that contain cracks and are undergoing contact, whose macroscopic constitutive behavior depends on the direction of the macroscopic strain, similarly to the case of bimodular materials [Zinno and Greco 2001; Greco 2009].

References

[Ambartsumyan 1965] S. A. Ambartsumyan, "The axisymmetric problem of a circular cylindrical shell of material with different stiffness in tension and compression", *Izv. Akad. Nauk SSSR Mekh.* **4** (1965), 77–85. In Russian; translation in Scientific and Technical Aerospace Reports N69-11070.

- [Ambartsumyan 1969] S. A. Ambartsumyan, "Basic equations and relations in the theory of anisotropic bodies with different moduli in tension and compression", *Inzh. Zhur. MTT* (Proc. Acad. Sci. USSR Eng. J. Mech. Solids) **3** (1969), 51–61. In Russian.
- [Ambartsumyan 1982] S. A. Ambartsumyan, *Разномодульная теория упругости*, Nauka, Moscow, 1982. Translated into Chinese as *不同模量弹性理论*, China Railway Publishing House, Beijing, 1986.
- [Baykara et al. 2005] C. Baykara, U. Guven, and I. Bayer, "Large deflections of a cantilever beam of nonlinear bimodulus material subjected to an end moment", *J. Reinf. Plast. Compos.* **24**:12 (2005), 1321–1326.
- [Bert 1977] C. W. Bert, "Models for fibrous composites with different properties in tension and compression", *J. Eng. Mater. Technol. (ASME)* **99**:4 (1977), 344–349.
- [Bert and Gordaninejad 1983] C. W. Bert and F. Gordaninejad, "Transverse shear effects in bimodular composite laminates", *J. Compos. Mater.* **17**:4 (1983), 282–298.
- [El-Tahan et al. 1989] W. W. El-Tahan, G. H. Staab, S. H. Advani, and J. K. Lee, "Structural analysis of bimodular materials", *J. Eng. Mech. (ASCE)* **115**:5 (1989), 963–981.
- [Ganapathi et al. 2004] M. Ganapathi, B. P. Patel, and A. V. Lele, "Static analysis of bimodulus laminated composite plates subjected to mechanical loads using higher-order shear deformation theory", *J. Reinf. Plast. Compos.* **23**:11 (2004), 1159–1171.
- [Gao et al. 1998] C. Gao, X. B. Liu, and X. Q. Lu, "Analysis for the plate with the theory of different extension compression elastic modulus", *Chinese J. Comput. Mech.* **15**:4 (1998), 448–455.
- [Greco 2009] F. Greco, "Homogenized mechanical behavior of composite micro-structures including micro-cracking and contact evolution", *Eng. Fract. Mech.* **76**:2 (2009), 182–208.
- [He et al. 2007a] X. T. He, S. L. Chen, and J. Y. Sun, "Applying the equivalent section method to solve beam subjected to lateral force and bending-compression column with different moduli", *Int. J. Mech. Sci.* **49**:7 (2007), 919–924.
- [He et al. 2007b] X. T. He, S. L. Chen, and J. Y. Sun, "Elasticity solution of simple beams with different modulus under uniformly distributed load", *Chinese J. Eng. Mech.* **24**:10 (2007), 51–56.
- [He et al. 2008] X. T. He, Z. L. Zheng, and S. L. Chen, "Approximate elasticity solution of bending-compression column with different tension-compression moduli", *J. Chongqing Univ. Nat. Sci. Ed.* **31**:3 (2008), 339–343.
- [He et al. 2009] X. T. He, Z. L. Zheng, J. Y. Sun, Y. M. Li, and S. L. Chen, "Convergence analysis of a finite element method based on different moduli in tension and compression", *Int. J. Solids Struct.* **46**:20 (2009), 3734–3740.
- [Jones 1976] R. M. Jones, "Apparent flexural modulus and strength of multimodulus materials", *J. Compos. Mater.* **10**:4 (1976), 342–354.
- [Jones 1977] R. M. Jones, "Stress-strain relations for materials with different moduli in tension and compression", *AIAA J.* **15**:1 (1977), 16–23.
- [Kamiya 1974] N. Kamiya, "An energy method applied to large elastic deflection of a thin plate of bimodulus material", *Mech. Based Design Struct. Mach.* **3**:3 (1974), 317–329.
- [Kamiya 1975a] N. Kamiya, "Large deflection of a different modulus circular plate", *J. Eng. Mater. Technol. (ASME)* **97**:1 (1975), 52–56.
- [Kamiya 1975b] N. Kamiya, "Transverse shear effect in a bimodulus plate", *Nucl. Eng. Des.* **32**:3 (1975), 351–357.
- [Khan et al. 2009] K. Khan, B. P. Patel, and Y. Nath, "Vibration analysis of bimodulus laminated cylindrical panels", *J. Sound Vib.* **321**:1–2 (2009), 166–183.
- [Liu and Zhang 2000] X. B. Liu and Y. Z. Zhang, "Modulus of elasticity in shear and accelerate convergence of different extension-compression elastic modulus finite element method", *J. Dalian Univ. Technol.* **40**:5 (2000), 527–530.
- [Maceri and Vairo 2009] F. Maceri and G. Vairo, "Anisotropic thin-walled beam models: a rational deduction from three-dimensional elasticity", *J. Mech. Mater. Struct.* **4**:2 (2009), 371–394.
- [Patel et al. 2004] B. P. Patel, A. V. Lele, M. Ganapathi, S. S. Gupta, and C. T. Sambandam, "Thermo-flexural analysis of thick laminates of bimodulus composite materials", *Compos. Struct.* **63**:1 (2004), 11–20.
- [Patel et al. 2005a] B. P. Patel, S. S. Gupta, M. Joshi, and M. Ganapathi, "Transient response analysis of bimodulus anisotropic laminated composite plates", *J. Reinf. Plast. Compos.* **24**:8 (2005), 795–821.

- [Patel et al. 2005b] B. P. Patel, S. S. Gupta, and R. Sarda, "Free flexural vibration behavior of bimodular material angle-ply laminated composite plates", *J. Sound Vib.* **286**:1–2 (2005), 167–186.
- [Reddy and Chao 1983] J. N. Reddy and W. C. Chao, "Nonlinear bending of bimodular-material plates", *Int. J. Solids Struct.* **19**:3 (1983), 229–237.
- [Srinivasan and Ramachandra 1989] R. S. Srinivasan and L. S. Ramachandra, "Large deflection analysis of bimodulus annular and circular plates using finite elements", *Comput. Struct.* **31**:5 (1989), 681–691.
- [Yang and Wang 2008] H. T. Yang and B. Wang, "An analysis of longitudinal vibration of bimodular rod via smoothing function approach", *J. Sound Vib.* **317**:3–5 (2008), 419–431.
- [Yang and Zhu 2006] H. T. Yang and Y. L. Zhu, "Solving elasticity problems with bi-modulus via a smoothing technique", *Chinese J. Comput. Mech.* **23**:1 (2006), 19–23.
- [Yang et al. 1999] H. T. Yang, K. J. Yang, and R. F. Wu, "Solution of 3-D elastic dual extension compression modulus problems using initial stress technique", *J. Dalian Univ. Technol.* **39**:4 (1999), 478–482.
- [Yao and Ye 2004a] W. J. Yao and Z. M. Ye, "Analytical solution of bending-compression column using different tension-compression modulus", *Appl. Math. Mech.* **25**:9 (2004), 983–993.
- [Yao and Ye 2004b] W. J. Yao and Z. M. Ye, "The analytical and numerical solution of retaining wall based on elastic theory of different modulus", *J. Shanghai Jiaotong Univ.* **38**:6 (2004), 1022–1027.
- [Yao and Ye 2004c] W. J. Yao and Z. M. Ye, "Analytical solution for bending beam subject to lateral force with different modulus", *Appl. Math. Mech.* **25**:10 (2004), 1107–1117.
- [Ye 1997] Z. M. Ye, "A new finite element formulation for planar elastic deformation", *Int. J. Numer. Methods Eng.* **40**:14 (1997), 2579–2591.
- [Ye et al. 2004] Z. M. Ye, T. Chen, and W. J. Yao, "Progresses in elasticity theory with different modulus in tension and compression and related FEM", *Chinese J. Mech. Eng.* **26**:2 (2004), 9–14.
- [Zhang and Wang 1989] Y. Z. Zhang and Z. F. Wang, "Finite element method of elasticity problem with different tension and compression moduli", *Chinese J. Comput. Struct. Mech. Appl.* **6**:1 (1989), 236–245.
- [Zinno and Greco 2001] R. Zinno and F. Greco, "Damage evolution in bimodular laminated composites under cyclic loading", *Compos. Struct.* **53**:4 (2001), 381–402.

Received 4 Oct 2009. Revised 2 Feb 2010. Accepted 2 Feb 2010.

XIAO-TING HE: xiaotinghe@163.com

College of Civil Engineering, Chongqing University, Chongqing 400045, China

and

Key Laboratory of New Technology for Construction of Cities in Mountain Area, Chongqing University, Ministry of Education, Chongqing 400045, China

QIANG CHEN: College of Civil Engineering, Chongqing University, Chongqing 400045, China
chenqiangcd@163.com

JUN-YI SUN: sun.junyi@yahoo.com.cn

College of Civil Engineering, Chongqing University, Chongqing 400045, China

ZHOU-LIAN ZHENG: zhqcqu@163.com

College of Civil Engineering, Chongqing University, Chongqing 400045, China

SHAN-LIN CHEN: ydlcqu@163.com

College of Civil Engineering, Chongqing University, Chongqing 400045, China

A NEW MODELING APPROACH FOR PLANAR BEAMS: FINITE-ELEMENT SOLUTIONS BASED ON MIXED VARIATIONAL DERIVATIONS

FERDINANDO AURICCHIO, GIUSEPPE BALDUZZI AND CARLO LOVADINA

This paper illustrates a new modeling approach for planar linear elastic beams. Referring to existing models, we first introduce the variational principles that could be adopted for the beam model derivation, discussing their relative advantages and disadvantages. Then, starting from the Hellinger–Reissner functional we derive some homogeneous and multilayered beam models, discussing some properties of their analytical solutions. Finally, we develop a planar beam finite element, following an innovative approach that could be seen as the imposition of equilibrium in the cross-section and compatibility along the axis. The homogeneous model is capable of reproducing the behavior of the Timoshenko beam, with the advantage that the shear correction factor appears naturally from the variational derivation; the multilayered beam is capable of capturing the local effects produced by boundary constraints and load distributions; the finite element is capable of predicting the cross-section stress distribution with high accuracy, and more generally the behavior of planar structural elements.

1. Introduction

To reproduce the mechanical behavior of structural elements characterized by having one dimension predominant with respect to the other two (that is, a beam) the classical approaches are the well-known Euler–Bernoulli (EB) and Timoshenko theories [Timoshenko 1955; Hjelmstad 2005]. Generally adopted for very slender elements, the EB beam model assumes the cross-section axial and transverse displacements as 1D unknown fields, converting the 3D elastic problem, formulated through a set of partial differential equations, into a simpler system of two ordinary differential equations (ODEs). On the other hand, the Timoshenko beam model, adopted for less slender structural elements, assumes the cross-section axial and transverse displacements, together with rotations, as 1D fields, leading to a set of three ODEs. As a consequence of the field assumptions, these models are often referred to in the literature as *first-order* models. Moreover, we denote these models as *displacement-based* to underline that usually these models consider only the displacements as independent variables and the stresses are evaluated by postprocessing.

Despite their simplicity (also related to the possibility of computing analytical solutions) and their excellent first-design ability, the EB and Timoshenko models have some well-known limitations:

- loss of accuracy for beams with a low ratio between the length and cross-sectional characteristic dimension,

Keywords: laminated linear elastic beam, analytical solution, finite element modeling, mixed variational formulation.

The authors would like to thank professors Elio Sacco, Alessandro Reali, and Giancarlo Sangalli for several helpful suggestions during the completion of this work.

- loss of accuracy in modeling nonhomogeneous beams (such as composites) as well as in modeling nonlinear material behavior, and
- difficulty in computing accurate stress profiles, connected to the fact that only mean-value displacements are assumed as field variables.

Hence, due to the need for more accurate 1D models, researchers have developed new approaches that can generally be classified as

- *higher-order displacement-based models*, which introduce more sophisticated cross-section kinematics, and
- *mixed or hybrid models*, which also introduce stresses — and sometimes even strains — as independent variables.

To give a few examples, an often cited model falling in the first category is the one proposed in [Reddy 1984] that introduces section warping in addition to Timoshenko displacements. As discussed in [Sheinman 2001], this model shows inconsistencies, since transverse displacement generates a constant cross-section shear distribution, whereas axial displacements yield a quadratic one. More complete kinematics are adopted in the model proposed by Lo et al. [1977a] where, considering both section warping and striction, authors eliminate such inconsistencies. For a general treatment of higher-order, planar, kinematic beam models and discussion of their analytical solutions readers may refer to the work of Sheinman [2001].

With respect to mixed models, a very interesting approach is the one proposed by Alessandrini et al. [1999], where, starting from 3D elasticity, the authors illustrate a clear derivation of some plate models, and also study the convergence of the models under consideration.

In terms of numerical modeling, the number of finite element (FE) implementations proposed in the literature is truly vast, since many different choices are possible, depending on

- *functional formulation and independent variables*: the simplest functionals consider only kinematic variables, as in displacement based beam models, while the most complicated also consider stresses and strains;
- *order of field approximation*: in addition to the first- versus higher-order classification, for the case of multilayered beams, *layerwise* models adopt piecewise layer-defined functions while *global* models use globally defined functions to describe the field distribution on a cross-section.

For both items, intermediate choices are possible, for example, only some stress components could be selected as independent variables, or some fields described layerwise, with the remaining ones assumed as global functions.

We note that in the available review papers (for example, [Carrera 2000; Wanji and Zhen 2008]), models are usually compared by considering different field approximations derived from the same principle. Therefore, it is possible to understand the effect of basis accuracy, but not improvements arising from the use of a more sophisticated variational principle. In Section 3 of this paper we review different variational principles that can be employed, briefly discussing their features and possible drawbacks.

The main aim of this paper is to propose a simple analytical model and an FE capable of capturing the section stress distribution with high accuracy as well as in a multilayered body. We opt for the *dimension reduction variational* approach, classical in beam modeling and used in Alessandrini et al. [1999] and

elsewhere for plate problems. This method might allow us to generalize the model to more complex situations, such as nonlinear constitutive laws.

A summary of the paper is as follows. In Section 2 we define the problem we are going to tackle. In Section 3 we introduce the functionals which may be used for the model derivation, listing for each one properties and developed models presented in the literature; by means of this discussion we are able to choose an appropriate variational principle as the starting point for the model derivations. In Section 4 we derive some 1D models. In Section 5 we present a few examples, giving some insight on the structure of the corresponding analytical solution. In Section 6 we develop suitable FE schemes, and present some results to illustrate their actual computational performances.

2. Problem definition

The object of our study is a planar beam Ω , not necessarily homogeneous along the thickness and modeled as a 2D body; this is equivalent to imposing the plane stress state hypotheses to a 3D body or to stating that the beam width is negligible. Moreover, we limit the discussion to linear elastic isotropic materials and small displacements.

We define the problem domain as: $\Omega = l \times A$, where the beam longitudinal axis l and the cross-section A are defined as:

$$l = \{x \in \mathbb{R} \mid x \in [0, \bar{l}]\}, \quad A = \left\{y \in \mathbb{R} \mid y \in \left[-\frac{h}{2}, \frac{h}{2}\right]\right\},$$

in which h is the beam thickness and \bar{l} is the beam length.

Obviously $\bar{l} \gg h$, so the longitudinal axis is the predominant dimension of the body. Figure 1 represents the domain and the adopted Cartesian coordinate system.

As illustrated in Figure 1 we define the lower and upper boundaries as S_0 and S_n , respectively, and the lateral cross-sections as A_0 and A_l . We denote the domain boundary as $\partial\Omega$, so that

$$\partial\Omega = (A_0 \cup A_l) \cup (S_0 \cup S_n).$$

For $\partial\Omega$, we consider the partition $\{\partial\Omega_t; \partial\Omega_s\}$, where $\partial\Omega_t$ and $\partial\Omega_s$ are the externally loaded and displacement constrained boundaries, respectively. The external load is defined as a line force density $t : \partial\Omega_t \rightarrow \mathbb{R}^2$ while the body load is defined as an area force density $f : \Omega \rightarrow \mathbb{R}^2$; we specify a sufficiently smooth boundary displacement function $\bar{s} : \partial\Omega_s \rightarrow \mathbb{R}^2$. Finally, we suppose that the beam is made of layers whose thickness is constant along the axial coordinate x , though not necessarily the same at each layer. Consequently, the Young's modulus E and the Poisson's ratio ν are scalar fields depending on the thickness coordinate y , that is, $E : A \rightarrow \mathbb{R}$ and $\nu : A \rightarrow \mathbb{R}$.

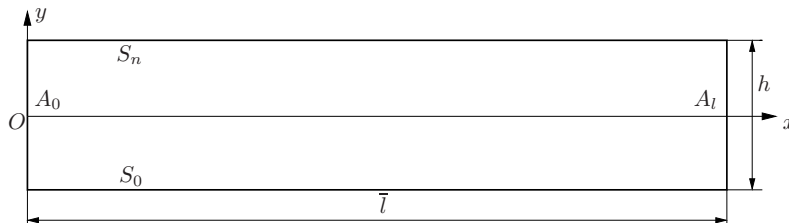


Figure 1. Planar beam geometry, coordinate system, dimensions, and adopted notations.

Introducing the independent variable fields $\boldsymbol{\sigma} : \Omega \rightarrow \mathbb{R}^{2 \times 2}$, $\boldsymbol{\varepsilon} : \Omega \rightarrow \mathbb{R}^{2 \times 2}$, and $\boldsymbol{s} : \Omega \rightarrow \mathbb{R}^2$, where the stress $\boldsymbol{\sigma}$ and the strain $\boldsymbol{\varepsilon}$ are symmetric tensors while the displacement \boldsymbol{s} is a vector, the strong formulation of the problem under investigation corresponds to the following boundary value problem:

$$\boldsymbol{\varepsilon} = \nabla^s \boldsymbol{s}, \quad \boldsymbol{\sigma} = \boldsymbol{D} : \boldsymbol{\varepsilon}, \quad \nabla \cdot \boldsymbol{\sigma} + \boldsymbol{f} = \mathbf{0} \quad \text{in } \Omega; \quad \boldsymbol{\sigma} \cdot \boldsymbol{n} = \boldsymbol{t} \quad \text{on } \partial\Omega_t; \quad \boldsymbol{s} = \bar{\boldsymbol{s}} \quad \text{on } \partial\Omega_s. \quad (1)$$

Here $\boldsymbol{\varepsilon} = \nabla^s \boldsymbol{s}$ is the compatibility relation, $\boldsymbol{\sigma} = \boldsymbol{D} : \boldsymbol{\varepsilon}$ is the material constitutive relation, in which \boldsymbol{D} is the appropriate fourth-order linear elastic tensor, and $\nabla \cdot \boldsymbol{\sigma} + \boldsymbol{f} = \mathbf{0}$ represents the equilibrium condition. The last two equations in (1) represent the boundary equilibrium and the boundary compatibility condition.

3. Variational problem formulations and modeling methods

In this section we are going to present different possible variational formulations for problem (1). In particular, we introduce approaches based on total potential energy and Hellinger–Reissner and Hu–Washizu functionals, considering for each different possible stationarity conditions. Restricting ourselves to the framework of Section 2, we emphasize that a variational beam model can be considered as the outcome of the following general procedure:

- **Step 1:** A variational principle is selected for the 2D planar elasticity problem. In particular, the functional spaces for the involved fields has to be appropriately chosen.
- **Step 2:** For each field involved, an approximation profile is selected. Typically, to develop a beam model, one chooses polynomial or piecewise polynomial shapes along the thickness direction, while no profile restrictions are imposed along the axial direction. However, the approximation fields should fit the functional framework of Step 1, at least if a *conforming* model is considered.
- **Step 3:** Integration along the thickness direction is performed. This way, the 2D variational problem is reduced to a 1D variational problem, which corresponds to a system of ODEs equipped with boundary conditions (that is, the beam model).

3.1. Total potential energy approach. Total potential energy (TPE) is the functional most frequently used in continuum mechanics and in the standard literature (for example, [Hjelmstad 2005]); several authors use it as a starting point to derive first-order beam models and the most popular corresponding FE formulations. The TPE functional can be expressed as follows:

$$J_{\text{TPE}}(\boldsymbol{s}) = \frac{1}{2} \int_{\Omega} \nabla^s \boldsymbol{s} : \boldsymbol{D} : \nabla^s \boldsymbol{s} \, d\Omega - \int_{\Omega} \boldsymbol{s} \cdot \boldsymbol{f} \, d\Omega. \quad (2)$$

Boundary conditions will be suitably imposed as follows. The critical point of the functional above corresponds to finding the energy minimizer, which is unique and stable in the usual framework of admissible displacement space.

Requiring stationarity of the TPE (2), we obtain the following weak problem: *Find $\boldsymbol{s} \in W^s$ such that, for all $\delta \boldsymbol{s} \in \bar{W}^s$,*

$$\delta J_{\text{TPE}}^s = \int_{\Omega} \nabla^s (\delta \boldsymbol{s}) : \boldsymbol{D} : \nabla^s \boldsymbol{s} \, d\Omega - \int_{\Omega} \delta \boldsymbol{s} \cdot \boldsymbol{f} \, d\Omega - \int_{\partial\Omega_t} \delta \boldsymbol{s} \cdot \boldsymbol{t} \, dS = 0, \quad (3)$$

where $W^s := \{\boldsymbol{s} \in H^1(\Omega) : \boldsymbol{s}|_{\partial\Omega_s} = \bar{\boldsymbol{s}}\}$ and $\bar{W}^s := \{\delta \boldsymbol{s} \in H^1(\Omega) : \delta \boldsymbol{s}|_{\partial\Omega_s} = \mathbf{0}\}$.

Equation (3) is called *symmetric TPE stationarity*. It is often used as a basis for FE development, leading obviously to a symmetric stiffness matrix.

Wanji and Zhen [2008] give a review of multilayered, elastic, displacement-based (that is, TPE derived) plate FE. Increasing orders of field approximation are considered, from the simplest models, in which displacements are globally defined along the cross-section, to the most sophisticated, in which displacements are defined layerwise. In the same reference it is noted that almost all the FEs presented perform only for specific problems, such as thick laminated plates or soft-core sandwiches; they are not able to accurately describe the shear distribution along the thickness in the general case.

An accurate evaluation of shear distribution is one of the aims of [Vinayak et al. 1996a; 1996b], in which the authors develop a multilayered planar beam FE starting from (3), using the field approximation proposed in [Lo et al. 1977a; 1977b] and appropriately treating the thickness heterogeneity. They propose two ways to evaluate the axial and transverse stresses: the first uses the compatibility and the constitutive relations (1)_{1,2}, while the second refines the shear and out-of-plane stress distributions using the equilibrium relation (1)₃. The resulting numerical schemes are generally satisfactory, but the computed solutions might exhibit instabilities near the boundary, and the stress distributions are not always sufficiently accurate.

As a general remark [Rohwer and Rolfe 1998; Rohwer et al. 2005], in TPE-based models the critical step is the postprocessing stress evaluation which could compromise the effectiveness of the method.

3.2. Hellinger–Reissner approach. The Hellinger–Reissner (HR) functional can be expressed as

$$J_{HR}(\boldsymbol{\sigma}, s) = \int_{\Omega} \boldsymbol{\sigma} : \nabla^s s \, d\Omega - \frac{1}{2} \int_{\Omega} \boldsymbol{\sigma} : \mathbf{D}^{-1} : \boldsymbol{\sigma} \, d\Omega - \int_{\Omega} s \cdot \mathbf{f} \, d\Omega. \tag{4}$$

How boundary conditions are enforced depends on the specific variational formulation employed to express the stationarity of the functional (see Sections 3.2.1 and 3.2.2). We also wish to remark that stationarity of this functional corresponds to a saddle point problem. Therefore, the model derivation based on the HR functional requires particular care in the displacement and stress field assumptions, otherwise the model risks leading to a problem which is not well-posed.

3.2.1. HR grad-grad stationarity. Requiring stationarity of the HR functional (4), we obtain the following weak problem: *Find* $s \in W_s^{gg}$ *and* $\boldsymbol{\sigma} \in S^{gg}$ *such that, for all* $\delta s \in \overline{W}^{gg}$ *and all* $\delta \boldsymbol{\sigma} \in S^{gg}$,

$$\delta J_{HR}^{gg} = \int_{\Omega} \nabla^s \delta s : \boldsymbol{\sigma} \, d\Omega + \int_{\Omega} \delta \boldsymbol{\sigma} : \nabla^s s \, d\Omega - \int_{\Omega} \delta \boldsymbol{\sigma} : \mathbf{D}^{-1} : \boldsymbol{\sigma} \, d\Omega - \int_{\Omega} \delta s \cdot \mathbf{f} \, d\Omega - \int_{\partial\Omega_t} \delta s \cdot \mathbf{t} \, dS = 0, \tag{5}$$

where $W_s^{gg} := \{s \in H^1(\Omega) : s|_{\partial\Omega_s} = \bar{s}\}$, $\overline{W}^{gg} := \{\delta s \in H^1(\Omega) : \delta s|_{\partial\Omega_s} = \mathbf{0}\}$, and $S^{gg} := \{\boldsymbol{\sigma} \in L^2(\Omega)\}$.

Equation (5) is called *HR grad-grad stationarity* because two gradient operators appear in the formulation. We remark that the kinematic boundary condition $s|_{\partial\Omega_s} = \bar{s}$ is directly enforced in the trial space W_s^{gg} (an *essential* boundary condition), while $\boldsymbol{\sigma} \cdot \mathbf{n}|_{\partial\Omega_t} = \mathbf{t}$ turns out to be a *natural* boundary condition.

As mentioned in Section 1, Alessandrini et al. [1999] derived some homogeneous plate models starting from HR grad-grad stationarity (5). They noticed that in many situations, models derived from (5) lead to displacement fields that minimize the potential energy in the class of the same kinematic assumptions. Therefore, in those cases HR grad-grad models are essentially equivalent to the corresponding models obtained by symmetric TPE stationarity (3).

Many researchers have derived multilayered plate and beam FEs using HR grad-grad stationarity. [Spilker 1982; Feng and Hoa 1998; Huang et al. 2002; Icardi and Atzori 2004] are among the most significant examples, since the computed solutions are generally satisfactory. The main drawback of these schemes, especially for the case of layerwise beams and plates, is the high number of degrees of freedom (DOFs), which leads to a heavy FE formulation. Spilker [1982] alleviates this problem by assuming the stress variables to be discontinuous along the plate extension so that they can be condensed at the element level reducing the mixed local stiffness matrix to a displacement-like one. An alternative is to consider some stress components as dependent variables, expressing them a priori in terms of the displacements. Reissner's mixed variational theorem [1986] follows this approach: the out of plane stresses τ_{xy} and σ_{yy} are considered as independent variables while the axial stress σ_{xx} is expressed as a function of displacements. In [Carrera 2000; 2001; Carrera and Demasi 2002; Demasi 2009a; 2009b; 2009c; 2009d; 2009e] various plate FEs are derived applying this viewpoint, with different choices of basis function, obtaining reasonable accuracy in the stress description. Unfortunately these authors are forced to use a high number of kinematic DOFs, drastically increasing the computational effort.

3.2.2. HR div-div stationarity. Integrating by parts, the first and the second terms of (5) become:

$$\int_{\Omega} \nabla^s \delta s : \sigma \, d\Omega = \int_{\partial\Omega} \delta s \cdot \sigma \cdot \mathbf{n} \, dS - \int_{\Omega} \delta s \cdot \nabla \cdot \sigma \, d\Omega, \quad \int_{\Omega} \delta \sigma : \nabla^s s \, d\Omega = \int_{\partial\Omega} \delta \sigma \cdot \mathbf{n} \cdot s \, dS - \int_{\Omega} \nabla \cdot \delta \sigma \cdot s \, d\Omega. \quad (6)$$

Hence, substituting (6) into (5), the weak formulation becomes: *Find $s \in W^{\text{dd}}$ and $\sigma \in S_t^{\text{dd}}$ such that, for all $\delta s \in W^{\text{dd}}$ and all $\delta \sigma \in \bar{S}^{\text{dd}}$,*

$$\delta J_{\text{HR}}^{\text{dd}} = - \int_{\Omega} \delta s \cdot \nabla \cdot \sigma \, d\Omega - \int_{\Omega} \nabla \cdot \delta \sigma \cdot s \, d\Omega - \int_{\Omega} \delta \sigma : \mathbf{D}^{-1} : \sigma \, d\Omega - \int_{\Omega} \delta s \cdot \mathbf{f} \, d\Omega + \int_{\partial\Omega_s} \delta \sigma \cdot \mathbf{n} \cdot \bar{s} \, dS = 0, \quad (7)$$

where $W^{\text{dd}} := \{s \in L^2(\Omega)\}$, $S_t^{\text{dd}} := \{\sigma \in H(\text{div}, \Omega) : \sigma \cdot \mathbf{n}|_{\partial\Omega_t} = \mathbf{t}\}$, $\bar{S}^{\text{dd}} := \{\delta \sigma \in H(\text{div}, \Omega) : \delta \sigma \cdot \mathbf{n}|_{\partial\Omega_t} = \mathbf{0}\}$. Here and in what follows, $H(\text{div}, \Omega)$ denotes the space of square-integrable vector functions whose divergence is still square-integrable.

Equation (7) is called *HR div-div stationarity* because two divergence operators appear in it. We remark that $s|_{\partial\Omega_s} = \bar{s}$ is now a *natural* boundary condition, while $\sigma \cdot \mathbf{n}|_{\partial\Omega_t} = \mathbf{t}$ becomes an *essential* boundary condition, as it is directly incorporated in the space S_t^{dd} .

Considering the HR div-div stationarity approach (7), Alessandrini et al. [1999] have derived some homogeneous plate models, which are more interesting than the ones stemming from the HR grad-grad stationarity (5). However, the techniques developed in that work cannot be directly applied to general heterogeneous plates, because the resulting models may be divergent; see [Auricchio et al. 2004].

3.3. Hu–Washizu approach. The Hu–Washizu (HW) functional may be expressed as

$$J_{\text{HW}}(\sigma, \boldsymbol{\varepsilon}, s) = \int_{\Omega} \sigma : (\nabla^s s - \boldsymbol{\varepsilon}) \, d\Omega + \frac{1}{2} \int_{\Omega} \boldsymbol{\varepsilon} : \mathbf{D} : \boldsymbol{\varepsilon} \, d\Omega - \int_{\Omega} s \cdot \mathbf{f} \, d\Omega. \quad (8)$$

Again, how boundary conditions are enforced depends on the specific variational formulation employed to express the stationarity of the functional. Here also the strain field is a primal variable. In the following variational formulations, we will not specify the functional frameworks for the involved fields, since they are similar to the ones of the HR-based corresponding variational formulations.

3.3.1. HW grad-grad stationarity. Stationarity of (8) can be expressed as

$$\delta J_{\text{HW}}^{\text{gg}} = \int_{\Omega} \nabla^s \delta s : \sigma \, d\Omega - \int_{\Omega} \delta \epsilon : \sigma \, d\Omega + \int_{\Omega} \delta \sigma : (\nabla^s s - \epsilon) \, d\Omega + \int_{\Omega} \delta \epsilon : \mathbf{D} : \epsilon \, d\Omega - \int_{\Omega} \delta s \cdot f \, d\Omega - \int_{\partial\Omega_t} \delta s \cdot t \, dS = 0, \quad (9)$$

where s satisfies $s|_{\partial\Omega_s} = \bar{s}$, while $\sigma \cdot \mathbf{n}|_{\partial\Omega_t} = \mathbf{t}$ is a natural boundary condition. Equation (9) is called *HW grad-grad stationarity*; an example of its use in multilayered plate modeling is presented in [Auricchio and Sacco 1999].

3.3.2. HW div-div stationarity. A second formulation of HW stationarity can be found by introducing (6) into (9), obtaining

$$\delta J_{\text{HW}}^{\text{dd}} = - \int_{\Omega} \delta s \cdot \nabla \cdot \sigma \, d\Omega - \int_{\Omega} \delta \epsilon : \sigma \, d\Omega - \int_{\Omega} \nabla \cdot \delta \sigma \cdot s \, d\Omega - \int_{\Omega} \delta \sigma : \epsilon \, d\Omega + \int_{\Omega} \delta \epsilon : \mathbf{D} : \epsilon \, d\Omega - \int_{\Omega} \delta s \cdot f \, d\Omega + \int_{\partial\Omega_s} (\delta \sigma \cdot \mathbf{n}) \cdot \bar{s} \, dS = 0, \quad (10)$$

where σ satisfies $\sigma \cdot \mathbf{n} = \mathbf{t}$ on $\partial\Omega_t$, while $s|_{\partial\Omega_s} = \bar{s}$ is a natural boundary condition. This is called *HW div-div stationarity*.

3.4. Conclusions on weak formulations. We summarize the previous discussion in a few observations (see also Table 1):

- All the weak formulations considered are symmetric.
- Each mixed weak formulation can be expressed in different formats: the grad-grad formulations (5) and (9) and the div-div formulations (7) and (10). The former require considering a priori smooth displacement fields and less regular stress fields ($s \in H^1(\Omega)$ and $\sigma \in L^2(\Omega)$), while the latter demand a priori less regular displacement fields and smooth stress fields ($s \in L^2(\Omega)$ and $\sigma \in H(\text{div}, \Omega)$).
- When selecting the approximation fields for the mixed model design (see Step 2 of the procedure described at the beginning of this section), the combination of the regularity requirements and the well-posedness of the corresponding saddle point problems typically leads to congruent models for the grad-grad formulations and self-equilibrated models for the div-div formulations.

In our view, one of the major limitations of the available elementary beam models is that equilibrium equations are not sufficiently enforced within the cross-section. For this reason we will focus on HR formulations, with some emphasis on the div-div form (7).

	Principle		
Displacement-based	TPE	Equation (3)	
Mixed	HR HW	grad-grad (5) grad-grad (9)	div-div (7) div-div (10)

Table 1. Functional stationarities classified in terms of the functionals from which they are derived and equation formats.

4. Model derivations

In this section we develop some beam models. We will start from the HR variational formulations of Section 3.2 (this is Step 1 of the procedure described at the beginning of Section 3), then define the approximated fields (Step 2), and perform the integration along the thickness (Step 3). To simplify further discussion, we will switch to engineering notation, the equivalence between tensor and engineering notation being summarized as follows, where $\mathbf{E}_1 = \begin{bmatrix} 1 & 0 & 0 \\ 0 & 0 & 1 \end{bmatrix}$ and $\mathbf{E}_2 = \begin{bmatrix} 0 & 0 & 0 \\ 0 & 1 & 1 \end{bmatrix}$:

Tensor notation	Engineering notation
$\nabla \cdot \boldsymbol{\sigma}$	$\left(\frac{d}{dx} \mathbf{E}_1 + \frac{d}{dy} \mathbf{E}_2 \right) \mathbf{P}_\sigma \hat{\boldsymbol{\sigma}}$
$\nabla^S s$	$\left(\frac{d}{dx} \mathbf{E}_1^T + \frac{d}{dy} \mathbf{E}_2^T \right) \mathbf{P}_s \hat{s}$
$\boldsymbol{\sigma} \cdot \mathbf{n}$	$(n_x \mathbf{E}_1 + n_y \mathbf{E}_2) \mathbf{P}_\sigma \hat{\boldsymbol{\sigma}}$

4.1. Profile approximation and notations. We now introduce the notation we use for a generic approximated field $\gamma(x, y)$ involved in the beam models. We first define a *profile* vector function $\mathbf{p}_\gamma(y) : A \rightarrow \mathbb{R}^m$. We insist that the m components of $\mathbf{p}_\gamma(y)$ are a set of *linearly independent* functions of the cross-section coordinate y . They may be global polynomials, as well as piece-wise polynomials or other shape functions. The approximate field $\gamma(x, y)$ is expressed as a linear combination of the components of $\mathbf{p}_\gamma(y)$, with arbitrary functions of the axial coordinate x as coefficients, collected in a vector $\hat{\boldsymbol{\gamma}}(x)$. Therefore, $\gamma(x, y)$ can be written as a scalar product between $\mathbf{p}_\gamma(y)$ and $\hat{\boldsymbol{\gamma}}(x)$, that is,

$$\gamma(x, y) = \mathbf{p}_\gamma^T(y) \hat{\boldsymbol{\gamma}}(x), \quad (11)$$

where superscript T denotes transposition and $\hat{\boldsymbol{\gamma}} : l \rightarrow \mathbb{R}^m$ contains the functional coefficients as components. We emphasize that, once the profile vector $\mathbf{p}_\gamma(y)$ has been assigned, the field $\gamma(x, y)$ is uniquely determined by the components of $\hat{\boldsymbol{\gamma}}(x)$. Such components, for all the involved fields, are indeed the *unknowns* of the beam models we will develop. We also remark that, due to assumption (11), the computation of partial derivatives is straightforward, since:

$$\frac{\partial}{\partial x} \gamma = \frac{\partial}{\partial x} (\mathbf{p}_\gamma^T \hat{\boldsymbol{\gamma}}) = \mathbf{p}_\gamma^T \frac{d}{dx} \hat{\boldsymbol{\gamma}} = \mathbf{p}_\gamma^T \hat{\boldsymbol{\gamma}}', \quad \frac{\partial}{\partial y} \gamma = \frac{\partial}{\partial y} (\mathbf{p}_\gamma^T \hat{\boldsymbol{\gamma}}) = \frac{d}{dy} \mathbf{p}_\gamma^T \hat{\boldsymbol{\gamma}} = \mathbf{p}_\gamma'^T \hat{\boldsymbol{\gamma}},$$

where we use a prime to indicate derivatives along both x and y , as there is no risk of confusion. Adopting the notation introduced in (11) and switching now to an engineering notation we set

$$\mathbf{s}(x, y) = \begin{Bmatrix} s_u(x, y) \\ s_v(x, y) \end{Bmatrix} = \begin{bmatrix} \mathbf{p}_u^T(y) & \mathbf{0} \\ \mathbf{0} & \mathbf{p}_v^T(y) \end{bmatrix} \begin{Bmatrix} \hat{\mathbf{u}}(x) \\ \hat{\mathbf{v}}(x) \end{Bmatrix} = \mathbf{P}_s \hat{\mathbf{s}}, \quad (12)$$

$$\boldsymbol{\sigma}(x, y) = \begin{Bmatrix} \sigma_{xx}(x, y) \\ \sigma_{yy}(x, y) \\ \tau_{xy}(x, y) \end{Bmatrix} = \begin{bmatrix} \mathbf{p}_{\sigma_x}^T(y) & \mathbf{0} & \mathbf{0} \\ \mathbf{0} & \mathbf{p}_{\sigma_y}^T(y) & \mathbf{0} \\ \mathbf{0} & \mathbf{0} & \mathbf{p}_\tau^T(y) \end{bmatrix} \begin{Bmatrix} \hat{\boldsymbol{\sigma}}_x(x) \\ \hat{\boldsymbol{\sigma}}_y(x) \\ \hat{\boldsymbol{\tau}}(x) \end{Bmatrix} = \mathbf{P}_\sigma \hat{\boldsymbol{\sigma}}, \quad (13)$$

where, for \mathbf{P}_s and \mathbf{P}_σ ($\hat{\mathbf{s}}$ and $\hat{\boldsymbol{\sigma}}$, respectively), we drop the explicit dependence on y (or x , respectively), for notational simplicity. The virtual fields are analogously defined as $\delta \mathbf{s} = \mathbf{P}_s \delta \hat{\mathbf{s}}$ and $\delta \boldsymbol{\sigma} = \mathbf{P}_\sigma \delta \hat{\boldsymbol{\sigma}}$.

In Section 3, \mathbf{D}^{-1} denotes the fourth-order elastic tensor; from now on, we use the same notation to indicate the corresponding square matrix obtained following engineering notation. Therefore, we have

$$\mathbf{D}^{-1} = \frac{1}{E} \begin{bmatrix} 1 & -\nu & 0 \\ -\nu & 1 & 0 \\ 0 & 0 & 2(1+\nu) \end{bmatrix}.$$

4.2. Formulation of the problems. We consider the special case of a beam for which

$$\bar{\mathbf{s}} = \mathbf{0} \text{ on } A_0 = \partial\Omega_s, \quad \mathbf{t} \neq \mathbf{0} \text{ on } A_l, \quad \mathbf{f} = \mathbf{0} \text{ in } \Omega, \quad \mathbf{t} = \mathbf{0} \text{ on } S_0 \cup S_n.$$

Hence, $\partial\Omega_t = A_l \cup S_0 \cup S_n$; the beam is clamped on the left-hand side A_0 , and is subjected to a nonvanishing traction field on the right-hand side A_l . Furthermore, we suppose that $\mathbf{t}|_{A_l}$ can be exactly represented using the chosen profiles for $\boldsymbol{\sigma} \cdot \mathbf{n}$. Recalling (13), and noting that $\mathbf{n}|_{A_l} = (1, 0)^T$, this means that there exist suitable vectors $\hat{\mathbf{t}}_x$ and $\hat{\mathbf{t}}_\tau$ such that

$$\mathbf{t} = \begin{Bmatrix} \mathbf{P}_{\sigma_x}^T \hat{\mathbf{t}}_x \\ \mathbf{P}_\tau^T \hat{\mathbf{t}}_\tau \end{Bmatrix}. \tag{14}$$

Therefore, the boundary condition $\boldsymbol{\sigma} \cdot \mathbf{n}|_{A_l} = \mathbf{t}$ may be written as (see (13))

$$\begin{Bmatrix} \hat{\boldsymbol{\sigma}}_x(\bar{l}) \\ \hat{\boldsymbol{\tau}}(\bar{l}) \end{Bmatrix} = \begin{Bmatrix} \hat{\mathbf{t}}_x \\ \hat{\mathbf{t}}_\tau \end{Bmatrix}. \tag{15}$$

All these assumptions can be modified to cover more general cases; nonetheless, this simple model is already adequate to illustrate the method’s capabilities.

4.2.1. HR grad-grad approach. In the notation of Section 4.1, the HR grad-grad stationarity (5) becomes

$$\begin{aligned} \delta J_{\text{HR}}^{\text{gg}} = & \int_{\Omega} \left[\left(\frac{d}{dx} \mathbf{E}_1^T + \frac{d}{dy} \mathbf{E}_2^T \right) \mathbf{P}_s \delta \hat{\mathbf{s}} \right]^T \mathbf{P}_\sigma \hat{\boldsymbol{\sigma}} d\Omega + \int_{\Omega} \delta \hat{\boldsymbol{\sigma}}^T \mathbf{P}_\sigma^T \left[\left(\frac{d}{dx} \mathbf{E}_1^T + \frac{d}{dy} \mathbf{E}_2^T \right) \mathbf{P}_s \hat{\mathbf{s}} \right] d\Omega \\ & - \int_{\Omega} \delta \hat{\boldsymbol{\sigma}}^T \mathbf{P}_\sigma^T \mathbf{D}^{-1} \mathbf{P}_\sigma \hat{\boldsymbol{\sigma}} d\Omega - \int_{\partial\Omega_t} \delta \hat{\mathbf{s}}^T \mathbf{P}_s^T \mathbf{t} dy = 0. \end{aligned} \tag{16}$$

Expanding (16) we obtain

$$\begin{aligned} \delta J_{\text{HR}}^{\text{gg}} = & \int_{\Omega} (\delta \hat{\mathbf{s}}^T \mathbf{P}_s^T \mathbf{E}_1 \mathbf{P}_\sigma \hat{\boldsymbol{\sigma}} + \delta \hat{\mathbf{s}}^T \mathbf{P}_s^T \mathbf{E}_2 \mathbf{P}_\sigma \hat{\boldsymbol{\sigma}}) d\Omega + \int_{\Omega} (\delta \hat{\boldsymbol{\sigma}}^T \mathbf{P}_\sigma^T \mathbf{E}_1^T \mathbf{P}_s \hat{\mathbf{s}}' + \delta \hat{\boldsymbol{\sigma}}^T \mathbf{P}_\sigma^T \mathbf{E}_2^T \mathbf{P}_s \hat{\mathbf{s}}) d\Omega \\ & - \int_{\Omega} \delta \hat{\boldsymbol{\sigma}}^T \mathbf{P}_\sigma^T \mathbf{D}^{-1} \mathbf{P}_\sigma \hat{\boldsymbol{\sigma}} d\Omega - \int_{A_l} \delta \hat{\mathbf{s}}^T \mathbf{P}_s^T \mathbf{t} dy = 0. \end{aligned} \tag{17}$$

Using the Fubini–Tonelli theorem, (17) can be written as

$$\delta J_{\text{HR}}^{\text{gg}} = \int_l (\delta \hat{\mathbf{s}}^T \mathbf{G}_{s\sigma} \hat{\boldsymbol{\sigma}} + \delta \hat{\mathbf{s}}^T \mathbf{H}_{s'\sigma} \hat{\boldsymbol{\sigma}} + \delta \hat{\boldsymbol{\sigma}}^T \mathbf{G}_{\sigma s} \hat{\mathbf{s}}' + \delta \hat{\boldsymbol{\sigma}}^T \mathbf{H}_{\sigma s'} \hat{\mathbf{s}} - \delta \hat{\boldsymbol{\sigma}}^T \mathbf{H}_{\sigma\sigma} \hat{\boldsymbol{\sigma}}) dx - \delta \hat{\mathbf{s}}^T \mathbf{T}_x \Big|_{x=\bar{l}} = 0, \tag{18}$$

where

$$\begin{aligned} \mathbf{G}_{s\sigma} &= \mathbf{G}_{\sigma s}^T = \int_A \mathbf{P}_s^T \mathbf{E}_1 \mathbf{P}_\sigma dy, & \mathbf{H}_{\sigma\sigma} &= \int_A \mathbf{P}_\sigma^T \mathbf{D}^{-1} \mathbf{P}_\sigma dy, \\ \mathbf{H}_{s'\sigma} &= \mathbf{H}_{\sigma s'}^T = \int_A \mathbf{P}_s^T \mathbf{E}_2 \mathbf{P}_\sigma dy, & \mathbf{T}_x &= \int_{A_l} \mathbf{P}_s^T \mathbf{t} dy. \end{aligned} \tag{19}$$

Equation (18) represents the weak form of the 1D beam model. To obtain the corresponding boundary value problem, we integrate by parts the first term of (18):

$$\int_l \delta \hat{s}'^T \mathbf{G}_{s\sigma} \hat{\sigma} dx = \delta \hat{s}^T \mathbf{G}_{s\sigma} \hat{\sigma} \Big|_{x=0}^{x=\bar{l}} - \int_l \delta \hat{s}^T \mathbf{G}_{s\sigma} \hat{\sigma}' dx. \quad (20)$$

Substituting (20) into (18), recalling that $\delta \hat{s} = \mathbf{0}$ on A_0 , and collecting the variables in a vector we obtain

$$\int_l [\delta \hat{s}; \delta \hat{\sigma}]^T \left(\mathbf{G} \begin{Bmatrix} \hat{s}' \\ \hat{\sigma}' \end{Bmatrix} + \mathbf{H}^{\text{gg}} \begin{Bmatrix} \hat{s} \\ \hat{\sigma} \end{Bmatrix} \right) dx + \delta \hat{s}^T (\mathbf{G}_{s\sigma} \hat{\sigma} - \mathbf{T}_x) \Big|_{x=\bar{l}} = 0, \quad (21)$$

in which

$$\mathbf{G} = \begin{bmatrix} \mathbf{0} & -\mathbf{G}_{s\sigma} \\ \mathbf{G}_{\sigma s} & \mathbf{0} \end{bmatrix}, \quad \mathbf{H}^{\text{gg}} = \begin{bmatrix} \mathbf{0} & \mathbf{H}_{s'\sigma} \\ \mathbf{H}_{\sigma s'} & -\mathbf{H}_{\sigma\sigma} \end{bmatrix}. \quad (22)$$

Requiring that (21) is satisfied for all the possible variations and imposing the *essential* boundary condition \hat{s} we finally obtain

$$\mathbf{G} \begin{Bmatrix} \hat{s}' \\ \hat{\sigma}' \end{Bmatrix} + \mathbf{H}^{\text{gg}} \begin{Bmatrix} \hat{s} \\ \hat{\sigma} \end{Bmatrix} = \begin{Bmatrix} \mathbf{0} \\ \mathbf{0} \end{Bmatrix} \quad \text{in } l, \quad \mathbf{G}_{s\sigma} \hat{\sigma} = \mathbf{T}_x \quad \text{at } x = \bar{l}, \quad \hat{s} = \mathbf{0} \quad \text{at } x = 0. \quad (23)$$

We remark that boundary value problem (23) is not necessarily well-posed. This depends on how the profile vectors have been chosen for all the involved fields. However, the well-posedness of (23) is guaranteed if the approximated fields are selected in accordance with the approximation theory of saddle-point problem (5) [Alessandrini et al. 1999].

4.2.2. HR div-div approach. Using the notation introduced in Section 4.1 in (7), the HR div-div functional stationarity becomes

$$\begin{aligned} \delta J_{\text{HR}}^{\text{dd}} = & - \int_{\Omega} \delta \hat{s}^T \mathbf{P}_s^T \left[\left(\frac{d}{dx} \mathbf{E}_1 + \frac{d}{dy} \mathbf{E}_2 \right) \mathbf{P}_{\sigma} \hat{\sigma} \right] d\Omega - \int_{\Omega} \left[\left(\frac{d}{dx} \mathbf{E}_1 + \frac{d}{dy} \mathbf{E}_2 \right) \mathbf{P}_{\sigma} \delta \hat{\sigma} \right]^T \mathbf{P}_s \hat{s} d\Omega \\ & - \int_{\Omega} \delta \hat{\sigma}^T \mathbf{P}_{\sigma}^T \mathbf{D}^{-1} \mathbf{P}_{\sigma} \hat{\sigma} d\Omega = 0. \end{aligned} \quad (24)$$

Expanding (24), the weak formulation becomes

$$\begin{aligned} \delta J_{\text{HR}}^{\text{dd}} = & - \int_{\Omega} (\delta \hat{s}^T \mathbf{P}_s^T \mathbf{E}_1 \mathbf{P}_{\sigma} \hat{\sigma}' + \delta \hat{s}^T \mathbf{P}_s^T \mathbf{E}_2 \mathbf{P}_{\sigma}' \hat{\sigma}) d\Omega - \int_{\Omega} (\delta \hat{\sigma}'^T \mathbf{P}_{\sigma}^T \mathbf{E}_1^T \mathbf{P}_s \hat{s} + \delta \hat{\sigma}^T \mathbf{P}_{\sigma}'^T \mathbf{E}_2^T \mathbf{P}_s \hat{s}) d\Omega \\ & - \int_{\Omega} \delta \hat{\sigma}^T \mathbf{P}_{\sigma}^T \mathbf{D}^{-1} \mathbf{P}_{\sigma} \hat{\sigma} d\Omega = 0. \end{aligned} \quad (25)$$

Again by the Fubini–Tonelli theorem, (25) becomes

$$\delta J_{\text{HR}}^{\text{dd}} = \int_l \left(-\delta \hat{s}^T \mathbf{G}_{s\sigma} \hat{\sigma}' - \delta \hat{s}^T \mathbf{H}_{s\sigma'} \hat{\sigma} - \delta \hat{\sigma}'^T \mathbf{G}_{\sigma s} \hat{s} - \delta \hat{\sigma}^T \mathbf{H}_{\sigma's} \hat{s} - \delta \hat{\sigma}^T \mathbf{H}_{\sigma\sigma} \hat{\sigma} \right) dx = 0, \quad (26)$$

where

$$\mathbf{H}_{\sigma's} = \mathbf{H}_{s\sigma'}^T = \int_A \mathbf{P}_{\sigma}'^T \mathbf{E}_2 \mathbf{P}_s dy$$

while the other matrices are as in (19).

Equation (26) represents the weak form of the 1D beam model. To obtain the corresponding boundary value problem, we integrate the third term by parts:

$$-\int_l \delta \hat{\boldsymbol{\sigma}}^T \mathbf{G}_{\sigma_s} \hat{\boldsymbol{\sigma}} dx = -\delta \hat{\boldsymbol{\sigma}}^T \mathbf{G}_{\sigma_s} \hat{\boldsymbol{\sigma}}|_{x=0}^{\bar{l}} + \int_l \delta \hat{\boldsymbol{\sigma}}^T \mathbf{G}_{\sigma_s} \hat{\boldsymbol{\sigma}}' dx. \quad (27)$$

Substituting (27) into (26), recalling that $\mathbf{G}_{s\sigma} \delta \hat{\boldsymbol{\sigma}} = \mathbf{0}$ at $x = \bar{l}$, and collecting the unknowns in a vector we obtain

$$\int_l [\delta \hat{\boldsymbol{\sigma}}; \delta \hat{\boldsymbol{\sigma}}']^T \left(\mathbf{G} \begin{Bmatrix} \hat{\boldsymbol{\sigma}}' \\ \hat{\boldsymbol{\sigma}} \end{Bmatrix} + \mathbf{H}^{\text{dd}} \begin{Bmatrix} \hat{\boldsymbol{\sigma}} \\ \hat{\boldsymbol{\sigma}}' \end{Bmatrix} \right) dx + \delta \hat{\boldsymbol{\sigma}}^T \mathbf{G}_{\sigma_s} \hat{\boldsymbol{\sigma}}|_{x=0} = 0, \quad (28)$$

where \mathbf{G} is defined as in (22) and \mathbf{H}^{dd} is defined as

$$\mathbf{H}^{\text{dd}} = \begin{bmatrix} \mathbf{0} & -\mathbf{H}_{s\sigma'} \\ -\mathbf{H}_{\sigma's} & -\mathbf{H}_{\sigma\sigma} \end{bmatrix}. \quad (29)$$

Requiring that (28) be satisfied for all possible variations, and imposing the *essential* boundary condition (15), we finally obtain

$$\mathbf{G} \begin{Bmatrix} \hat{\boldsymbol{\sigma}}' \\ \hat{\boldsymbol{\sigma}} \end{Bmatrix} + \mathbf{H}^{\text{dd}} \begin{Bmatrix} \hat{\boldsymbol{\sigma}} \\ \hat{\boldsymbol{\sigma}}' \end{Bmatrix} = \begin{Bmatrix} \mathbf{0} \\ \mathbf{0} \end{Bmatrix} \quad \text{in } l, \quad \hat{\boldsymbol{\sigma}}_x = \hat{\boldsymbol{t}}_x \quad \text{at } x = \bar{l}, \quad \hat{\boldsymbol{\tau}} = \hat{\boldsymbol{t}}_{\boldsymbol{\tau}} \quad \text{at } x = \bar{l}, \quad \mathbf{G}_{\sigma_s} \hat{\boldsymbol{\sigma}} = \mathbf{0} \quad \text{at } x = 0. \quad (30)$$

We remark that boundary value problem (30) is not necessarily well-posed. This depends on how the profile vectors have been chosen for all the fields involved. However, (30) is guaranteed to be well-posed if the approximated fields are selected according to the approximation theory of the saddle-point problem (7); see [Alessandrini et al. 1999].

4.3. Conclusions on the derived beam models. From the development in this section, we can make the following remarks.

- Starting from different versions of the HR stationarity condition — grad-grad (5) and div-div (7) — and introducing hypothesis (11), we obtain two different classes of 1D beam models. Both classes may be described by a boundary value problem of the following type:

$$\mathbf{G} \begin{Bmatrix} \hat{\boldsymbol{\sigma}}' \\ \hat{\boldsymbol{\sigma}} \end{Bmatrix} + \mathbf{H} \begin{Bmatrix} \hat{\boldsymbol{\sigma}} \\ \hat{\boldsymbol{\sigma}}' \end{Bmatrix} = \begin{Bmatrix} \mathbf{0} \\ \mathbf{0} \end{Bmatrix} \quad + \text{ suitable boundary conditions.} \quad (31)$$

The difference between models based on the HR grad-grad and HR div-div formulations lies in the \mathbf{H} matrix. More precisely:

- $\mathbf{H} = \mathbf{H}^{\text{gg}}$ for the HR grad-grad formulation. In this case, derivatives are applied to the displacement fields through the symmetric gradient operator, and the resulting models most likely strongly satisfy the compatibility law, though not necessarily the equilibrium equation.
- $\mathbf{H} = \mathbf{H}^{\text{dd}}$ for the HR div-div formulation. In this case, derivatives are applied to the stress fields through the divergence operator, and the resulting models most likely strongly satisfy the equilibrium equation, though not the necessarily the compatibility equation.
- The boundary value problem (30) can be explicitly written as

$$-\mathbf{G}_{s\sigma} \hat{\boldsymbol{\sigma}}' - \mathbf{H}_{s\sigma'} \hat{\boldsymbol{\sigma}} = \mathbf{0}, \quad \mathbf{G}_{\sigma_s} \hat{\boldsymbol{\sigma}}' - \mathbf{H}_{\sigma's} \hat{\boldsymbol{\sigma}} - \mathbf{H}_{\sigma\sigma} \hat{\boldsymbol{\sigma}} = \mathbf{0} \quad + \text{ suitable boundary conditions.}$$

We can compute $\hat{\sigma}$ from the second equation and substitute it into the first, obtaining a displacement-like formulation of the problem:

$$A\hat{s}'' + B\hat{s}' + C\hat{s} = 0 \quad + \text{ suitable boundary conditions,} \quad (32)$$

where

$$A = -G_{s\sigma} H_{\sigma\sigma}^{-1} G_{\sigma s}, \quad B = -G_{s\sigma} H_{\sigma\sigma}^{-1} H_{\sigma' s} + H_{s\sigma'} H_{\sigma\sigma}^{-1} G_{\sigma s}, \quad C = H_{s\sigma'} H_{\sigma\sigma}^{-1} H_{\sigma' s}.$$

Similar considerations apply to problem (23).

5. Examples of beam models

In this section we give two examples of beam models developed using the strategies of Section 4. More precisely, starting from the HR div-div approach in Equation (30), we derive

- a single layer beam model in which we use a first-order displacement field, thus showing that the approach under discussion is able to reproduce the classical models; and
- a multilayer beam model, in which we consider also higher-order kinematic and stress fields, thus illustrating how the approach can produce a refined model with a reasonable solution.

5.1. Single layer beam. Considering a homogeneous beam, we assume a first-order kinematic (as in the Timoshenko model) and the usual cross-section stress distributions (obtained from Jourawsky theory). In other words, we make the following hypotheses:

$$\begin{aligned} u &= u_0(x) + yu_1(x), & \text{that is,} & & \mathbf{p}_u &= \{1 \ y\}^T, & \hat{\mathbf{u}} &= \{u_0 \ u_1\}^T, \\ v &= v(x), & \text{that is,} & & \mathbf{p}_v &= \{1\}, & \hat{\mathbf{v}} &= \{v\}, \\ \sigma_{xx} &= \sigma_{x0}(x) + y\sigma_{x1}(x), & \text{that is,} & & \mathbf{p}_{\sigma_x} &= \{1 \ y\}^T, & \hat{\sigma}_x &= \{\sigma_{x0} \ \sigma_{x1}\}^T, \\ \sigma_{yy} &= 0, & \text{that is,} & & \mathbf{p}_{\sigma_y} &= \{0\}, & \hat{\sigma}_y &= \{0\}, \\ \tau &= (1 - 4y^2/h^2)\tau(x), & \text{that is,} & & \mathbf{p}_\tau &= \{1 - 4y^2/h^2\}, & \hat{\tau} &= \{\tau\}. \end{aligned}$$

The matrices \mathbf{G} and \mathbf{H}^{dd} defined in (22) and (29), and entering into the beam model (30), are explicitly given by

$$\mathbf{G} = \begin{bmatrix} 0 & 0 & 0 & -h & 0 & 0 \\ 0 & 0 & 0 & 0 & -\frac{h^3}{12} & 0 \\ 0 & 0 & 0 & 0 & 0 & -\frac{2}{3}h \\ h & 0 & 0 & 0 & 0 & 0 \\ 0 & \frac{h^3}{12} & 0 & 0 & 0 & 0 \\ 0 & 0 & \frac{2}{3}h & 0 & 0 & 0 \end{bmatrix}, \quad \mathbf{H}^{\text{dd}} = \begin{bmatrix} 0 & 0 & 0 & 0 & 0 & 0 \\ 0 & 0 & 0 & 0 & 0 & \frac{2}{3}h \\ 0 & 0 & 0 & 0 & 0 & 0 \\ 0 & 0 & 0 & -\frac{h}{E} & 0 & 0 \\ 0 & 0 & 0 & 0 & -\frac{h^3}{12} \frac{1}{E} & 0 \\ 0 & \frac{2}{3}h & 0 & 0 & 0 & -\frac{8}{15}h \frac{2(1+\nu)}{E} \end{bmatrix}. \quad (33)$$

Since the problem (30) is governed by an ODE system with constant coefficients, the homogeneous

solution can be analytically computed. For example, choosing $h = 1$ mm, $l = 10$ mm, $E = 10^5$ MPa, and $\nu = 0.25$, the homogeneous solution is given by

$$\begin{aligned} u_0 &= 5.00 \cdot 10^{-6} C_4 x + C_1, & u_1 &= 4.00 \cdot 10^{-6} C_6 x^2 + 5.00 \cdot 10^{-6} C_5 x + C_2, \\ v &= -(1.33 \cdot 10^{-5} C_6 x^3 + 5.00 \cdot 10^{-6} C_5 x^2 + 5.00 \cdot 10^{-1} C_2 x + C_3) + 10^{-5} C_6 x, \\ \sigma_{x0} &= C_4, & \sigma_{x1} &= 4.00 C_6 x + C_5, & \tau &= C_6, \end{aligned} \tag{34}$$

in which the C_i are arbitrary constants, which may be determined by imposing the boundary conditions specified in (30). Indeed, for the beam model under consideration, the boundary conditions in (30) lead to a set of six linearly independent equations, since the matrix \mathbf{G}_{σ_s} of (19) and (22) is invertible.

We remark that the solution (34) is compatible with the one obtained by the Timoshenko beam model. However, we underline that the stress distributions along the beam axis are obtained directly from the model solution, and not by means of the displacement derivatives, as happens in classical formulations.

We also notice that, reducing the model to the displacement formulation (see (32)), we obtain the ODE system

$$\begin{aligned} h E u_0'' = 0, & \quad \frac{h^3}{12} E u_1'' - \frac{5}{6} \frac{E h}{2(1+\nu)} (v' + u_1) = 0, & \quad \frac{5}{6} \frac{E h}{2(1+\nu)} (v'' + u_1') = 0 \end{aligned} \tag{35}$$

+ suitable boundary conditions.

Not surprisingly, we again recover the classical Timoshenko equations, in which, however, the exact shear correction factor $\frac{5}{6}$ automatically appears. The same result holds true in the framework of variational plate modeling proposed in [Alessandrini et al. 1999].

5.2. Multilayered beam. We now consider a beam composed of n layers, as illustrated in Figure 2. The geometric and material parameters for the generic i -th layer are the thickness h_i , the Young’s modulus E_i , and the Poisson ratio ν_i , collected in the n -dimensional vectors \mathbf{h} , \mathbf{E} , and $\mathbf{\nu}$.

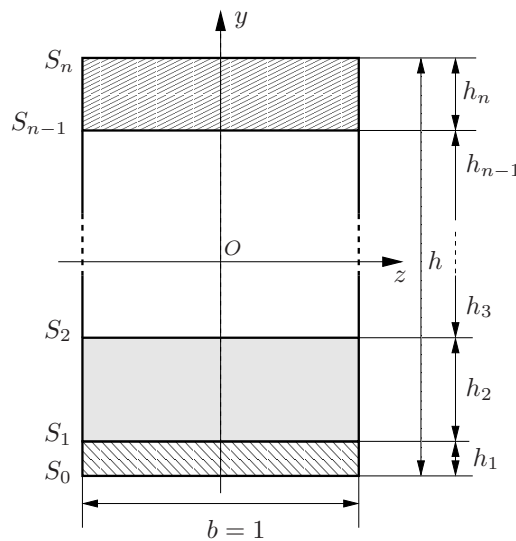


Figure 2. Cross-section geometry, coordinate system, dimensions, and adopted notations.

To design a multilayered beam model, we follow a two-step procedure:

- (1) In each layer, we choose suitable profiles for every field involved in the modeling. Of course, given a generic field, the simplest choice, which we use here, is to use the same profiles for every layer.
- (2) Across each interlayer, we impose the necessary continuity to ensure that the stresses belong to $H(\text{div})$.

As a consequence, given a generic field γ , it is possible to define its profile vector \mathbf{p}_γ , which is characterized by

- the highest polynomial degree with respect to y used in a generic layer, denoted by $\deg \mathbf{p}_\gamma$, and
- regularity across each interlayer: continuity may or may not be required.

Since a main aim of this paper is to develop a model with an accurate stress description, a natural choice is to assume $\deg \mathbf{p}_\tau = 2$, as in Jourawsky theory. To ensure the well-posedness of the resulting model, we select the fields according to Table 2, where we also show the numbers of layer and global DOFs. Furthermore, we notice that we have to impose $\sigma_y = \tau = 0$ at the top and bottom of the beam.

Remark 5.1. More generally, to design a well-posed beam model one could choose

$$\deg \mathbf{p}_{\sigma_x} = \deg \mathbf{p}_u = \deg \mathbf{p}_\tau - 1, \quad \deg \mathbf{p}_\tau = \deg \mathbf{p}_v = \deg \mathbf{p}_{\sigma_y} - 1, \quad (36)$$

together with the $H(\text{div})$ regularity for the stress field.

5.2.1. A test case. We now present an easy case to test the robustness of the model: We consider a *homogeneous* beam, but treat it as if it were formed by three layers. The geometric and material properties are described by:

$$\mathbf{h} = \begin{Bmatrix} 0.300 \\ 0.367 \\ 0.333 \end{Bmatrix} \text{ mm}, \quad \mathbf{E} = \begin{Bmatrix} 10^5 \\ 10^5 \\ 10^5 \end{Bmatrix} \text{ MPa}, \quad \mathbf{v} = \begin{Bmatrix} 0.25 \\ 0.25 \\ 0.25 \end{Bmatrix}.$$

As a consequence, the total number of cross-section variables is 34. The boundary value problem (30) is uniquely solvable in this case. However, now the rank of \mathbf{G} is 22, which means that (30) is actually a differential-algebraic boundary value problem. Thus, 22 variables are solutions of a differential problem, while the remaining 12 unknowns are algebraically determined by the former ones. We also remark that the boundary conditions in (30) actually lead to 22 independent constraints, since $\text{rank}(\mathbf{G}_{\sigma_s}) = 11$.

	$\deg \mathbf{p}_\gamma$	Interlayer continuity	Layer DOFs	Global DOFs
\mathbf{p}_u	1	no	2	$2n$
\mathbf{p}_v	2	no	3	$3n$
\mathbf{p}_{σ_x}	1	no	2	$2n$
\mathbf{p}_{σ_y}	3	yes	4	$3n - 1$
\mathbf{p}_τ	2	yes	3	$2n - 1$

Table 2. Polynomial degrees of the profile vectors, continuity properties, and number of DOFs for a multilayered beam.

We now give the solution of the generalized eigenvalue problem $\det(\lambda \mathbf{G} + \mathbf{H}^{dd}) = 0$, which goes into the construction of the homogeneous solution of (30):

$$\lambda = \begin{matrix} \sim 0 & [6] \\ 11.430 \pm 3.870i & [1] \\ -11.430 \pm 3.870i & [1] \\ 7.481 \pm 2.585i & [1] \\ -7.481 \pm 2.585i & [1] \\ 4.023 \pm 2.520i & [1] \\ -4.023 \pm 2.520i & [1] \\ 15.520 \pm 6.021i & [1] \\ -15.520 \pm 6.021i & [1] \end{matrix}$$

where the numbers on the right are the eigenvalue multiplicities and the notation ~ 0 denotes eigenvalues that vanish up to the machine precision. We notice that the number of eigenvalues (22 in total) corresponds exactly to the rank of \mathbf{G} .

It is also possible to evaluate the homogeneous solution but, given the complexity of the problem, it is huge and we will not report it. Nevertheless it is possible to discuss its structure and make some important remarks:

- The zero eigenvalues lead to polynomial terms analogous to the Timoshenko homogeneous solution described in Section 5.1.
- The complex conjugate eigenvalues ($a \pm ib$) lead to functions like $C_i e^{ax} \sin(bx + C_j)$, which describe local effects near the boundaries, as happens in several other beam models [Ladevèze and Simmonds 1998; Allix and Duplex-Couderc 2009].

6. Numerical multilayered beam model

In this section we develop the FE corresponding to the multilayered beam model introduced in Section 5.2. This is equivalent to introducing a dimension reduction also along the beam axis, which leads to a purely algebraic system. The discretization of the axial fields $\hat{\mathbf{s}}$ and $\hat{\boldsymbol{\sigma}}$ can be generally described by

$$\begin{aligned} \hat{\mathbf{s}}(x) \cong \mathbf{N}_s \tilde{\mathbf{s}} &= \begin{bmatrix} N_u(x) & \mathbf{0} \\ \mathbf{0} & N_v(x) \end{bmatrix} \begin{Bmatrix} \tilde{\mathbf{u}} \\ \tilde{\mathbf{v}} \end{Bmatrix}, & \hat{\boldsymbol{\sigma}}(x) \cong \mathbf{N}_\sigma \tilde{\boldsymbol{\sigma}} &= \begin{bmatrix} N_{\sigma_x}(x) & \mathbf{0} & \mathbf{0} \\ \mathbf{0} & N_{\sigma_y}(x) & \mathbf{0} \\ \mathbf{0} & \mathbf{0} & N_\tau(x) \end{bmatrix} \begin{Bmatrix} \tilde{\boldsymbol{\sigma}}_x \\ \tilde{\boldsymbol{\sigma}}_y \\ \tilde{\boldsymbol{\tau}} \end{Bmatrix}, \\ \hat{\mathbf{s}}'(x) \cong \mathbf{B}_s \tilde{\mathbf{s}} &= \begin{bmatrix} N'_u(x) & \mathbf{0} \\ \mathbf{0} & N'_v(x) \end{bmatrix} \begin{Bmatrix} \tilde{\mathbf{u}} \\ \tilde{\mathbf{v}} \end{Bmatrix}, & \hat{\boldsymbol{\sigma}}'(x) \cong \mathbf{B}_\sigma \tilde{\boldsymbol{\sigma}} &= \begin{bmatrix} N'_{\sigma_x}(x) & \mathbf{0} & \mathbf{0} \\ \mathbf{0} & N'_{\sigma_y}(x) & \mathbf{0} \\ \mathbf{0} & \mathbf{0} & N'_\tau(x) \end{bmatrix} \begin{Bmatrix} \tilde{\boldsymbol{\sigma}}_x \\ \tilde{\boldsymbol{\sigma}}_y \\ \tilde{\boldsymbol{\tau}} \end{Bmatrix}. \end{aligned} \tag{37}$$

From now on, for notational simplicity, we will drop the explicit dependency on x for fields.

6.1. Weak problem formulation. We now make explicit the weak formulation we will use as a starting point for the FE discretization. To this end, we first recall the beam model variational formulation (26). Then, we integrate by parts with respect to the x direction both the first and third terms of (26). We thus

obtain: Find $\hat{\mathbf{s}} \in \tilde{W}$ and $\hat{\boldsymbol{\sigma}} \in \tilde{S}$ such that, for every $\delta\hat{\mathbf{s}} \in \tilde{W}$ and for every $\delta\hat{\boldsymbol{\sigma}} \in \tilde{S}$,

$$\delta J_{\text{HR}} = \int_l (\delta\hat{\mathbf{s}}'^T \mathbf{G}_{s\sigma} \hat{\boldsymbol{\sigma}} - \delta\hat{\mathbf{s}}^T \mathbf{H}_{s\sigma'} \hat{\boldsymbol{\sigma}} + \delta\hat{\boldsymbol{\sigma}}^T \mathbf{G}_{\sigma s} \hat{\mathbf{s}}' - \delta\hat{\boldsymbol{\sigma}}^T \mathbf{H}_{\sigma' s} \hat{\mathbf{s}} - \delta\hat{\boldsymbol{\sigma}}^T \mathbf{H}_{\sigma\sigma} \hat{\boldsymbol{\sigma}}) dx - \delta\hat{\mathbf{s}}^T \mathbf{T}_x|_{x=\bar{l}} = 0, \quad (38)$$

where $\tilde{W} := \{\hat{\mathbf{s}} \in H^1(l) : \hat{\mathbf{s}}|_{x=0} = \mathbf{0}\}$ and $\tilde{S} := L^2(l)$.

Notice that all the derivatives with respect to x are applied to displacement variables, whereas the derivatives with respect to y (incorporated into the \mathbf{H} matrices) are applied to cross-section stress vectors. The resulting variational formulation has the following features:

- The obtained weak formulation (38) is symmetric.
- y -derivatives applied to stresses and the essential conditions of S_t^{dd} (see Section 3.2.2) most likely lead to a formulation which accurately solves the equilibrium equation in the y direction, that is, in the cross-section.
- x derivatives applied to displacements and the essential condition in \tilde{W} most likely lead to a formulation which accurately solves the compatibility equation along the beam axis.

The FE discretization simply follows from the application of (37) to the variational formulation (38):

$$\delta J_{\text{HR}} = \int_l (\delta\tilde{\mathbf{s}}^T \mathbf{B}_s^T \mathbf{G}_{s\sigma} \mathbf{N}_\sigma \tilde{\boldsymbol{\sigma}} - \delta\tilde{\mathbf{s}}^T \mathbf{N}_s^T \mathbf{H}_{s\sigma'} \mathbf{N}_\sigma \tilde{\boldsymbol{\sigma}} + \delta\tilde{\boldsymbol{\sigma}}^T \mathbf{N}_\sigma^T \mathbf{G}_{\sigma s} \mathbf{B}_s \tilde{\mathbf{s}}') dx - \int_l (\delta\tilde{\boldsymbol{\sigma}}^T \mathbf{N}_\sigma^T \mathbf{H}_{\sigma' s} \mathbf{N}_s \tilde{\mathbf{s}} + \delta\tilde{\boldsymbol{\sigma}}^T \mathbf{N}_\sigma^T \mathbf{H}_{\sigma\sigma} \mathbf{N}_\sigma \tilde{\boldsymbol{\sigma}}) dx - \delta\tilde{\mathbf{s}}^T \mathbf{N}_s^T \mathbf{T}_x|_{x=\bar{l}} = 0. \quad (39)$$

Collecting unknown coefficients in a vector and requiring (39) to be satisfied for all possible virtual fields we obtain

$$\begin{bmatrix} \mathbf{0} & \mathbf{K}_{s\sigma} \\ \mathbf{K}_{\sigma s} & \mathbf{K}_{\sigma\sigma} \end{bmatrix} \begin{Bmatrix} \tilde{\mathbf{s}} \\ \tilde{\boldsymbol{\sigma}} \end{Bmatrix} = \begin{Bmatrix} \tilde{\mathbf{T}} \\ \mathbf{0} \end{Bmatrix}, \quad (40)$$

where

$$\mathbf{K}_{s\sigma} = \mathbf{K}_{\sigma s}^T = \int_l (\mathbf{B}_s^T \mathbf{G}_{s\sigma} \mathbf{N}_\sigma - \mathbf{N}_s^T \mathbf{H}_{s\sigma'} \mathbf{N}_\sigma) dx, \quad \mathbf{K}_{\sigma\sigma} = - \int_l \mathbf{N}_\sigma^T \mathbf{H}_{\sigma\sigma} \mathbf{N}_\sigma dx, \quad \tilde{\mathbf{T}} = \mathbf{N}_s^T \mathbf{T}_x|_{x=\bar{l}}.$$

In what follows we will focus, for all variables involved, on the finite element spaces shown in Table 3; we also recall the profile properties which have led to the multilayered beam model. For the polynomial degrees and continuity requirements we use the same notation as in Section 5.2. Thus, for example, the field v is approximated by means of piecewise cubic polynomials, continuous along the axial direction.

	deg p_γ	y continuity	deg N_γ	x continuity
u	1	no	2	yes
v	2	no	3	yes
σ_x	1	no	1	no
σ_y	3	yes	3	no
τ	2	yes	2	no

Table 3. Degree and continuity properties of shape functions with respect to the y and x directions.

We remark that this choice of the FE shape functions assures the stability and convergence of the resulting discrete scheme. We also notice that the stresses are discontinuous across elements along the x direction, so that it is possible to statically condensate them out at the element level, reducing the dimension of the global stiffness matrix and improving efficiency.

6.2. Multilayered homogeneous beam. We now consider the same three layer homogeneous beam of Section 5.2.1. Together with the clamping condition in A_0 , we assume that $\bar{l} = 10$ mm and the beam is loaded along A_l by the quadratic shear stress distribution $\mathbf{t}|_{A_l} = [0, 3/2(1 - 4y^2)]^T$ MPa.

6.2.1. Convergence. In Table 4 we report on the mean value of the transverse displacement along A_l , as obtained by employing (a) the classical Euler–Bernoulli beam model; (b) the classical Timoshenko beam model; (c) the numerical model under investigation, in which the solution is computed using a mesh of 64 elements; (d) a 2D FE scheme in ABAQUS, using a fine regular grid of 3500×350 elements.

Due to the large number of elements used, we consider the latter solution as the reference solution, and we denote with v_{ex} its mean value along A_l .

In Table 4 we also report the relative error, defined by

$$e_{\text{rel}} = \frac{|v - v_{\text{ex}}|}{|v_{\text{ex}}|}, \tag{41}$$

where v is the mean value along A_l computed by the various procedures. This e_{rel} gives an indication of the accuracy of the model, even though it is not the usual error measure in terms of the natural norms.

Table 4 shows the superior performance of the three-layered mixed FE with respect to the other 1D models considered.

In Figure 3 we study the convergence of our numerical model. More precisely, we plot the relative quantity defined in (41), evaluated considering different mesh sizes δ in the x direction, and i layers of thickness $h_i = 1/i$, for $i = 1, 3, 5, 7$. From Figure 3a we notice that:

- using even a few elements the quantity e_{rel} is under 1%;
- the error e_{rel} decreases as the number of layers increases;
- using a highly refined mesh, the relative error e_{rel} increases, even as it apparently converges to a constant close to 10^{-3} . This behavior can be explained by recalling that a modeling error necessarily arises. Indeed, the solution of the 2D elastic problem and the solution of the multilayered beam mixed model do differ from each other, for a fixed length and thickness of the beam.

Beam theory	v [10^{-2} mm]	e_{rel} [10^{-3}]
Euler–Bernoulli	4.000000	6.192
Timoshenko	4.030000	1.261
Three-layered mixed FE	4.026460	0.382
2D solution	4.024924	

Table 4. Transverse displacements and relative errors of the free edge of a cantilever ($\bar{l} = 10$ mm and $h = 1$ mm) obtained by different beam theories.

In Figure 3b we consider another relative quantity, e_{rel}^* , similar to that defined in (41), but using as the reference solution the one obtained by FE analysis of the multilayered model using the most refined x -direction mesh. We notice that: the sequences of errors e_{rel}^* converge monotonically to zero; and for a fixed number of layers, the log-log plots of errors suggest a convergence rate of the order of α , with $\alpha \approx 1$.

Finally, in Figure 3c we plot the relative error e_{rel} versus the number of layers (with the results obtained using a mesh of 32 elements). It is evident that the relative error decreases when incrementing the number of layers even if the succession is not linear.

6.2.2. Boundary effects. As already noticed in Section 5.2.1, the model under investigation is capable of capturing some local effects near the clamped boundary; we here present some results focused on that issue. Even though this study is far from being exhaustive, it gives an indication of the model's potential. In what follows the computations are performed using a mesh of 64 elements. To highlight the boundary

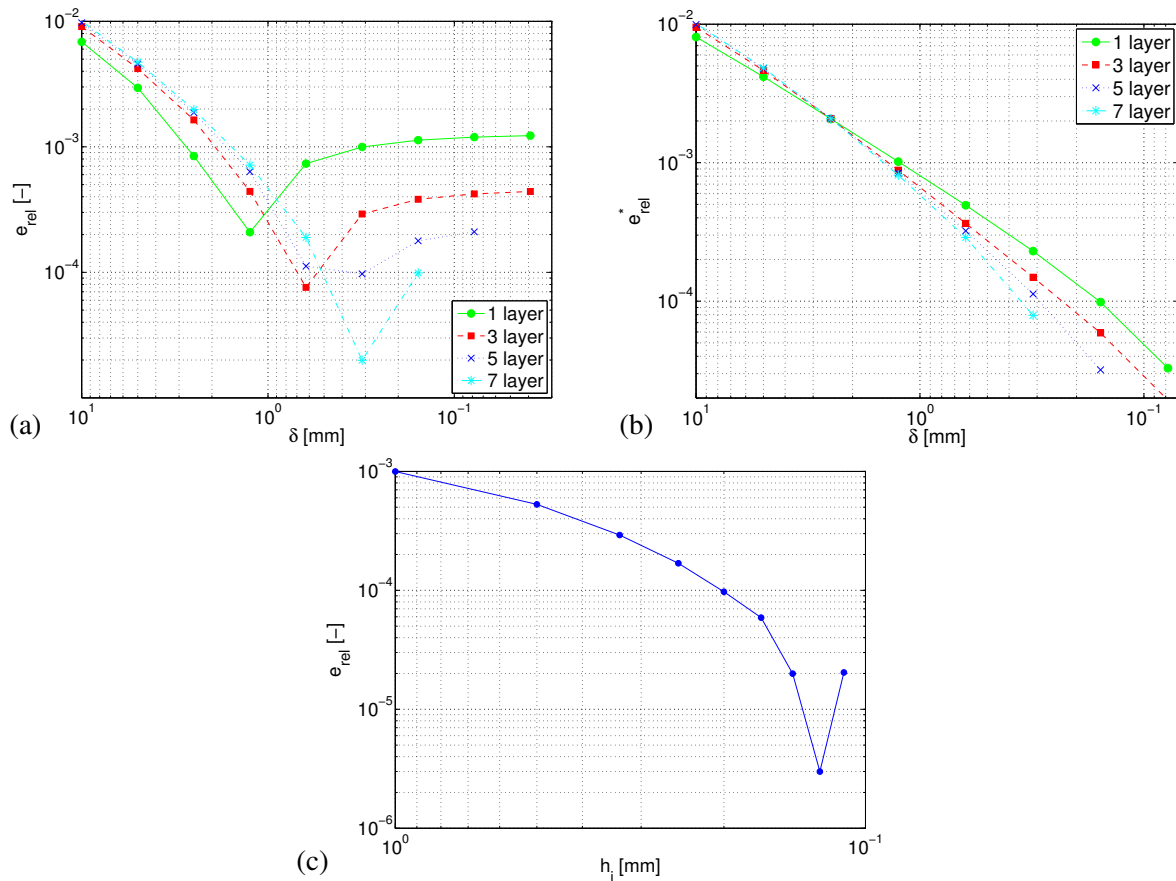


Figure 3. Relative errors on free-edge and transverse displacement for different mesh sizes δ and different numbers of layers. (a) Relative error e_{rel} , evaluated assuming v_{ex} is the 2D numerical solution. (b) Relative error e_{rel}^* , evaluated assuming v_{ex} is the 1D numerical solution obtained using the most refined x -direction mesh. (c) Relative error, plotted as a function of the layer thickness h_i , with mesh size $\delta = 0.3125$ mm.

effects we consider a beam analogous to the one introduced at the beginning of Section 6.2 in which we set $\bar{l} = 2.5$ mm. The results are reported in Figures 4, 5, and 6. We can appreciate the following:

- Far from the boundary, it is possible to recognize the classical beam solution: constant shear stress $\tau(x)$, linear axial stress $\sigma_x(x)$, quadratic horizontal displacement $u(x)$, and cubic transverse displacement $v(x)$.
- As expected, boundary effects decay as damped harmonic functions.
- The local effects decay very rapidly, so that only the first oscillation is significant. This result is consistent with the other models capable of capturing these kind of boundary effects.

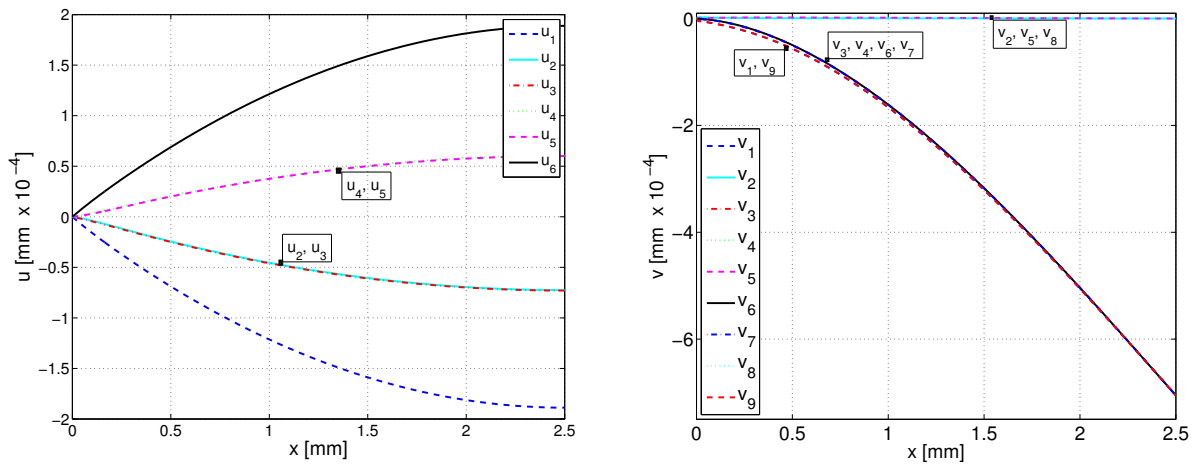


Figure 4. Axial displacements \hat{u} (left) and transverse displacements \hat{v} (right) as functions of x for a three-layer homogeneous cantilever, clamped at $x = 0$, loaded at $x = 2.5$ by a quadratic shear distribution, and modeled with 64 elements.

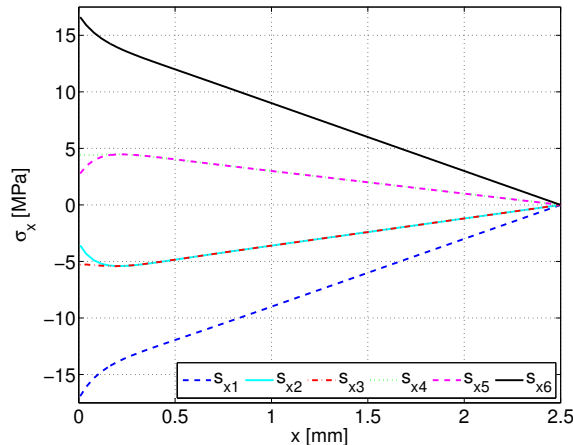


Figure 5. Axial stress $\hat{\sigma}_x(x)$ of a three-layer homogeneous cantilever, clamped at $x = 0$, loaded at $x = 2.5$ by a quadratic shear distribution, and modeled with 64 elements.

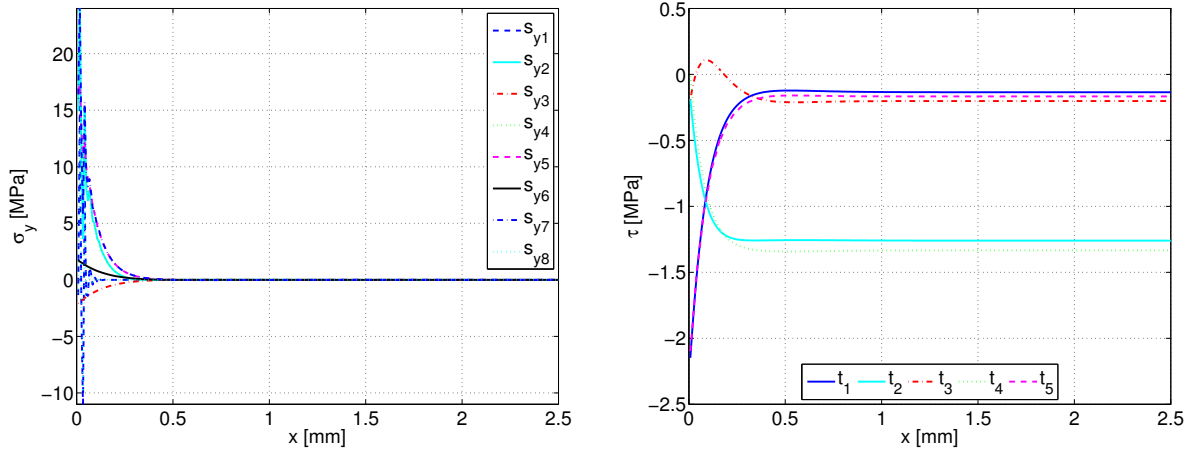


Figure 6. Transverse compressive stress $\hat{\sigma}_y$ (left) and shear stress $\hat{\tau}$ (right) as functions of x for a three-layer homogeneous cantilever, clamped at $x = 0$, loaded at $x = 2.5$ by a quadratic shear distribution, and modeled with 64 elements.

- Section striction, described by the quadratic displacement terms v_2 , v_5 , and v_8 , is negligible, as assumed in first-order theories.

As specified in Table 3, in the numerical model under discussion we do not a priori impose displacement continuity across layers. In Figure 7 we plot the jump of the displacement field across the interlayer surfaces S_1 and S_2 . Figure 7, right, highlights that the transverse displacement jump rapidly decays far from the clamped boundary. On the other hand, from the left half of the figure we see that, far from the clamped boundary, the axial displacement jump $|u(x)^+ - u(x)^-|$ tends to a value different from zero (of the order of 10^{-7} mm). However, we notice that the displacement field is much greater, since it is of the order of 10^{-4} mm.

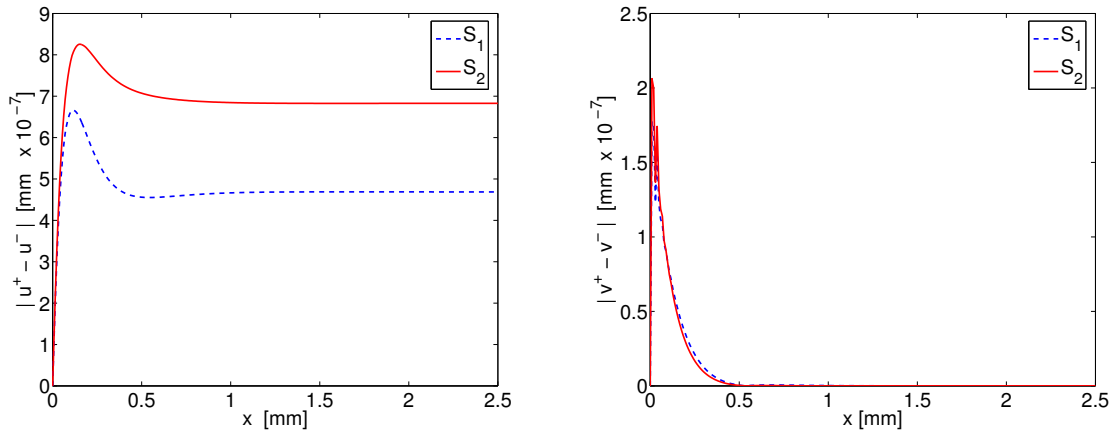


Figure 7. Compatibility mismatches on interlayer surfaces $y = -\frac{1}{5}$ (labeled S_1) and $y = \frac{1}{6}$ (S_2): axial displacement jump $|u(x)^+ - u(x)^-|$ (left) and transverse displacement jump $|v(x)^+ - v(x)^-|$ (right).

6.3. Multilayered nonhomogeneous beams. We now consider two nonhomogeneous beams, focusing particularly on the cross-section stress distributions, since such quantities are only seldom accurately captured in classical beam models.

6.3.1. Symmetric section. Figure 8 plots the stress distributions at different sections ($x = 2.5, 0.5,$ and 0.125) calculated for a cantilever composed of three layers, clamped at A_0 , for which $\bar{l} = 5$ mm and

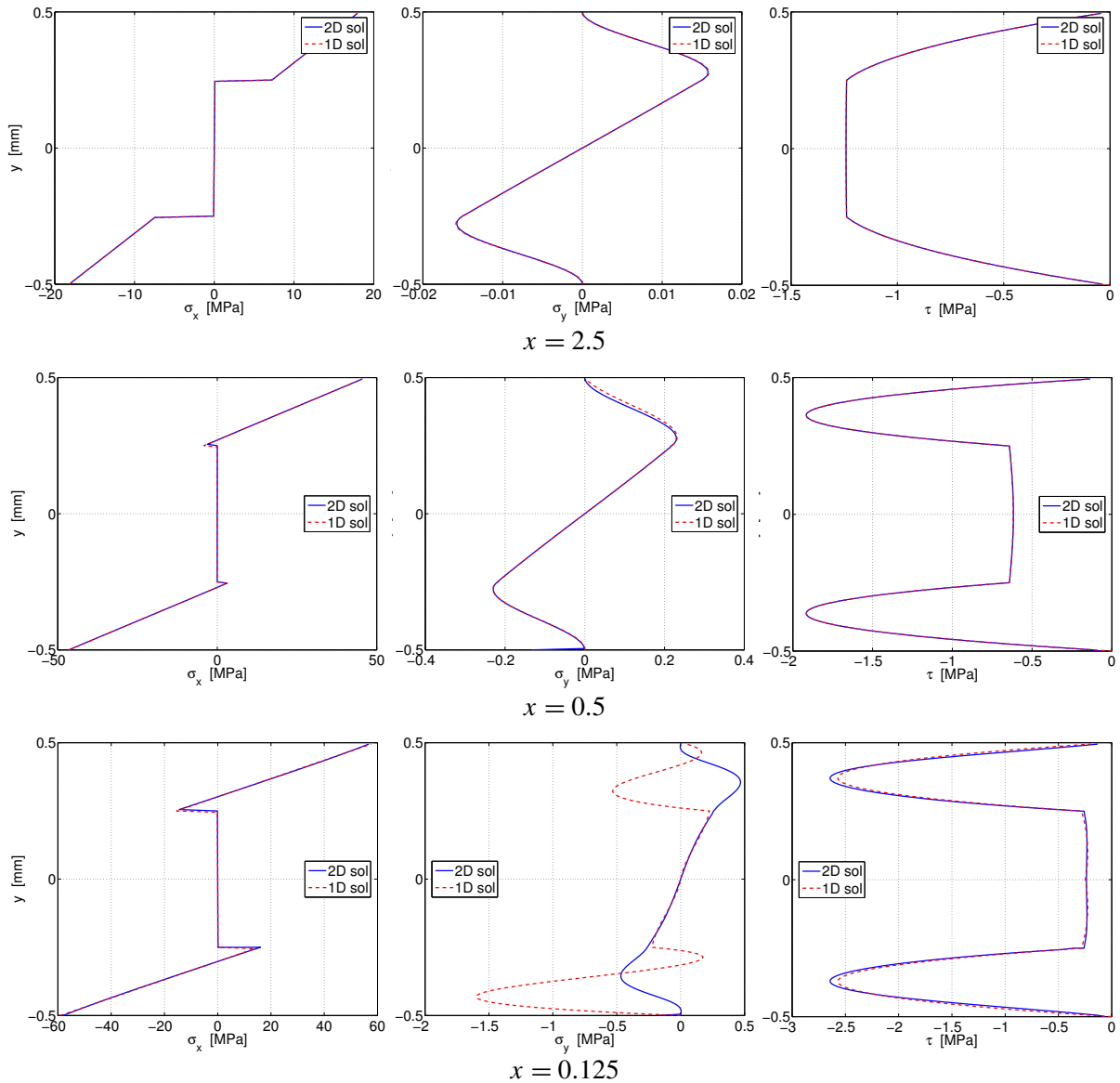


Figure 8. Cross-section stresses σ_x (left), σ_y (middle), and τ (right), as functions of y : one- and two-dimensional solutions for the symmetric section. Three cross-sections are considered, at various distances from the clamped boundary: far ($x = -2.5$, top), close ($x = 0.5$, middle), and very close ($x = 0.125$, bottom).

$t|_{A_I} = [0, \frac{3}{2}(1-4y^2)]^T$ MPa, and whose geometry and mechanical properties are specified by

$$\mathbf{h} = \begin{Bmatrix} 0.25 \\ 0.50 \\ 0.25 \end{Bmatrix} \text{ mm}, \quad \mathbf{E} = \begin{Bmatrix} 1 \cdot 10^5 \\ 1 \cdot 10^3 \\ 1 \cdot 10^5 \end{Bmatrix} \text{ MPa}, \quad \mathbf{v} = \begin{Bmatrix} 0.25 \\ 0.25 \\ 0.25 \end{Bmatrix}.$$

The solution of the 1D model was evaluated with a mesh size of $\delta = 0.15625$ mm (32 elements), and the 2D solution using ABAQUS with a mesh of 200×1000 square elements.

The ability of the numerical model to reproduce the stress distribution very accurately, far from the clamped boundary, is clearly seen from the top row of Figure 8. A similar feature is also maintained close to the clamped boundary (middle and bottom rows), even though some error progressively arises as we approach $x = 0$. In particular, the axial stress σ_x and the shear stress τ are very accurately described, whereas the σ_y approximation exhibits a worse performance (maybe also because some kind of instability arises; see Figure 6, left).

6.3.2. Nonsymmetric section. Figure 9 plots the stress distributions at the section $x = 2.5$ calculated for a cantilever composed of four layers, clamped at A_0 , for which $\bar{l} = 5$ mm and $t = \dots$ and whose geometric and mechanical properties of the section are specified by

$$\mathbf{h} = \begin{Bmatrix} 0.25 \\ 0.25 \\ 0.25 \\ 0.25 \end{Bmatrix} \text{ mm}, \quad \mathbf{E} = \begin{Bmatrix} 1 \cdot 10^5 \\ 1 \cdot 10^3 \\ 1 \cdot 10^5 \\ 1 \cdot 10^3 \end{Bmatrix} \text{ MPa}, \quad \mathbf{v} = \begin{Bmatrix} 0.25 \\ 0.25 \\ 0.25 \\ 0.25 \end{Bmatrix}.$$

We evaluate the 1D and 2D solutions using the same meshes as for the symmetric case just discussed.

As in the symmetric case, there is no significant difference between the 1D and the 2D cross-section stress distributions. We only notice a small deviation (below 1%) in the plot of σ_y .

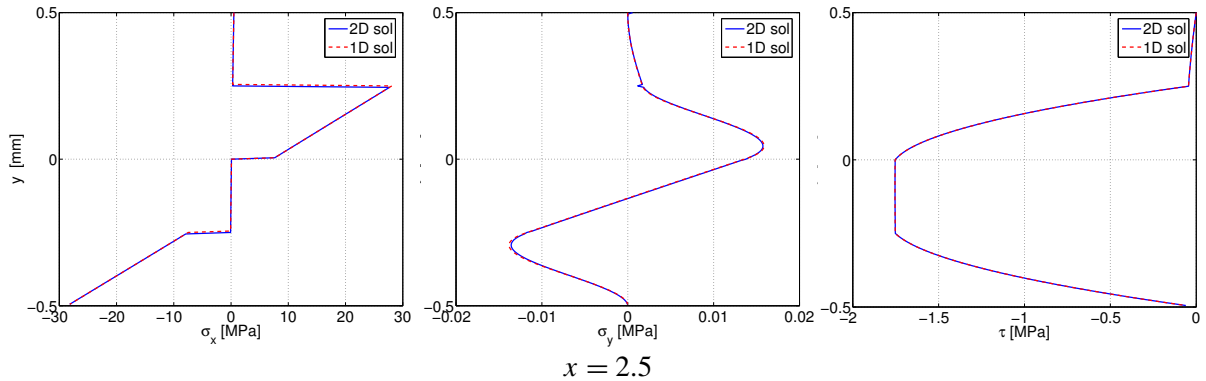


Figure 9. Cross-section stresses σ_x (left), σ_y (middle), and τ (right), as functions of y : one- and two-dimensional solutions for the nonsymmetric section.

7. Conclusions

In this paper we developed planar beam models based on dimension reduction by a variational approach. More precisely, we selected a suitable variational formulation among the ones available in the literature.

Our choice of the variational principle was motivated by the need to accurately describe the stress profiles. In Sections 4 and 5 we gave the general derivation of the beam models, together with a couple of examples. In Section 6 we focused on the multilayered model introduced in Section 5, for which we developed an efficient finite element scheme, as assessed by the presented numerical results.

Future developments of this work could include rigorous mathematical study of the models, generalization to 3D beams with variable cross-section, and the treatment of more sophisticated constitutive laws.

References

- [Alessandrini et al. 1999] S. M. Alessandrini, D. N. Arnold, R. S. Falk, and A. L. Madureira, “Derivation and justification of plate models by variational methods”, pp. 1–20 in *Plates and shells* (Quebec, 1996), edited by M. Fortin, CRM Proc. Lecture Notes **21**, Amer. Math. Soc., Providence, RI, 1999.
- [Allix and Dupleix-Couderc 2009] O. Allix and C. Dupleix-Couderc, “A plate theory as a mean to compute precise 3D solutions including edge effects and related issues”, *New Trends in Thin Structures* **519** (2009), 1–28.
- [Auricchio and Sacco 1999] F. Auricchio and E. Sacco, “A mixed-enhanced finite-element for the analysis of laminated composite plates”, *Int. J. Numer. Methods Eng.* **44** (1999), 1481–1504.
- [Auricchio et al. 2004] F. Auricchio, C. Lovadina, and A. L. Madureira, “An asymptotically optimal model for isotropic heterogeneous linearly elastic plates”, *M2AN Math. Model. Numer. Anal.* **38**:5 (2004), 877–897.
- [Carrera 2000] E. Carrera, “Assessment of mixed and classical theories on global and local response of multilayered orthotropic plates”, *Compos. Struct.* **50** (2000), 183–198.
- [Carrera 2001] E. Carrera, “Developments, ideas and evaluations based upon Reissner’s mixed variational theorem in the modeling of multilayered plates and shells”, *Applied Mechanics Review* **54** (2001), 301–329.
- [Carrera and Demasi 2002] E. Carrera and L. Demasi, “Classical and advanced multilayered plate elements based upon PVD and RMVT, I: derivation of finite element matrices”, *Int. J. Numer. Methods Eng.* **55**:2 (2002), 191–231.
- [Demasi 2009a] L. Demasi, “Mixed plate theories based on the generalized unified formulation, I: governing equations”, *Compos. Struct.* **87** (2009), 1–11.
- [Demasi 2009b] L. Demasi, “Mixed plate theories based on the generalized unified formulation, II: layerwise theories”, *Compos. Struct.* **87** (2009), 12–22.
- [Demasi 2009c] L. Demasi, “Mixed plate theories based on the generalized unified formulation, III: advanced mixed high order shear deformation theories”, *Compos. Struct.* **87** (2009), 183–194.
- [Demasi 2009d] L. Demasi, “Mixed plate theories based on the generalized unified formulation, IV: zig-zag theories”, *Compos. Struct.* **87** (2009), 195–205.
- [Demasi 2009e] L. Demasi, “Mixed plate theories based on the generalized unified formulation, V: results”, *Compos. Struct.* **88** (2009), 1–16.
- [Feng and Hoa 1998] W. Feng and S. V. Hoa, “Partial hybrid finite elements for composite laminates”, *Finite Elem. Anal. Des.* **30** (1998), 365–382.
- [Hjelmstad 2005] K. D. Hjelmstad, *Fundamentals of structural mechanics*, Springer, 2005.
- [Huang et al. 2002] Y. Huang, S. Di, C. Wu, and H. Sun, “Bending analysis of composite laminated plates using a partially hybrid stress element with interlaminar continuity”, *Comput. Struct.* **80** (2002), 403–410.
- [Icardi and Atzori 2004] U. Icardi and A. Atzori, “Simple, efficient mixed solid element for accurate analysis of local effects in laminated and sandwich composites”, *Adv. Engng. Software* **35** (2004), 843–859.
- [Ladevèze and Simmonds 1998] P. Ladevèze and J. Simmonds, “New concepts for linear beam theory with arbitrary geometry and loading”, *Eur. J. Mech. A Solids* **17**:3 (1998), 377–402.
- [Lo et al. 1977a] K. H. Lo, R. M. Christensen, and E. M. Wu, “A high order theory for plate deformations, I: homogeneous plates”, *J. Appl. Mech. (ASME)* **44** (1977), 663–668.

- [Lo et al. 1977b] K. H. Lo, R. M. Christensen, and E. M. Wu, “A high order theory for plate deformations, II: laminated plates”, *J. Appl. Mech. (ASME)* **44** (1977), 669–676.
- [Reddy 1984] J. N. Reddy, “A simple higher-order theory of laminated composite plates”, *ASME, Journal of Applied Mechanics of Composite Materials* **51** (1984), 745–752.
- [Reissner 1986] E. Reissner, “On a variational theorem and on shear deformable plate theory”, *Int. J. Numer. Methods Eng.* **23** (1986), 193–198.
- [Rohwer and Rolfes 1998] K. Rohwer and R. Rolfes, “Calculating 3D stresses in layered composite plates and shells”, *Mech. Compos. Mater.* **34** (1998), 355–362.
- [Rohwer et al. 2005] K. Rohwer, S. Friedrichs, and C. Wehmeyer, “Analyzing laminated structures from fiber-reinforced composite material — an assessment”, *Tech. Mech.* **25** (2005), 59–79.
- [Sheinman 2001] I. Sheinman, “On the analytical closed-form solution of high-order kinematic models in laminated beam theory”, *Int. J. Numer. Methods Eng.* **50** (2001), 919–936.
- [Spilker 1982] R. L. Spilker, “Hybrid-stress eight-node elements for thin and thick multilayer laminated plates”, *Int. J. Numer. Methods Eng.* **18** (1982), 801–828.
- [Timoshenko 1955] S. Timoshenko, *Strength of materials, I: elementary theory and problems*, 3rd ed., Van Nostrand, New York, 1955.
- [Vinayak et al. 1996a] R. U. Vinayak, G. Prathap, and B. P. Naganarayana, “Beam elements based on a higher order theory, I: formulation and analysis of performance”, *Comput. Struct.* **58** (1996), 775–789.
- [Vinayak et al. 1996b] R. U. Vinayak, G. Prathap, and B. P. Naganarayana, “Beam elements based on a higher order theory, II: boundary layer sensitivity and stress oscillations”, *Comput. Struct.* **58** (1996), 791–796.
- [Wanji and Zhen 2008] C. Wanji and W. Zhen, “A selective review on recent development of displacement-based laminated plate theories”, *Recent Patents Mech. Engng.* **1** (2008), 29–44.

Received 3 Dec 2009. Revised 1 Jun 2010. Accepted 16 Jun 2010.

FERDINANDO AURICCHIO: auricchio@unipv.it

Dipartimento di Meccanica Strutturale, Università degli Studi di Pavia, Via Ferrata 1, 27100 Pavia, Italy
<http://www.unipv.it/auricchio/>

GIUSEPPE BALDUZZI: giuseppe.balduzzi@unipv.it

Dipartimento di Meccanica Strutturale / Dipartimento di Matematica, Università degli Studi di Pavia, Via Ferrata 1, 27100 Pavia, Italy
<http://www-2.unipv.it/compmech/members/giuseppebalduzzi.html>

CARLO LOVADINA: carlo.lovadina@unipv.it

Dipartimento di Matematica, Università degli Studi di Pavia, Via Ferrata 1, 27100 Pavia, Italy
<http://www-dimat.unipv.it/lovadina/>

SIFS OF RECTANGULAR TENSILE SHEETS WITH SYMMETRIC DOUBLE EDGE DEFECTS

XIANGQIAO YAN, BAOLIANG LIU AND ZHAOHUI HU

Tensile sheets with symmetrically placed cracks on opposite edges are studied using the displacement discontinuity method with crack-tip elements. Three cases are considered: a rectangular sheet, one with half-circle indentations on the cracked edges, and one with notch indentations. Solutions for the stress intensity factors (SIFs) of the three problems are given, revealing the effect of the geometric parameters. By comparing the three cases, one observes that the indentations have a shielding effect.

1. Introduction

In plates with holes under the action of fatigue loading, crack initiation is most likely at the hole edges due to stress concentration around the hole. Consequently, a number of papers have dealt with hole edge crack problems. Bowie [1956] gave solutions for a circular hole with a single edge crack and a pair of symmetrical edge cracks in a plate under tension. Newman [1971], using the boundary collocation method, and Murakami [1978], using the body force method, analyzed the tension problem for an elliptical hole with symmetrical edge cracks. Tweed and Rooke [1973] used the Mellin transform technique to make analyses of biaxial tensions for a branching crack emanating from a circle hole. Isida and Nakamura [1980] made an analysis of a slant crack emanating from an elliptical hole under uniaxial tension and shear at infinity by using the body force method.

Here we consider the related problem of rectangular tensile sheets with symmetric double edge defects, in the shapes illustrated in Figure 1. In [Yan 2003a] we proposed a method, based on the displacement

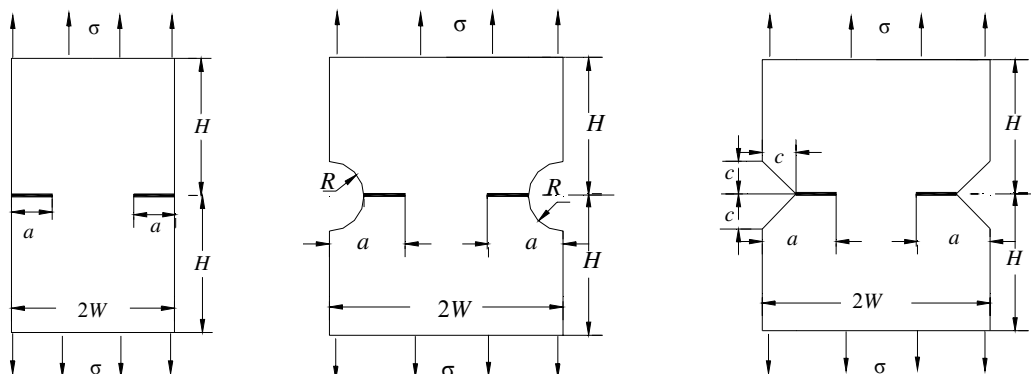


Figure 1. Rectangular tensile sheet with symmetric cracks emanating from straight edges (left), from half-circle indentations (middle), and from half-square notches (right).

Keywords: double edge defects, stress intensity factors, edge crack, half-circular indentation, half-square indentation. Special thanks to the National Natural Science Foundation of China for supporting the present work (grant #10272037).

discontinuity method with crack-tip elements, for the analysis of general plane elastic crack problems. It was found in that paper, as well as in subsequent ones such as [Yan 2003b; 2006a; 2006b], that this method is accurate and effective for analyzing such problems.

We therefore use this method to perform a numerical analysis of the problem involving the shapes in Figure 1, focusing specifically on the stress intensity factors (SIFs). Murakami [1987] reported the SIFs for the plane elastic crack problems shown in the first two cases (simple crack and crack in semicircle indentation) when the aspect ratio H/W is large (narrow strip); but to our knowledge, detailed solutions to the SIFs for this geometry have not been obtained when H/W is less than 2. The same reference also reports the solutions to the SIFs of cracks emanating from a square hole in infinite plate in tension.

The effect of the geometric parameters of the cracked bodies on the SIFs is discussed for all three cases, and it is found that the half-circle and notch indentations have a shielding effect on the SIFs. The study illustrates the use of the boundary element method, which proves to be simply and accurate for calculating the SIFs of complex crack problems in a finite plate.

2. Brief description of the boundary element method

We briefly review the method introduced in [Yan 2003a], which in turn is based on [Crouch and Starfield 1983]. In this latter reference, the displacement discontinuity

$$D_x = u_x(x, 0_-) - u_x(x, 0_+), \quad D_y = u_y(x, 0_-) - u_y(x, 0_+), \quad (1)$$

defined as the difference in displacement between the two sides of the segment, is used to solve for the displacements, which take on the values

$$\begin{aligned} u_x &= D_x(2(1-\nu)F_3(x, y) - yF_5(x, y)) + D_y(-(1-2\nu)F_2(x, y) - yF_4(x, y)), \\ u_y &= D_x((1-2\nu)F_2(x, y) - yF_4(x, y)) + D_y(2(1-\nu)F_3(x, y) + yF_5(x, y)), \end{aligned} \quad (2)$$

and the stresses, whose values are

$$\begin{aligned} \sigma_{xx} &= 2GD_x(2F_4(x, y) + yF_6(x, y)) + 2GD_y(-F_5(x, y) + yF_7(x, y)), \\ \sigma_{yy} &= 2GD_x(-yF_6(x, y)) + 2GD_y(-F_5(x, y) - yF_7(x, y)), \\ \sigma_{xy} &= 2GD_x(-F_5(x, y) + yF_7(x, y)) + 2GD_y(-yF_6(x, y)), \end{aligned} \quad (3)$$

In these equations, G is the shear modulus and ν the Poisson's ratio; the functions F_2 through F_7 are described in [Crouch and Starfield 1983].

By using (2) and (3), we gave formulas in [Yan 2003a] for the left and right crack-tip displacement discontinuity elements. For the left crack-tip, the displacement discontinuity functions are chosen as

$$D_x = H_s \left(\frac{a_{\text{tip}} + \xi}{a_{\text{tip}}} \right)^{1/2}, \quad D_y = H_n \left(\frac{a_{\text{tip}} + \xi}{a_{\text{tip}}} \right)^{1/2}, \quad (4)$$

where H_s and H_n are the tangential and normal displacement discontinuities at the center of the element, and a_{tip} is half the length of crack-tip element. Note that the element has the same unknowns as the two-dimensional constant displacement discontinuity element. We have shown that the displacement discontinuity functions in (4) can model the displacement fields around the crack tip. The stress field determined by the displacement discontinuity functions (4) has an $r^{-1/2}$ singularity around the crack tip.

Based on (2) and (3), the displacements at a point (x, y) due to the left crack-tip displacement discontinuity element can be obtained as

$$\begin{aligned} u_x &= H_s(2(1-\nu)B_3(x, y) - yB_5(x, y)) + H_n(-(1-2\nu)B_2(x, y) - yB_4(x, y)), \\ u_y &= H_s((1-2\nu)B_2(x, y) - yB_4(x, y)) + H_n(2(1-\nu)B_3(x, y) + yB_5(x, y)), \end{aligned} \quad (5)$$

and the stresses as

$$\begin{aligned} \sigma_{xx} &= 2GH_s(2B_4(x, y) + yB_6(x, y)) + 2GH_n(-B_5(x, y) + yB_7(x, y)), \\ \sigma_{yy} &= 2GH_s(-yB_6(x, y)) + 2GH_n(-B_5(x, y) - yB_7(x, y)), \\ \sigma_{xy} &= 2GH_s(-B_5(x, y) + yB_7(x, y)) + 2GH_n(-yB_6(x, y)), \end{aligned} \quad (6)$$

where the functions B_2 through B_7 are described in [Yan 2003a].

Implementation of the numerical approach. The objective of many analyses of linear elastic crack problems is to obtain the stress intensity factors K_I and K_{II} . Crouch and Starfield [1983] used relations (2) and (3) to set up the constant displacement discontinuity boundary element method. Similarly, we can use (5) and (6) to set up boundary element equations associated with the crack-tip elements. The constant displacement discontinuity element together with the crack-tip elements is combined to form a very effective numerical approach for calculating the SIFs of general plane cracks. In the boundary element implementation, the left or the right crack-tip element is placed locally at the corresponding left or right crack tip on top of the constant displacement discontinuity elements that cover the entire crack surface and the other boundaries. This is called the displacement discontinuity method with crack-tip elements. Based on the displacement field around the crack tip, we can write

$$K_I = -\frac{\sqrt{2\pi}GH_n}{4(1-\nu)\sqrt{a_{\text{tip}}}}, \quad K_{II} = -\frac{\sqrt{2\pi}GH_s}{4(1-\nu)\sqrt{a_{\text{tip}}}}, \quad (7)$$

3. Numerical results and discussion

We report here the results of SIF calculations for the plane elastic crack problems of Figure 1. We start with the simple rectangular plate (left in the figure), taking the following ratios:

$$\begin{aligned} a/W &= 0.1, 0.2, 0.3, 0.4, 0.5, 0.6, 0.7 \\ H/W &= 0.4, 0.5, 0.6, 0.7, 0.8, 0.9, 1.0, 1.2, 1.5, 2.0 \end{aligned}$$

Regarding discretization, 30 boundary elements with of equal size, $a/30$, on the right edge crack are discretized and the other boundaries are discretized according to the limitation that all boundary elements have approximately the same length [Yan 2003a]. The calculated SIFs normalized by $\sigma\sqrt{\pi a}$ are given in Table 1. For comparison, the table also lists the numerical results reported in [Murakami 1987], with which our numerical results are in good agreement.

Table 1 makes it clear that one must consider the effect of H/W on the SIF:

- (1) For a shallow defect ($a/W = 0.1$) the SIF with a $H/W = 0.4$ (low aspect ratio) is 16% larger than that when $H/W = 2$.

a/W	H/W										liter.
	0.4	0.5	0.6	0.7	0.8	0.9	1.0	1.2	1.5	2.0	
0.1	1.2902	1.2344	1.2007	1.1773	1.1596	1.1459	1.1356	1.1228	1.1154	1.1129	–
0.2	1.6499	1.4900	1.3879	1.3139	1.2576	1.2142	1.1820	1.1425	1.1193	1.1123	1.118
0.3	2.0845	1.8093	1.6213	1.4813	1.3750	1.2959	1.2386	1.1700	1.1305	1.1183	1.120
0.4	2.5464	2.1422	1.8537	1.6393	1.4834	1.3719	1.2943	1.2045	1.1536	1.1377	1.132
0.5	2.9943	2.4333	2.0329	1.7521	1.5611	1.4315	1.3449	1.2478	1.1937	1.1765	1.163
0.6	3.3400	2.5980	2.1104	1.8006	1.6046	1.4792	1.3979	1.3090	1.2603	1.2446	1.226
0.7	3.3959	2.5553	2.0776	1.8032	1.6406	1.5410	1.4782	1.4107	1.3739	1.3618	1.343

Table 1. Normalized SIFs for the rectangular plate in Figure 1, left. Literature values on the last column, taken from [Murakami 1987], refer to a high value of H/W .

- (2) As a/W increases, this effect becomes more obvious. For $a/W = 0.6$, for example, the SIF when $H/W = 0.4$ is 2.68 times the one when $H/W = 2.0$. But when H/W is larger than 2 this effect is negligible regardless of the size of a/W , which perhaps is the reason for taking $H/W = 2$ in calculating the SIFs of crack problems in finite width plates [Newman 1971].

Cracks emanating from half-circle indentations. Two sorts of experiments are reported for the geometry shown in Figure 1, middle. First, we consider a crack that is much larger than the corresponding indentation, to approximate the situation just discussed, where the crack emanates from a straight edge. For example, if we take

$$H/W = 1, \quad a/R = 7, \quad a/W = 0.5,$$

we expect that the effect of the half-circle indentation on the SIFs will be negligible. For the discretization, the number of boundary elements on a quarter-circle is taken as 50 and the other boundaries are discretized according to the limitation that all boundary elements have approximately the same length. The calculated SIF normalized by $\sigma\sqrt{\pi a}$ is 1.3200, which is indeed close to the corresponding value (1.3449) listed in Table 1.

Secondly, we systematically vary the three relevant ratios to study their effect on the SIF. The following cases are considered:

$$\begin{aligned} a/R &= 1.02, 1.04, 1.06, 1.08, 1.1, 1.15, 1.2, 1.5, 2.0 \\ H/W &= 0.5, 0.6, 0.7, 0.8, 0.9, 1.0, 1.5, 2.0 \\ a/W &= 0.2, 0.3, 0.4, 0.5, 0.6, 0.7 \end{aligned}$$

For the discretization, the number of boundary elements on a quarter-circle is chosen according to a/R as follows:

a/R	1.02	1.04	1.06	1.08	1.1	1.15	1.2	1.5	2.0
# elements	250	200	167	175	160	133	100	100	50

The other boundaries are discretized so that all boundary elements have approximately the same length. The calculated SIFs normalized by $\sigma\sqrt{\pi a}$ are given in Table 2.

To study the effect of the half-circle indentations on the SIF, we compare the numbers in Table 2 with those in Table 1. Recall that Table 1 corresponds to a ratio $a/R = \infty$. We find that, as a/R increases

H/W	a/R									
	1.02	1.04	1.06	1.08	1.1	1.15	1.2	1.5	2.0	
$a/W = 0.2$	0.5	0.5949	0.8122	0.9541	1.0511	1.1284	1.2528	1.3298	1.4469	1.4701
	0.6	0.5526	0.7558	0.8883	0.9796	1.0523	1.1700	1.2413	1.3525	1.3719
	0.7	0.5211	0.7141	0.8402	0.9270	0.9969	1.1093	1.1774	1.2835	1.3008
	0.8	0.4969	0.6822	0.8029	0.8866	0.9532	1.0620	1.1282	1.2304	1.2469
	0.9	0.4782	0.6575	0.7743	0.8555	0.9204	1.0263	1.0905	1.1899	1.2053
	1.0	0.4645	0.6394	0.7533	0.8327	0.8959	0.9994	1.0625	1.1599	1.1745
$a/W = 0.3$	0.5	0.7321	0.9937	1.1663	1.2812	1.3765	1.5247	1.6161	1.7600	1.7909
	0.6	0.6507	0.8856	1.0396	1.1452	1.2298	1.3648	1.4478	1.5776	1.6036
	0.7	0.5903	0.8048	0.9449	1.0430	1.1202	1.2453	1.3231	1.4440	1.4669
	0.8	0.5446	0.7441	0.8747	0.9664	1.0393	1.1566	1.2291	1.3437	1.3628
	0.9	0.5113	0.7000	0.8233	0.9107	0.9793	1.0915	1.1598	1.2689	1.2859
	1.0	0.4879	0.6688	0.7870	0.8707	0.9366	1.0447	1.1102	1.2150	1.2303
	1.5	0.4460	0.6128	0.7214	0.7987	0.8593	0.9589	1.0192	1.1146	1.1264
	2.0	0.4410	0.6063	0.7139	0.7903	0.8505	0.9491	1.0088	1.1028	1.1147
$a/W = 0.4$	0.5	0.8732	1.1806	1.3870	1.5282	1.6393	1.8193	1.9272	2.0990	2.1327
	0.6	0.7429	1.0081	1.1843	1.3076	1.4034	1.5606	1.6565	1.8100	1.8400
	0.7	0.6459	0.8792	1.0362	1.1444	1.2318	1.3731	1.4594	1.5988	1.6266
	0.8	0.5782	0.7898	0.9309	1.0307	1.1089	1.2385	1.3178	1.4467	1.4704
	0.9	0.5334	0.7293	0.8591	0.9525	1.0249	1.1454	1.2195	1.3405	1.3614
	1.0	0.5038	0.6896	0.8125	0.9006	0.9692	1.0834	1.1531	1.2672	1.2852
	1.5	0.4567	0.6254	0.7358	0.8151	0.8762	0.9779	1.0388	1.1373	1.1491
	2.0	0.4518	0.6189	0.7280	0.8060	0.8664	0.9665	1.0267	1.1224	1.1338
$a/W = 0.5$	0.5	0.9212	1.2521	1.4940	1.6714	1.8128	2.0510	2.1822	2.4130	2.4433
	0.6	0.7921	1.0827	1.2809	1.4204	1.5301	1.7130	1.8200	1.9978	2.0276
	0.7	0.6683	0.9162	1.0847	1.2040	1.2989	1.4577	1.5532	1.7128	1.7420
	0.8	0.5889	0.8088	0.9573	1.0637	1.1479	1.2893	1.3763	1.5232	1.5500
	0.9	0.5413	0.7428	0.8787	0.9759	1.0531	1.1827	1.2618	1.3967	1.4212
	1.0	0.5123	0.7029	0.8301	0.9218	0.9933	1.1144	1.1879	1.3134	1.3351
	1.5	0.4748	0.6489	0.7625	0.8441	0.9066	1.0110	1.0731	1.1755	1.1887
	2.0	0.4721	0.6449	0.7573	0.8374	0.8990	1.0013	1.0619	1.1603	1.1723
$a/W = 0.6$	0.6	0.7403	1.0268	1.2295	1.3895	1.5211	1.7382	1.8682	2.0894	2.1171
	0.7	0.6480	0.8978	1.0726	1.2013	1.3038	1.4778	1.5852	1.7667	1.7958
	0.8	0.5810	0.8028	0.9553	1.0669	1.1560	1.3078	1.4028	1.5664	1.5955
	0.9	0.5455	0.7505	0.8889	0.9905	1.0703	1.2066	1.2921	1.4419	1.4694
	1.0	0.5273	0.7226	0.8535	0.9476	1.0225	1.1478	1.2262	1.3632	1.3887
	1.5	0.5124	0.6964	0.8150	0.8993	0.9638	1.0695	1.1335	1.2391	1.2549
2.0	0.5132	0.6965	0.8143	0.8974	0.9606	1.0642	1.1260	1.2261	1.2401	
$a/W = 0.7$	0.7	0.6090	0.8397	1.0073	1.1430	1.2497	1.4436	1.5626	1.7776	1.8041
	0.8	0.5915	0.8125	0.9648	1.0772	1.1676	1.3259	1.4251	1.6063	1.6353
	0.9	0.5851	0.7958	0.9366	1.0383	1.1182	1.2570	1.3442	1.5041	1.5331
	1.0	0.5849	0.7905	0.9246	1.0198	1.0938	1.2200	1.2984	1.4429	1.4701
	1.5	0.5961	0.7983	0.9248	1.0115	1.0768	1.1824	1.2450	1.3507	1.3686
	2.0	0.5990	0.8022	0.9283	1.0147	1.0791	1.1821	1.2428	1.3413	1.3568

Table 2. Normalized SIFs for rectangular plate with semicircle cutout (Figure 1, middle).

from 1.02 to 2, the SIF increases monotonously regardless of the value of a/W . When a/R reaches 2, the SIF almost equals its asymptotic value in Table 1. This suggests the following observations:

- (1) The half-circle indentations have a shielding effect on the edge cracks.
- (2) The closer the depth of the indentations is to the overall defect size (that is, the lower a/R is), the larger the shielding effect.
- (3) When a/R is more than 2, meaning that the crack itself is longer than the characteristic size of the indentation, the shielding effect can be neglected.

Cracks emanating from half-square notches. We next turn to the geometry in Figure 1, right, varying the three relevant ratios to study their effect on the SIF. The following cases are considered:

$$\begin{aligned} a/c &= 1.02, 1.04, 1.06, 1.08, 1.1, 1.15, 1.2, 1.5, 2.0 \\ H/W &= 0.5, 0.6, 0.7, 0.8, 0.9, 1.0, 1.5, 2.0 \\ a/W &= 0.2, 0.3, 0.4, 0.5, 0.6, 0.7 \end{aligned}$$

For the discretization, the number of boundary elements on a side of the notch is chosen according to a/c as follows:

a/c	1.02	1.04	1.06	1.08	1.1	1.15	1.2	1.5	2.0
# elements	250	200	167	175	160	133	100	100	50

The other boundaries are discretized so that all boundary elements have approximately the same length. The calculated SIFs normalized by $\sigma\sqrt{\pi a}$ are given in Table 3.

As in the previous subsection, we compare these numbers with those on Table 1, and see that as a/c increases from 1.02 to 2, the SIF increases monotonously regardless of the value of a/W . When a/c reaches 2, the SIF almost equals its asymptotic value in Table 1. To summarize:

- (1) The half-square notches have a shielding effect on the edge cracks.
- (2) The closer the notch depth is to the overall defect size (that is, the lower a/c is), the larger the shielding effect.
- (3) When a/c is more than 2, meaning that the crack itself is longer than the characteristic size of the notch, the shielding effect can be neglected.

Comparison between effects of half-circle and half-square indentations. We briefly compare the results for the two indented geometries: half-circle indentations versus half-square notches. Figure 2 shows the evolution of the SIF with the size of the indentation relative to the crack size, for both geometries, in two particular cases: when case $a/W = 0.2$ and $H/W = 0.5$, and when $a/W = 0.5$ and $H/W = 1.0$. We see that the shielding effect of the half-circle indentations is much stronger effect than for the notches, in agreement with the expectation that a geometry with a sharp concave angle is more vulnerable to the stress concentration effect.

H/W	a/R									
	1.02	1.04	1.06	1.08	1.1	1.15	1.2	1.5	2.0	
$a/W = 0.2$	0.5	1.3537	1.3919	1.4164	1.4240	1.4356	1.4479	1.4582	1.4595	1.4667
	0.6	1.2663	1.3018	1.3240	1.3313	1.3417	1.3530	1.3614	1.3631	1.3683
	0.7	1.2023	1.2360	1.2570	1.2636	1.2742	1.2844	1.2918	1.2928	1.2975
	0.8	1.1533	1.1858	1.2054	1.2119	1.2209	1.2312	1.2386	1.2389	1.2435
	0.9	1.1156	1.1471	1.1659	1.1721	1.1811	1.1910	1.1977	1.1979	1.2021
	1.0	1.0878	1.1184	1.1368	1.1429	1.1512	1.1607	1.1674	1.1675	1.1713
$a/W = 0.3$	0.5	1.6376	1.6881	1.7173	1.7270	1.7428	1.7583	1.7707	1.7759	1.7842
	0.6	1.4729	1.5157	1.5407	1.5503	1.5634	1.5777	1.5879	1.5924	1.5987
	0.7	1.3503	1.3905	1.4125	1.4216	1.4326	1.4442	1.4542	1.4571	1.4630
	0.8	1.2577	1.2942	1.3146	1.3227	1.3335	1.3439	1.3521	1.3552	1.3594
	0.9	1.1892	1.2237	1.2426	1.2507	1.2598	1.2698	1.2768	1.2792	1.2826
	1.0	1.1399	1.1725	1.1905	1.1980	1.2065	1.2161	1.2223	1.2243	1.2274
	1.5	1.0478	1.0773	1.0934	1.1000	1.1075	1.1155	1.1209	1.1218	1.1236
	2.0	1.0364	1.0656	1.0818	1.0880	1.0958	1.1037	1.1090	1.1096	1.1117
$a/W = 0.4$	0.5	1.9434	2.0042	2.0405	2.0545	2.0723	2.0924	2.1037	2.1141	2.1182
	0.6	1.6795	1.7304	1.7633	1.7720	1.7900	1.8074	1.8180	1.8266	1.8320
	0.7	1.4872	1.5329	1.5595	1.5700	1.5829	1.5980	1.6088	1.6149	1.6216
	0.8	1.3501	1.3898	1.4125	1.4224	1.4332	1.4473	1.4563	1.4619	1.4667
	0.9	1.2533	1.2905	1.3107	1.3202	1.3298	1.3418	1.3500	1.3544	1.3587
	1.0	1.1868	1.2212	1.2402	1.2487	1.2577	1.2689	1.2757	1.2795	1.2828
	1.5	1.0700	1.0999	1.1158	1.1231	1.1299	1.1386	1.1436	1.1453	1.1466
	2.0	1.0561	1.0856	1.1014	1.1081	1.1152	1.1237	1.1287	1.1296	1.1312
$a/W = 0.5$	0.5	2.2054	2.2793	2.3213	2.3445	2.3649	2.3896	2.3990	2.4169	2.4140
	0.6	1.8419	1.9018	1.9372	1.9535	1.9698	1.9895	2.0001	2.0111	2.0128
	0.7	1.5843	1.6354	1.6656	1.6776	1.6933	1.7106	1.7211	1.7305	1.7344
	0.8	1.4123	1.4567	1.4827	1.4938	1.5068	1.5226	1.5329	1.5406	1.5459
	0.9	1.2998	1.3394	1.3619	1.3728	1.3836	1.3976	1.4068	1.4139	1.4183
	1.0	1.2265	1.2628	1.2830	1.2931	1.3024	1.3149	1.3232	1.3292	1.3331
	1.5	1.1061	1.1368	1.1532	1.1611	1.1682	1.1772	1.1825	1.1850	1.1864
	2.0	1.0925	1.1227	1.1387	1.1460	1.1530	1.1618	1.1668	1.1683	1.1698
$a/W = 0.6$	0.6	1.8981	1.9675	2.0061	2.0293	2.0482	2.0720	2.0819	2.0961	2.0928
	0.7	1.6192	1.6749	1.7088	1.7256	1.7413	1.7612	1.7715	1.7827	1.7838
	0.8	1.4430	1.4910	1.5201	1.5334	1.5477	1.5655	1.5761	1.5866	1.5897
	0.9	1.3339	1.3770	1.4028	1.4141	1.4271	1.4431	1.4526	1.4623	1.4664
	1.0	1.2674	1.3068	1.3293	1.3402	1.3510	1.3651	1.3744	1.3825	1.3866
	1.5	1.1659	1.1983	1.2155	1.2239	1.2317	1.2416	1.2473	1.2509	1.2529
2.0	1.1553	1.1867	1.2039	1.2116	1.2189	1.2281	1.2338	1.2358	1.2375	
$a/W = 0.7$	0.7	1.6035	1.6654	1.7015	1.7240	1.7415	1.7652	1.7765	1.7901	1.7886
	0.8	1.4669	1.5193	1.5506	1.5668	1.5825	1.6026	1.6135	1.6262	1.6277
	0.9	1.3856	1.4320	1.4589	1.4734	1.4863	1.5041	1.5146	1.5265	1.5295
	1.0	1.3371	1.3804	1.4045	1.4168	1.4285	1.4444	1.4539	1.4646	1.4679
	1.5	1.2720	1.3065	1.3247	1.3339	1.3422	1.3525	1.3598	1.3641	1.3667
	2.0	1.2654	1.2990	1.3168	1.3253	1.3332	1.3431	1.3493	1.3524	1.3548

Table 3. Normalized SIFs for Double Edge Half-Square-Hole Cracks ($a/W = 0.7$)

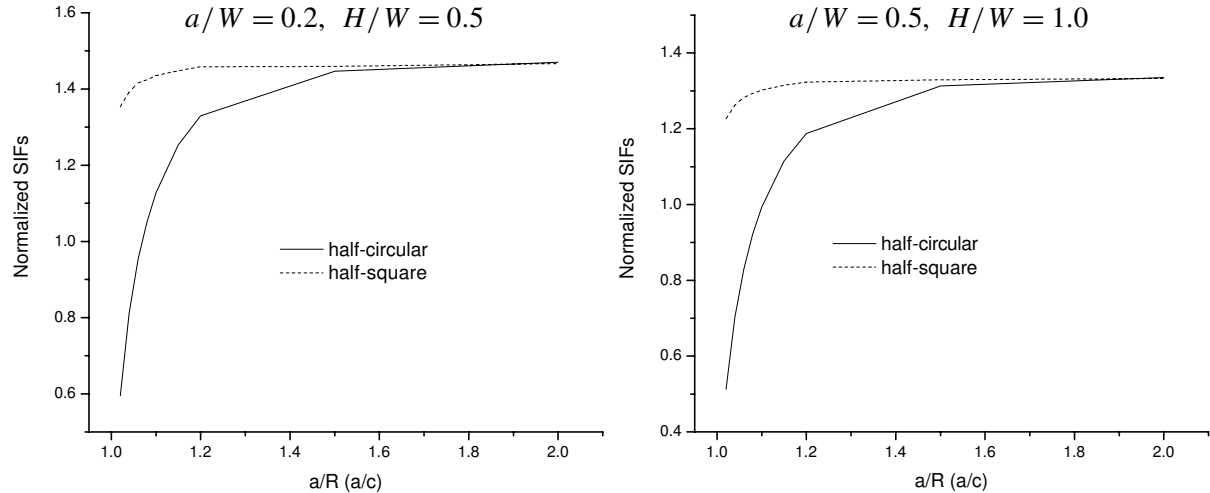


Figure 2. Effect of half-circle and half-square indentations on the SIF, for representative choices of the parameters a/W and H/W .

4. Conclusions

A numerical analysis of double edge defects in rectangular plates in tension (Figure 1) was performed, and the stress intensity factors calculated for a variety of values of the geometric parameters. By comparing the calculated SIFs for the three geometries, it was found that the presence of an indentation at the base of the crack has a shielding effect, lowering the SIF. The effect is more pronounced when the indentation is a half-circle than when it is a half-square notch. The shielding effect gradually decreases with the size of the indentation; When the characteristic size (depth) of the indentation is less than the length of the crack proper (that is, the ratio a/R or a/c in Figure 1 exceeds 2), the effect becomes negligible.

This study illustrates how the displacement discontinuity method with crack-tip elements can be of value in calculating SIFs for complex crack problems involving a finite plate.

References

- [Bowie 1956] O. L. Bowie, "Analysis of an infinite plate containing radial cracks originating at the boundary of an internal circular hole", *J. Math. Phys. (MIT)* **35** (1956), 60–71.
- [Crouch and Starfield 1983] S. L. Crouch and A. M. Starfield, *Boundary element methods in solid mechanics: with applications in rock mechanics and geological engineering*, Allen & Unwin, London, 1983.
- [Isida and Nakamura 1980] M. Isida and Y. Nakamura, "Edge cracks originating from an elliptical hole in a wide plate subjected to tension and in-plane shear", *Trans. Jpn. Soc. Mech. Eng. A* **46**:409 (1980), 947–956. In Japanese.
- [Murakami 1978] Y. Murakami, "A method of stress intensity factor calculation for the crack emanating from an arbitrarily shaped hole or the crack in the vicinity of an arbitrarily shaped hole", *Trans. Jpn. Soc. Mech. Eng.* **44**:378 (1978), 423–432. In Japanese.
- [Murakami 1987] Y. Murakami (editor), *Stress intensity factors handbook*, Pergamon, Oxford, 1987.
- [Newman 1971] J. C. Newman, Jr., "An improved method of collocation for the stress analysis of cracked plates with various shaped boundaries", NASA Technical Note TN D-6376, Langley Research Center, Hampton, VA, 1971, available at <http://hdl.handle.net/2060/19710022830>.

- [Tweed and Rooke 1973] J. Tweed and D. P. Rooke, "The distribution of stress near the tip of a radial crack at the edge of a circular hole", *Int. J. Eng. Sci.* **11**:11 (1973), 1185–1195.
- [Yan 2003a] X. Yan, "Analysis of the interference effect of arbitrary multiple parabolic cracks in plane elasticity by using a new boundary element method", *Comput. Methods Appl. Mech. Eng.* **192**:47–48 (2003), 5099–5121.
- [Yan 2003b] X. Yan, "An effective method of stress intensity factor calculation for cracks emanating from a triangular or square hole under biaxial loads", *Fatigue Fract. Eng. Mater. Struct.* **26**:12 (2003), 1127–1133.
- [Yan 2006a] X. Yan, "Cracks emanating from circular hole or square hole in rectangular plate in tension", *Eng. Fract. Mech.* **73**:12 (2006), 1743–1754.
- [Yan 2006b] X. Yan, "A numerical analysis of cracks emanating from an elliptical hole in a 2-D elasticity plate", *Eur. J. Mech. A Solids* **25**:1 (2006), 142–153.

Received 6 Dec 2009. Revised 31 May 2010. Accepted 10 Jun 2010.

XIANGQIAO YAN: yanxiangqiao@hotmail.com

Research Laboratory on Composite Materials, Harbin Institute of Technology, Harbin 150001, China

BAOLIANG LIU: baoliangliu2008@163.com

Research Laboratory on Composite Materials, Harbin Institute of Technology, Harbin 150001, China

ZHAOHUI HU: zhaohuihu@163.com

Research Laboratory on Composite Materials, Harbin Institute of Technology, Harbin 150001, China

A NONLINEAR MODEL OF THERMOELASTIC BEAMS WITH VOIDS, WITH APPLICATIONS

YING LI AND CHANG-JUN CHENG

We generalize the traditional Hamilton principle and give a complete nonlinear mathematical model of thermoelastic beams with voids based on this generalization, including the influences of the axial force, neutral layer inertia and rotation inertia. The differential quadrature method is used to discretize the nonlinear system on the spatial domain, and the Newton–Raphson method and Runge–Kutta method are adopted to solve the static and dynamical behaviors of the beam, respectively. The influences of the parameters on the nonlinear mechanical behavior of beam are studied in detail. The results show that the presence of voids enlarges beam deflection. And also one can see that the DQM has advantages of fewer workload, higher precision, better convergence, and so on.

1. Introduction

Thermoelastic materials with voids, which are common in various types of geological, biological and synthetic materials, are of practical utility in both structural and functional forms. Porous materials have extensive applications in aerospace, electronic communications, construction, metallurgy, nuclear energy, petrochemical, mechanical, medical and environmental protection due to their advantageous properties, such as low relative density, high specific strength and surface area, light weight, thermal and acoustical insulation and good permeability [Xi 2007].

Cowin and Nunziato [1983] proposed a linear theory of elastic materials with voids, which has practical utility for investigating various types of porous materials. Their theory is concerned with elastic materials consisting of a distribution of small voids, in which the void volume is included among the kinematic variables, and the theory reduces to the classical theory of elasticity in the limit case of the volume tending to zero. Iesan [1986] developed a linear theory of thermoelastic materials with voids. Puri and Cowin [1985] studied the behavior of plane waves in linear elastic materials with voids. Chiriță and Scalia [2001] considered the spatial and temporal behaviors in linear thermoelasticity of materials with voids. Scalia et al. [2004] studied the steady time-harmonic oscillation in thermoelastic materials with voids. Chiriță and Ciarletta [2008] discussed the structural stability of thermoelastic model of porous media. Cicco and Diaco [2002] developed a theory of thermoelastic materials with voids without energy dissipation. Ciarletta et al. [2007] studied thermoporoacoustic acceleration waves in elastic materials with voids without energy dissipation. Singh [2007] studied the wave propagation in a generalized

Keywords: generalized Hamilton variational principle, thermoelastic beam with voids, differential quadrature method, nonlinear mechanical behavior.

Work supported by Shanghai Leading Academic Discipline Project (S30106) and Innovation Fund for Graduate of Shanghai University.

thermoelastic material with voids. Kumar and Rani [2005] investigated the dynamic response of a homogeneous, isotropic, thermoelastic half-space with voids subjected to time harmonic normal force and thermal source.

In [Sheng and Cheng 2004; Cheng et al. 2006], the Gurtin-type variational principles of viscoelastic Timoshenko beams and thick plates with damage were established, damage being regarded as voids in materials. These works also studied quasistatic problems of viscoelastic beams and dynamical behaviors of viscoelastic plates. Bîrsan [2003] presented a bending theory of porous thermoelastic plates. Sharma et al. [2008] investigated the three-dimensional vibration of a thermoelastic cylindrical panel with voids.

As one kind of the most basic structural components, beams are widely applied to engineering and science, for example, bridges and beam-column systems of constructions, nanoscale bioprobes and piezoelectric devices, heat exchanger tubes in production equipment, titanium alloy artificial bones. Besides, rockets, missiles and other flying slender cylindrical structures can be approximated as a free-free beam to study the dynamical response and failure analysis under transient dynamical loads [Yu et al. 1996]. The structural elements mentioned above, which may be thermoelastic materials with voids, might be subject to a variety of static loads and external excitations, such as mechanical forces, seismic waves, shock waves, aerodynamic forces, thermal and nonthermal loads, etc. Therefore, it is very important to present a suitable nonlinear mathematical model of thermoelastic beams with voids.

For the linear thermoelastodynamics, there exist plenty of papers for variational principles and solving methods. Zhang [2007] presented a Gurtin-type variational formulation for functionally graded thermoviscoelastic beams by using the convolution bilinear form and the classical cartesian bilinear form. But for the thermoelastic problems with geometric nonlinearity, there are two difficulties to set up the corresponding Hamilton variational principles:

- (1) The terms with the first-order time-derivative in the equation for the balance of entropy are not potential operators.
- (2) The traditional Hamilton principle is used to characterize dynamical problems at the initial and final time.

Luo et al. [2002] presented unconventional Hamilton-type variational principles for nonlinear thermoelastodynamics, which can characterize this kind of the initial-boundary-value problems. However, there are seldom reports for the variational principles and numerical methods of thermoelastic beams with both voids and geometric nonlinearity.

In this paper, the traditional Hamilton principle is first generalized, a complete finite deformation theory of thermoelastic beams with voids is presented from the generalized Hamilton principle, in which, the influences of the axial force, neutral layer and rotation inertia are all considered. The theory exhibits a set of nonlinear equations about three displacements, one void moment and one thermal moment. As application, the plane bending of beams is studied. To improve the computational efficiency and accuracy, the differential quadrature method (DQM) is used to discrete the nonlinear system on the spatial domain, then the Newton–Raphson method and Runge–Kutta method are adopted to calculate and analyze the static and dynamical response of nonlinear systems of thermoelastic beams with voids, respectively. The mechanical behavior of beams is investigated under four cases, that is, thermoelastic materials with/without voids and elastic materials with/without voids. The influences of the parameters are studied in detail.

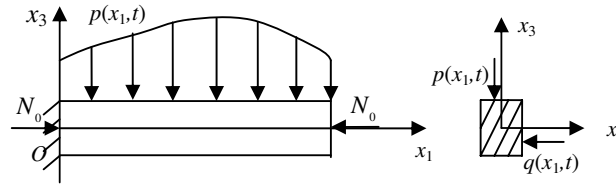


Figure 1. Model of a beam.

2. Basic equations of thermoelastic beams with voids

Consider a beam subjected to distributed transverse loads, as in Figure 1. Assume the beam’s cross-section is uniform, the length is l , the width is b , and the thickness is h . Choose the x_1 -axis so it contains the center of the section, the x_2 - and x_3 -axes as the orthogonal principal axes of the cross-section. Assume the displacements of the neutral axis are $u_i(x_1, t)$, for $i = 1, 2, 3$; we call $u_3(x_1, t)$ the deflection. Based on the Kirchhoff–Love hypothesis and finite deformation theory, we have the nonlinear geometry relations

$$\varepsilon_{11} = \varepsilon_{11}^0 - x_2 u_{2,11} - x_3 u_{3,11}, \quad \varepsilon_{11}^0 = u_{1,1} + (u_{2,1})^2/2 + (u_{3,1})^2/2, \tag{1}$$

where ε_{11} is the total strain component and ε_{11}^0 is the strain component along the neutral axis.

Following the theory presented in [Iesan 1986], the basic equations for thermoelastic materials with voids are given tensorially as follows:

$$\rho \ddot{u}_i = \sigma_{ji,j} + \rho f_i \quad \text{and} \quad \rho \chi \ddot{\varphi} = h_{i,i} + g + \rho l \tag{2}$$

are the equations of balance of linear momentum and equilibrated force, where σ_{ij} is the symmetric stress tensor, f_i is the body force vector, ρ is the density in the reference configuration, φ is the change in the volume fraction field, χ is the equilibrated inertia, h_i is the equilibrated stress vector, g is the intrinsic equilibrated body force, and ρl is the extrinsic equilibrated body force;

$$\rho T_0 \dot{\eta} = q_{i,i} + \rho S \tag{3}$$

is the equation for the balance of entropy, where S and η are the entropy and the external heat supply per unit initial mass, while q_i and T_0 are the heat flux and the absolute temperature in the reference configuration; and

$$\begin{aligned} \sigma_{11} &= D_0 \varepsilon_{11} + b_v \varphi - \beta \theta, & g &= -b_v \varepsilon_{11} - \xi_v \varphi + m_v \theta, \\ h_i &= \alpha_v \varphi_{,i}, & \rho \eta &= \beta \varepsilon_{11} + m_v \varphi + (\rho c_e / T_0) \theta, & q_i &= K \theta_{,i} \end{aligned} \tag{4}$$

are the constitutive relations of isotropic thermoelastic beams with voids, where K the thermal conductivity, c_e the specific heat at the constant strain, σ_{11} be the beam’s bending stress, $\alpha_v, b_v, \xi_v, m_v$ are parameters of the voids, θ denotes the absolute temperature with T_0 subtracted, D_0 is given by

$$D_0 = \frac{E(1 - \nu)}{(1 + \nu)(1 - 2\nu)}, \tag{5}$$

in which E, ν are the elastic modulus and Poisson’s ratio, and finally $\beta = \alpha_t E / (1 - 2\nu)$, where α_t is the linear expansion coefficient.

3. The Hamilton principle and mathematical model of thermoelastic beams with voids

In order to present the nonlinear mathematical model of the problem, we first derive a generalized Hamilton principle for thermoelastic beams with voids under geometric nonlinearity.

Let

$$M_\varphi = \iint_A \varphi(x_i, t) x_2 x_3 dA \quad \text{and} \quad M_\theta = \iint_A \theta(x_i, t) x_2 x_3 dA \quad (6)$$

be the moments caused by the change of the volume fraction $\varphi(x_i, t)$ and temperature $\theta(x_i, t)$, respectively. Set

$$\begin{aligned} q_\varphi &= \alpha_v \iint_A x_2 x_3 (\varphi_{,22} + \varphi_{,33}) dA \\ &= \alpha_v \left(\int_{-b/2}^{b/2} ((x_3 \varphi_{,3})|_{-h/2}^{h/2} - \varphi|_{-h/2}^{h/2}) x_2 dx_2 + \int_{-h/2}^{h/2} ((x_2 \varphi_{,2})|_{-b/2}^{b/2} - \varphi|_{-b/2}^{b/2}) x_3 dx_3 \right), \\ q_\theta &= \frac{K}{T_0} \iint_A x_2 x_3 (\theta_{,22} + \theta_{,33}) dA \\ &= \frac{K}{T_0} \left(\int_{-b/2}^{b/2} ((x_3 \theta_{,3})|_{-h/2}^{h/2} - \theta|_{-h/2}^{h/2}) x_2 dx_2 + \int_{-h/2}^{h/2} ((x_2 \theta_{,2})|_{-b/2}^{b/2} - \theta|_{-b/2}^{b/2}) x_3 dx_3 \right). \end{aligned} \quad (7)$$

According to [Cowin and Nunziato 1983], on the surfaces of the beam, $\varphi(x_i, t)$ needs to satisfy the conditions $\varphi_{,2}|_{x_2=\pm b/2} = 0$ and $\varphi_{,3}|_{x_3=\pm h/2} = 0$, so the expression for q_φ simplifies to

$$q_\varphi = -\alpha_v \left(\int_{-b/2}^{b/2} (\varphi|_{-h/2}^{h/2}) x_2 dx_2 + \int_{-h/2}^{h/2} (\varphi|_{-b/2}^{b/2}) x_3 dx_3 \right) \quad (8)$$

The thermal boundary conditions of the beam may be given as

$$\begin{aligned} K\theta_{,2}|_{x_2=b/2} &= \hbar(T_\infty - \theta_{b/2}), & K\theta_{,2}|_{x_2=-b/2} &= -\hbar(T_\infty - \theta_{-b/2}), \\ K\theta_{,3}|_{x_3=h/2} &= \hbar(T_\infty - \theta_{h/2}), & K\theta_{,3}|_{x_3=-h/2} &= -\hbar(T_\infty - \theta_{-h/2}), \end{aligned} \quad (9)$$

where \hbar is the heat transfer coefficient, $\theta_{b/2}$, $\theta_{-b/2}$, $\theta_{h/2}$, and $\theta_{-h/2}$ denote the temperatures on the surfaces $x_2 = \pm b/2$ and $x_3 = \pm h/2$, and T_∞ is the temperature of surrounding medium. If we assume that $T_\infty = 0$, the absolute temperature is equal to the reference temperature. The second expression of (7) then simplifies to

$$q_\theta = -\left(\frac{h\hbar/2 + K}{T_0} \int_{-b/2}^{b/2} (\theta|_{-h/2}^{h/2}) x_2 dx_2 + \frac{b\hbar/2 + K}{T_0} \int_{-h/2}^{h/2} (\theta|_{-b/2}^{b/2}) x_3 dx_3 \right). \quad (10)$$

To evaluate (8) and (10), we express the change of the volume fraction and temperature as the series

$$\varphi(x_i, t) = \sum_{m=0}^{\infty} \sum_{n=0}^{\infty} \varphi_{mn}(x_1, t) x_2^m x_3^n, \quad \theta(x_i, t) = \sum_{m=0}^{\infty} \sum_{n=0}^{\infty} \vartheta_{mn}(x_1, t) x_2^m x_3^n \quad (11)$$

Substituting (11) into (6) yields

$$M_\varphi = \bar{A} \varphi_{11}(x_1, t) + o(b^3 h^3), \quad M_\theta = \bar{A} \vartheta_{11}(x_1, t) + o(b^3 h^3), \quad (12)$$

where $\varphi_{11}(x_1, t)$ and $\vartheta_{11}(x_1, t)$ are the terms of (11) when $m = n = 1$. The term $o(b^3h^3)$, indicating higher-order quantities than b^3h^3 , can be omitted in the calculation.

From (8), (10), (11), (12), we have

$$q_\varphi \approx -\frac{(I_y + I_z)\alpha_v}{\bar{A}}M_\varphi, q_\theta \approx -\left(\frac{(h\hbar/2) + K}{T_0}\frac{I_z}{\bar{A}} + \frac{(b\hbar/2) + K}{T_0}\frac{I_y}{\bar{A}}\right)M_\theta, \tag{13}$$

where $\bar{A} = \iint_A (x_2x_3)^2 dA = (b^3/12)(h^3/12)$, $I_y = \iint_A x_3^2 dA = h^3b/12$, and $I_z = \iint_A x_2^2 dA = b^3h/12$.

According to the theory of beams, the strain energy of a beam in terms of displacements, void moment and thermal moment may be expressed as

$$U = \frac{1}{2} \int_0^l \iint_A D_0 \varepsilon_{11} \varepsilon_{11} dA dx_1 + \frac{1}{2(I_y + I_z)} \int_0^l (\alpha_v M_{\varphi,1} M_{\varphi,1} + \xi_v M_\varphi^2 - q_\varphi M_\varphi - \frac{\rho c_e}{T_0} M_\theta^2) dx_1 - \frac{1}{I_y + I_z} \int_0^l (b_v M_\varphi - \beta M_\theta)(I_z u_{2,11} + I_y u_{3,11}) dx_1 - \frac{1}{I_y + I_z} \int_0^l m_v M_\varphi M_\theta dx_1. \tag{14}$$

Assume that the total kinetic energy of the beam is $T = T_1 + T_2$, in which T_1 is caused by displacements and void moment, T_2 is caused by rotation; these terms are given as

$$T_1 = \frac{\rho h b}{2} \int_0^l (\dot{u}_1^2 + \dot{u}_2^2 + \dot{u}_3^2) dx_1 + \frac{1}{2(I_y + I_z)} \int_0^l \rho \chi \dot{M}_\varphi \dot{M}_\varphi dx_1, \tag{15}$$

$$T_2 = \frac{\rho}{2} \int_0^l \iint_A ((x_2 \dot{u}_{2,1})^2 + (x_3 \dot{u}_{3,1})^2) dA dx_1 = \frac{\rho}{2} \int_0^l (I_z (\dot{u}_{2,1})^2 + I_y (\dot{u}_{3,1})^2) dx_1.$$

Define the symbol

$$D(M_\theta) = \frac{1}{2(I_y + I_z)} \int_0^l \int_0^{t_1} \left(\frac{K}{T_0} M_{\theta,1} M_{\theta,1} - q_\theta M_\theta\right) dt_1 dx_1. \tag{16}$$

Assume that the beam is subjected to an arbitrary transverse distributed load q_i in the x_i -direction, that the two ends are subjected to an axial force N_0 , and that all the forces are conservative. In the absence of external equilibrated force and heat source, the external work may be given as

$$W = \int_0^l q_i u_i dx_1 + \frac{N_0}{2} \int_0^l (u_{2,1}^2 + u_{3,1}^2) dx_1 + N_0 u_1(0) - N_0 u_1(a) \tag{17}$$

Let

$$\Pi_B = \int_0^l \rho h b ((u_1|_{t=0} - u_1^0) \dot{u}_1 - \dot{u}_1^0 u_1 + (u_3|_{t=0} - u_3^0) \dot{u}_3 - \dot{u}_3^0 u_3) dx_1 + \int_0^l \frac{\rho \chi}{I_y + I_z} ((M_\varphi|_{t=0} - M_\varphi^0) \dot{M}_\varphi - \dot{M}_\varphi^0 M_\varphi) dx_1 + \int_0^l \frac{1}{I_y + I_z} \left(\int_0^{t_1} \frac{\rho c_e}{T_0} (M_\theta|_{t=0} - M_\theta^0) M_\theta dt \right) dx_1. \tag{18}$$

Generalized Hamilton principle for thermoelastic beams with voids. In all possible displacement fields $u_i(x_1, t)$, volume fraction field $\varphi(x_i, t)$ and temperature field $\theta(x_i, t)$ satisfying the geometric constraint conditions and having the appointed motions at the initial and final time, the actual displacements

$u_i(x_1, t)$, volume fraction $\varphi(x_i, t)$ and temperature $\theta(x_i, t)$ make the following functional arrive at the stationary value

$$\Pi(u_i, \varphi, \theta) = \int_0^t (T + W + D - U) dt + \Pi_B, \quad (19)$$

where $H = T + W + D - U$ is a generalized Hamilton function.

Applying a variational calculation to (19) (whose detailed formulas are given in the Appendix) and substituting the results obtained into the variational equation of (19), that is, $\delta\Pi = 0$, then integrating (19) with regard to time from 0 to the final time t , and observing the beam has the appointed motions at the initial and final time, as well as the arbitrariness of the variables δu_i , δM_φ , δM_θ on the interval $[0, l]$, we obtain the differential equations of motion in terms of u_i , M_φ , M_θ , in which the balance of entropy has been differentiated relative to t_1 :

$$\begin{aligned} D_0 h b \left(u_{1,1} + \frac{(u_{2,1})^2 + (u_{3,1})^2}{2} \right)_{,1} + q_1 &= \rho h b \ddot{u}_1, \\ D_0 h b \left(\left(u_{1,1} + \frac{(u_{2,1})^2 + (u_{3,1})^2}{2} \right) u_{2,1} \right)_{,1} - D_0 I_z u_{2,1111} \\ &+ \frac{I_z}{I_y + I_z} (b_v M_\varphi - \beta M_\theta)_{,11} + q_2 - N_0 u_{2,11} = \rho h b \ddot{u}_2 - \rho I_z \ddot{u}_{2,11}, \\ D_0 h b \left(\left(u_{1,1} + \frac{(u_{2,1})^2 + (u_{3,1})^2}{2} \right) u_{3,1} \right)_{,1} - D_0 I_y u_{3,1111} \\ &+ \frac{I_y}{I_y + I_z} (b_v M_\varphi - \beta M_\theta)_{,11} + q_3 - N_0 u_{3,11} = \rho h b \ddot{u}_3 - \rho I_y \ddot{u}_{3,11}, \\ \alpha_v M_{\varphi,11} + b_v (I_z u_{2,11} + I_y u_{3,11}) - \xi_v M_\varphi + q_\varphi + m_v M_\theta &= \rho \chi \ddot{M}_\varphi, \\ K M_{\theta,11} + \beta T_0 (I_z \dot{u}_{2,11} + I_y \dot{u}_{3,11}) - m_v T_0 \dot{M}_\varphi + q_\theta &= \rho c_e \dot{M}_\theta. \end{aligned} \quad (20)$$

This is a set of coupled nonlinear equations for u_i , M_φ and M_θ , in which the effects of the axial forces N_0 , the neutral layer inertia $\rho h b \ddot{u}_1$, and the rotation inertias $\rho I_z \ddot{u}_{2,11}$ and $\rho I_y \ddot{u}_{3,11}$ are included.

It can be also seen that the boundary conditions at the end designated forces may be derived from the boundary virtual work equation in the variational equation $\delta\Pi = 0$. If we only consider a clamped-beam without axial forces, the boundary conditions at the ends ($x_1 = 0, l$) are

$$u_i = 0, u_{2,1} = 0, u_{3,1} = 0, M_{\varphi,1} = 0, M_\theta = 0. \quad (21)$$

Observing that formula (18) is included in (19), the initial conditions at the initial time are given as

$$u_i = u_i^0, M_\varphi = M_\varphi^0, M_\theta = M_\theta^0, \dot{u}_i = \dot{u}_i^0, \dot{M}_\varphi = \dot{M}_\varphi^0, \quad (22)$$

in which u_i^0 , M_φ^0 , M_θ^0 , \dot{u}_i^0 , \dot{M}_φ^0 are the known functions of x_1 . Especially, if the beam is at rest at the initial time, these functions are equal to zeros.

4. Solution method

As application of the mathematical model above, the nonlinear mechanical characteristics of a two end fixed beam without the axial force are investigated, and the influences of parameters are considered. For

convenience, we here study the plane bending of the beam only, that is, $u_2(x_1, t) \equiv 0$. As it is difficult to obtain the solution of the problem directly, we will apply the differential quadrature method (DQM) to discretize the nonlinear system on the spatial domain.

The DQM is a numerical technique for solving boundary-valued problems. It was developed in [Bellman and Casti 1971], and since then it has been successfully employed to solve all kinds of problems in engineering and science due to the DQM owns the advantages of little amount of nodes and computation, high precision and good convergence and so on.

The DQM approximates the derivative of a function, with respect to the independent variable at a given discrete point, as a weighted linear sum of the values of the function at all the discrete points chosen in the solution domain of the independent variable, in which the weighting coefficients are only associated with the given discrete points in the solution domain and independent of a certain problem. Therefore, any differential equations can be transformed into a set of the corresponding algebraic equations.

Introduce the nondimensional variables and parameters

$$\begin{aligned}
 X &= \frac{x_1}{h}, \quad U = \frac{u_1}{h}, \quad W = \frac{u_3}{h}, \quad \beta_1 = \frac{h}{l}, \quad \tau = t \frac{V_1}{l}, \quad \psi = 12 \frac{M_\varphi}{h^2}, \quad \Theta = 12 \frac{M_\theta}{T_0 h^2}, \quad (23) \\
 a_1 &= \frac{b_v}{D_0}, \quad a_2 = \frac{\beta T_0}{D_0}, \quad a_3 = \frac{b_v h^2}{\alpha_v}, \quad a_4 = \frac{\xi_v h^2}{\alpha_v}, \quad a_5 = \frac{m_v T_0 h^2}{\alpha_v}, \quad a_6 = \left(\frac{V_1}{V_3}\right)^2, \quad a_8 = \frac{\beta}{\rho c_e}, \\
 a_9 &= \frac{m_v}{\rho c_e}, \quad a_{10} = \frac{\hbar}{2\rho c_e V_1}, \quad a_{11} = \frac{\rho c_e V_1 h}{K}, \quad \bar{p} = \frac{q_3}{D_0}, \quad V_1 = \sqrt{\frac{D_0}{\rho}}, \quad V_3 = \sqrt{\frac{\alpha_v}{\rho \chi}}. \quad (24)
 \end{aligned}$$

From (24), one sees that the coefficients a_1 and a_3 are the coupling deformation-void parameters, which represent the coupling degree of the deformation and volume fraction field. The coefficient a_6 is the ratio of the longitudinal wave velocity to the volume fraction wave velocity, which represents the ratio of the elastic constant to the void constant. The coefficient a_4 is a void parameter. The coefficients a_2 and a_8 are the coupling deformation-heat parameters, which represent the coupling degree of the deformation and temperature field. The coefficient a_{10} is a convection heat transfer parameter, and a_{11} is the ratio of dilational wave velocity to thermal conductive coefficient. The coefficients a_5 and a_9 are the coupling void-heat parameters, which represent the coupling degree of the volume fraction and temperature field.

The differential quadrature discretization forms of the nondimensional differential equations are

$$\begin{aligned}
 &\sum_{k=1}^N A_{ik}^{(2)} U_k + \beta_1 \sum_{k=1}^N A_{ik}^{(1)} W_k \cdot \sum_{l=1}^N A_{il}^{(2)} W_l = \ddot{U}_i, \\
 &\beta_1 \left(\sum_{k=1}^N A_{ik}^{(2)} U_k \cdot \sum_{l=1}^N A_{il}^{(1)} W_l + \sum_{k=1}^N A_{ik}^{(1)} U_k \cdot \sum_{l=1}^N A_{il}^{(2)} W_l \right) + \frac{3}{2} \beta_1^2 \left(\sum_{k=1}^N A_{ik}^{(1)} W_k \right)^2 \sum_{l=1}^N A_{il}^{(2)} W_l \\
 &\quad - \frac{\beta_1^2}{12} \sum_{k=1}^N A_{ik}^{(4)} W_k + \frac{a_1}{12} \sum_{k=1}^N A_{ik}^{(2)} \psi_k - \frac{a_2}{12} \sum_{k=1}^N A_{ik}^{(2)} \Theta_k + \frac{\bar{p}}{\beta_1^2} = \ddot{W}_i - \frac{\beta_1^2}{12} \sum_{k=1}^N A_{ik}^{(2)} \ddot{W}_k, \quad (25) \\
 &\sum_{k=1}^N A_{ik}^{(2)} \psi_k + a_3 \sum_{k=1}^N A_{ik}^{(2)} W_k - \frac{a_4 + 12}{\beta_1^2} \psi_i + \frac{a_5}{\beta_1^2} \Theta_i = a_6 \ddot{\psi}_i, \\
 &\frac{\beta_1}{a_{11}} \sum_{k=1}^N A_{ik}^{(2)} \Theta_k + a_8 \beta_1^2 \sum_{k=1}^N A_{ik}^{(2)} \dot{W}_k - a_9 \dot{\psi}_i - \left(a_{10} + \frac{1}{a_{11}} \right) \frac{12}{\beta_1} \frac{\theta_+ - \theta_-}{T_0} = \dot{\Theta}_i,
 \end{aligned}$$

where i ranges from 1 to N , the number of discrete points, and $A_{ik}^{(j)}$ is the weighting coefficient of the j -th partial derivative of the function with respect to the independent variable X . In this paper, the polynomial function is adopted as the test function to obtain the weighting coefficient, and the zeros of the Chebyshev–Lobatto polynomial are adopted as the coordinates of the grid points [Bellman and Casti 1971].

The DQ discretization forms of the nondimensional boundary conditions can be expressed as

$$\begin{aligned} U_1 = U_N = 0, \quad W_1 = W_N = 0, \quad \Theta_1 = \Theta_N = 0, \\ \sum_{k=1}^N A_{1k}^{(1)} \psi_k = \sum_{k=1}^N A_{Nk}^{(1)} \psi_k = 0, \quad \sum_{k=1}^N A_{1k}^{(1)} W_k = \sum_{k=1}^N A_{Nk}^{(1)} W_k = 0. \end{aligned} \quad (26)$$

If the initial values of variables are all zero, we have the initial conditions of nondimensional forms

$$U(0) = \dot{U}(0) = W(0) = \dot{W}(0) = \psi(0) = \dot{\psi}(0) = \Theta(0) = 0 \quad (27)$$

Assuming that the temperature distribution is given by $\theta(x_1, x_3) = \theta_0(1/2 + x_3/h)$, we have $\theta_+ = \theta_0$, $\theta_- = 0$.

Hence, the static problem is converted to solving the nonlinear algebraic equations (25) under the boundary conditions (26); while the dynamical problem is converted to solving the nonlinear ordinary differential equations (25) under the boundary conditions (26) and initial condition (27). The Newton–Raphson and Runge–Kutta methods are adopted in the calculation of the static and dynamical problems, respectively.

To illustrate the correctness of the theory and method in this paper, a simply supported elastic beam subjected to a uniformly distributed load \bar{p} is considered. The analytic solution is available in the case of small deformation. Figure 2a shows the comparison between the analytic solution and the numerical result obtained from the theory and method of this paper when $\bar{p} = 10^{-5}$ and 7 nodes are collocated. It can be seen that the results are accordant. Figure 2b shows the comparison between the analytic solution and the numerical results when $\bar{p} = 10^{-4}$ and 7 and 9 nodes are collocated, respectively. It is seen that the solutions of linear elastic beam under small deformation and the nonlinear theory are no longer consistent. The DQ solution is slightly less than the analytical solution due to the nonlinear effect. From Figure 2b, one can see that the DQ solution has good convergence also.

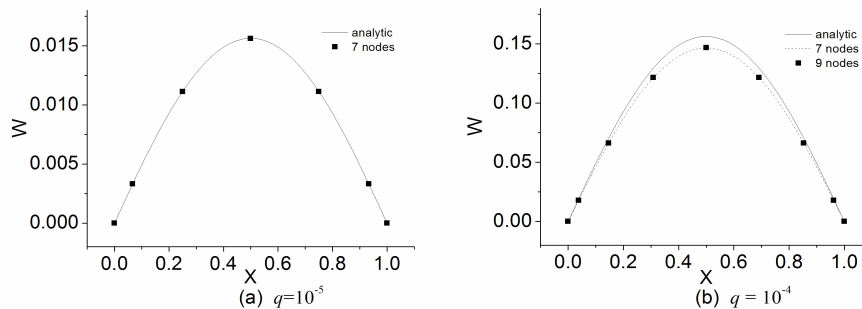


Figure 2. Comparison of the DQ solution with the analytic solution.

5. Nonlinear mechanical characteristics of thermoelastic beam with voids

Nonlinear static behavior of thermoelastic beams with voids. The Newton–Raphson method is used to solve the static system (25)–(26) numerically. In this situation, the thermal moment, which is independent of the deflection and void moment but just dependent of the lower and upper surface temperature, can be solved directly from (25)₄. In Table 1 we give the effects of the node distribution on the DQ solution of the dimensionless deflection and void moment at the middle point of the beam for four different materials. The parameters are chosen as follows (see [Puri and Cowin 1985; Kumar and Rani 2005]):

$$\beta_1 = 0.1, \quad a_1 = 0.33, \quad a_2 = 0.027, \quad a_3 = 5, \quad a_4 = 6, \quad a_{11} = 4.56 \times 10^6, \quad \theta_0 = 10, \quad \bar{p} = 0.0001.$$

One can see that satisfactory results can be obtained when 9 nodes are collocated on the physical interval [0, 1] for elastic beams (EB) and thermoelastic beams (TEB), while 15 nodes are needed for elastic beams with voids (EVB) and thermoelastic beams with voids (TEVB). Hence, we set $N = 15$ in the calculation. When $\theta_0 > 0$, this means that the beam is subjected to a thermal moment, which is just opposite to the bending moment of external force. From the comparison of the deflections of EB and EVB, we see that the deflections of EVB are larger than the ones of EB. We can conclude that the presence of voids enlarges the deflection.

Effect of a_1 . It can be observed from Figure 3 that the deflection and void moment of EVB increase with a_1 . From Figure 4 it is seen that the deflection of TEVB decreases as a_1 increases, while the corresponding void moment increases.

Effect of a_3 . As for EVB, the results are similar to Figure 3, that is to say, the deflection and void moment of EVB increases with a_3 . From Figure 5, one can see that the deflection of TEVB increases with an increase in a_3 , while the void moment decreases.

Effect of a_4 . Figure 6 shows that the deflection and void moment of EVB decrease with an increase in a_4 . Figure 7 suggests that the deflection of TEVB increases with an increase in a_4 , while the corresponding void moment decreases.

Effect of a_2 . As for TEB and TEVB, the temperature can be solved directly because the energy equation is an ordinary differential equation about X . So, the parameter a_2 has no effect on the temperature. The

nodes	EB	TEB	EVB		TEVB	
	W	W	W	ψ	W	ψ
7	0.031232	-0.25341	0.034650	-0.0015148	-0.20074	-0.095229
9	0.031228	-0.25123	0.034422	-0.0015084	-0.20265	-0.095241
11	0.031228	-0.25123	0.034351	-0.0015074	-0.20373	-0.095229
13	0.031228	-0.25123	0.034330	-0.0015066	-0.20406	-0.095216
15	0.031228	-0.25123	0.034323	-0.0015065	-0.20416	-0.095216
17	0.031228	-0.25123	0.034322	-0.0015065	-0.20419	-0.095215
19	0.031228	-0.25123	0.034322	-0.0015065	-0.20420	-0.095215
21	0.031228	-0.25123	0.034322	-0.0015065	-0.20420	-0.095215

Table 1. Effect of the node distribution on the DQ solutions for static system.

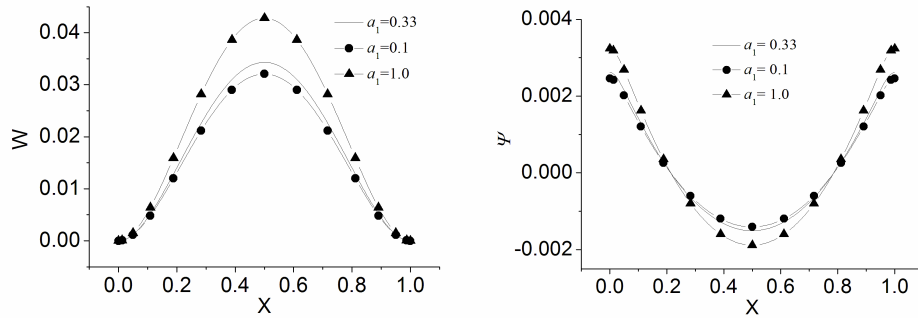


Figure 3. Variation of deflection W and void moment ψ of EVB with X , for various a_1 .

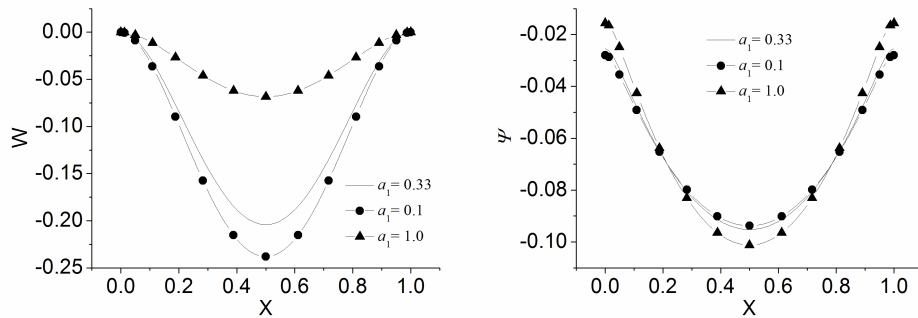


Figure 4. Variation of deflection W and void moment ψ of TEVB with X , for various a_1 .

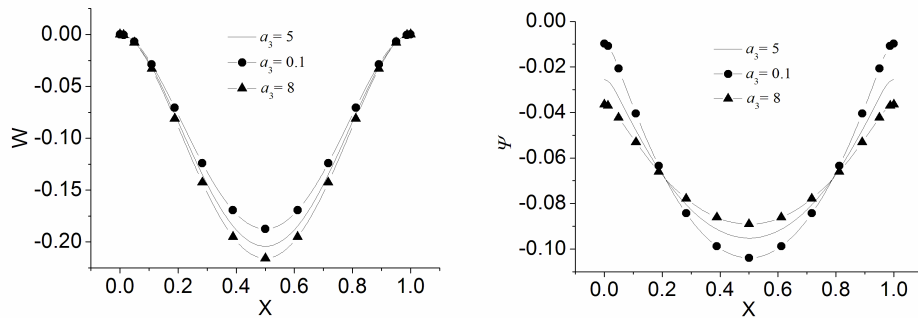


Figure 5. Variation of deflection W and void moment ψ of TEVB with X , for various a_3 .

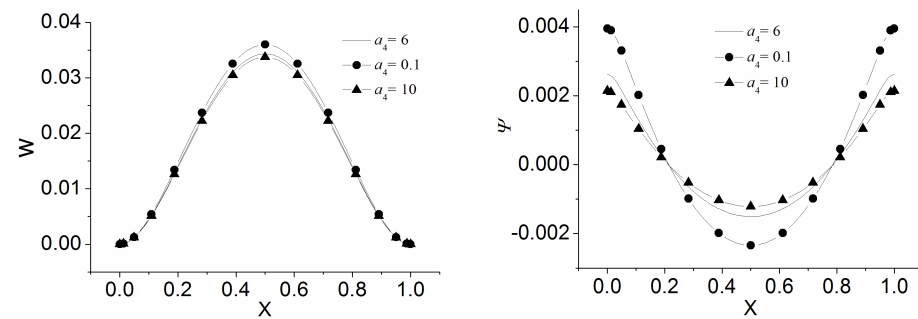


Figure 6. Variation of deflection W and void moment ψ of EVB with X , for various a_4 .

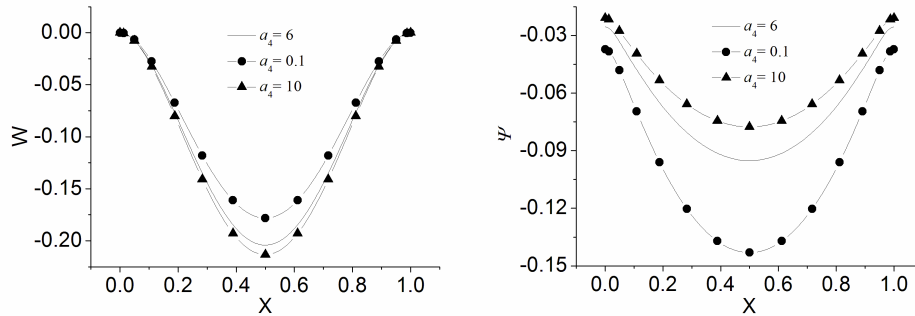


Figure 7. Variation of deflection W and void moment ψ of TEVB with X , for various a_4 .

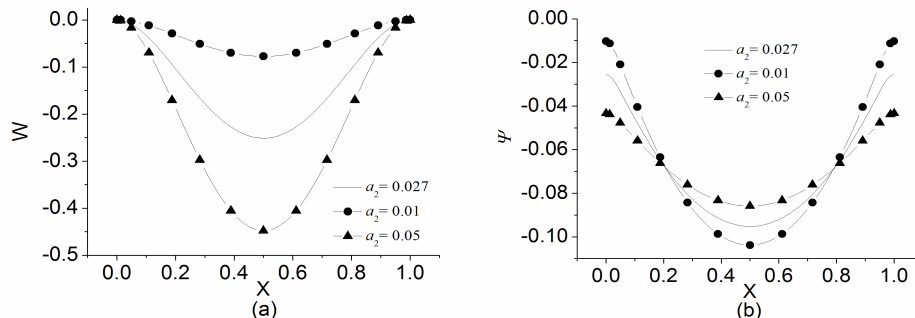


Figure 8. Variation of deflection W of EVB and void moment ψ of TEVB with X , for various a_2 .

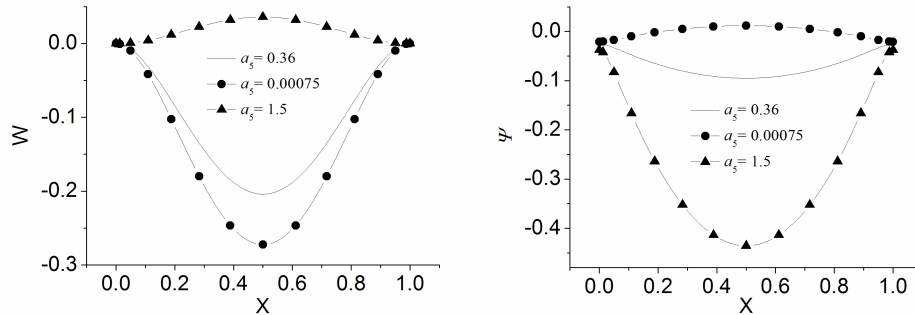


Figure 9. Variation of deflection W and void moment ψ of TEVB with X , for various a_5 .

deflection of TEB increases with an increase in a_2 , as seen in Figure 8a, and so does the deflection of TEVB. In contrast, the void moment of TEVB decreases with an increase in a_2 , as seen in Figure 8b.

Effect of a_5 . The parameter a_5 is a coupling one of volume fraction and temperature field. Figure 9 shows that the deflection of TEVB varies from negative to positive with an increase in a_5 , while the void moment varies from positive to negative.

Effect of a_{10} and a_{11} . When $a_{10} = 0$, the boundary of the beam is adiabatic, meanwhile, the temperature is independent of a_{11} but just dependent of the thickness-length ratio of the beam. When $a_{10} \rightarrow \infty$, the

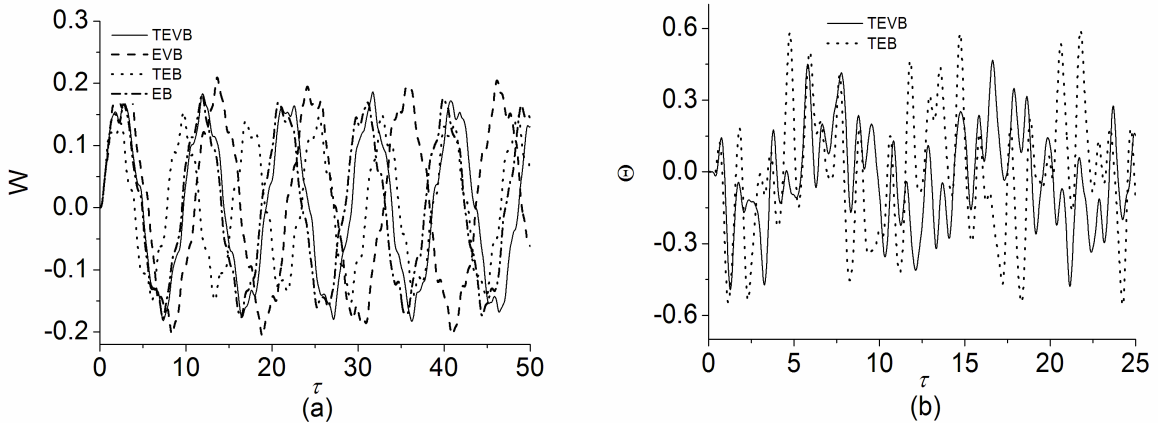


Figure 10. Time-history curves of the beams deflection W and thermal moment Θ .

boundary of beam is isothermal. The numerical calculation shows that the deflection, void moment and thermal moment all increase with an increase in a_{10} and a_{11} , respectively.

To summarize, we can see that the effect of the parameters a_1, a_2, a_3, a_4, a_5 on the deflection and the void moment is significant for the static problem.

Nonlinear dynamical behavior of thermoelastic beams with voids. The Runge–Kutta method of fourth order is used to solve the nonlinear dynamical system (25)–(27) numerically, to obtain time-history curves of the corresponding variables at the middle point of the beam. In computation, setting $N = 15$, the parameters are given as follows (see [Puri and Cowin 1985; Kumar and Rani 2005]):

$$\beta_1 = 0.1, \quad \bar{p} = 0.005 \sin(2\pi\tau), \quad h = 0.1, \quad \theta_0 = 100, \quad a_1 = 1.0, \quad a_2 = 0.05, \quad a_3 = 5.0, \\ a_4 = 6.0, \quad a_5 = 0.36, \quad a_6 = 0.6, \quad a_8 = 10.0, \quad a_9 = 8.0, \quad a_{10} = 1.0 \times 10^{-8}, \quad a_{11} = 4.56 \times 10^6.$$

For comparison, the time-history curves of the deflection for four beams (EB, TEB, EVB, TEVB) are presented in Figure 10a, and those of the thermal moment for TEB and TEVB are shown in Figure 10b. It can be observed that the presence of voids enlarges beam deflection, while the thermal effect is the opposite: maybe the external work is partially transformed to thermal energy and dissipated. It is also seen that the thermal moment increases due to the presence of voids. Comparing the time-history curves of the void moment of TEVB and EVB, one can see that void moment of TEVB is slightly larger.

Next, the effect of parameters will be investigated. For the static problem, the parameters a_6, a_8, a_9 are absent. For the dynamical problem, the parameter a_6 has no influence on the dynamical behavior; one only has to study the effects of a_8 and a_9 .

Effect of a_8 . Figure 11 depicts the time-history curves of thermal moment of TEVB and TEB. It can be observed that thermal moment decreases sharply then increases with the decrease of a_8 for TEVB, from Figure 11a; while the thermal moment just decreases sharply with the decrease of a_8 for TEB, from Figure 11b. Meanwhile, the deflection of these beams increases with the decrease of a_8 , and the void moment has barely changes.

Effect of a_9 . The effect of the parameter a_9 on the deflection and void moment of TEVB is negligible, but Figure 12a shows that the thermal moment of TEVB increases with the decrease of a_9 .

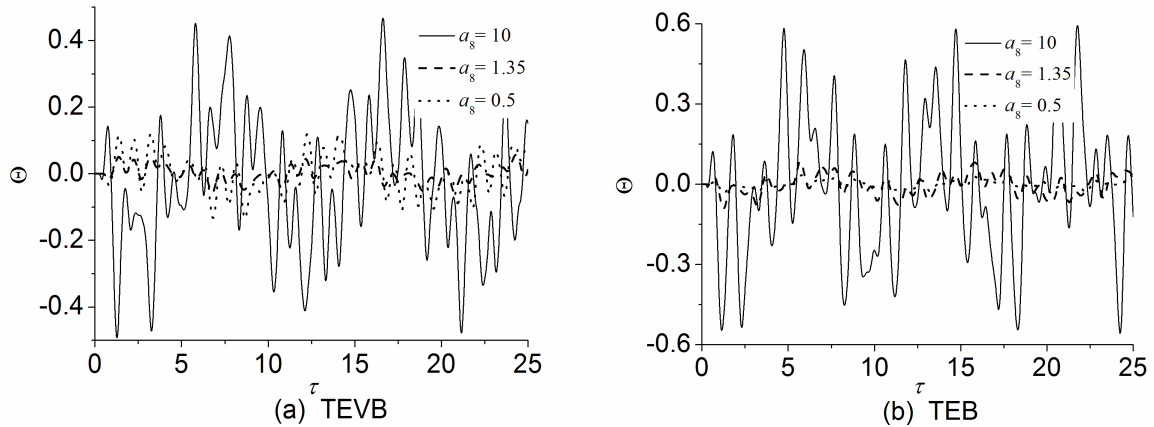


Figure 11. Time-history curves of the thermal moment of TEVB and TEB, for various values of a_8 .

Effect of other parameters. For EVB and TEVB, the deflection and void moment all decrease with the decrease of the parameters a_1, a_3, a_5 , respectively, while increase with the decrease of a_4 . Similarly to the static results, the effect of the parameters a_3 and a_4 on the void moment of EVB is prominent, at the same time, the effect of the parameters a_3, a_4 and a_5 on the void moment of TEVB is significant, but on the corresponding thermal moment may be negligible.

For TEVB, the deflection, void moment and thermal moment all increase with the decrease of a_2 , and the latter two vary more obviously. As for TEB, the deflection and thermal moment also increase with the decrease of a_2 .

For TEVB and TEB, the effect of the parameter a_{10} on the deflection is negligible. The thermal moment no longer vibrates with the X -axis but gradually deviated from the X -axis downward with time with an increase in a_{10} , this means that the boundary of beam varies from adiabatic to isothermal. Figure 12b shows the time-history curves of the thermal moment of TEVB for different a_{10} . Besides, the curves of the void moment are similar to the thermal moment, but the value changes slightly.

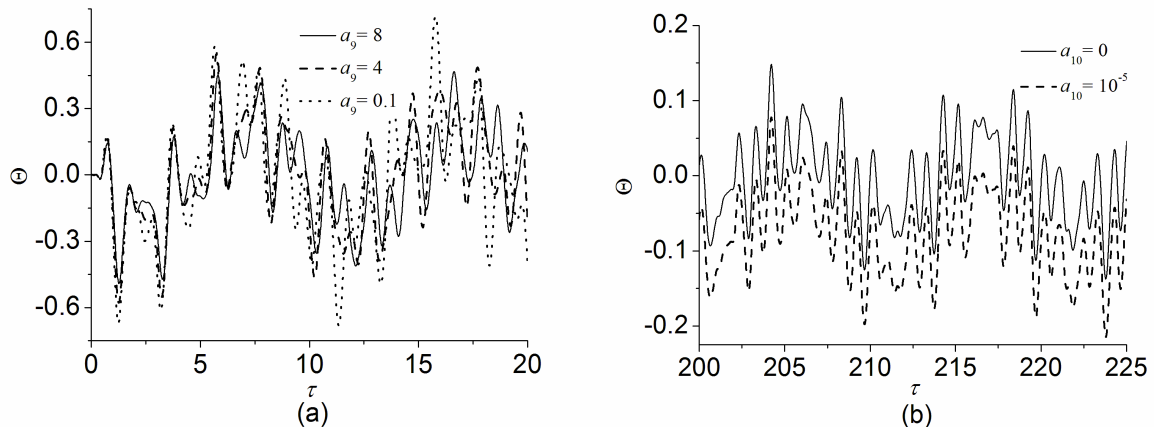


Figure 12. Time-history curves of thermal moment of TEVB, for various values of a_9 (left) and a_{10} (right).

For TEVB and TEB, the amplitudes of deflection all decrease slightly with time as the parameter a_{11} increases. Besides, the variations of the void moment and thermal moment with a_{11} are similar to a_{10} .

6. Conclusion

In this paper, the equation for the balance of entropy is firstly converted to an equivalent form without the first-order time-derivative by integral, and introducing the moments caused by the change of the void volume fraction and temperature, the Hamilton variational principle is extended to the three-dimensional thermoelastic beams with voids under finite deformations. A nonlinear theory of thermoelastic beams with voids is established based on the Kirchhoff–Love hypothesis, in which the influences of the axial forces, neutral layer inertia and rotation inertia are considered. The theory presents a set of coupling nonlinear differential equations of three displacements, one void moment and one thermal moment, in which not only the accelerations of the deflection and void moment are included, but also the effects of the neutral layer inertia and rotation inertia. So the theory is a complete nonlinear mathematical model of thermoelastic beams with voids under the Kirchhoff–Love hypothesis.

To illustrate the correctness of the theory and method of this paper, the plane bending problem of a simply supported elastic beam with small deformations is first studied, and the results are compared with the analytic solution. One can see that the numerical solution obtained from the DQM is accordant with the analytic solution, and the DQ solution has good convergence also.

As application, the static and dynamic responses of the plane bending of a fixed-fixed beam are studied. It is difficult to obtain the analytic solution of the nonlinear problem, so one kind of numerical methods is adopted to solve the problem. Firstly, the DQM is used to discrete the nonlinear system on the spatial domain, a set of nonlinear algebraic equations or ordinary differential equations are obtained for the static or dynamic problem, respectively. Then, the Newton–Raphson method and Runge–Kutta method are adopted to calculate the static and dynamical system, respectively. Mechanical characteristics of the system are investigated for four beams, that is, TEVB, TEB, EVB and EB, and the influences of parameters are all investigated. The general conclusion is that the presence of voids enlarges beam deflection. The deformation-void coupling parameters mainly bring changes in the deflection and void moment. The effect of the deformation-heat coupling parameters is significant. The void-heat coupling parameters change the void moment and thermal moment greatly, but the effect on the deflection is little. Beam deflection increases with an increase in a_1 , a_3 , a_5 but decreases with an increase in a_2 , a_4 , a_8 . The effect of other parameters on the deflection is not obvious. For the dynamical problem, the effects of the temperature on the deflection and void moment are less obvious than the static case, which maybe the external work is transformed to the thermal energy partially and to be dissipated.

Appendix: Derivation of Hamilton variational principle of thermoelastic beam with voids

Letting $u_2(x_1, t) \equiv 0$ in the equations above corresponds to considering only plane bending of the beam. Applying a variational calculation to (19), we then obtain the variational formulas

$$\delta T_1 = - \iint_{\Omega} \{ \rho h (\ddot{u}_1 \delta u_1 + \ddot{u}_3 \delta u_3) + \rho \chi \ddot{M}_\varphi \delta M_\varphi \} d\Omega + \iint_{\Omega} \frac{\partial}{\partial t} \{ \rho h (\dot{u}_1 \delta u_1 + \dot{u}_3 \delta u_3) + \rho \chi \dot{M}_\varphi \delta M_\varphi \} d\Omega,$$

$$\delta T_2 = I\rho \oint_{\partial\Omega} \left(\frac{\partial \dot{u}_3}{\partial x_1} l \right) \delta \dot{u}_3 ds - I\rho \iint_{\Omega} \left(\frac{\partial}{\partial t} \left(\frac{\partial^2 \dot{u}_3}{\partial x_1^2} \delta u_3 \right) - \frac{\partial^2 \ddot{u}_3}{\partial x_1^2} \delta u_3 \right) d\Omega,$$

$$\delta W = \iint_{\Omega} (q_1 \delta u_1 + q_3 \delta u_3) d\Omega + N_{x0} \delta u_1(0) - N_{xa} \delta u_1(a),$$

$$\delta D(M_\theta) = \iint_{\Omega} \int_0^{t_1} \left(-\frac{K}{T_0} M_{\theta,11} \delta M_\theta + \left(\frac{h\hbar}{2T_0} + \frac{K}{T_0} \right) \frac{12}{h^2} M_\theta \delta M_\theta \right) dt_1 d\Omega + \oint_{\partial\Omega} \int_0^{t_1} \frac{K}{T_0} (l M_{\theta,1} \delta M_\theta) dt_1 ds,$$

$$\begin{aligned} \delta U = & -(\lambda + 2\mu)h \iint_{\Omega} \left(\frac{\partial \varepsilon_{11}^0}{\partial x_1} \delta u_1 + \frac{\partial}{\partial x_1} \left(\varepsilon_{11}^0 \frac{\partial u_3}{\partial x_1} \right) \delta u_3 \right) d\Omega + \frac{(\lambda + 2\mu)h^3}{12} \iint_{\Omega} \frac{\partial^4 u_3}{\partial x_1^4} \delta u_3 d\Omega \\ & + \iint_{\Omega} \left(-\alpha_v M_{\varphi,11} \delta M_\varphi + \xi_v M_\varphi \delta M_\varphi + \frac{12\alpha_v}{h^2} M_\varphi \delta M_\varphi \right) d\Omega - \iint_{\Omega} m_v (M_\varphi \delta M_\theta + M_\theta \delta M_\varphi) d\Omega \\ & - \frac{h^3}{12} \iint_{\Omega} \left((b_v \delta M_\varphi - \beta \delta M_\theta) \frac{\partial^2 u_3}{\partial x_1^2} + \left(b_v \frac{\partial^2 M_\varphi}{\partial x_1^2} - \beta \frac{\partial^2 M_\theta}{\partial x_1^2} \right) \delta u_3 \right) d\Omega - \iint_{\Omega} \frac{\rho c_e}{T_0} M_\theta \delta M_\theta d\Omega + \delta U_B, \end{aligned}$$

in which

$$\begin{aligned} \delta U_B = & (\lambda + 2\mu)h \oint_{\partial\Omega} \left(l \varepsilon_{11}^0 \delta u_1 + l \varepsilon_{11}^0 \frac{\partial u_3}{\partial x_1} \delta u_3 \right) ds + \frac{(\lambda + 2\mu)h^3}{12} \oint_{\partial\Omega} \left(l \frac{\partial^2 u_3}{\partial x_1^2} \delta \frac{\partial u_3}{\partial x_1} - l \frac{\partial^3 u_3}{\partial x_1^3} \delta u_3 \right) ds \\ & + \oint_{\partial\Omega} \left(\alpha_v \left(l \frac{\partial M_\varphi}{\partial x_1} \delta M_\varphi \right) - \frac{h^3}{12} \left(l (b_v M_\varphi - \beta M_\theta) \delta \frac{\partial u_3}{\partial x_1} \right) + \frac{h^3}{12} \left(l (b_v M_\varphi - \beta M_\theta)_{,1} \right) \delta u_3 \right) ds, \end{aligned}$$

$$\begin{aligned} \delta \Pi_B = & \int_0^t \left(\int_{\partial V_\sigma} \bar{T}_\alpha \delta u_\alpha ds + \int_{\partial V_u} (u_\alpha - \bar{u}_\alpha) \delta T_\alpha ds + \int_{\partial V_h} \bar{M}_h \delta M_\varphi ds + \int_{\partial V_\varphi} (M_\varphi - \bar{M}_\varphi) \delta M_h ds \right. \\ & \left. + \int_{\partial V_Q} \frac{1}{T_0} \bar{M}_Q \delta M_\theta ds + \int_{\partial V_\theta} \frac{1}{T_0} (M_\theta - \bar{M}_\theta) \delta M_Q ds \right) dt + \iint_{\Omega} \rho h ((u_\alpha|_{t=0} - u_\alpha^0) \delta \dot{u}_\alpha - \dot{u}_\alpha^0 \delta u_\alpha) d\Omega \\ & + \iint_{\Omega} \rho \chi h ((M_\varphi|_{t=0} - M_\varphi^0) \delta \dot{M}_\varphi - \dot{M}_\varphi^0 \delta M_\varphi) d\Omega + \iint_{\Omega} h \left(\int_0^{t_1} \frac{\rho c_e}{T_0} (M_\theta|_{t=0} - M_\theta^0) \delta M_\theta dt \right) d\Omega. \end{aligned}$$

Substituting these variational formulas into $\delta \Pi = 0$, we can obtain the differential equations of motion in terms of $u_1, u_3, M_\varphi, M_\theta$, that is, Equations (20).

Boundary conditions can be derived from the following boundary virtual work equation in variational equation:

$$\begin{aligned} (\lambda + 2\mu)h \oint_{\partial\Omega} \left(l \varepsilon_{11}^0 \delta u_1 + l \varepsilon_{11}^0 \frac{\partial u_3}{\partial x_1} \delta u_3 \right) ds + \frac{(\lambda + 2\mu)h^3}{12} \oint_{\partial\Omega} \left(l \frac{\partial^2 u_3}{\partial x_1^2} \delta \frac{\partial u_3}{\partial x_1} - l \frac{\partial^3 u_3}{\partial x_1^3} \delta u_3 \right) ds \\ + \oint_{\partial\Omega} \left(\alpha_v \left(l \frac{\partial M_\varphi}{\partial x_1} \delta M_\varphi \right) - \frac{h^3 l}{12} (b_v M_\varphi - \beta M_\theta) \delta \frac{\partial u_3}{\partial x_1} + \frac{h^3 l}{12} (b_v M_\varphi - \beta M_\theta)_{,1} \delta u_3 \right) ds \\ + \oint_{\partial\Omega} \int_0^{t_1} \frac{K}{T_0} (l M_{\theta,1} \delta M_\theta) dt_1 ds - N_{xa} \delta u_1(a) + N_{x0} \delta u_1(0) = 0. \end{aligned}$$

References

[Bellman and Casti 1971] R. E. Bellman and J. Casti, "Differential quadrature and long-term integration", *J. Math. Anal. Appl.* **34:2** (1971), 235–238.

- [Birsan 2003] M. Birsan, “A bending theory of porous thermoelastic plates”, *J. Therm. Stresses* **26**:1 (2003), 67–90.
- [Cheng et al. 2006] C.-J. Cheng, D.-F. Sheng, and J.-J. Li, “Quasi-static analysis for viscoelastic Timoshenko beams with damage”, *Appl. Math. Mech.* **27**:3 (2006), 295–304.
- [Chiriță and Ciarletta 2008] S. Chiriță and M. Ciarletta, “On the structural stability of thermoelastic model of porous media”, *Math. Methods Appl. Sci.* **31**:1 (2008), 19–34.
- [Chiriță and Scalia 2001] S. Chiriță and A. Scalia, “On the spatial and temporal behavior in linear thermoelasticity of materials with voids”, *J. Therm. Stresses* **24**:5 (2001), 433–455.
- [Ciarletta et al. 2007] M. Ciarletta, B. Straughan, and V. Zampoli, “Thermo-poroacoustic acceleration waves in elastic materials with voids without energy dissipation”, *Int. J. Eng. Sci.* **45**:9 (2007), 736–743.
- [Cicco and Diaco 2002] S. D. Cicco and M. Diaco, “A theory of thermoelastic materials with voids without energy dissipation”, *J. Therm. Stresses* **25**:5 (2002), 493–503.
- [Cowin and Nunziato 1983] S. C. Cowin and J. W. Nunziato, “Linear elastic materials with voids”, *J. Elasticity* **13**:2 (1983), 125–147.
- [Iesan 1986] D. Iesan, “A theory of thermoelastic materials with voids”, *Acta Mech.* **60**:1-2 (1986), 67–89.
- [Kumar and Rani 2005] R. Kumar and L. Rani, “Interaction due to mechanical and thermal sources in thermoelastic half-space with voids”, *J. Vib. Control* **11**:4 (2005), 499–517.
- [Luo et al. 2002] E. Luo, J.-S. Kuang, W.-J. Huang, and Z.-G. Luo, “Unconventional Hamilton-type variational principles for nonlinear coupled thermoelastodynamics”, *Sci. China, A* **45**:6 (2002), 783–794.
- [Puri and Cowin 1985] P. Puri and S. C. Cowin, “Plane waves in linear elastic materials with voids”, *J. Elasticity* **15**:2 (1985), 167–183.
- [Scalia et al. 2004] A. Scalia, A. Pompei, and S. Chiriță, “On the behavior of steady time-harmonic oscillations in thermoelastic materials with voids”, *J. Therm. Stresses* **27**:3 (2004), 209–226.
- [Sharma et al. 2008] P. K. Sharma, D. Kaur, and J. N. Sharma, “Three-dimensional vibration analysis of a thermoelastic cylindrical panel with voids”, *Int. J. Solids Struct.* **45**:18-19 (2008), 5049–5058.
- [Sheng and Cheng 2004] D.-F. Sheng and C.-J. Cheng, “Dynamical behaviors of nonlinear viscoelastic thick plates with damage”, *Int. J. Solids Struct.* **41**:26 (2004), 7287–7308.
- [Singh 2007] B. Singh, “Wave propagation in a generalized thermoelastic material with voids”, *Appl. Math. Comput.* **189**:1 (2007), 698–709.
- [Xi 2007] B. Q. Xi, “Analysis of the features of porous materials”, *Science and technology information* **23** (2007), 316. In Chinese.
- [Yu et al. 1996] T. X. Yu, J. L. Yang, S. R. Reid, and C. D. Austin, “Dynamic behaviour of elastic-plastic free-free beams subjected to impulsive loading”, *Int. J. Solids Struct.* **33**:18 (1996), 2659–2680.
- [Zhang 2007] N.-H. Zhang, “Thermo-viscoelastic bending of functionally graded beam under thermal load”, *Chinese Quarterly of Mechanics* **28**:2 (2007), 240–245. in Chinese.

Received 20 Dec 2009. Revised 11 Apr 2010. Accepted 16 Apr 2010.

YING LI: liying982@hotmail.com

Shanghai Institute of Applied Mathematics and Mechanics, Shanghai University, Shanghai 200072, China

CHANG-JUN CHENG: chjcheng@mail.shu.edu.cn

Shanghai Institute of Applied Mathematics and Mechanics, Department of Mechanics, Shanghai University, Shanghai 200072, China

DYNAMIC STIFFNESS VIBRATION ANALYSIS OF THICK SPHERICAL SHELL SEGMENTS WITH VARIABLE THICKNESS

ELIA EFRAIM AND MOSHE EISENBERGER

A dynamic stiffness method is presented for determining the free vibration frequencies and mode shapes of thick spherical shell segments with variable thickness and different boundary conditions. The analysis uses the equations of the two-dimensional theory of elasticity, in which the effects of both transverse shear stresses and rotary inertia are accounted for. The displacement components are taken to be sinusoidal in time, periodic in the circumferential direction, constant through the thickness, and solved exactly in the meridional direction using the exact element method. The shape functions are derived from the exact solutions for the system of the differential equation of motion with variable coefficients. The dynamic stiffness matrix is derived from the exact shape functions and their derivatives. High-precision numerical results are presented for thick spherical shell segments with constant or linearly varying thickness and for several combinations of boundary conditions. Comparison is made with results of published research and with two- and three-dimensional finite element analyses.

1. Introduction

Spherical shells are extensively used in civil, mechanical, aircraft, and naval structures. The free vibration of solid and hollow spheres has been a subject of study for more than a century. Historical reviews of the research into the vibrations of spherical shell are given in [Leissa 1973; Kang and Leissa 2000; Qatu 2002]. For segmented spherical shells very few studies can be found. Gautham and Ganesan [1992] used finite elements to study the free vibration analysis of open spherical shells, based on a thick (two-dimensional) shell theory. A thick shell finite element was derived and vibration frequencies were obtained for spherical caps with and without center cutout having simply supported or clamped boundary conditions. Lim et al. [1996] analyzed spherical shells with variable thickness using two-dimensional shell theory and the Ritz method, and the results were compared with finite element and experimental ones. For spherical shell segments based on three-dimensional analysis, Kang and Leissa [2000] used the Ritz method to obtain accurate frequencies for thick spherical shell segments of uniform or varying thickness. Their method does not yield exact solutions, but with proper use of displacement components in the form of algebraic polynomials, one is able to obtain frequency upper bounds, that are as close to the exact values as desired. Corrected results for the test cases in that paper appeared subsequently in [Kang and Leissa 2006].

In this paper the equations of motion for a thick spherical shell segment with variable thickness are derived. Then, these are solved for the dynamic stiffness matrix of the segment, and assembled for a complete structure.

Keywords: vibrations, thick shell, spherical shell, variable thickness, dynamic stiffness, exact element method.

Support given this research to the first author by the Technion – Israel Institute of Technology is gratefully acknowledged.

2. Equations of motion

The shell coordinates and shell parameters for axisymmetric spherical shells with thickness varying along the meridian are shown in Figure 1, left, where ϕ and θ are spherical angle coordinates, z is thickness coordinate from middle surface, R_0 is radius of curvatures of the middle surface of the shell in both meridian and circumferential directions and $R_p(\phi)$ describes the perpendicular distance to the axis of revolution of the generating line. The location of the shell segment is defined by either the angle of the beginning of the shell ϕ_b , or the angle of the end of the shell segment ϕ_e , and the meridional dimension of the shell is defined by the opening angle ϕ_0 .

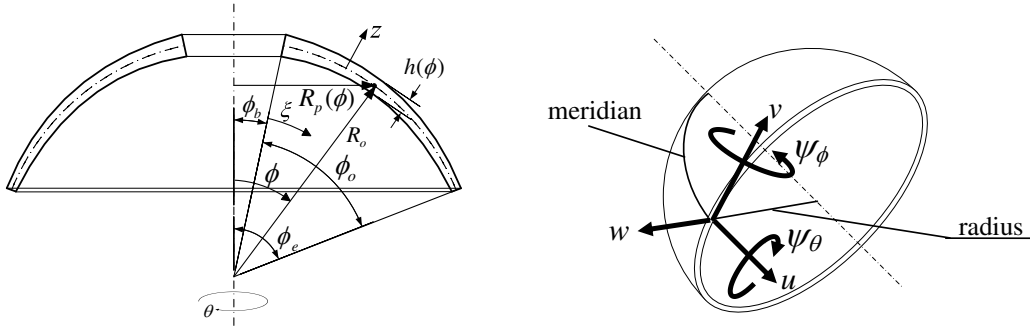


Figure 1. Left: geometry and coordinates of a spherical shell segment. Right: displacement field according to the thick shell theory.

The strain-displacement equations of the first order shear deformation shell theory of thick shells are obtained by satisfying the Kirchoff–Love hypothesis, such that normal to the shell mid-surface during deformation remain straight, and suffer no extension, but are not necessarily normal to the mid-surface after deformation. According to these assumptions the displacement of every point of the shell (see Figure 1, right) may be expressed as

$$\begin{aligned} u(\phi, \theta, z, t) &= U_0(\phi, \theta, t) + z\Psi_\phi(\phi, \theta, t), \\ v(\phi, \theta, z, t) &= V_0(\phi, \theta, t) + z\Psi_\theta(\phi, \theta, t), \\ w(\phi, \theta, z, t) &= W_0(\phi, \theta, t) \end{aligned} \quad (1)$$

and the strain-displacement equations given in [Leissa and Chang 1996] for a general spherical shell become, for a spherical shell segment,

$$\begin{aligned} \epsilon_\phi &= \frac{\epsilon_{0\phi} + zk_\phi}{1 + z/R_0}, & \epsilon_\theta &= \frac{\epsilon_{0\theta} + zk_\phi}{1 + z/R_0}, \\ \gamma_{\phi\theta} &= \frac{\gamma_{0\phi\theta} + z\tau_{\phi\theta} + \gamma_{0\theta\phi} + z\tau_{\theta\phi}}{1 + z/R_0}, \\ \gamma_{\phi z} &= \frac{\gamma_{0\phi z}}{1 + z/R_0}, & \gamma_{\theta z} &= \frac{\gamma_{0\theta z}}{1 + z/R_0}, \end{aligned} \quad (2)$$

where we have denoted by $\epsilon_{0..}$, $\gamma_{0..}$ and k . the strains and curvatures of the middle surface of the shell, given by the expressions

$$\begin{aligned}
 \epsilon_{0\phi} &= \frac{1}{R_0} \frac{\partial U_0}{\partial \phi} + \frac{W_0}{R_0}, & \epsilon_{0\theta} &= \frac{1}{R_p} \frac{\partial V_0}{\partial \theta} + \frac{U_0}{R_0 R_p} \frac{\partial R_p}{\partial \phi} + \frac{W_0}{R_0}, \\
 k_\phi &= \frac{1}{R_0} \frac{\partial \Psi_\phi}{\partial \phi}, & k_\theta &= \frac{1}{R_p} \frac{\partial \Psi_\theta}{\partial \theta} + \frac{\Psi_\phi}{R_0 R_p} \frac{\partial R_p}{\partial \phi}, \\
 \gamma_{0\phi\theta} &= \frac{1}{A} \frac{\partial V_0}{\partial \phi}, & \gamma_{0\theta\phi} &= \frac{1}{R_p} \frac{\partial U_0}{\partial \theta} - \frac{V_0}{R_0 R_p} \frac{\partial R_p}{\partial \phi}, \\
 \gamma_{0\phi z} &= \frac{1}{R_0} \frac{\partial W_0}{\partial \phi} \frac{U_0}{R_0} + \Psi_\phi, & \gamma_{0\theta z} &= \frac{1}{R_p} \frac{\partial W_0}{\partial \theta} - \frac{V_0}{R_0} + \Psi_\theta.
 \end{aligned} \tag{3}$$

Substituting the shell parameters into the five equations of motion of general shells [Leissa and Chang 1996] using the relations for principle shell coordinates ($\alpha_1 = \phi, \alpha_2 = \theta$), Lamé’s coefficients ($A = R_0, B = R_p(\phi) = R_0 \sin \phi$) and radii of curvatures ($R_1 = R_2 = R_0$) yields the five equilibrium equations for a spherical shell segment with variable thickness:

$$\left. \begin{aligned}
 &\frac{dR_p(\phi)}{d\phi} N_\phi(\phi, \theta) + R_p(\phi) \frac{\partial N_\phi(\phi, \theta)}{\partial \phi} + R_0 \frac{\partial N_{\theta\phi}(\phi, \theta)}{\partial \theta} - \frac{\partial R_p(\phi)}{\partial \phi} N_\theta(\phi, \theta) \\
 &\quad + R_0 R_p(\phi) Q_\phi(\phi, \theta) - R_p(\phi) (R_0 I_1(\phi) \ddot{U}_0(\phi, \theta, t) + 2I_3(\phi) \ddot{\Psi}_\phi(\phi, \theta, t)) = 0, \\
 &R_0 \frac{\partial N_\theta(\phi, \theta)}{\partial \theta} + \frac{dR_p(\phi)}{d\phi} N_{\phi\theta}(\phi, \theta) + R_p(\phi) \frac{\partial N_{\phi\theta}(\phi, \theta)}{\partial \phi} + \frac{dR_p(\phi)}{d\phi} N_{\theta\phi}(\phi, \theta) \\
 &\quad + R_p(\phi) Q_\theta(\phi, \theta) - R_p(\phi) (R_0 I_1(\phi) \ddot{V}_0(\phi, \theta, t) + 2I_3(\phi) \ddot{\Psi}_\theta(\phi, \theta, t)) = 0, \\
 &-R_p(\phi) N_\phi(\phi, \theta) - R_p(\phi) N_\theta(\phi, \theta) + \frac{\partial R_p(\phi)}{\partial \phi} Q_\phi(\phi, \theta) \\
 &\quad + R_p(\phi) \frac{\partial Q_\phi(\phi, \theta)}{\partial \phi} + R_0 \frac{\partial Q_\theta(\phi, \theta)}{\partial \theta} - R_0 R_p(\phi) I_1(\phi) \ddot{W}_0(\phi, \theta, t) = 0, \\
 &\frac{dR_p(\phi)}{d\phi} M_\phi(\phi, \theta) + R_p(\phi) \frac{\partial M_\phi(\phi, \theta)}{\partial \phi} + R_0 \frac{\partial M_{\theta\phi}(\phi, \theta)}{\partial \theta} - \frac{\partial R_p(\phi)}{\partial \theta} M_\theta(\phi, \theta) \\
 &\quad - R_0 R_p(\phi) Q_\phi(\phi, \theta) - R_p(\phi) (2I_3(\phi) \ddot{U}_0(\phi, \theta, t) + R_0(\phi) I_3(\phi) \ddot{\Psi}_\phi(\phi, \theta, t)) = 0, \\
 &R_0 \frac{\partial M_\theta(\phi, \theta)}{\partial \theta} + \frac{dR_p(\phi)}{d\phi} M_{\phi\theta}(\phi, \theta) + R_p(\phi) \frac{\partial M_{\phi\theta}(\phi, \theta)}{\partial \phi} + \frac{\partial R_p(\phi)}{\partial \phi} M_{\theta\phi}(\phi, \theta) \\
 &\quad - R_0 R_p(\phi) Q_\theta(\phi, \theta) - R_p(\phi) (2I_3(\phi) V_0(\phi, \theta, t) + R_0 I_3(\phi) \ddot{\Psi}_\theta(\phi, \theta, t)) = 0.
 \end{aligned} \right\} \tag{4}$$

with variable quantities $I_1(\phi), I_3(\phi)$ obtained by integration of the material density through the thickness as follows:

$$I_1(\phi) = \int_{-h(\phi)/2}^{+h(\phi)/2} \rho dz = \rho h(\phi), \quad I_3(\phi) = \int_{-h(\phi)/2}^{+h(\phi)/2} \rho z^2 dz = \frac{\rho h^3(\phi)}{12}. \tag{5}$$

The stress-strain relations for an isotropic material are given by

$$\begin{Bmatrix} \sigma_\phi \\ \sigma_\theta \\ \sigma_{\phi\theta} \\ \sigma_{\phi z} \\ \sigma_{\theta z} \end{Bmatrix} = \frac{E}{1-\mu^2} \begin{bmatrix} 1 & \mu & 0 & 0 & 0 \\ \mu & 1 & 0 & 0 & 0 \\ 0 & 0 & (1-\mu)/2 & 0 & 0 \\ 0 & 0 & 0 & (1-\mu)/2 & 0 \\ 0 & 0 & 0 & 0 & (1-\mu)/2 \end{bmatrix} \begin{Bmatrix} \epsilon_\phi \\ \epsilon_\theta \\ \gamma_{\phi\theta} \\ \gamma_{\phi z} \\ \gamma_{\theta z} \end{Bmatrix}, \quad (6)$$

where E is the modulus of elasticity and μ is Poisson's ratio. For isotropic materials the force and moment resultants are obtained by integrating the stresses through the shell thickness, which in this case is variable along the meridian:

$$\begin{Bmatrix} N_\phi(\phi, \theta) \\ N_\theta(\phi, \theta) \\ N_{\phi\theta}(\phi, \theta) \\ N_{\theta\phi}(\phi, \theta) \end{Bmatrix} = \int_{-h(\phi)/2}^{+h(\phi)/2} \begin{Bmatrix} \sigma_\phi(z) \\ \sigma_\theta(z) \\ \sigma_{\phi\theta}(z) \\ \sigma_{\theta\phi}(z) \end{Bmatrix} \left(1 + \frac{z}{R_0}\right) dz, \quad (7)$$

$$\begin{Bmatrix} Q_\phi(\phi, \theta) \\ Q_\theta(\phi, \theta) \end{Bmatrix} = \kappa \int_{-h(\phi)/2}^{+h(\phi)/2} \begin{Bmatrix} \sigma_{\phi z}(z) \\ \sigma_{\theta z}(z) \end{Bmatrix} \left(1 + \frac{z}{R_0}\right) dz, \quad (8)$$

$$\begin{Bmatrix} M_\phi(\phi, \theta) \\ M_\theta(\phi, \theta) \\ M_{\phi\theta}(\phi, \theta) \\ M_{\theta\phi}(\phi, \theta) \end{Bmatrix} = \int_{-h(\phi)/2}^{+h(\phi)/2} \begin{Bmatrix} \sigma_\phi(z) \\ \sigma_\theta(z) \\ \sigma_{\phi\theta}(z) \\ \sigma_{\theta\phi}(z) \end{Bmatrix} \left(1 + \frac{z}{R_0}\right) z dz, \quad (9)$$

where κ is a shear correction factor. Various derivations of the shear correction factor have been proposed. Mindlin [1951] gave an implicit result for the shear correction factor for isotropic elastic plates that depends on Poisson ratio μ . Hutchinson [1984] determined the shear coefficient in a Mindlin plate equation based on matching a mode of the Mindlin plate theory to the exact Rayleigh–Lamb frequency equation for the flexural wave response at long wavelengths and proposed the value $\kappa = 5/(6 - \mu)$. Later, Stephen [1997] reexamined this solution, and called this the “best” shear coefficient. In the present work this value of Hutchinson's shear coefficient is used in the calculations.

Considering the stress-strain relations, the kinematical relations for shells with variable thickness the constitutive relations become

$$\begin{aligned} N_\phi(\phi, \theta) &= \frac{E}{1-\mu^2} h(\phi) (\epsilon_{0\phi} + \mu \epsilon_{0\theta}), & N_\theta(\phi, \theta) &= \frac{E}{1-\mu^2} h(\phi) (\mu \epsilon_{0\phi} + \epsilon_{0\theta}), \\ Q_\phi(\phi, \theta) &= \frac{\kappa E}{2(1+\mu)} h(\phi) \gamma_{0\phi n}, & Q_\theta(\phi, \theta) &= \frac{\kappa E}{2(1+\mu)} h(\phi) \gamma_{0\theta n}, \\ N_{\phi\theta}(\phi, \theta) &= \frac{E}{2(1+\mu)} h(\phi) (\gamma_{0\phi\theta} + \gamma_{0\theta\phi}), & N_{\theta\phi}(\phi, \theta) &= N_{\phi\theta}(\phi, \theta), \\ M_\phi(\phi, \theta) &= \frac{E}{1-\mu^2} \frac{h^3(\phi)}{12} (k_\phi + \mu k_\theta), & M_\theta(\phi, \theta) &= \frac{E}{1-\mu^2} \frac{h^3(\phi)}{12} (\mu k_\phi + k_\theta), \\ M_{\phi\theta}(\phi, \theta) &= \frac{E}{2(1+\mu)} \frac{h^3(\phi)}{12} (\tau_{\phi\theta} + \tau_{\theta\phi}), & M_{\theta\phi}(\phi, \theta) &= M_{\phi\theta}(\phi, \theta). \end{aligned} \quad (10)$$

3. Solution procedure

We introduce a nondimensional coordinate $\xi = (\phi - \phi_b)/\phi_0$ that vary from 0 to 1. The variation of the geometric parameters h and R_p is taken in a polynomial form as follows:

$$h(\phi) \implies h(\xi) = \sum_{i=0}^{nh} h_i \xi^i, \quad R_p(\phi) \implies R_p(\xi) = \sum_{i=0}^{nR_p} R_{pi} \xi^i, \quad (11)$$

Spherical shell segments with a wide range of meridian opening angles, concave or convex thickness variation can be described in this way, up to any desired accuracy. In case of shell with wavy or corrugated surface, it could be represented by segmented shell with sequential shell segments with convex and concave thickness variation.

When the force and moment resultants are substituted into the equations of motion (4), assuming harmonic vibrations, and using the assumed displacement field

$$\begin{aligned} U_0(\phi, \theta, t) &= u(\phi) \cos n\theta \sin \omega t, \\ V_0(\phi, \theta, t) &= v(\phi) \sin n\theta \sin \omega t, \\ W_0(\phi, \theta, t) &= w(\phi) \cos n\theta \sin \omega t, \\ \Psi_\phi(\phi, \theta, t) &= \psi_\phi(\phi) \cos n\theta \sin \omega t, \\ \Psi_\theta(\phi, \theta, t) &= \psi_\theta(\phi) \sin n\theta \sin \omega t, \end{aligned} \quad (12)$$

with the notation

$$U(\phi) = \{u(\phi), v(\phi), w(\phi), \psi_\phi(\phi), \psi_\theta(\phi)\}^T \quad (13)$$

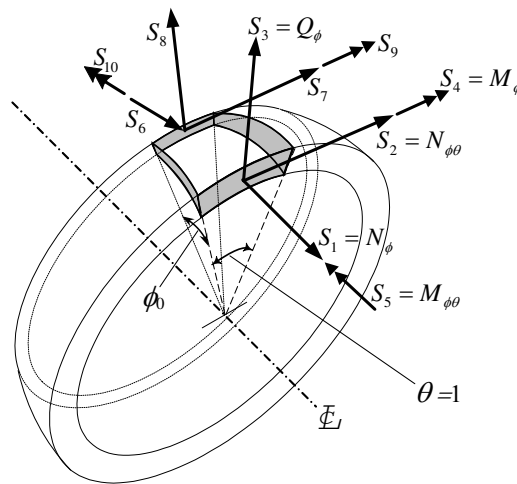


Figure 2. Dynamic stiffnesses defined by resultant forces along a unit angle segment of the perimeter of the shell edges ($\xi = 0, \xi = 1$).

after transformation to the nondimensional coordinate ξ , we obtain the equations of motion in term of the displacements as

$$\mathbf{K}^{(0)}(\xi, \omega)\mathbf{U}(\xi) + \mathbf{K}^{(1)}(\xi)\mathbf{U}'(\xi) + \mathbf{K}^{(2)}(\xi)\mathbf{U}''(\xi) = 0, \quad (14)$$

where primes refer to derivatives with respect to ξ , and the terms in the matrices $\mathbf{K}^{(0)}$, $\mathbf{K}^{(1)}$, and $\mathbf{K}^{(2)}$ are given in the Appendix. The solution is obtained using the exact element method algorithm [Eisenberger 1990] by assuming the solution as infinite power series

$$\mathbf{U}(\xi) = \sum_{i=0}^{\infty} \mathbf{u}_i \xi^i, \quad (15)$$

and following the procedure in [Eisenberger 1990] we get the five basic shape functions for each case of unit displacement on the shell edges. Based on the values of the shape functions and their derivatives at the two edges of the segment ($\xi = 0$; $\xi = 1$) we get the terms in the dynamic stiffness matrix as the resultant forces along the unit angle segment of the perimeter of the shell, as shown in Figure 2, as

$$\begin{aligned} \left. \begin{matrix} S_1 \\ S_6 \end{matrix} \right\} &= N_\phi \Big|_{\substack{\xi=0 \\ \xi=1}} = \frac{E}{1-\mu^2} \left[\frac{R'_p \Phi}{R_0} \mu u + \frac{R_p \Phi}{R_0} u' + \mu n v + \left(\frac{R_p}{R_0} (1+\mu) \right) w \right] \Big|_{\substack{\xi=0 \\ \xi=1}}, \\ \left. \begin{matrix} S_2 \\ S_7 \end{matrix} \right\} &= N_{\phi\theta} \Big|_{\substack{\xi=0 \\ \xi=1}} = \frac{E}{2(1+\mu)} \left[-nu - \frac{R'_p \Phi}{R_0} v + \frac{R_p \Phi}{R_0} v' \right] \Big|_{\substack{\xi=0 \\ \xi=1}}, \\ \left. \begin{matrix} S_3 \\ S_8 \end{matrix} \right\} &= Q_\phi \Big|_{\substack{\xi=0 \\ \xi=1}} = \frac{\kappa E}{2(1+\mu)} \left[-\frac{R_p}{R_0} u + \frac{R_p \Phi}{R_0} w' + \psi_s \right] \Big|_{\substack{\xi=0 \\ \xi=1}}, \\ \left. \begin{matrix} S_4 \\ S_9 \end{matrix} \right\} &= M_\phi \Big|_{\substack{\xi=0 \\ \xi=1}} = \frac{E}{(1-\mu^2)} \frac{h^3}{12} \left[\mu \frac{R'_p \Phi}{R_0} \psi_\phi + \frac{R_p \Phi}{R_0} \psi'_\phi + \mu n \psi_\phi \right] \Big|_{\substack{\xi=0 \\ \xi=1}}, \\ \left. \begin{matrix} S_5 \\ S_{10} \end{matrix} \right\} &= M_{\phi\theta} \Big|_{\substack{\xi=0 \\ \xi=1}} = \frac{E}{2(1+\mu)} \frac{h^3}{12} \left[-n \psi_\phi - \frac{R'_p \Phi}{R_0} \psi_\theta + \left(\frac{R_p}{R_0} \right) \Phi \psi'_\theta \right] \Big|_{\substack{\xi=0 \\ \xi=1}}. \end{aligned} \quad (16)$$

The dynamic stiffness matrix for a segment, having ten degrees of freedom, five on each edge, is then assembled for the structure in the usual procedure of structural analysis. The natural frequencies of vibration are found as the values of the frequency that will cause the assembled dynamic stiffness matrix of the structure to become singular.

When the cut-outs size becomes relatively small ($R_{p,\text{in}}/R_{p,\text{out}} < 0.1$) the shape functions series converges rather slowly and have relatively large number of terms. Therefore, in order speed the convergence process one can divide the shell into sections with ratio $R_{p,\text{in}} = 0.3R_{p,\text{out}}$ for each section. So, by adding a small number of elements one can solve for shells with very small cut-outs (e.g., three elements for $R_{p,\text{in}} = 0.03R_{p,\text{out}}$ and four elements for $R_{p,\text{in}} = 0.01R_{p,\text{out}}$).

4. Numerical examples

In order to obtain a high-precision solution for vibration problems of thick spherical shells, numerical calculations have been performed for a spherical shells with different thickness-radius ratios, and various

<i>n</i>	<i>h/R</i> = 0.1						<i>h/R</i> = 0.2					
	Clamped-Free			SS-Free			Clamped-Free			SS-Free		
	5 DOF	Lit.	Diff.%	7 DOF	Lit.	Diff.%	5 DOF	Lit.	Diff.%	7 DOF	Lit.	Diff.%
0	0.9810	0.978	0.30	0.9079	0.906	0.21	1.1403	1.133	0.64	1.0516	1.047	0.44
	1.3025	1.297	0.42	1.3025	1.297	0.42	1.3025	1.297	0.42	1.3022	1.297	0.40
	1.3398	1.340	-0.01	1.3398	1.340	-0.02	1.4212	1.427	-0.40	1.3583	1.358	0.02
1	0.7052	0.704	0.17	0.6593	0.658	0.19	0.7553	0.753	0.30	0.6785	0.678	0.08
	1.0757	1.073	0.25	1.0172	1.014	0.32	1.2999	1.295	0.38	1.2065	1.203	0.29
	1.6828	1.684	-0.07	1.5745	1.572	0.16	1.9858	1.982	0.19	1.9829	1.965	0.91
2	0.4477	0.445	0.61	0.4111	0.409	0.51	0.6530	0.653	0.00	0.5687	0.571	-0.41
	1.2783	1.275	0.26	1.1921	1.185	0.60	1.6917	1.688	0.22	1.5586	1.550	0.56
	1.8342	1.835	-0.05	1.7248	1.722	0.16	2.0241	2.022	0.10	2.0181	2.007	0.55
3	0.7617	0.764	-0.30	0.7453	0.747	-0.23	1.1415	1.157	-1.34	1.0726	1.086	-1.24
	1.4676	1.465	0.17	1.3656	1.357	0.63	2.0931	2.087	0.29	1.9374	1.922	0.80
	2.1411	2.142	-0.04	1.9834	1.979	0.22	2.4381	2.435	0.13	2.4306	2.428	0.11
4	1.1698	1.176	-0.52	1.1406	1.145	-0.38	1.6949	1.719	-1.40	1.6041	1.622	-1.11
	1.7184	1.718	0.02	1.6085	1.602	0.41	2.5572	2.557	0.01	2.4219	2.426	-0.17
	2.4824	2.776	-10.6	2.3148	2.311	0.17	3.1124	3.107	0.17	3.0877	3.087	0.02
5	1.5177	1.525	-0.48	1.4576	1.461	-0.23	2.2095	2.235	-1.14	2.0996	2.118	-0.87
	2.1060	2.109	-0.14	1.9964	1.994	0.12	3.1445	3.151	-0.21	3.0215	3.024	-0.08
	2.8804	2.885	-0.16	2.7240	2.721	0.11	3.8489	3.860	-0.29	3.8133	3.851	-0.98

Table 1. Nondimensional frequency $\lambda = \omega R \sqrt{\rho/E}$ for a hemispherical shell with a 30° cutout at the apex, with free boundary conditions at the cutout and different boundary conditions at the base. The columns “5 DOF” and “7 DOF” give the result with the present method (one exact element and the specified number of degrees of freedom). “Lit.” refers to [Gautham and Ganesan 1992]. “Diff.%” is the ratio $(\lambda_{\text{exact}} - \lambda_{\text{FE}})/\lambda_{\text{FE}}$.

combinations of boundary conditions: constant thickness hemispherical caps with annular cutout at the apex, variable thickness spherical annular segment, and variable thickness spherical barrel shell.

The results for the constant thickness hemispherical shells are set out in Tables 1 and 2 for two cutout sizes (60° and 30°), and with two types of boundary conditions at the base: clamped and simply supported, and two thickness/radius ratios: 0.1 and 0.2. A comparison is made with the results of the FE analysis of [Gautham and Ganesan 1992] that were obtained by using Nagdhi’s basic relations that take the transverse shear and the normal strain into consideration. Three-noded finite elements with 7 DOF per node were used for solving the problem. Good general agreement of the results is shown. Some fictitious frequencies given by FE analysis can be observed (marked in bold).

Table 3, left, presents a comparison of the natural frequencies for an annular hemispherical shell with linearly varying thickness ($\phi_0 = 60^\circ$, $h_b/h_e = 1/3$) (Figure 3, left). The comparison is performed with the results from FE analysis using the commercial code ABAQUS, and the results from a three-dimensional analysis by the Ritz method reported in [Kang and Leissa 2006]. The results of the present

n	$h/R = 0.1$						$h/R = 0.2$					
	Clamped-Free			SS-Free			Clamped-Free			SS-Free		
	5 DOF	Lit.	Diff.%	7 DOF	Lit.	Diff.%	5 DOF	Lit.	Diff.%	7 DOF	Lit.	Diff.%
0	1.1353	1.139	-0.32	1.0722	1.072	0.02	1.2777	1.289	-0.88	1.0583	1.059	-0.06
	2.0232	2.014	0.45	1.7280	1.726	0.12	2.0232	2.013	0.50	2.0223	2.014	0.41
	2.1232	2.125	-0.08	2.0231	2.010	0.65	2.7504	2.747	0.12	2.4947	2.487	0.31
1	0.9833	0.984	-0.07	0.8890	0.887	0.22	1.1492	1.152	-0.24	0.8968	0.895	0.20
	2.1026	2.106	-0.16	1.7584	1.756	0.14	2.3395	2.337	0.11	2.3347	2.332	0.12
	2.4140	2.408	0.25	2.3790	2.369	0.42	2.8142	2.810	0.15	2.5781	2.565	0.51
2	0.7965	0.794	0.32	0.6507	0.648	0.41	1.0567	1.053	0.35	0.7540	0.751	0.40
	2.2267	2.232	-0.24	1.8775	2.038	-7.88	2.8075	2.822	-0.51	2.6616	2.670	-0.31
	3.0967	3.088	0.28	3.0846	2.764	11.6	3.1626	3.150	0.40	3.1131	3.087	0.85
3	0.7515	0.748	0.47	0.5844	0.581	0.58	1.1578	1.154	0.33	0.8790	0.879	0.00
	2.4119	2.416	-0.17	2.0644	2.522	-18.1	3.0761	3.099	-0.74	2.9268	2.939	-0.42
	3.3919	3.398	-0.18	3.3843	2.524	34.1	3.6591	3.634	0.69	3.5337	3.459	2.16
4	0.8764	0.873	0.39	0.7344	0.731	0.47	1.4400	1.441	-0.07	1.2250	1.230	-0.40
	2.6411	2.643	-0.07	2.2964	2.307	-0.46	3.3779	3.407	-0.85	3.2616	3.278	-0.50
	3.5287	3.532	-0.09	3.5250	3.477	1.38	3.8222	3.782	1.06	3.6590	3.586	2.03
5	1.1272	1.126	0.11	1.0160	1.014	0.20	1.8473	1.853	-0.31	1.6855	1.693	-0.44
	2.8959	2.894	0.06	2.5589	2.546	0.51	3.7419	3.772	-0.80	3.6600	3.675	-0.41
	3.7873	3.789	-0.04	3.7869	3.780	0.18	4.0686	4.025	1.08	3.8853	3.818	1.76

Table 2. Nondimensional frequency $\lambda = \omega R \sqrt{\rho/E}$ for hemispherical shells with 60° cutout at the apex, with free boundary conditions at the cutout and different boundary conditions at the base. The columns “5 DOF” and “7 DOF” give the result with the present method (one exact element and the specified number of degrees of freedom). “Lit.” refers to [Gautham and Ganesan 1992]. “Diff.%” is the ratio $(\lambda_{\text{exact}} - \lambda_{\text{FE}})/\lambda_{\text{FE}}$.

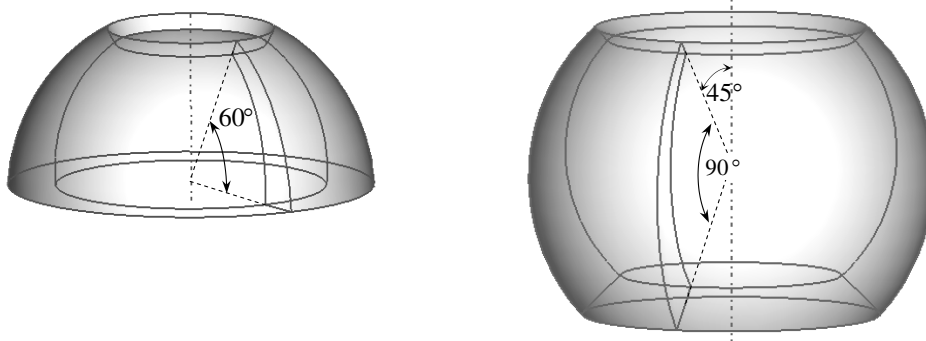


Figure 3. Left: hemispherical annular shell with linearly varying thickness; $\phi_0 = 60^\circ$, $h_b/h_e = 1/3$ (results in Table 3, left). Right: spherical barrel shell with variable thickness; $\phi_b = 45^\circ$, $\phi_e = 135^\circ$, $(h_b + h_e)/2R = 0.2$, $h_b/h_e = 1/3$, $\mu = 0.3$ (results in Table 3, right, and Figures 4–7).

n	2D FE 1600 S4R shell els. 10080 DOF	3D FE 2095 C3D20R solid els. 43020 DOF	[Kang and Leissa 2006] 3D, Ritz	Present DSM with 2 exact els. 15 DOF	3D FE 2095 C3D20R solid els. 43020 DOF	[Kang and Leissa 2006] 3D, Ritz	Present DSM with 3 exact els. 20 DOF
0 (A)	1.5357	1.5361	1.536	1.5347	1.5345	1.535	1.5299
	2.1152	2.0862	2.090	2.1138	1.9099	1.911	1.9268
	2.3992	2.4216	2.423	2.4057	1.9632	1.963	1.9651
	4.3117	4.3143	4.322	4.3041	2.4772	2.487	2.4846
	5.9909	5.8511	5.844	5.9780	3.8292	3.844	3.8355
0 (T)	3.7144	3.6775	3.669	3.7053	2.4774	2.470	2.4938
	6.5151	6.3843	6.385	6.4586	4.2877	4.290	4.3343
	9.5088	9.1976	9.200	9.3248	6.1689	6.172	6.2411
					NA	8.093	8.1862
1	1.5666	1.5687	1.568	1.5645	1.3915	1.390	1.3898
	2.4016	2.3730	2.374	2.3990	1.7690	1.771	1.7688
	2.4824	2.4819	2.485	2.4845	2.3793	2.379	2.4037
	4.4149	4.4072	4.414	4.4101	2.5836	2.594	2.5915
	4.6268	4.5782	4.572	4.6131	3.4497	3.445	3.4897
2	0.3495	0.3495	0.349	0.3494	0.3593	0.362	0.3613
	0.7135	0.7031	0.705	0.7136	0.6065	0.604	0.6076
	1.8514	1.8563	1.857	1.8443	1.6842	1.690	1.6977
	2.8071	2.8044	2.809	2.8093	2.0238	2.027	2.0281
	3.6503	3.5714	3.572	3.6372	2.8902	2.901	2.9006
3	0.9382	0.9368	0.934	0.9364	0.9085	0.918	0.9169
	1.6815	1.6615	1.666	1.6794	1.4032	1.400	1.3997
	2.6617	2.6422	2.646	2.6436	2.2845	2.298	2.3155
	3.3486	3.3397	3.346	3.3494	2.6510	2.651	2.6687
	4.8367	4.7495	4.746	4.8121	3.3737	3.385	3.3824
4	1.6823	1.6757	1.671	1.6753	1.5436	1.561	1.5597
	2.6672	2.6368	2.643	2.6577	2.1947	2.196	2.1917
	3.6246	3.5577	3.564	3.5878	2.9024	2.911	2.9192
	4.0553	4.0540	4.060	4.0547	3.5713	3.579	3.6300
	5.8216	5.8013	5.793	5.8063	4.0506	4.059	4.0507
5	2.5319	2.5140	2.507	2.5144	2.2465	2.271	2.2696
	3.6775	3.6304	3.637	3.6558	2.9445	2.954	2.9478
	4.5940	4.4686	4.475	4.5297	3.6991	3.707	3.7014
	4.9368	4.9436	4.951	4.9250	4.4644	4.477	4.5276
	6.6094	6.6536	6.665	6.6166	4.9457	4.952	4.9700

Table 3. Comparison of the nondimensional natural frequency $\Omega = \omega R \sqrt{\rho/G}$ for completely free spherical shells with linearly varying thickness. Left: annular shell with $\phi_b = 30^\circ$ and $\phi_e = 90^\circ$ (Figure 3, left). Right: barrel shell with $\phi_b = 45^\circ$ and $\phi_e = 135^\circ$ (Figure 3, right). In both cases, $(h_b + h_e)/2R = 0.2$, $h_b/h_e = 1/3$, and $\mu = 0.3$. “A” stands for axisymmetric modes, “T” for torsional modes.

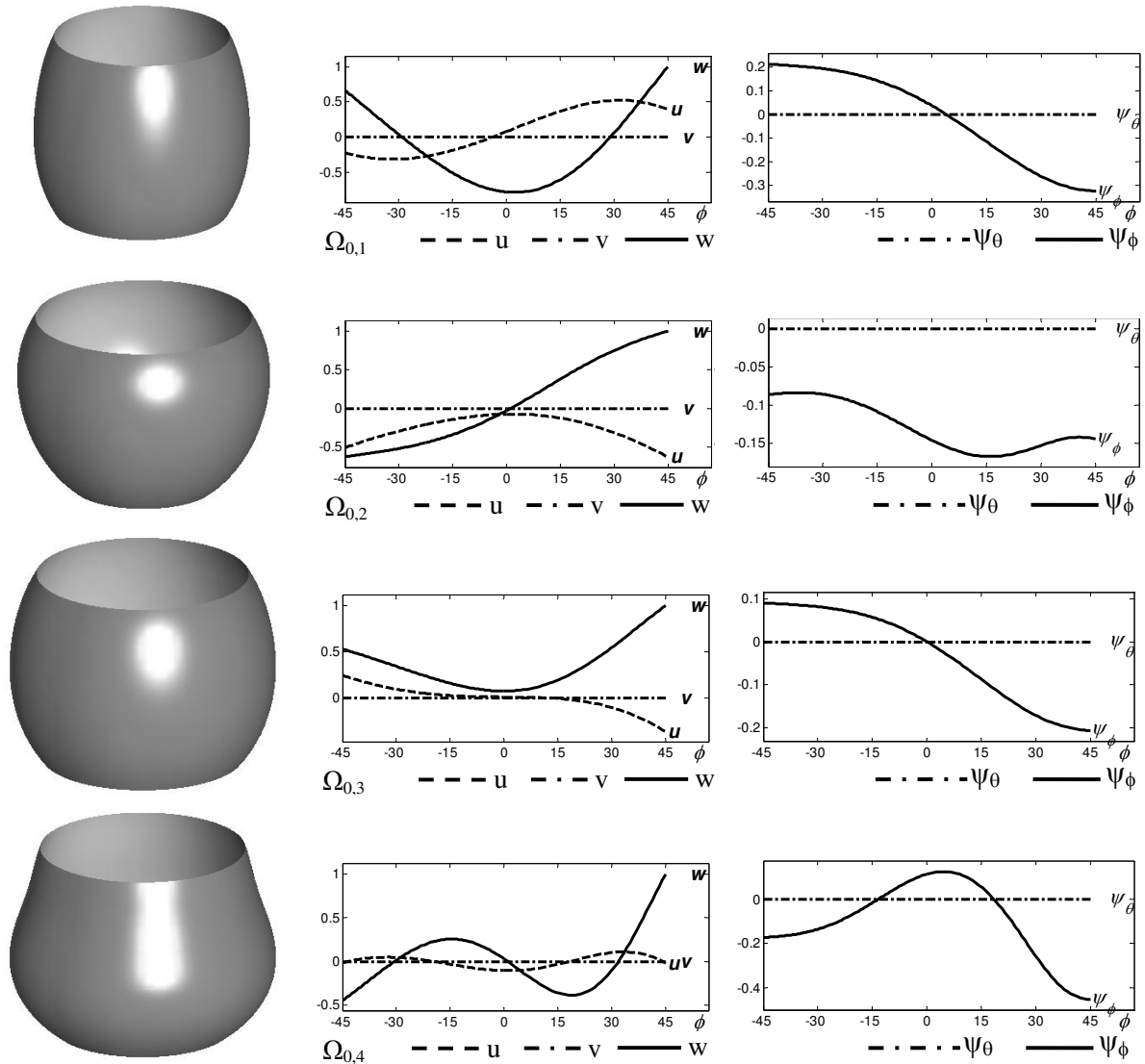


Figure 4. The first four mode shapes of axisymmetric vibrations ($n = 0$) of completely free spherical barrel shell with variable thickness (Figure 3, right).

exact analysis are generally lower than the results from the two-dimensional FE analysis, and for some modes the frequency is a little bit higher due to the difference in the shear correction factor that was used: $5/(6 - \mu)$ in the present analysis versus $5/6$ in the FE analysis. Comparison with the three-dimensional Ritz solution shows that the torsional modes in the present analysis are higher than the values in the three-dimensional analysis due to kinematical simplifications of the first order shear deformation shell theory. In other vibrational modes no clear tendency is observed.

The same conclusions are obtained from comparison of frequency results for barrel spherical shell ($\phi_b = 45^\circ$, $\phi_e = 135^\circ$, $(h_b + h_e)/2R = 0.2$, $h_b/h_e = 1/3$, $\mu = 0.3$) presented in Table 3, right. Figures 4,

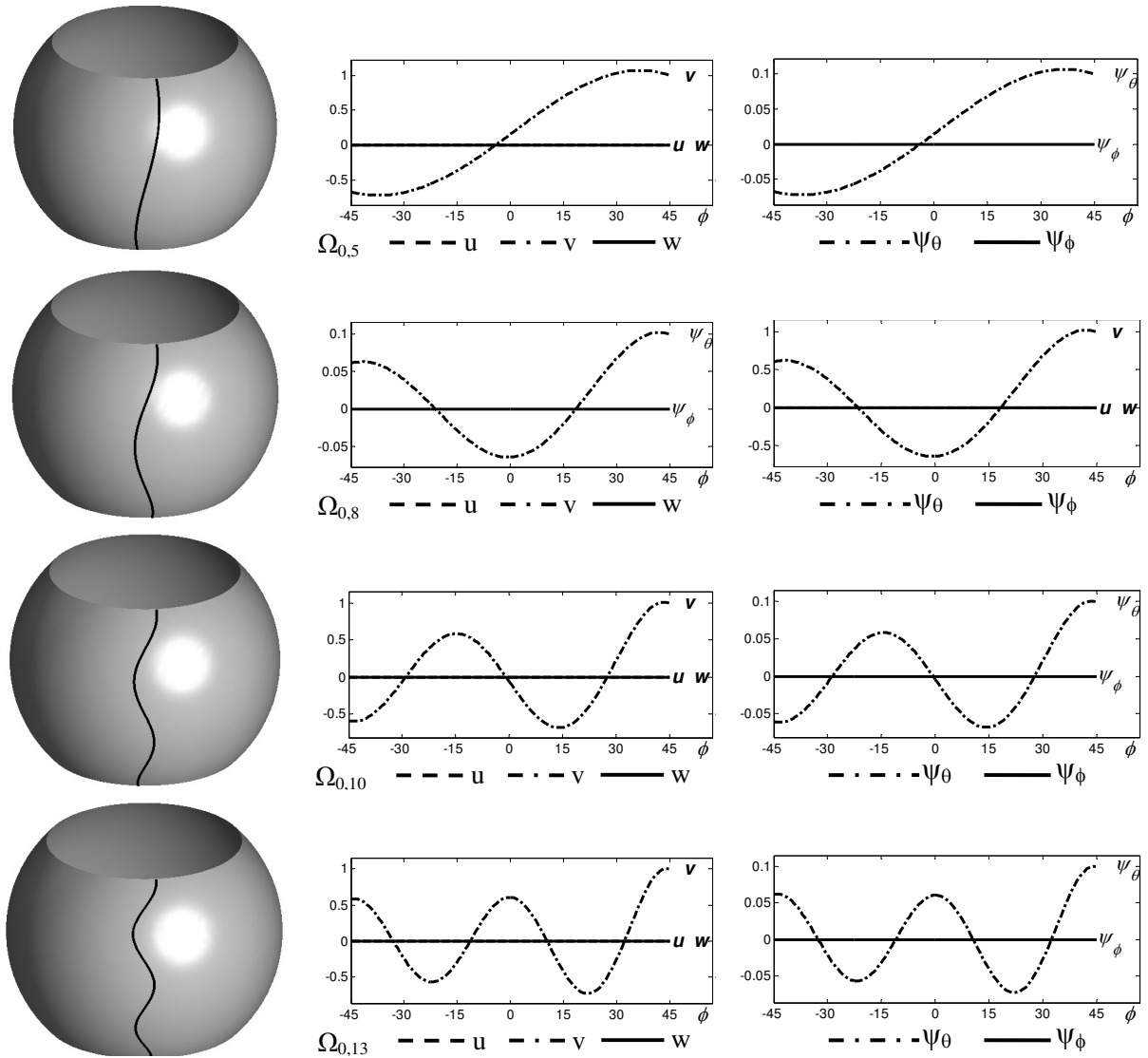


Figure 5. The first four mode shapes of pure torsional vibrations ($n = 0$) of completely free spherical barrel shell with variable thickness (Figure 3, right).

5, 6, and 7 show the three-dimensional vibrational modes and the exact displacement shape functions obtained by the present method.

5. Conclusions

The natural frequencies for spherical shells of revolution with different boundary conditions have been investigated using the Dynamic Stiffness method. This approach is combined with the exact element method for the vibration analysis of spherical shell segments with curved meridian and variable cross-section. The analysis uses the equations of the two-dimensional theory of elasticity, in which the effects

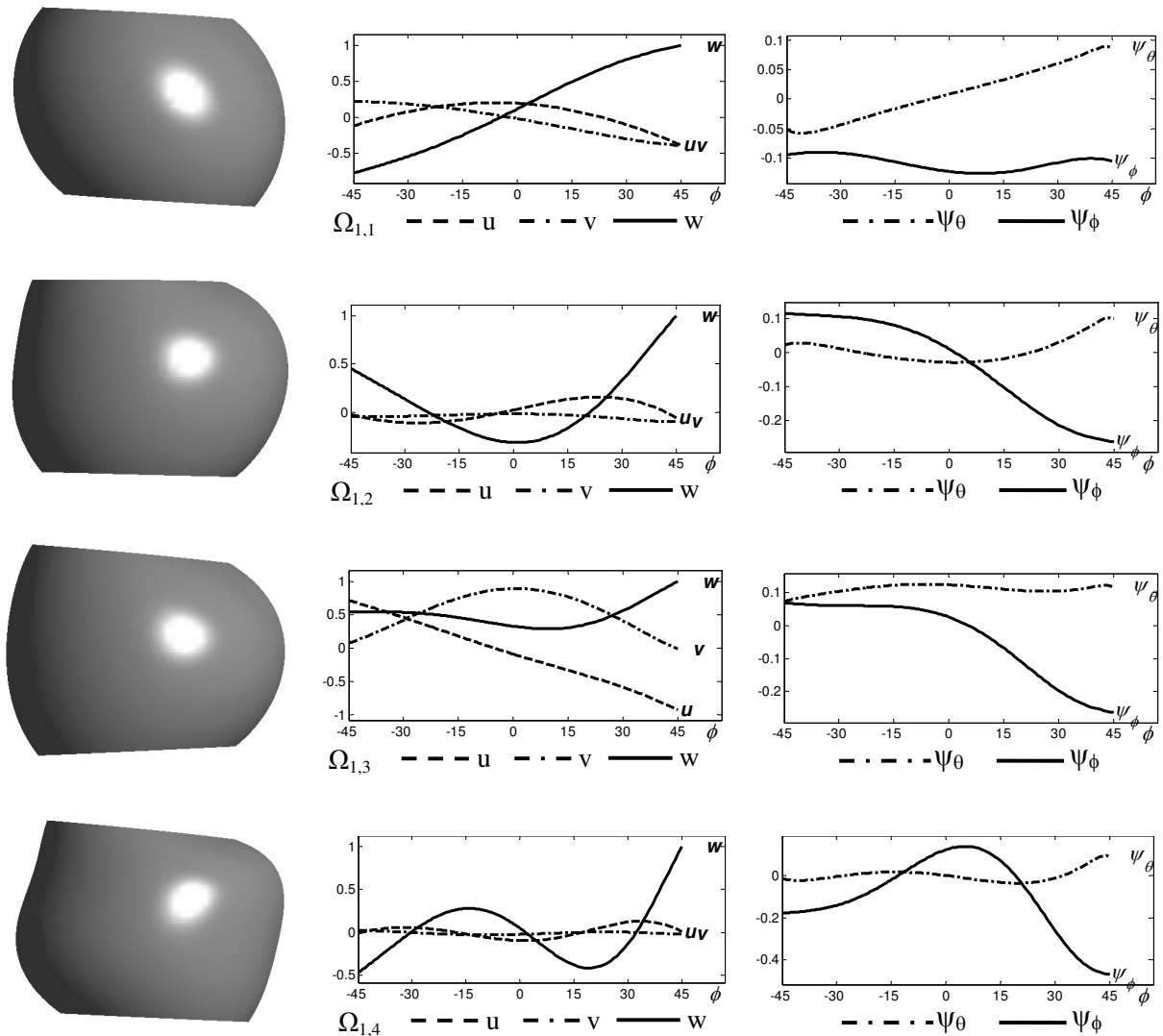


Figure 6. Mode shapes of vibrations with one circumferential waves ($n = 1$) of a completely free spherical barrel shell with variable thickness (Figure 3, right).

of both transverse shear stresses and rotary inertia are accounted for, in their general forms for isotropic homogeneous materials. The proposed method shows the following advantages:

- (1) Any polynomial variation of the thickness of the shell along the meridian can be considered.
- (2) The method is mesh-free, and dividing the surface to many elements doesn't improve the solution. No convergence study is necessary to obtain the true results.
- (3) The shape functions are derived automatically and they are the exact solutions for the system of the differential equation of motion with variable coefficients. As a result, the solution for free vibrations

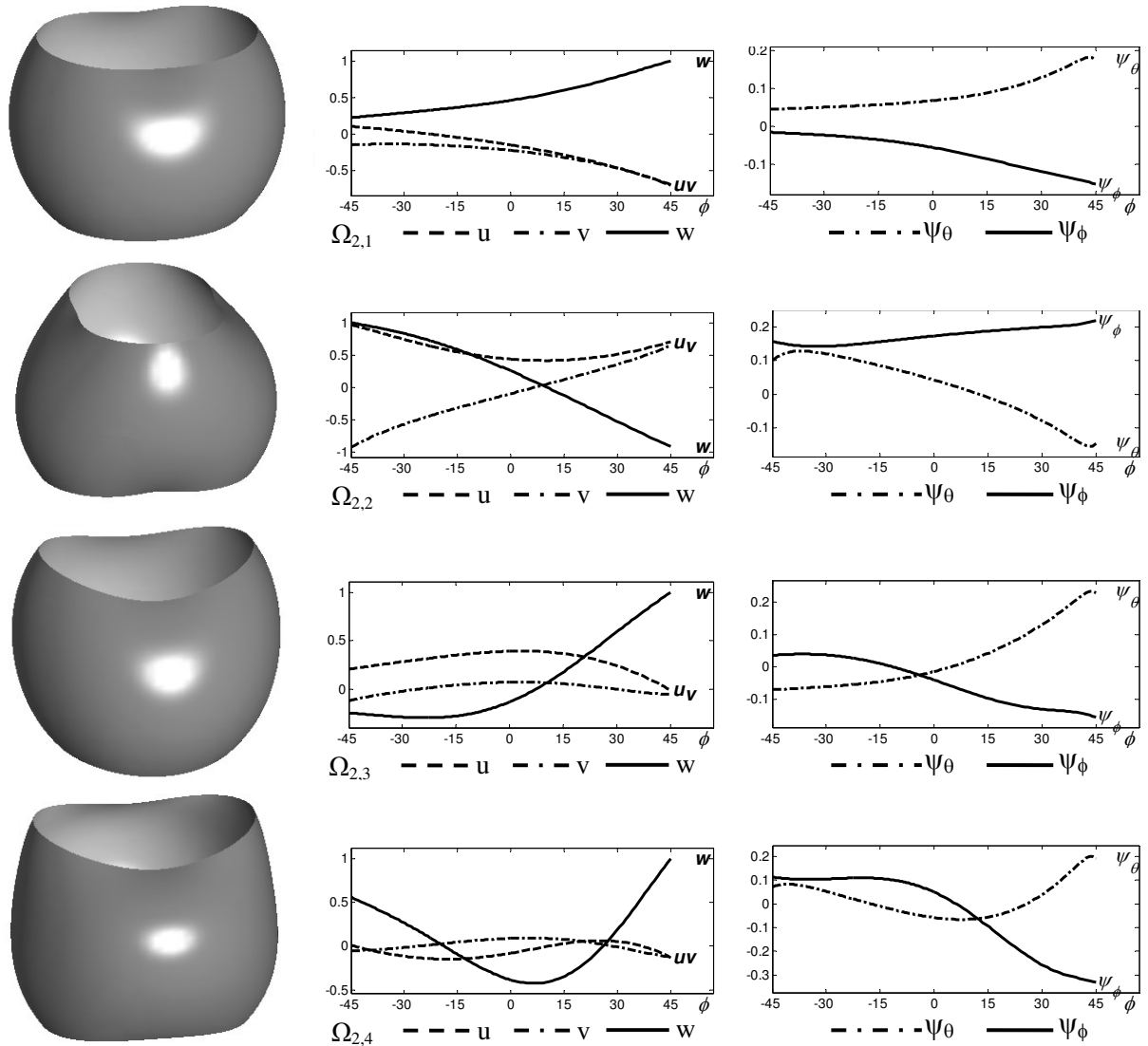


Figure 7. Mode shapes of vibrations with two circumferential waves ($n = 2$) of a completely free spherical barrel shell with variable thickness (Figure 3, right).

problem is a highly accurate solution (depending only on the accuracy of the numerical calculations).

- (4) The order of the frequency determinants which are required for the solution by the present method are at least an order of magnitude smaller than those needed by a finite element analysis of comparable accuracy.
- (5) The derived dynamic stiffness matrix allows combination of spherical shell segments into complex assemblies with different combinations of shell types, variable thickness, and analyzing them with small number of elements.

Appendix: Entries of the coefficient matrices $K^{(0)}$, $K^{(1)}$, and $K^{(2)}$ in Equation (14)

Only nonzero entries are listed. We set $\Phi = 1/\phi_0$.

$$\begin{aligned}
K_{11}^{(0)} &= \omega^2(\rho/E)(1-\mu^2)R_p^2R_0^3h + R_pR_0(R_p'h' + R_p''h)\Phi^2\mu - \frac{1}{2}(1-\mu)(R_p^2R_0\kappa h + R_0^3hn^2) \\
K_{12}^{(0)} &= \frac{1}{2}R_0^2n\Phi R_p'h(\mu-3) + R_0^2n\Phi R_p'h'\mu \\
K_{13}^{(0)} &= R_p^2R_0h'\Phi(1+\mu) & K_{14}^{(0)} &= \frac{1}{6}\omega^2(\rho/E)(1-\mu^2)R_p^2R_0^2h^3 + \frac{1}{2}(1-\mu)R_p^2R_0^2\kappa h \\
K_{21}^{(0)} &= \frac{1}{2}R_0^2n\Phi R_p'h(\mu-3) - \frac{1}{2}R_0^2n\Phi(1-\mu)R_p'h' \\
K_{22}^{(0)} &= \omega^2(1-\mu^2)(\rho/E)R_p^2R_0^3h - \frac{1}{2}(1-\mu)R_pR_p''R_0h\Phi^2\mu - \frac{1}{2}(1-\mu)R_pR_p'R_0h'\Phi^2 - R_0^3hn^2 \\
&\quad - \frac{1}{2}(1-\mu)R_p^2R_0\kappa h - \frac{1}{2}(1-\mu)R_p^2R_0h\Phi^2 \\
K_{23}^{(0)} &= -(1+\mu)R_pR_0^2hn - \frac{1}{2}(1-\mu)R_pR_0^2\kappa hn & K_{25}^{(0)} &= \frac{1}{6}\omega^2(\rho/E)(1-\mu^2)R_p^2R_0^2h^3 + \frac{1}{2}(1-\mu)R_p^2R_0^2\kappa h \\
K_{31}^{(0)} &= -(1+\mu)R_pR_p'R_0\Phi h - \frac{1}{2}(1-\mu)R_pR_p'R_0\kappa h\Phi - \frac{1}{2}(1-\mu)R_p^2R_0\kappa h'\Phi \\
K_{32}^{(0)} &= K_{23}^{(0)} & K_{33}^{(0)} &= \omega^2(\rho/E)(1-\mu^2)R_p^2R_0^3h - \frac{1}{2}(1-\mu)R_0^3\kappa hn^2 - 2(1+\mu)R_p^2R_0h \\
K_{34}^{(0)} &= \frac{1}{2}(1-\mu)(R_p^2R_0^2\kappa h' + R_pR_p'R_0^2\Phi\kappa h) & K_{35}^{(0)} &= \frac{1}{2}(1-\mu)R_pR_0^3\kappa hn \\
K_{41}^{(0)} &= K_{14}^{(0)} \\
K_{44}^{(0)} &= \frac{1}{12}\omega^2(\rho/E)(1-\mu^2)R_p^2R_0^3h^3 - \frac{1}{24}(1-\mu)R_0^3h^3n^2 - \frac{1}{12}R_p^2R_0h^3\Phi^2(1+\mu) \\
&\quad - \frac{1}{2}(1-\mu)R_p^2R_0^3\kappa h + \frac{1}{12}R_pR_p''R_0h^3\Phi^2\mu + \frac{1}{4}R_pR_p'R_0h'h^2\Phi^2\mu \\
K_{45}^{(0)} &= \frac{1}{4}n\mu R_pR_0^2h'h^2\Phi - \frac{1}{24}R_p^2R_0^2n\Phi h^3(3-\mu) \\
K_{52}^{(0)} &= K_{25}^{(0)} & K_{53}^{(0)} &= K_{35}^{(0)} & K_{54}^{(0)} &= -\frac{1}{8}(1-\mu)nR_pR_0^2h'h^2\Phi - \frac{1}{24}R_p^2R_0^2n\Phi h^3(3-\mu) \\
K_{55}^{(0)} &= \frac{1}{12}\omega^2(\rho/E)(1-\mu^2)R_p^2R_0^3h^3 + \frac{1}{24}(1-\mu)R_pR_p''R_0h^3\Phi^2 + \frac{1}{8}(1-\mu)R_pR_p'R_0h'h^2\Phi^2\mu \\
&\quad - \frac{1}{2}(1-\mu)R_p^2R_0^3\kappa h - \frac{1}{12}R_0^3n^2h^3 - \frac{1}{12}R_p^2R_0h^3\Phi^2(1-\mu) \\
\\
K_{11}^{(1)} &= R_pR_p'R_0h\Phi^2 + R_p^2R_0h'\Phi^2 \\
K_{12}^{(1)} &= \frac{1}{2}(1+\mu)R_pR_0^2hn\Phi & K_{13}^{(1)} &= (1+\mu)R_p^2R_0\Phi h + \frac{1}{2}(1-\mu)R_p^2R_0K\Phi h \\
K_{21}^{(1)} &= -K_{12}^{(1)} & K_{22}^{(1)} &= \frac{1}{2}(1-\mu)R_pR_p'R_0h\Phi^2 + \frac{1}{2}(1-\mu)R_p^2R_0h'\Phi^2 \\
K_{31}^{(1)} &= -K_{13}^{(1)} \\
K_{33}^{(1)} &= \frac{1}{2}(1-\mu)(R_p^2R_0\kappa h'\Phi^2 + R_pR_p'R_0^2\Phi^2\kappa h) & K_{34}^{(1)} &= \frac{1}{2}(1-\mu)R_p^2R_0^2\kappa h\Phi \\
K_{43}^{(1)} &= K_{34}^{(1)} \\
K_{44}^{(1)} &= \Phi^2R_0\left(\frac{1}{12}R_pR_p'h^3 + \frac{1}{4}R_p^2h'h^2\right) & K_{45}^{(1)} &= \frac{1}{24}(1+\mu)R_pR_0^2\Phi h^3n \\
K_{54}^{(1)} &= -K_{45}^{(1)} & K_{55}^{(1)} &= \frac{1}{8}(1-\mu)2\Phi^2R_p^2R_0h'h^2 + \frac{1}{24}(1-\mu)R_pR_p'R_0h^3\Phi^2
\end{aligned}$$

$$\begin{aligned}
K_{11}^{(2)} &= R_p^2 R_0 h \Phi^2 \\
K_{22}^{(2)} &= \frac{1}{2}(1 - \mu) R_p^2 R_0 h \Phi^2 \\
K_{33}^{(2)} &= \frac{1}{2}(1 - \mu) R_p^2 R_0 \kappa h \Phi^2 \\
K_{44}^{(2)} &= \frac{1}{12} R_p^2 R_0 \Phi^2 h^3 \\
K_{55}^{(2)} &= \frac{1}{24}(1 - \mu) R_p^2 R_0 \Phi^2 h^3
\end{aligned}$$

References

- [Eisenberger 1990] M. Eisenberger, "An exact element method", *Int. J. Numer. Methods Eng.* **30** (1990), 363–370.
- [Gautham and Ganesan 1992] B. P. Gautham and N. Ganesan, "Free vibration analysis of thick spherical shells", *Comput. Struct.* **2**:45 (1992), 307–313.
- [Hutchinson 1984] J. R. Hutchinson, "Vibrations of thick free circular plates, exact versus approximate solutions", *J. Appl. Mech. (ASME)* **51** (1984), 581–585.
- [Kang and Leissa 2000] J. H. Kang and A. W. Leissa, "Three-dimensional vibrations of thick spherical shell segments with variable thickness", *Int. J. Solids Struct.* **37** (2000), 4811–4823.
- [Kang and Leissa 2006] J. H. Kang and A. W. Leissa, "Corrigendum to Three-dimensional vibrations of thick spherical shell segments with variable thickness", *Int. J. Solids Struct.* **43** (2006), 2848–2851.
- [Leissa 1973] A. W. Leissa, *Vibrations of shells*, US Government Printing Office, 1973. Reprinted Acoustical Soc. Amer., New York, 1993.
- [Leissa and Chang 1996] A. W. Leissa and J. D. Chang, "Elastic deformation of thick, laminated composite shells", *Compos. Struct.* **35** (1996), 153–170.
- [Lim et al. 1996] C. W. Lim, S. Kitipornchai, and K. M. Liew, "Modeling the vibration of a variable thickness ellipsoidal dish with central point clamp or concentric surface clamp", *J. Acoust. Soc. Am.* **1**:99 (1996), 362–372.
- [Mindlin 1951] R. D. Mindlin, "Influence of rotatory inertia and shear on flexural motions of isotropic, elastic plates", *J. Appl. Mech. (ASME)* **18** (1951), 31–38.
- [Qatu 2002] M. S. Qatu, "Recent research advances in the dynamic behavior of shells: 1989–2000, Part 2: Homogeneous shells", *Appl. Mech. Rev.* **5**:55 (2002), 415–434.
- [Stephen 1997] N. G. Stephen, "Mindlin plate theory: best shear coefficient and higher spectra validity", *J. Sound Vib.* **202**:4 (1997), 539–553.

Received 3 Jan 2010. Revised 19 Apr 2010. Accepted 3 May 2010.

ELIA EFRAIM: efraime@ariel.ac.il

Department of Civil Engineering, Ariel University Center of Samaria, 40700 Ariel, Israel

MOSHE EISENBERGER: cvrmosh@technion.ac.il

Faculty of Civil and Environmental Engineering, Technion – Israel Institute of Technology, Technion City, 32000 Haifa, Israel

APPLICATION OF A MATRIX OPERATOR METHOD TO THE THERMOVISCOELASTIC ANALYSIS OF COMPOSITE STRUCTURES

ANDREY V. PYATIGORETS, MIHAI O. MARASTEANU,
LEV KHAZANOVICH AND HENRYK K. STOLARSKI

The problem of thermal stress development in composite structures containing one linear isotropic viscoelastic phase is considered. The time-temperature superposition principle is assumed to be applicable to the viscoelastic media under consideration. Two methods of solution based on the reduction of the original viscoelastic problem to the corresponding elastic one are discussed. It is argued that the use of a method based on the Laplace transform is impractical for some problems, such as those involving viscoelastic asphalt binders. However, the solution can be obtained by means of the second method considered in the paper, the Volterra correspondence principle, in which the integral operator corresponding to the master relaxation modulus is presented in matrix form. The Volterra principle can be applied to the solution of viscoelastic problems with complex geometry if the analytical solution for the corresponding elastic problem is known. Numerical examples show that the proposed method is simple and accurate. The approach is suitable to the solution of problems involving viscoelastic materials, whose rheological properties strongly depend on temperature. In particular, it can be found useful in the analysis of the low-temperature thermal cracking of viscoelastic asphalt binders.

1. Introduction

Composite structures consisting of elastic and viscoelastic materials play an important role in today's engineering applications. Such structures are used in various environmental conditions, often involving temperature variations. Due to the effects of thermal expansion and contraction of the materials, it is important to be able to predict the behavior of composite structures subjected to varying temperature. For the case of elastic media, temperature effects can be easily incorporated in the analysis since the material's elastic properties are time- and temperature independent. However, temperature changes in viscoelastic media cause changes in the material's rheological properties, which makes the analysis of thermoviscoelastic problems more complex.

Methods of solution of linear viscoelastic problems fall into two major categories: approaches based on the approximate and iterative solutions in the time domain and methods based on the solution of the corresponding elastic problem formulated in the frequency (transformed) domain. Time-stepping algorithms (see [Mesquita et al. 2001], for instance), widely used in the finite element and boundary element methods, belong to the first category. The second category includes approaches based on the application of integral transformations, such as the Laplace or Fourier transforms, to reduce a time-dependent problem to one that depends on the transform parameter only [Lee et al. 1959; Findley et al. 1976]. In the case of nonisothermal conditions, some of these methods can be adopted to the solution of

Keywords: viscoelastic, composite, Volterra correspondence principle, thermal stress, asphalt binder.

thermoviscoelastic problems by using, for example, the time-temperature superposition (TTS) principle, whereas other methods fail.

TTS is widely used to describe the effect of temperature on the mechanical response of a certain class of viscoelastic materials [Ferry 1961; Findley et al. 1976; Wineman and Rajagopal 2000]. Theoretical and experimental results indicate that for such materials the response to a load at high temperature over a short period of time is identical to that at lower temperature but over a longer period, and vice versa. Thus, at any temperature, a material property such as relaxation modulus or creep compliance can be expressed in terms of the material property at the reference temperature and another material property known as the time-shift factor. Following [Schwarzl and Staverman 1952], materials for which the mechanical behavior due to temperature is equivalent to a corresponding shift in the logarithmic time scale are called thermorheologically simple.

A number of studies have been devoted to the solution of thermoviscoelastic problems with the use of TTS. Taylor et al. [1970] proposed an integration scheme that was used together with the Prony series approximation of viscoelastic properties to obtain a recursive expression for the solution of thermoviscoelastic problems at each next time step. Chien and Tzeng [1995] considered the problem of a thick laminated composite cylinder under elevated temperature change. The dependency of creep compliances on time was presented in the form of a simple power function that allowed them to obtain closed form relations in the Laplace domain and use analytical Laplace inversion. Ekel'chik et al. [1994] studied the problem of a thick-walled orthotropic viscoelastic ring; the authors applied a procedure of numerical inversion of the Laplace transform after the solution of the corresponding problem was obtained. A review of some other methods of solving quasistatic problems of linear thermoviscoelasticity is provided in [Bykov et al. 1971].

The aim of this work is to demonstrate, for the first time, that the use of the Volterra correspondence principle can be an effective tool for solving complex thermoviscoelastic problems, such as those encountered in pavement engineering. While the Volterra correspondence principle is well known and has been applied to the solution of a number of viscoelastic problems (in [Rabotnov 1966; Khazanovich 2008], for instance), its application to problems involving thermal effects is, to our knowledge, new. The approach proposed here employs a discrete representation of time-varying functions, and the integral operator corresponding to the master relaxation modulus is presented in matrix form. This technique is a modification of the approach of [Bažant 1972]. Special attention is devoted to thermal stress development in the binders. If tensile stress in asphalt binders or mixtures exceeds their strength upon cooling, cracking occurs. The importance of the study of low-temperature cracking of asphalt pavements stems from the fact that this is one of the dominant distresses occurring in cold climates, where temperature variation can be significant over short periods of time.

This paper is organized as follows. Section 2 summarizes the two approaches used for reducing a viscoelastic problem to an elastic one. Section 3 provides the basic definitions of time-temperature superposition and the description of functional dependencies used for materials characterization. Sections 4 and 5 deal with the relaxation operator and its discrete representation. A simple problem of a restrained bar is considered in Section 6. The solution of this problem can be directly found in the time domain, which allows for comparison results and evaluating the accuracy of the present approach. Section 7 deals with the problem of a composite ring or cylinder undergoing thermal loading, and includes results for thermal stresses and strains in the Asphalt Binder Cracking Device [Kim 2005].

2. Elastic-viscoelastic correspondence principles

One of the most powerful approaches in solving linear viscoelastic problems consists in the reduction to a corresponding elastic problem. This can provide an analytical solution for time-dependent problems and usually is simpler to implement than numerical algorithms for calculating time-varying fields in homogeneous or heterogeneous viscoelastic materials.

Two techniques can be used to obtain a corresponding elastic problem. The first is based on the application of the Laplace transform to all governing equations and boundary conditions describing a viscoelastic body in equilibrium. The Laplace transform of a real function $f(t)$ is defined as

$$f^*(s) = \mathcal{L}[f(t)] = \int_0^{\infty} f(t)e^{-st} dt \quad (1)$$

where s is the complex transform parameter.

In the case of simple deformations, such as uniaxial tension or shear, the Boltzmann superposition principle for linear viscoelastic materials [Findley et al. 1976] states that the stress σ is related to the mechanical strain ε by

$$\sigma(t) = \int_0^t E(t-\tau) \frac{\partial \varepsilon(\tau)}{\partial \tau} d\tau, \quad \varepsilon(t) = \varepsilon_{\text{tot}}(t) - \varepsilon_{\text{th}}(t), \quad (2)$$

where E is the relaxation modulus, t is time, ε_{tot} results from a given displacement field, and ε_{th} is related to the effect of thermal expansion. In more general cases, the relaxation modulus E has to be replaced by a tensor of creep functions, and stress and strain tensors should be used. Applying the Laplace transform to the convolution integral (2), an expression formally equivalent to Hooke's law is obtained:

$$\sigma^*(s) = sE^*(s)\varepsilon^*(s). \quad (3)$$

The idea of the approach is to formulate the corresponding elastic problem by replacing time-varying parameters with their transformed counterparts, solve the obtained problem, and apply an inversion of the Laplace transform to arrive at the time domain solution. However, the use of this approach may be limited by the fact that strain or stress histories and/or material properties may be complicated functions of time, whose Laplace transform cannot be found in a closed form. This makes impossible to obtain the solution of the corresponding elastic problem.

The Volterra correspondence principle [1913] can be used in the case when the Laplace transform is not applicable [Rabotnov 1966]. The principle is based on the representation of hereditary integrals of type (2) as integral operators acting on time-varying functions. This technique also leads to the reduction of a time-dependent problem to a corresponding elastic problem.

Consider the case of a simple deformation caused by uniaxial tension of a linear viscoelastic body. Evaluating the integral (2) by parts, it can be found that

$$\sigma(t) = E(0)\varepsilon(t) - \int_0^t \varepsilon(\tau) dE(t-\tau) \equiv \tilde{E} \cdot \varepsilon(t) \quad (4)$$

where \tilde{E} is an integral operator acting on a function of time, and $E(0)$ is the value of the relaxation modulus at zero time. It is seen that (4) is formally equivalent to Hooke's law. The operator \tilde{E} is referred to as the relaxation operator. In more general cases, it can be shown [Rabotnov 1966] that other

viscoelastic parameters, such as creep compliance, viscoelastic bulk or shear moduli, can be expressed in an operator form in such a way that the constitutive equations written with the use of these operators resemble elastic constitutive equations. This implies that in order to solve a viscoelastic problem, one has to solve a corresponding elastic problem, and substitute the elastic properties with the corresponding integral operators in the obtained elastic solution for each physical variable of interest. Since superposition holds for elasticity, the viscoelastic solution for any physical variable $\gamma(t)$ can be presented as a combination of functions of one or more commutative integral operators¹ acting on known functions of time $f_i(t)$, which can be time-dependent boundary parameters, body forces, temperature, etc. In the case of an isotropic viscoelastic material, such a relation can be presented as

$$\gamma(t) = \sum_i F_i[\tilde{E}, \tilde{\nu}] \cdot f_i(t), \quad (5)$$

where $\tilde{\nu}$ is the integral operator corresponding to the viscoelastic Poisson's ratio and the F_i are functions of operators. Analytical evaluation of the result of the action of integral operators on known functions of time is often a complicated and impractical task, and numerical approximations are used to represent integral operators in matrix form. Thus, the solution of a time-dependent problem is formulated in terms of matrix operators acting on vectors obtained from the discretization of the time functions:

$$\underline{\gamma} = \sum_i F_i[\underline{E}, \underline{\nu}] \cdot \underline{f}_i, \quad (6)$$

where \underline{E} and $\underline{\nu}$ are matrix operators and $\underline{\gamma}$ and \underline{f} are vectors representing the discrete values of functions $\gamma(t)$ and $f(t)$. In the present work it is assumed that the viscoelastic Poisson's ratio ν does not change in time; hence the corresponding matrix operator is represented as ν times the identity matrix.

3. Time-temperature superposition

The problem of deformation of viscoelastic media coupled with temperature variation can be treated with the use of the time-temperature superposition principle [Ferry 1961; Findley et al. 1976; Wineman and Rajagopal 2000]. It follows from the principle that real time t in (2) has to be replaced by reduced time ξ to account for the change in material's properties with temperature. The constitutive equation (2) is now written as

$$\sigma(\xi) = \int_0^{\xi} E(\xi - \xi') \frac{\partial \varepsilon(\xi')}{\partial \xi'} d\xi', \quad (7)$$

where $\varepsilon(\xi) = \varepsilon_{\text{tot}}(\xi) - \varepsilon_{\text{th}}(\xi)$. For transient temperature conditions, the reduced time is connected to the real time by an integral:

$$\xi(t) = \int_0^t \frac{d\tau}{a_T[T(\tau)]} \quad (8)$$

where a_T is shift function (factor) obtained during the process of the construction of the material's master curve. Different functions can be used to fit the plot for the shift factor. The shift factor described by the Williams–Landau–Ferry equation [Williams et al. 1955] is often used to describe the behavior

¹The term “commutativity” is understood here in the sense used in [Rabotnov 1966; Arutyunyan and Zevin 1997]. Note that the operators are commutative only for the case of nonaging viscoelasticity; see the second of these references.

of polymers. In this work, a linear function is adopted to describe the decimal logarithm of the shift factor a_T :

$$\log a_T = C_1 - C_2 T, \quad (9)$$

where C_1 and C_2 are constants determined through least squares fitting. It was found that (9) provides accurate fitting for the experimental data used in this work.

The thermal strain ε_{th} is given by

$$\varepsilon_{\text{th}} = \alpha \Delta T, \quad (10)$$

where α is the coefficient of thermal expansion (assumed to be constant) and ΔT is the temperature change. For simplicity, the temperature variation is considered to be linear in time:

$$\Delta T(t) = C_0 t, \quad (11)$$

where C_0 is the constant temperature rate. (Nonlinear temperature changes can be treated similarly.) The temperature at time t is thus

$$T = T_0 + \Delta T, \quad (12)$$

where T_0 is the reference temperature.

Combining equations (8)–(11), one obtains the relation between real time t and reduced time ξ , as well as relations between thermal strain ε_{th} and reduced time ξ . These relations are

$$\xi(t) = A_1(1 - 10^{C_0 C_2 t}) \quad \text{with } A_1 = -(C_0 C_2 10^{(C_1 - C_2 T_0)} \ln 10)^{-1}, \quad (13)$$

$$t(\xi) = \frac{1}{C_0 C_2} \log(1 - \xi/A_1), \quad \varepsilon_{\text{th}}(\xi) = \frac{\alpha}{C_2} \log(1 - \xi/A_1). \quad (14)$$

Because the time shift is zero at the reference temperature, we have $10^{(C_1 - C_2 T_0)} = 1$ in (13).

For asphalt binders, the master relaxation modulus curve is obtained (see Appendix) using the CAM model of [Marasteanu and Anderson 1999], given by the equation

$$E(\xi) = E_g \left(1 + \left(\frac{\xi}{t_c} \right)^v \right)^{-w/v} \quad (15)$$

where E_g is the glassy modulus, t_c is the crossover time, and v and w are the parameters of the model, which, in general, are some rational numbers. The CAM model is considered an effective phenomenological model for characterizing the linear viscoelastic behavior of asphalt binders at low temperatures.

4. Relaxation operator with varying temperature

The approaches presented in Section 2 can be used to solve problems of thermal stress evolution in viscoelastic composite materials. However, when the CAM model (15) is adopted to describe viscoelastic material behavior, its Laplace transform cannot be found in a closed form. Another degree of complexity is introduced by the fact that the Laplace transform of the thermal strain described by (14) is a complex-valued function of s . Because of this, it seemed impractical to use the elastic-viscoelastic correspondence principle based on the Laplace transform for the analysis of the problem. Therefore, we use here the integral operator representation approach.

Because for each value of reduced time ξ one can find a corresponding value of real time t (and vice versa), the stress and strain in the reduced time domain can be replaced by their values found for the

corresponding real time: $\sigma(\xi) \equiv \sigma(\xi(t)) \equiv \sigma(t)$, $\varepsilon(\xi) \equiv \varepsilon(\xi(t)) \equiv \varepsilon(t)$. Therefore, it is possible to simplify expression (7):

$$\sigma(t) = \int_0^t E(\xi(t) - \xi'(\tau)) \cdot \frac{\partial \varepsilon(\tau(\xi'))}{\partial \tau(\xi')} \underbrace{\frac{\partial \tau(\xi')}{\partial \xi'} \cdot \frac{\partial \xi'}{\partial \tau(\xi')}}_{\equiv 1} d\tau(\xi') = \int_0^t E(\xi(t) - \xi'(\tau)) \frac{\partial \varepsilon(\tau)}{\partial \tau} d\tau. \quad (16)$$

The integral (16) is now similar to (2), with the only difference that the master relaxation modulus is still given in the reduced time domain. This allows us to use the stress-strain relation in the form

$$\sigma(t) = \tilde{E} \cdot \varepsilon(t), \quad (17)$$

where the integral operator (relaxation operator) \tilde{E} is now defined as

$$\tilde{E} \cdot f(t) \equiv E(0) \cdot \left(f(t) - \frac{1}{E(0)} \int_0^t f(\tau) dE[\xi(t) - \xi'(\tau)] \right). \quad (18)$$

5. Matrix representation of the relaxation operator

For the analysis of viscoelastic problems considered in the present work, a procedure of numerical solution based on the representation of relaxation operator \tilde{E} given by (18) as a matrix operator is adopted.

Consider a discrete set of time moments t_0, t_1, \dots, t_n , with $t_0 = 0$ and $t_n \equiv t$. Strain ε , as well as temperature variation $\Delta T(t)$ are presented as column vectors

$$\underline{\varepsilon} \equiv \varepsilon_k = \varepsilon(t_k) \quad \text{and} \quad \underline{\Delta T} \equiv \Delta T_k = T(t_k) - T(t_0). \quad (19)$$

To obtain a matrix representation for the integral operator \tilde{E} , we integrate numerically using the trapezoid rule [Bažant 1972]. Thus, the expression $\sigma = \tilde{E} \cdot \varepsilon$ for each moment of time k can be written as

$$\begin{aligned} \sigma_k \equiv (\tilde{E} \cdot \varepsilon)_k &= E(0) \cdot \left(\varepsilon_k - \frac{1}{E(0)} \int_0^{t_k} \varepsilon(\tau) dE(\xi(t) - \xi'(\tau)) \right) \\ &= E_{k,k} \varepsilon_k - \frac{1}{2} \sum_{i=1}^k (\varepsilon_i + \varepsilon_{i-1}) (E_{k,i} - E_{k,i-1}), \end{aligned} \quad (20)$$

where $E_{k,i} \equiv E(\xi(t_k) - \xi(t_i))$ and $E_{k,k} \equiv E(0)$. Recalling that $\varepsilon_0 \equiv 0$ and rearranging terms in (20), the result is a column vector $\underline{\sigma}$ consisting of terms

$$\sigma_k = \frac{1}{2} \left(\sum_{i=1}^{k-1} (E_{k,i-1} - E_{k,i+1}) \varepsilon_i + (E_{k,k-1} + E_{k,k}) \varepsilon_k \right), \quad k = 1, \dots, n, \quad (21)$$

or, in matrix form,

$$\underline{\sigma} = \underline{E} \cdot \underline{\varepsilon}. \quad (22)$$

The matrix $\underline{\underline{E}}$ is lower triangular:

$$\underline{\underline{E}} = \begin{pmatrix} E_{1,0} + E_{1,1} & 0 & 0 & \dots & 0 \\ E_{2,0} - E_{2,2} & E_{2,1} + E_{2,2} & 0 & \dots & 0 \\ E_{3,0} - E_{3,2} & E_{3,1} - E_{3,3} & E_{3,2} + E_{3,3} & \dots & 0 \\ \vdots & \vdots & \vdots & \ddots & \vdots \\ E_{n,0} - E_{n,2} & E_{n,1} - E_{n,3} & E_{n,2} - E_{n,4} & \dots & E_{n,n-1} + E_{n,n} \end{pmatrix}, \tag{23}$$

and

$$\underline{\underline{\varepsilon}} = \begin{pmatrix} \varepsilon_1 \\ \varepsilon_2 \\ \vdots \\ \varepsilon_n \end{pmatrix} = \begin{pmatrix} \varepsilon_{\text{tot } 1} \\ \varepsilon_{\text{tot } 2} \\ \vdots \\ \varepsilon_{\text{tot } n} \end{pmatrix} - \alpha \begin{pmatrix} \Delta T_1 \\ \Delta T_2 \\ \vdots \\ \Delta T_n \end{pmatrix}. \tag{24}$$

The lower triangular structure of $\underline{\underline{E}}$ represents the history-dependent nature of viscoelastic problems. Thus, it is obvious that for longer time histories the size of the matrix $\underline{\underline{E}}$ grows, which may reduce the numerical efficiency. However, it has been found that for the problems considered in the present study, a relatively small number of subdivisions in the trapezoidal rule is sufficient to obtain accurate solutions over a large interval of temperatures (for instance, ranging from -50°C to $+20^\circ\text{C}$).

In general case of a boundary value problem describing an isotropic viscoelastic material, two integral operators are present in the solution. The problem can be simplified greatly, if one assumes that Poisson’s ratio is independent of time and temperature. This allows using only relaxation operator \tilde{E} in the analysis of the problem. The assumption of constant Poisson’s ratio is employed in the present work due to the following facts. Experimental data reveal that the Poisson’s ratio of viscoelastic asphalt mixtures varies very little at low temperatures, and therefore it can be considered constant [Huang 1993; Levenberg and Uzan 2007]. Furthermore, the study of asphalt binders in [Marasteanu and Anderson 2000] indicates that binders’ Poisson’s ratio can be reasonably assumed constant at low temperatures. In addition, the results of numerical simulations conducted in the present work also indicate that using constant but different values of Poisson’s ratio within a realistic range has very small effect on the final results. Therefore, the solution for viscoelastic problems can be represented in discrete form as a function of the only matrix operator $\underline{\underline{E}}$ multiplied by a vector of a known time function, e.g.,

$$\underline{\underline{\sigma}} = F[\underline{\underline{E}}] \cdot \underline{\underline{\varepsilon}}_{\text{tot}} + G[\underline{\underline{E}}] \cdot \underline{\underline{\Delta T}} \tag{25}$$

where F and G are some functions of matrices. In many cases it is much easier to calculate rational functions of matrices than functions of integral operators.

6. Analysis of a viscoelastic restrained bar

Consider the problem of thermal stress evolution in a restrained isotropic homogeneous viscoelastic bar (Figure 1). The total strain in this case is zero, and $\varepsilon = -\alpha \Delta T$. The problem is described by (16), which simplifies to the form

$$\sigma(t) = -\alpha C_0 \int_0^t E(\xi(t) - \xi'(\tau)) d\tau. \tag{26}$$



Figure 1. Geometry for the problem of a restrained bar.

Due to the simple structure of the integrand in (26), one can use various numerical integration techniques to obtain the thermal stress in the bar. Comparison of the results of integration with those obtained from (22)–(24) allows us to evaluate the accuracy of the present approach for the considered class of functions describing material properties (CAM model).

In the present analysis, we used the parameters obtained by the procedure in the Appendix for a modified asphalt binder tested at temperatures -24°C , -30°C , and -36°C .² These parameters are as follows:

$$\begin{aligned} \text{(CAM model)} \quad & E_g = 3 \text{ GPa}, \quad t_c = 1.04655 \cdot 10^{-6} \text{ sec}, \quad \nu = 0.177585, \quad w = 0.359506, \\ \text{(Other)} \quad & \alpha = 2 \times 10^{-4} \text{ }^{\circ}\text{C}^{-1}, \quad C_2 = 0.18562 \text{ }^{\circ}\text{C}^{-1}, \quad C_0 = -10^{\circ}\text{C/hour}, \quad T_0 = 20^{\circ}\text{C}. \end{aligned}$$

The tensile stress in the bar caused by the temperature drop was determined by the present approach and by numerical integration using 24-point Gaussian quadrature, a technique that provides highly accurate results and whose application to this problem was originally proposed by Voller [Marasteanu et al. 2004].

The comparative plots are presented in Figure 2. It is apparent from the figure that both approaches produce virtually identical results. By testing the accuracy of the present method on various asphalt

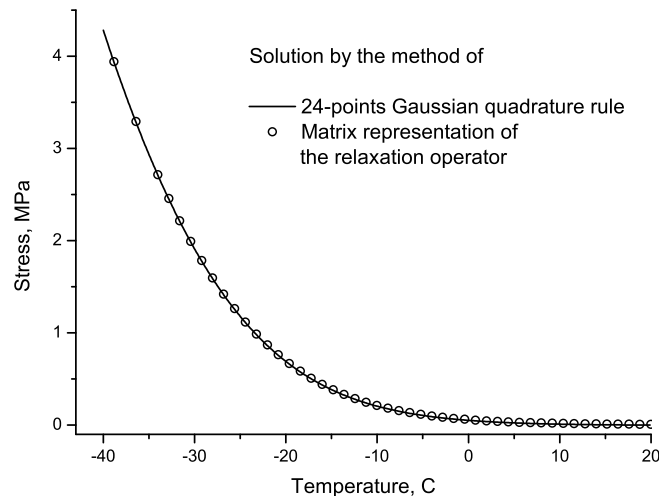


Figure 2. Comparison of stresses obtained from (26) using 24-point Gaussian quadrature and by the method of matrix representation of the relaxation operator \tilde{E} .

²The binder was modified with styrene-butadiene diblock copolymer (Black MaxTM) and produced by Husky Energy (Canada). The binder's performance grade is PG 64-34 [AASHTO 2005]. The binder was tested in the Pavement Laboratory of the Department of Civil Engineering at the University of Minnesota. More information about its properties can be found in [Marasteanu et al. 2007]

binders described by the CAM model (15), it was found that quite accurate results can be obtained for the number of integration points $n \gtrsim 1000$ used in the trapezoid rule. The results presented in Figure 2 are obtained with $n = 2000$. Note that for longer time histories more segments in the trapezoidal rule have to be used to obtain accurate results. For the case when the properties of viscoelastic materials cannot be described by the CAM model and/or a linear shift function, the use of a more accurate integration rule such as Simpson’s rule may be required.

7. Analysis of viscoelastic composite cylinder/ring

Consider the problem of a composite cylinder subjected to uniform temperature variation. The geometry of the problem is given in Figure 3. The hollow inner cylinder (inclusion) is assumed to be elastic and the outer (binder) to be linearly viscoelastic. The plane strain condition is assumed, but the plane stress solution can also be easily obtained by replacing the elastic Young’s moduli and Poisson’s ratios [Barber 1992] in the corresponding elastic problem. A perfect bond between the binder and inclusion is assumed; the distribution of circumferential stresses and strains in each cylinder is of primary interest.

To obtain the solution of the corresponding elastic problem, we assume the binder is an elastic material with Young’s modulus E_b , Poisson’s ratio ν_b , and coefficient of thermal expansion α_b . The material properties of the inner cylinder (inclusion) are denoted by E_i , ν_i and α_i . The elastic solution for the circumferential stresses in the binder can be obtained in the form

$$\sigma_{\theta\theta}^{\text{bind}}(r) = \frac{a(r)E_i + b(r)E_b}{cE_i + E_b} E_b \Delta T, \tag{27}$$

where c is a constant and the parameters a and b depend on the radius. Expressions for these parameters are given in the Appendix as relations (A3) and (A4), following an outline of the derivation of (27).

Assuming that the Poisson’s ratio of the binder does not vary with time and temperature, the solution for time-dependent circumferential stresses corresponding to the viscoelastic problem is

$$\underline{\sigma}_{\theta\theta}^{\text{bind}}(r) = [aE_i\underline{I} + b\underline{E}_b] \cdot [cE_i\underline{I} + \underline{E}_b]^{-1} \cdot \underline{E}_b \underline{\Delta T}, \tag{28}$$

where $\underline{\sigma}_{\theta\theta}^{\text{bind}}$ and $\underline{\Delta T}$ are vectors of size n , \underline{I} is identity $n \times n$ matrix, and \underline{E}_b is $n \times n$ matrix of relaxation functions given by (23). It is seen from (28) that the calculation of the inverse of matrix $\underline{M} = (cE_i\underline{I} + \underline{E}_b)$ is required. This operation can be easily performed, since \underline{M} is a lower triangular matrix.

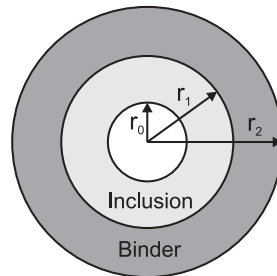


Figure 3. Geometry of an axisymmetric problem with a hollow inner part.

The solutions for circumferential strains in the binder and in the inclusion can be obtained in a form similar to (28). In particular, the total circumferential strain $\varepsilon_{\theta\theta}^{\text{inc}}(r)$ in the inclusion is

$$\varepsilon_{\theta\theta}^{\text{inc}}(r) = [\alpha_i F_1(r, \underline{E}_b) + \alpha_b F_2(r, \underline{E}_b)] \cdot \underline{\Delta T} \quad (29)$$

where we omit the subscript “tot”, and the matrix functions $F_1(r, \underline{E}_b)$ and $F_2(r, \underline{E}_b)$ are given by

$$\begin{aligned} F_1(r, \underline{E}_b) &= (1 + \nu_i) \underline{I} - 2 \frac{r_1^2}{r^2} (1 - \nu_i^2) [d \underline{I} + g E_i(\underline{E}_b)^{-1}]^{-1}, \\ F_2(r, \underline{E}_b) &= 2 \frac{r_1^2}{r^2} (1 - \nu_i) (1 + \nu_b) [d \underline{I} + g E_i(\underline{E}_b)^{-1}]^{-1}, \end{aligned} \quad (30)$$

with constants d and g given as (A5) in the Appendix.

Comparison with the analytical solution. The calculations presented in the analysis of the bar problem (Section 6) were simple and did not involve evaluating the inverse of \tilde{E} . The present problem of a composite cylinder (Figure 3) is a more realistic test of accuracy. The plane strain elastic solution for this problem is given by (28)–(30). The results are compared with an analytical solution obtained by the application of the Laplace transform. To be able to use the Laplace transform, the expression for the shift factor a_T given by (9) is replaced with linear function

$$\hat{a}_T(T) = \hat{C}_1 - \hat{C}_2 T, \quad (31)$$

(The hat over the quantities means that they have a different interpretation from before — say in (9).) Using (31) and (10), the reduced time becomes

$$\hat{\xi} = -\frac{1}{\hat{C}_0 \hat{C}_2} \ln \left| 1 + \frac{\hat{C}_2(T_0 - T)}{\hat{C}_1 - \hat{C}_2 T_0} \right| \quad (32)$$

and we have

$$\hat{t}(\xi) = \frac{\hat{C}_1 - \hat{C}_2 T_0}{\hat{C}_0 \hat{C}_2} (1 - \exp(-\hat{C}_0 \hat{C}_2 \xi)), \quad \Delta \hat{T}(\xi) = \left(\frac{\hat{C}_1}{\hat{C}_2} - T_0 \right) (1 - \exp(-\hat{C}_0 \hat{C}_2 \xi)). \quad (33)$$

Despite the fact that the expressions (31)–(33) do not have a physical interpretation (e.g., $\hat{C}_1 - \hat{C}_2 T_0 \neq 0$, which follows from (32)), the choice of a linear form for \hat{a}_T allows the determination of the Laplace transform of $\Delta \hat{T}(\xi)$:

$$\Delta \hat{T}^*(s) = \left(\frac{\hat{C}_1}{\hat{C}_2} - T_0 \right) \frac{\hat{C}_0 \hat{C}_2}{s(s + \hat{C}_0 \hat{C}_2)}. \quad (34)$$

Similarly, the CAM model used for the description of the master relaxation modulus is replaced by a function for which the Laplace transform can be easily found. A series of several exponents (Prony series) is used instead of (15):

$$\hat{E}(\xi) = \sum_i \hat{E}_i \exp(\hat{\gamma}_i \xi), \quad \hat{E}^*(s) = \sum_i \frac{\hat{E}_i}{s - \hat{\gamma}_i}. \quad (35)$$

For illustration purposes it is enough to use only a few terms in the series; we preserve them up to $i = 3$.

Even though, for comparison purposes, the parameters \hat{C}_1 , \hat{C}_2 , \hat{E}_i , and $\hat{\gamma}_i$ could be chosen arbitrarily, we chose them via a least squares fitting of the functions $a_T(T)$ and $E(\xi)$ experimentally obtained for a modified asphalt binder (PG58-40). (It is not essential to have perfect fitting of experimental data with the new functions $\hat{a}_T(T)$ and $\hat{E}(\xi)$; we just need to use the same functions in solving the problem using the two approaches being compared.)

The values of the parameters involved in $\hat{a}_T(T)$ are

$$\hat{C}_1 = 41.156640, \quad \hat{C}_2 = 2.276346^\circ\text{C}^{-1}.$$

Those appearing in $\hat{E}(\xi)$ are

$$\begin{aligned} \text{(in MPa)} \quad \hat{E}_0 &= 38.598647, \quad \hat{E}_1 = 349.348243, \quad \hat{E}_2 = 195.939985, \quad \hat{E}_3 = 126.336051, \\ \text{(in sec}^{-1}\text{)} \quad \hat{\gamma}_0 &= 0, \quad \hat{\gamma}_1 = -0.517286 \cdot 10^9, \quad \hat{\gamma}_2 = -0.265315 \cdot 10^8, \quad \hat{\gamma}_3 = -0.137463 \cdot 10^7. \end{aligned}$$

We next present the parameters of the composite cylinder, chosen according to an ABCD specimen described in detail in the next subsection. The specimen consisted of an elastic ring with thickness $r_1 - r_0$, surrounded by a viscoelastic binder with thickness $r_2 - r_1$ (compare Figure 3 on page 845). These geometric parameters are

$$r_0 = 23.75 \cdot 10^{-3} \text{ m}, \quad r_1 = 25.4 \cdot 10^{-3} \text{ m}, \quad r_2 = 31.75 \cdot 10^{-3} \text{ m}, \quad (36)$$

while the remaining parameters are

$$T_0 = 18^\circ\text{C}, \quad C_0 = -1^\circ\text{C}/\text{hour}, \quad \alpha_1 = 1.4 \cdot 10^{-6} \text{ }^\circ\text{C}^{-1}, \quad \alpha_2 = 2.0 \cdot 10^{-4} \text{ }^\circ\text{C}^{-1}, \quad E_1 = 141 \text{ GPa}, \quad \nu_1 = 0.3, \quad \nu_2 = 0.33. \quad (37)$$

Figure 4 compares the analytical plane strain solution for $\sigma_{\theta\theta}^{\text{bind}}(r_1)$ obtained with the use of the Laplace

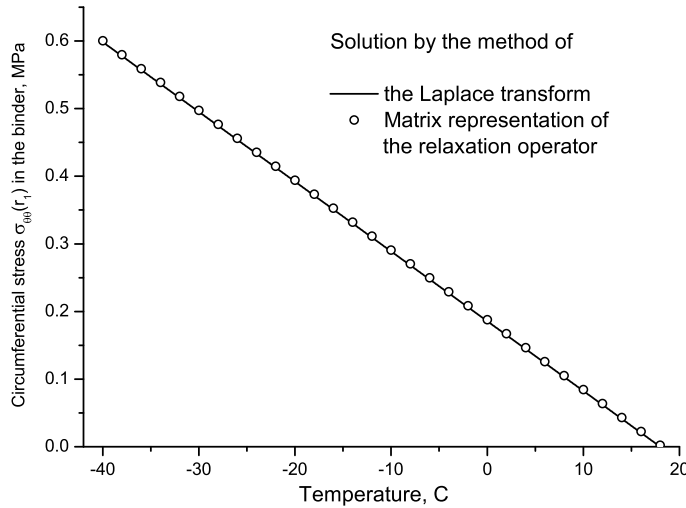


Figure 4. Comparison of circumferential stress $\sigma_{\theta\theta}^{\text{bind}}(r_1)$ in the composite cylinder problem obtained analytically (Laplace transform method) and numerically by the matrix representation of the relaxation operator \tilde{E} of (22)–(24).

transform with the numerical solution found by the present approach for $n = 2500$. As in the previous problem, the results from the both methods match very well. The stress rises linearly in this case due to the use of modified shift factor $\hat{a}_T(T)$, which depends linearly on temperature.

Simulation of thermal stresses in Asphalt Binder Cracking Device. This section is devoted to the study of viscoelastic fields evolution in specimens undergoing thermal loading in the Asphalt Binder Cracking Device (ABCD). ABCD was developed in [Kim 2005; Kim et al. 2006] for direct measurements of cracking temperature of asphalt binders. Based on the present approach, it is possible to relate measured strains to time-dependent thermal stresses that cause the cracking of the binder and determine its strength at the cracking temperature.

The ABCD, schematically represented in Figure 5, consists of a hollow invar (Ni-Fe alloy) ring with uniform thickness surrounded by a layer of asphalt binder. A silicone mold (not shown in the figure) is used to form asphalt binder into a ring. The mold contains a cylindrical protrusion (shown as a hole in Figure 5) that extends through the thickness of the binder and touches the invar ring. An electrical strain gage is glued on the inner surface of the invar ring across the protrusion. To determine the cracking temperature, the whole structure is placed into a temperature chamber, where it is cooled down. Because the coefficient of thermal expansion of asphalt binders ($\alpha \sim 2 \cdot 10^{-4} \text{ }^\circ\text{C}^{-1}$) is much larger than invar's ($\alpha = 1.4 \cdot 10^{-6} \text{ }^\circ\text{C}^{-1}$), the contraction of the binder is constrained, which causes tensile circumferential stress development in the binder. As a result of cooling, the binder cracks around the hole, where the thickness (in the axial direction) is least. At the moment of cracking the accumulated stress is relieved, and this is expressed as a sudden drop in the strain readings by the strain gage. Thus, the cracking temperature of the asphalt binder can be determined as the temperature at which the sudden drop in measured strain occurs.

In contrast with the cracking temperature, the magnitude of tensile stress in the binder that causes cracking cannot be directly determined from the strain gage readings. Using the present approach, it is possible to simulate both circumferential strain on the inner surface of the invar ring and circumferential stress in the binder. The knowledge of such strain-stress relations can provide a simple tool for the measurement of the tensile circumferential stress causing the crack. This stress can be referred to as the binder's strength at the cracking temperature.

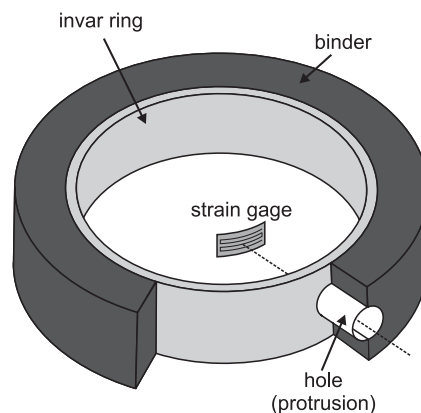


Figure 5. An ABCD specimen consisting of an elastic ring surrounded by a viscoelastic binder.

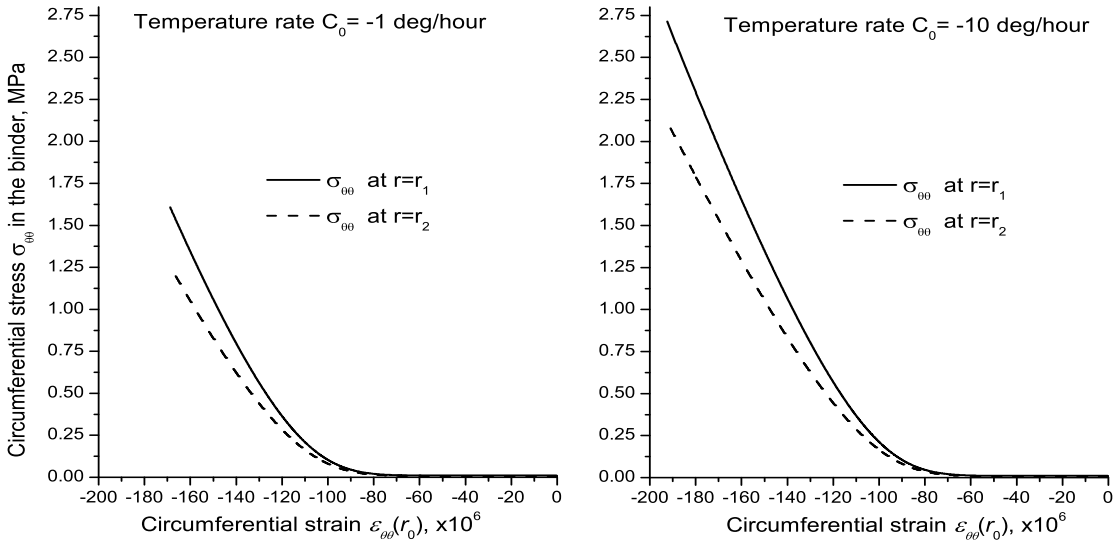


Figure 6. Stress-strain curves for strains on the inner surface of the invar ring and stresses in asphalt binder.

In order to simulate thermal stresses and strains in an ABCD specimen, the model of a composite cylinder (Figure 3) under the condition of plane stress is used. Circumferential strain at the inner side of the invar ring is given by (29), and the expression (28) is used to calculate circumferential stress in the binder. The material properties corresponding to a modified asphalt binder³ are used, as follows:

(CAM model) $E_g = 3 \text{ GPa}, \quad t_c = 148.381583 \text{ sec}, \quad \nu = 0.11346, \quad w = 3.73643,$

(Other) $C_1 = 3.03155, \quad C_2 = 0.16842^\circ\text{C}^{-1}, \quad T_0 = 18^\circ\text{C}.$

The rest of the parameters is given in (36) and (37) on page 847.

The stress-strain relations obtained for the temperature rates $C_0 = -1^\circ\text{C}/\text{hour}$ and $C_0 = -10^\circ\text{C}/\text{hour}$ are shown in Figure 6. Circumferential stress is found at $r = r_1$ (inner surface of the binder ring) and $r = r_2$ (outer surface of the binder ring). The plots in Figure 6 reveal that the magnitude of circumferential stress is higher at the inner surface of the binder ring. Based on this, it is reasonable to conclude that cracking starts from the inner side of the binder ring. Simulation results also show that at the same strain value, stresses in the binder are larger when the magnitude of temperature rate is larger. This is related to the fact that stress in the binder is not able to fully relax when the temperature drops faster. Plots similar to those given in Figure 6 can be obtained for other binders.

The results just presented are for a model that does not take into account the presence of the hole in the asphalt binder. To estimate the influence of the hole on the stress/strain fields around it, an elastic finite element (FE) model replicating the geometry of an ABCD specimen was built. The effect of the influence of the hole in viscoelastic case would be qualitatively similar to that in the elastic problem. A

³This binder was modified with styrene-butadiene-styrene copolymer and produced by Flint Hills (USA). Binder’s performance grade (PG) is PG 58-40 [AASHTO 2005]. This binder was tested in the Pavement Laboratory of the Department of Civil Engineering at the University of Minnesota. For more on the properties of this binder, see [Marasteanu et al. 2007].

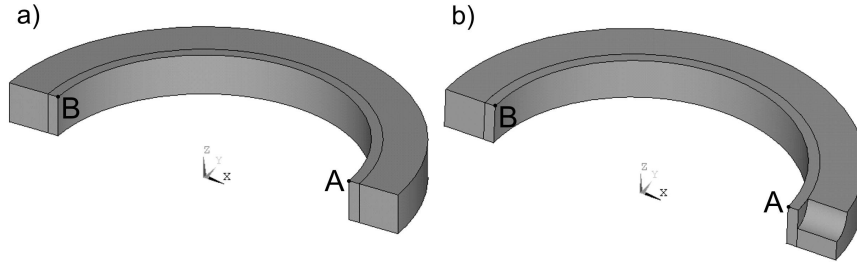


Figure 7. Finite element models used for simulations.

full viscoelastic finite element analysis would be beyond the scope of this paper, though it is possible to conduct such an analysis.

For simplicity, the Young’s modulus of the binder in FE model was taken to be constant: $E = 3 \text{ GPa}$, the initial value of the binder’s relaxation modulus. The properties of the inner ring and geometric parameters corresponded to those of an actual ABCD specimen, and are listed on page 847. A full bond between the binder and the invar ring was assumed. Due to the symmetry of the problem, only a quarter of the ABCD rings had to be modeled. Two models, one without a hole (Figure 7a) and another with a hole in the external ring (Figure 7b), were considered. Both were subjected to a temperature change of $\Delta T = -50^\circ\text{C}$, and the circumferential strain along the arc AB in Figure 7 was determined.

The results of the FE simulations, shown in Figure 8, reveal that the magnitude of circumferential strain in the model with a hole (Figure 7b) increases significantly at point A. At this location the difference reaches $\sim 55\%$ in comparison with the case when no hole is present in the outer ring. Indeed, the presence of the hole causes stress concentration around it, and the additional stress causes local bending of the invar ring. This suggests that experimental strain measurements conducted across the hole cannot be directly used for the calculation of thermal stresses in the binder based on the results given in Figure 6. As follows from Figure 8, thermal stress may be estimated more accurately if strain measurements are

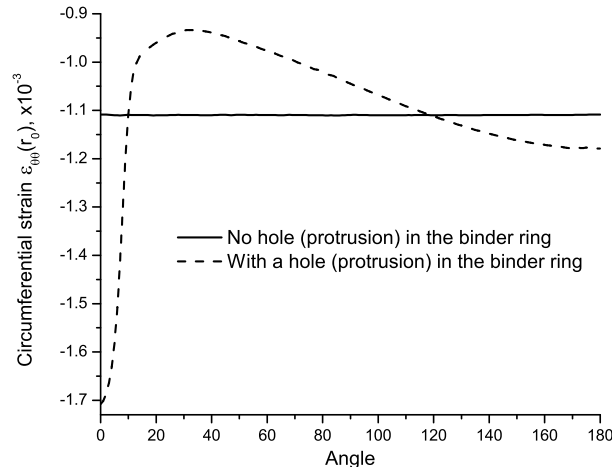


Figure 8. Circumferential strain $\epsilon_{\theta\theta}(r_0)$ along the arc AB of the finite element models (Figure 7), with A corresponding to 0° and B to 180° .

conducted at an angle different from 0° . Measurements taken at angles around 120° are likely to provide more accurate results.

In order to be able to fully incorporate the advantages of the present approach into the calculations of thermal stresses in ABCD specimens, a binder ring should be tested without a hole in it. In this case strain measurements can be conducted at any location. Based on this suggestion, it may be concluded that using ABCD (without a hole) together with the present approach may substitute two separate tests, the bending beam rheometer and indirect tensile tests, which are currently used for determining thermal stresses in binders, their strength and cracking temperature [AASHTO 2007; 2008].

8. Conclusion

A problem of thermal stress development in composite structures containing one linear isotropic viscoelastic phase is considered. The study is particularly devoted to problems involving viscoelastic asphalt binders, whose properties strongly depend on temperature. The ability to determine thermal stresses in asphalt binders and/or mixtures and the knowledge of their strength is critical for the proper design of road pavements. The approach presented in the paper can be equally useful for the calculation of thermal stresses in other viscoelastic composite structures made of materials — including many polymers and resins — for which the time-temperature superposition principle is applicable.

Two methods of solution of viscoelastic problems are discussed. Both are based on the reduction of viscoelastic problem to an elastic one. It is argued that the use of the method based on the application of the Laplace transform to the analysis of the problems involving viscoelastic asphalt binders is impractical. Therefore, an approach based on the use of the Volterra correspondence principle is adopted.

It is assumed that the Poisson's ratios of the materials do not depend on time and temperature, which allows reducing the number of integral operators to one for the case of an isotropic linear viscoelastic material. This assumption is valid for asphalt binders at low temperatures. Incorporating a numerical technique of solution, the integral operator corresponding to the master relaxation modulus is presented in matrix form. The solution of a problem of viscoelastic composite structures is then reduced to the calculation of functions of matrices, the form of which is determined by the corresponding elastic solution. The application of this technique to the analysis of composite structures (including viscoelastic and elastic constituents) under varying temperature is novel.

Several examples are discussed, in an attempt to estimate the accuracy of the method. It is shown that for the case of viscoelastic asphalt binders, the simple integration technique adopted in the method provides accurate results. For the case of other viscoelastic materials, it may be necessary to use a more accurate integration scheme in the derivation of the matrix representation of the relaxation operator. The last example involves an approach that can potentially be used for the calculation of thermal stresses and binder strength in the Asphalt Binder Cracking Device.

The method can be applied to isotropic viscoelastic problems in which both material parameters change with time and temperature. This is because the integral operators for the case of nonaging viscoelasticity commute with each other.

Composite materials with complex internal structure, such as asphalt mixtures, can be treated with the present method if effective mechanical and thermal properties are used. The method can also be extended to problems involving temperature gradients and heat transfer. However, the application may

be limited in the following cases: the solution of the corresponding elastic problem is a transcendental function of elastic properties; the viscoelastic medium exhibits strong aging effects; the time-temperature superposition principle is not applicable. These are topics for future research.

Appendix

Master relaxation modulus curve. The master relaxation modulus $E(\xi)$ of asphalt binders is determined from experimental data for creep compliances, which are obtained with the use of the bending-beam rheometer (BBR) test. In this test [AASHTO 2008], a small beam made of an asphalt binder or asphalt mix is subjected to three-point bending at different low temperatures (for example, -18°C , -24°C , -30°C). The deflection and the applied load are measured in real time. According to Euler–Bernoulli beam theory, the maximum elastic deflection at the mid-span of the beam is

$$\delta_{\max} = \frac{PL^3}{48EI}, \quad (\text{A1})$$

where P is the concentrated load, L the beam span, I the moment of inertia, and E the Young's modulus of the material. Using (A1), the creep compliance of the viscoelastic beam $D(t)$ can be determined to be

$$D(t) = \frac{48I}{PL^3} \delta(t),$$

where $\delta(t)$ is the mid-span deflection history of the beam caused by a constant load P applied at zero time.

The creep compliance $D(t)$ is converted to the relaxation modulus $E(t)$ using the Hopkins–Hamming method [1957] of numerical integration of a convolution integral:

$$\int_0^t E(t)D(t-\tau) d\tau = t.$$

After $E(t)$ is obtained for each testing temperature, the shift function $a_T(T)$ can be found by shifting each relaxation curve along time axis in such a way that they create a single smooth curve, called the master relaxation curve. The direction of shifting is chosen in correspondence with the reference and current temperatures. The master curve is fitted using least squares by the CAM model (15), and the shift function is fitted using expression (9). This finally yields the constants C_1 and C_2 and reduced time $\xi(t)$.

Outline of the solution of the composite elastic cylinder problem. (Refer to Figure 3.) The constitutive equations for total strains in each cylinder are written in polar coordinates (r, θ) as

$$\varepsilon_{rr} = \frac{1+\nu}{E}((1-\nu)\sigma_{rr} - \nu\sigma_{\theta\theta} + \alpha E \Delta T), \quad \varepsilon_{\theta\theta} = \frac{1+\nu}{E}((1-\nu)\sigma_{\theta\theta} - \nu\sigma_{rr} + \alpha E \Delta T). \quad (\text{A2})$$

It is assumed that only radial displacement u exists, and the strain components are expressed (see, e.g., [Ugural and Fenster 2003]) as

$$\varepsilon_{rr} = u_{,r}, \quad \varepsilon_{\theta\theta} = \frac{u}{r}, \quad \varepsilon_{r\theta} = 0.$$

where the subscript comma means derivative. Substituting these expressions into (A2) and using the equilibrium equation

$$\frac{\partial \sigma_{rr}}{\partial r} + \frac{\sigma_{rr} - \sigma_{\theta\theta}}{r} = 0,$$

it is straightforward to obtain the solution for the unknown radial displacement. After cancellation of the terms containing temperature, the result is

$$u = c_1 r + \frac{c_2}{r},$$

where c_1 and c_2 are constants. The general solution for the stresses in each elastic cylinder is

$$\sigma_{rr} = \frac{E}{1+\nu} \left(\frac{c_1}{1-2\nu} - \frac{c_2}{r^2} \right) - \frac{E}{1-2\nu} \alpha \Delta T, \quad \sigma_{\theta\theta} = \sigma_{rr} + r \sigma_{r,r}.$$

Using the boundary conditions for the problem of composite cylinder (Figure 3), namely

$$\sigma_{rr}^{\text{inc}} = 0 \quad \text{at } r = r_0, \quad \sigma_{rr}^{\text{inc}} = \sigma_{rr}^{\text{bind}} \quad \text{at } r = r_1, \quad u_r^{\text{inc}} = u_r^{\text{bind}} \quad \text{at } r = r_1, \quad \sigma_{rr}^{\text{bind}} = 0 \quad \text{at } r = r_2,$$

the constants c_1 and c_2 are found for each cylindrical layer. Then the solution for the circumferential stresses in the binder is given by (27)–(28), in which

$$a(r) = -\frac{r_1^2}{r^2} \cdot \frac{r_0^2 - r_1^2}{r_1^2 - r_2^2} \cdot \frac{r^2 + r_2^2}{r^2 - 2\nu_i r_1^2 + r_0^2} \cdot \frac{\alpha_b(\nu_b + 1) - (\nu_i + 1)}{\nu_i + 1}, \quad (\text{A3})$$

$$b(r) = -\frac{r_1^2}{r^2} \cdot \frac{r^2 + r_2^2}{r_1^2 - 2\nu_b r_1^2 + r_2^2} \cdot \frac{(\alpha_i - 1)(\nu_i + 1)}{\nu_b + 1}, \quad c = \frac{r_0^2 - r_1^2}{r_1^2 - r_2^2} \cdot \frac{r_1^2 - 2\nu_b r_1^2 + r_2^2}{r^2 - 2\nu_i r_1^2 + r_0^2} \cdot \frac{\nu_b + 1}{\nu_i + 1}. \quad (\text{A4})$$

The solution for the total circumferential strains in the inclusion is given by (29)–(30), in which

$$d = 1 + (1 - 2\nu_i) \frac{r_1^2}{r_0^2}, \quad g = \frac{r_1^2}{r_0^2} \cdot \frac{r_0^2 - r_1^2}{r_1^2 - r_2^2} \left(1 - 2\nu_b + \frac{r_2^2}{r_1^2} \right) \frac{1 + \nu_b}{1 + \nu_i}. \quad (\text{A5})$$

References

- [AASHTO 2005] “Standard specification for performance graded asphalt binder”, standard M320-05, American Association of State Highway and Transportation Officials, Washington, DC, 2005.
- [AASHTO 2007] “Standard method of test for determining the fracture properties of asphalt binder in direct tension (DT)”, standard T314-07, American Association of State Highway and Transportation Officials, Washington, DC, 2007.
- [AASHTO 2008] “Standard method of test for determining the flexural creep stiffness of asphalt binder using the bending beam rheometer (BBR)”, standard T313-08, American Association of State Highway and Transportation Officials, Washington, DC, 2008.
- [Arutyunyan and Zevin 1997] N. K. Arutyunyan and A. A. Zevin, *Design of structures considering creep*, A. A. Balkema, Brookfield, VT, 1997.
- [Barber 1992] J. R. Barber, *Elasticity*, Kluwer, Dordrecht, 1992.
- [Bažant 1972] Z. P. Bažant, “Numerical determination of long-range stress history from strain history in concrete”, *Mater. Struct.* **5** (1972), 135–141.
- [Bykov et al. 1971] D. L. Bykov, A. A. Il'yushin, P. M. Ogibalov, and B. E. Pobedrya, “Some fundamental problems of the theory of thermoviscoelasticity”, *Mech. Compos. Mater.* **7**:1 (1971), 36–49.
- [Chien and Tzeng 1995] L. S. Chien and J. T. Tzeng, “A thermal viscoelastic analysis for thick-walled composite cylinders”, *J. Compos. Mat.* **29**:4 (1995), 525–548.
- [Ekel'chik et al. 1994] V. S. Ekel'chik, L. V. Konovalova, and V. M. Ryabov, “Use of the Laplace transform to calculate temperature stresses in viscoelastic bodies during uniform cooling”, *Mech. Compos. Mater.* **29**:5 (1994), 516–519.
- [Ferry 1961] J. D. Ferry, *Viscoelastic properties of polymers*, 2nd ed., Wiley, New York, 1961.
- [Findley et al. 1976] W. N. Findley, J. S. Lai, and K. Onaran, *Creep and relaxation of nonlinear viscoelastic materials*, Series Appl. Math. Mech. **18**, North-Holland, Amsterdam, 1976. Reprinted Dover, New York, 1989.

- [Hopkins and Hamming 1957] I. L. Hopkins and R. W. Hamming, “On creep and relaxation”, *J. Appl. Phys.* **28**:8 (1957), 906–909.
- [Huang 1993] Y. H. Huang, *Pavement analysis and design*, Prentice-Hall, Englewood Cliffs, NJ, 1993.
- [Khazanovich 2008] L. Khazanovich, “The elastic-viscoelastic correspondence principle for non-homogeneous materials with time translation non-invariant properties”, *Int. J. Solids Struct.* **45**:17 (2008), 4739–4747.
- [Kim 2005] S. S. Kim, “Direct measurement of asphalt binder thermal cracking”, *J. Mat. in Civ. Engng.* **17**:6 (2005), 632–639.
- [Kim et al. 2006] S. S. Kim, Z. D. Wyson, and J. Kovach, “Low-temperature thermal cracking of asphalt binder by asphalt binder cracking device”, *Transportation Research Record: Journal of the Transportation Research Board* **1962** (2006), 28–35.
- [Lee et al. 1959] E. Lee, J. R. M. Radok, and W. B. Woodward, “Stress analysis for linear viscoelastic materials”, *Trans. Soc. Rheology* **3**:1 (1959), 41–59.
- [Levenberg and Uzan 2007] E. Levenberg and J. Uzan, “Uniqueness of the viscoelastic time-function for asphalt-aggregate mixes”, pp. 35–48 in *International Conference on Advanced Characterization of Pavement and Soil Engineering*, edited by A. Loizos et al., Athens, 2007.
- [Marasteanu and Anderson 1999] M. O. Marasteanu and D. A. Anderson, “Improved model for bitumen rheological characterization”, pp. 133 in *Eurobitume Workshop on Performance Related Properties for Bituminous Binders*, Luxembourg, 1999.
- [Marasteanu and Anderson 2000] M. O. Marasteanu and D. A. Anderson, “Comparison of moduli for asphalt binders obtained from different test devices”, *J. Assoc. Asphalt Paving Technol.* **69** (2000), 574–607.
- [Marasteanu et al. 2004] M. O. Marasteanu, A. Basu, S. Hesp, and V. Voller, “Time-temperature superposition and AASHTO MP1a critical temperature for low-temperature cracking”, *Int. J. Pavement Engng.* **5**:1 (2004), 31–38.
- [Marasteanu et al. 2007] M. O. Marasteanu, M. A. Zofka, M. Turos, et al., “Investigation of low temperature cracking in asphalt pavements”, *National Pooled Fund Study 776, Minnesota Department of Transportation* (2007).
- [Mesquita et al. 2001] A. D. Mesquita, H. B. Coda, and W. S. Venturini, “Alternative time marching process for BEM and FEM viscoelastic analysis”, *Int. J. Num. Meth. Engng.* **51** (2001), 1157–1173.
- [Rabotnov 1966] Y. N. Rabotnov, *Ползучесть элементов конструкций*, Nauka, Moscow, 1966. Translated as *Creep problems in structural members*, Series Appl. Math. Mech **7**, North-Holland, Amsterdam, 1969, and as *Creep in structural elements: selected chapters*, Air Force Systems Command, Wright-Patterson AFB, 1970.
- [Schwarzl and Staverman 1952] F. Schwarzl and A. J. Staverman, “Time-temperature dependence of linear viscoelastic behavior”, *J. Appl. Phys.* **23**:8 (1952), 838–843.
- [Taylor et al. 1970] R. L. Taylor, K. S. Pister, and G. L. Goudreau, “Thermochemical analysis of viscoelastic solids”, *Int. J. Num. Meth. Engng.* **2** (1970), 45–59.
- [Ugural and Fenster 2003] A. C. Ugural and S. K. Fenster, *Advanced strength and applied elasticity*, 4th ed., Prentice-Hall, New Jersey, 2003.
- [Volterra 1913] V. Volterra, *Leçons sur les fonctions de lignes*, Gauthier-Villars, Paris, 1913.
- [Williams et al. 1955] M. L. Williams, R. F. Landel, and J. D. Ferry, “The temperature dependence of relaxation mechanism in amorphous polymers and other glass-liquids”, *J. American Chem. Soc.* **77** (1955), 3701–3707.
- [Wineman and Rajagopal 2000] A. S. Wineman and K. R. Rajagopal, *Mechanical response of polymers: an introduction*, Cambridge University Press, New York, 2000.

Received 27 Jan 2010. Revised 13 Jul 2010. Accepted 25 Jul 2010.

ANDREY V. PYATIGORETS: pyati002@umn.edu

Department of Civil Engineering, University of Minnesota, 500 Pillsbury Drive SE, Minneapolis, MN 55455, United States

MIHAI O. MARASTEANU: maras002@umn.edu

Department of Civil Engineering, University of Minnesota, 500 Pillsbury Drive SE, Minneapolis, MN 55455, United States

LEV KHAZANOVICH: khaza001@umn.edu

Department of Civil Engineering, University of Minnesota, 500 Pillsbury Drive SE, Minneapolis, MN 55455, United States

HENRYK K. STOLARSKI: stola001@umn.edu

Department of Civil Engineering, University of Minnesota, 500 Pillsbury Drive SE, Minneapolis, MN 55455, United States

SUBMISSION GUIDELINES

ORIGINALITY

Authors may submit manuscripts in PDF format online at the Submissions page. Submission of a manuscript acknowledges that the manuscript is original and has neither previously, nor simultaneously, in whole or in part, been submitted elsewhere. Information regarding the preparation of manuscripts is provided below. Correspondence by email is requested for convenience and speed. For further information, write to one of the Chief Editors:

Davide Bigoni	bigoni@ing.unitn.it
Iwona Jasiuk	ijasiuk@me.concordia.ca
Yasuhide Shindo	shindo@material.tohoku.ac.jp

LANGUAGE

Manuscripts must be in English. A brief abstract of about 150 words or less must be included. The abstract should be self-contained and not make any reference to the bibliography. Also required are keywords and subject classification for the article, and, for each author, postal address, affiliation (if appropriate), and email address if available. A home-page URL is optional.

FORMAT

Authors can use their preferred manuscript-preparation software, including for example Microsoft Word or any variant of T_EX. The journal itself is produced in L^AT_EX, so accepted articles prepared using other software will be converted to L^AT_EX at production time. Authors wishing to prepare their document in L^AT_EX can follow the example file at www.jomms.org (but the use of other class files is acceptable). At submission time only a PDF file is required. After acceptance, authors must submit all source material (see especially Figures below).

REFERENCES

Bibliographical references should be complete, including article titles and page ranges. All references in the bibliography should be cited in the text. The use of BibT_EX is preferred but not required. Tags will be converted to the house format (see a current issue for examples); however, for submission you may use the format of your choice. Links will be provided to all literature with known web locations; authors can supply their own links in addition to those provided by the editorial process.

FIGURES

Figures must be of publication quality. After acceptance, you will need to submit the original source files in vector format for all diagrams and graphs in your manuscript: vector EPS or vector PDF files are the most useful. (EPS stands for Encapsulated PostScript.)

Most drawing and graphing packages—Mathematica, Adobe Illustrator, Corel Draw, MATLAB, etc.—allow the user to save files in one of these formats. Make sure that what you're saving is vector graphics and not a bitmap. If you need help, please write to graphics@mathscipub.org with as many details as you can about how your graphics were generated.

Please also include the original data for any plots. This is particularly important if you are unable to save Excel-generated plots in vector format. Saving them as bitmaps is not useful; please send the Excel (.xls) spreadsheets instead. Bundle your figure files into a single archive (using zip, tar, rar or other format of your choice) and upload on the link you been given at acceptance time.

Each figure should be captioned and numbered so that it can float. Small figures occupying no more than three lines of vertical space can be kept in the text (“the curve looks like this:”). It is acceptable to submit a manuscript with all figures at the end, if their placement is specified in the text by means of comments such as “Place Figure 1 here”. The same considerations apply to tables.

WHITE SPACE

Forced line breaks or page breaks should not be inserted in the document. There is no point in your trying to optimize line and page breaks in the original manuscript. The manuscript will be reformatted to use the journal's preferred fonts and layout.

PROOFS

Page proofs will be made available to authors (or to the designated corresponding author) at a Web site in PDF format. Failure to acknowledge the receipt of proofs or to return corrections within the requested deadline may cause publication to be postponed.

Journal of Mechanics of Materials and Structures

Volume 5, No. 5

May 2010

-
- Axial compression of hollow elastic spheres** ROBERT SHORTER, JOHN D. SMITH,
VINCENT A. COVENEY and JAMES J. C. BUSFIELD 693
- Coupling of peridynamic theory and the finite element method**
BAHATTIN KILIC and ERDOGAN MADENCI 707
- Genetic programming and orthogonal least squares: a hybrid approach to
modeling the compressive strength of CFRP-confined concrete cylinders**
AMIR HOSSEIN GANDOMI, AMIR HOSSEIN ALAVI, PARVIN ARJMANDI,
ALIREZA AGHAEIFAR and REZA SEYEDNOUR 735
- Application of the Kirchhoff hypothesis to bending thin plates with different
moduli in tension and compression** XIAO-TING HE, QIANG CHEN, JUN-YI
SUN, ZHOU-LIAN ZHENG and SHAN-LIN CHEN 755
- A new modeling approach for planar beams: finite-element solutions based on
mixed variational derivations**
FERDINANDO AURICCHIO, GIUSEPPE BALDUZZI and CARLO LOVADINA 771
- SIFs of rectangular tensile sheets with symmetric double edge defects**
XIANGQIAO YAN, BAOLIANG LIU and ZHAOHUI HU 795
- A nonlinear model of thermoelastic beams with voids, with applications**
YING LI and CHANG-JUN CHENG 805
- Dynamic stiffness vibration analysis of thick spherical shell segments with variable
thickness** ELIA EFRAIM and MOSHE EISENBERGER 821
- Application of a matrix operator method to the thermoviscoelastic analysis of
composite structures** ANDREY V. PYATIGORETS, MIHAI O.
MARASTEANU, LEV KHAZANOVICH and HENRYK K. STOLARSKI 837



1559-3959(2010)5:5;1-D